UNIVERSITY OF SOUTHAMPTON

OPTICAL GAS SENSORS BASED ON CORRELATION SPECTROSCOPY USING A FABRY-PEROT INTERFEROMETER

Everardo Vargas-Rodriguez

Thesis for the degree of Doctor of Philosophy

OPTOELECTRONICS RESEARCH CENTRE

FACULTY OF ENGINEERING, SCIENCE AND MATHEMATICS

AUGUST 2007

Dedicated to my lovely wife Landy and my sweet daughter Hannah.

UNIVERSITY OF SOUTHAMPTON

ABSTRACT

FACULTY OF ENGINEERING, SCIENCE AND MATHEMATICS

OPTOELECTRONICS RESEARCH CENTRE

Doctor of Philosophy

OPTICAL GAS SENSORS BASED ON CORRELATION SPECTROCOPY USING A FABRY-PEROT INTERFEROMETER

by Everardo Vargas-Rodriguez

In this work we present an analysis of gas sensors based on correlation spectroscopy with a Fabry-Perot interferometer (FPI). In this technique the spectral FPI transmission fringe pattern is matched with ro-vibrational absorption lines. To produce the cross correlation principle the FPI fringe pattern must be shifted along the frequency axis. Hence as the spectral FPI fringes are equidistant and symmetric therefore the ro-vibrational absorption lines of the target molecule must be almost equidistant. Well resolved ro-vibrational lines with Lorentzian line shapes and with almost equidistant spectral separation are characteristics of most diatomic and linear molecules, i.e. CO_2, CO, N_2O, and some specific absorptions bands of symmetric top and spherical top molecules eg. NH_3, CH_4 at one atmosphere pressure.

In this work we review two general sensor designs, in the first the FPI it is illuminated with a collimated beam and in the second design the FPI it is illuminated by a converging beam. In the collimated beam design all the rays reaching the FPI have the same angle of incidence whilst in converging beam the incident rays have different angles of incidence. Hence the spectral FPI fringe pattern it is affected by the different angles of incidence and therefore it is essential to consider these effects during the evaluation of the sensor response.

A novel analytical method based on the Fourier transform which gives a good insight of the gas sensor design based on correlation spectroscopy with a FPI it is presented which we call the convolution method. The method provides a simple way to evaluate much faster the sensor response, and using the Fourier transform characteristics the functions involved in the mathematical model of the sensor response the optimal cavity length of the FPI can be directly determined and it is shown that if the sensor signal will be recovered by a Phase Sensitivity Detector the optimum mirror reflectivity is 0.41 regardless of the other parameters. Moreover using the convolution method the optimal FPI mirror reflectivity can be quickly evaluated. The method also gives us guidance on selecting the best bandpass filter for the application. In this work we also review the effects of the blackbody converging beam and some possible solutions to minimize the effect of the degraded FPI fringe pattern are proposed. In this case it is important to consider the spurious FPI fringe patterns produced by reflection within the mirrors substrates of FPI mirrors.

Finally based on all these knowledge we describe a full methodology to simulate the sensor response. It is important to mention that in our methodology we not use ‘fitting parameters’ to adjust the simulated results with experimental measurements. Our experimental measurements strongly support the simulated sensor response obtained with our methodology. Therefore the methodology can be applied to design other gas sensors based on cross correlation spectroscopy with a FPI as a modulator. Moreover it is shown that these sensors present an almost negligible sensitivity to molecules other than the target. Finally based on our simulated and experimental results we can conclude that this sensor design configuration is viable to fabricate commercial gas sensors if the FPI and the detector are integrated within a MEMS structure.

Contents

1. Gas Sensors. 1

1.1. Electrochemical Gas Sensors. 4

1.1.1. Conductivity Gas Sensors. 4

1.1.2. Piezoelectric Gas Sensors. 5

1.1.3. Amperometric Gas Sensors. 6

1.2. Optical Gas Sensors. 8

1.2.1. Interaction of light with molecules. 8

1.2.1.1 Mid Infrared ro-vibrational transitions 11

1.2.2. Types of Optical Gas sensors 14

1.2.2.1 Dispersive Optical Gas Sensors 14

1.2.2.2 Non-Dispersive Optical Gas Sensors 15

1.3. Optical Gas sensors as concentration monitors 16

1.3.1. NDS Optical Gas sensor as concentration monitor 16

1.3.2. Optical Gas Sensors based on Ellipsometry 17

1.3.3. Optical Gas Sensors based on the Stark Effect. 18
1.3.4. Optical gas sensors based cavity ring-down spectroscopy. ... 19
1.4. NDS Optical Gas sensors as concentration monitors.....21
1.4.1. NDS Basic Components..... 22
1.4.1.1 Sources for MIR-NDS.....22
1.4.1.2 Detectors for MIR-NDS.....27
1.4.2. NDS Single-Beam Single-Wavelength..... 29
1.4.3. NDS Single-Beam Dual-Wavelength 31
1.4.4. NDS, Tuneable Absorption Spectroscopy (TAS). 32
1.5. NDS based on Cross Correlation Spectroscopy 36
1.6. NDS-based on Fabry-Perot Cross Correlation Spectroscopy.41
1.6.1. NDS gas sensors with Fabry-Perot Interferometers that do not satisfy the Correlation Spectroscopy principle. 44
1.6.1.1 The medium gap FPI.....44
1.6.1.2 The narrow gap FPI gas sensor.....45
1.7. Optical Gas sensors based on Micromachined Fabry-Perot Interferometers (MFPI). 46
1.8. Potential applications of MFPIs for cross correlation spectroscopy. 48
1.9. Thesis Outline. 48
1.10. References.....51
2. High resolution spectroscopic modelling. 58
2.1. Absorption Spectra for diatomic and linear molecules. 59
2.1.1. Carbon Dioxide Absorption Model 60
2.1.1.1. Symmetry elements and operations.....60
2.1.1.2. Line position at high resolution.....62
2.1.1.3. Types of Infrared bands.....63
2.1.1.4. Symmetry effects.....65
2.1.1.5. Ro-vibrational Line Strength.....66
2.1.1.6. Absorption Line Shape.....69

2.1.1.7. Validation of the CO_2 model. 76
2.1.2. Nitrous Oxide Spectroscopic Model 81
2.1.2.1. Validation of the N_2O model. 85
2.1.3. Carbon Monoxide Spectroscopic Model 89
2.1.3.1. Validation of CO model. 94
2.2. Water vapour Spectroscopic Models 98
2.2.1. The ν_2 Absorption Band of $H_2{}^{16}O$. 99
2.2.1.1. The Watson Hamiltonian, A reduction. 100
2.2.1.2. Energy Levels 102
2.2.1.3. Selection Rules and Line Positions. 103
2.2.1.4. Line Intensities 105
2.2.2. The $2\nu_2$, ν_1 and ν_3 Bands of $H_2{}^{16}O$. 111
2.2.2.1. Hamiltonian Matrix, and Energy Levels. 112
2.2.2.2. Selection Rules 114
2.2.2.3. Line Intensities for the $2\nu_2$, ν_1, and ν_3 bands of $H_2{}^{16}O$. 120
2.2.3. Validation of the H_2O model. 125
2.3. References 129
3. Optimal system parameters. 133
3.1. System Mathematical Model 134
3.2. Definition of the Mathematical Model Functions 138
3.3. System Response described as a convolution. 141
3.3.1. The convolution method 143
3.4. Fourier transform characterisation of the system functions. 147
3.4.1. Fourier characterisation of the FPI fringes 147
3.4.2. Fourier characterisation of the system response. 151
3.4.3. Fourier characterisation of the $G(\nu)$ function. 151
3.4.3.1. Optimal value of the cavity length 155
3.4.4. Optimal Reflectivity value. 158
3.4.5. Design of a CO gas sensor an example 160

3.5. Filter selection approach.....163
3.5.1.1. Minimising the Background modulation for the CO_2 sensor.....165
3.5.1.2. Minimising the Background modulation in for CO sensor.....169
3.5.2. Manufacturing errors.....171
3.6. Conclusions.....174
3.7. References.....174
4. Analysis of a FPI illuminated with a converging beam.176
4.1. The Gas Sensor Optical Setup.....177
4.2. Flux Distribution as a function of the solid angle.....179
4.3. FPI fringes considering the $f/\#$.....182
4.3.1. $f/\#$ effect and FPI's optical thickness.....184
4.3.1.1. Narrow gap FPI.....184
4.3.1.2. Medium gap FPI.....186
4.3.1.3. Wide gap FPI.....187
4.4. Parasitic reflection effects.....189
4.4.1.1. Narrow gap FPI and SPRF.....193
4.4.1.2. Medium gap FPI and SPRF.....194
4.4.1.3. Wide gap FPI and SPRF.....196
4.4.2. Minimizing the SPRF effects.....198
4.5. Conclusions.....202
4.6. References.....202
5. Experimental Sensor Results.....203
5.1. Sensor Response Modelling.....204
5.1.1. CH_4 Gas Sensor Design.....210
5.1.1.1. Optimum Cavity length d and $f/\#$.....210
5.1.1.2. Optimum Reflectivity R.....211
5.1.2. CO_2 Gas Sensor Design.....213
5.1.2.1. Optimum Cavity length d and $f/\#$.....213
5.1.2.2. Optimum Reflectivity R.....216
5.1.3. CO Gas Sensor Design.....216

5.1.3.1. Optimum Cavity length d and $f/\#$ 217
5.1.3.2. Optimum Reflectivity R. 218
5.2. Experimental Setup. 220
5.2.1.1. FPI Mirrors 222
5.2.1.2. FPI Contrast Measurement 225
5.2.1.3. The cavity length scan and the PZT image effect. 229
5.2.1.4. Detector output, PZT image effect, and detector responsivity. 229
5.3. CH_4 Experimental Measurements 239
5.3.1. Amplitude Modulation as a function of the CH_4 concentration 241
5.4. CO_2 Experimental Measurements 242
5.4.1. CO_2 Sensor Response as a function of the Concentration ... 244
5.5. CO Experimental Measurements 245
5.5.1. CO Sensor Response as a function of the Concentration 246
5.6. Noise and Minimum Detectable Gas Concentrations. 247
5.6.1. System Noise 247
5.6.1.1. Detector noise 248
5.6.1.2. Resistor Noise 251
5.6.1.3. PSD input Noise 252
5.6.2. Noise Bandwidth 253
5.6.3. Minimum detectable CH_4 concentration 255
5.6.4. Minimum detectable CO concentration. 258
5.6.5. Minimum detectable CO_2 concentration. 262
5.7. Cross Sensitivity 264
5.7.1. CH_4 sensor cross sensitivity 265
5.7.2. CO sensor cross sensitivity 267
5.7.3. CO_2 sensor cross sensitivity 270
5.8. Conclusions 270
5.9. References 271
6. Summary of Results and Conclusions. 273

6.1.1. Recapitulation of Thesis Objectives 273

6.2. Remarks on the analysis of the design with a collimated beam. 274

6.2.1.1 The convolution method 274

6.3. Remarks on the analysis of the design with converging beam. 276

6.4. Experimental Results. 277

6.5. Future Work. 277

6.6. References.....278

A. Publication List.....279

List of Figures

Figure 1.1- Transitions (a) absorption, (b) stimulated emission and (c) scattering. 9
Figure 1.2- Linear molecule. 11
Figure 1.3- Ro-vibrational absorption spectra. a)CO, b)H_2O and c) CH_4. 13
Figure 1.4- Dispersive Gas Sensor. 14
Figure 1.5- Non-Dispersive gas sensor. 15
Figure 1.6- Setup of some optical gas sensor for concentration monitoring. a) basic NDR sensor; b) Ellipsometric gas sensor (redraw from Wang et al [38]); c) Gas sensor based on the Stark modulation; d) Optical gas sensor based cavity ring-down spectroscopy (redraw from O'Keefe and Deacon [39]). 17
Figure 1.7- Spectral radiance of a blackbody at different temperatures. 23
Figure 1.8- Emission spectral profile for a LED with peak emission at $\lambda = 4.2$µm. Graphic taken from Ioffe LED LTd. 25
Figure 1.9- Spectral Emission Laser a) Multimode (bottom) and single mode (top) laser. b) Spectral emission profile of a quantum cascade laser DFB electrically tuned along the wavelength. Graphs taken from (a) nanonoplus GmbH and (b) Alpes Lasers SA. 25

Figure 1.10- Spectral response D^* for different detectors. Graph taken from Hamamatsu [52] 28
Figure 1.11- Simulated ro-vibrational spectra of CO, CO_2 and H_2O and a typical spectral band pass filter response. Here $S(\nu) = 1$. 29
Figure 1.12- Simulated ro-vibrational spectra of CO, CO_2 and H_2O showing the changes of increasing the CO_2 concentration and H_2O. b) Detail showing how the H_2O absorptions overlap the CO absorptions. Here $S(\nu) = 1$ 30
Figure 1.13- Optical Gas sensor with *Single-Beam Dual-Wavelength.* 32
Figure 1.14- Simulated ro-vibrational spectra of CO, CO_2 and H_2O . The measurement channel it is defined by $Fil_1(\nu)$ and the reference channel by $Fil_2(\nu)$. 32
Figure 1.15- Ideal laser emission tuned to match a single ro-vibrational of CO_2. For clarity the spectral region close to the narrow laser emission and the ro-vibrational transition are shown in the inset. 34
Figure 1.16- Goody's Cross-Correlation Gas Sensor Setup [60]. 37
Figure 1.17- Ro-vibrational transmission spectra of a target molecule shifted along the wavenumber axis as required by the cross correlation function. 38
Figure 1.18- Dakin's Cross-Correlation Gas Sensor Setup [43, 61]. 40
Figure 1.19- Plane Fabry-Perot Interferometer 42
Figure 1.20- FPI transmission fringes matched with CH_4 rotational lines here $d = 0.055$ cm^{-1}. A slight change in the cavity length $d + \Delta d$ shifts the FPI fringes along the wavenumber axis. The CH_4 spectrum is shifted up 0.4 units for clarity. 42
Figure 1.21- NDS Gas sensor setup based with an FPI. 43
Figure 1.22- Simulated wide FPI fringe for a CH_4 medium gap sensor. The CH_4 absorption spectrum is shifted up 0.4 units for clarity. FPI cavity length $d = 5 \times 10^{-4}$ cm. 45
Figure 1.23- Simulated narrow gap FPI modulator with $d = 0$ µm. For ON state $\Delta d_1 = 0$ µm and for the OFF state $\Delta d_2 = 3.3/4$ µm. For clarity the CH_4 absorption band is shifted up 0.4 units. 46
Figure 2.1- Molecule with a centre of symmetry 61
Figure 2.2- Molecules with a p-*fold axes.* a) Molecule with a C_2-*fold* axis; b) Molecule with a ∞-*fold axes.* 62
Figure 2.3- Simulated absorption spectrum of CO_2. This spectrum includes several bands due to $^{12}C^{16}O_2$, $^{13}C^{16}O_2$ and $^{16}O^{12}C^{18}O$ isotopomers. 75

Figure 2.4- Residual difference in line position between our calculated positions and HITRAN 2004 for the $00011 \leftarrow 00000$ of $^{12}C^{16}O_2$. 78

Figure 2.5- Residual difference in line position between our calculated positions and HITRAN 2004 for the $00011 \leftarrow 00000$ of $^{13}C^{16}O_2$. 78

Figure 2.6- Residual difference in line position between our calculated positions and HITRAN 2004 for the $00011 \leftarrow 00000$ of $^{16}O^{12}C^{18}O_2$. 79

Figure 2.7- Error in Line intensities between HITRAN 2004 and the computed values 2004 for the $00011 \leftarrow 00000$ of $^{12}C^{16}O_2$. 79

Figure 2.8- Error in Line intensities between HITRAN 2004 and the computed values 2004 for the $00011 \leftarrow 00000$ of $^{13}C^{16}O_2$. 80

Figure 2.9- Error in Line intensities between HITRAN 2004 and the computed values 2004 for the $00011 \leftarrow 00000$ of $^{16}O^{12}C^{18}O_2$. 80

Figure 2.10- Simulated absorption spectra of N_2O. In the lower figure, the strong band shown is due to the fundamental band $1000 \leftarrow 0000$ centred at 1284.90 cm^{-1}; while the weaker band is due to the overtone 0200-000. In the upper figure the strong absorptions are due to the $0001 \leftarrow 0000$ band centred at 2223.7 cm^{-1} 83

Figure 2.11- Residual difference in line position between our calculated positions and HITRAN 2004 for the $0001 \leftarrow 0000$ of $^{14}N^{14}N^{16}O$. 85

Figure 2.12- Residual difference in line position between our calculated positions and HITRAN 2004 for the $0001 \leftarrow 0000$ of $^{14}N^{15}N^{16}O$. 86

Figure 2.13- Error in Line intensities between HITRAN 2004 and the computed values 2004 for the $0001 \leftarrow 0000$ of $^{14}N^{14}N^{16}O$. 87

Figure 2.14- Error in Line intensities between HITRAN 2004 and the computed values 2004 for the $0001 \leftarrow 0000$ of $^{14}N^{15}N^{16}O$. 88

Figure 2.15- Simulated CO absorption spectrum at 4.7 μm. This plot includes the 1-0 fundamental bands of the $^{12}C^{16}O$, $^{13}C^{16}O$, and $^{12}C^{18}O$ isotopomers. 91

Figure 2.16- Residual difference in line position between our calculated positions and HITRAN 2004 for the $1 \leftarrow 0$ of $^{12}C^{16}O$. 95

Figure 2.17- Residual difference in line position between our calculated positions and HITRAN 2004 for the $1 \leftarrow 0$ of $^{13}C^{16}O$. 96

Figure 2.18- Error in Line intensities between HITRAN 2004 and the computed values 2004 for the $1 \leftarrow 0$ of $^{12}C^{16}O$. 96

Figure 2.19- Error in Line intensities between HITRAN 2004 and the computed values 2004 for the $1 \leftarrow 0$ of $^{13}C\,^{16}O$. 97

Figure 2.20- Simulated $010 \leftarrow 000$ band of water vapour (the ν_2 bending mode). Monochromatic absorption coefficient (1/molecules-cm^{-2}). 107

Figure 2.21- Hamiltonian submatrices for an even J level [28] 117

Figure 2.22- Hamiltonian submatrices for an odd J level [28]. 118

Figure 2.23- Hamiltonian submatrices for special cases of J level [28]. 119

Figure 2.24- Absorption spectrum of the $2\nu_2$, ν_1, and ν_3 bands of $H_2{}^{16}O$. 124

Figure 2.25- Difference in line position between our calculated positions and HITRAN 2004 for the ν_2 of $H_2{}^{16}O$ considering up to $J'' \leq 5$. 126

Figure 2.26- Difference in line position between our calculated positions and HITRAN 2004 for the ν_2 of $H_2{}^{16}O$ for $J'' = 8$ and $J'' = 9$. 127

Figure 2.27- Error in Line intensities between HITRAN 2004 and the computed values for the ν_2 of $H_2{}^{16}O$ considering up to $J'' \leq 5$. 128

Figure 2.28- Error in Line intensities between HITRAN 2004 and the computed values for the ν_2 of $H_2{}^{16}O$ for $J'' = 8$ and $J'' = 9$. 128

Figure 3.1- Basic configuration of a gas sensors based on correlation spectroscopy that use a Fabry-Perot Interferometer (FPI) as a modulator. 134

Figure 3.2- FPI's fringes and ro-vibrational lines due to CO_2. a) Absorption lines are matched to the FPI's fringes. b) FPI's fringes shifted along the wavenumber axis. The CO_2 spectrum is shifted up 0.4 units for clarity. 135

Figure 3.3- Simulated transmission through the system as a function of the cavity length Δd. 136

Figure 3.4- Simulated monochromatic absorption spectrum of CO_2. It model includes the spectra for the $^{12}C^{16}O_2$, $^{13}C^{16}O_2$ and $^{16}O^{12}C^{18}O$ isotopomers. 140

Figure 3.5- Transmission Profile $G(\nu)$. 140

Figure 3.6- Filter response and some ro-vibrational absorption lines of CO_2 144

Figure 3.7- Amplitude Modulation as a function of the gas concentration (Amplitude Modulation in Arbitrary Units). 145

Figure 3.8- Fourier Transform of the Airy Function $I_{FP}(R, n, d, \xi)$. 150

Figure 3.9- Magnitude for the impulses of $I_{FP}(R, n, d, \xi)$ as a function of the reflectivity. 150

Figure 3.10- Typical $|G(\xi)$ for a CO_2 sensor. 152

Figure 3.11- Fourier transform of the monochromatic absorption coefficient $(|\alpha(\xi)|)$ for the CO_2 at 4.3 μm. The inset figures show the Fourier Transform $(|\alpha(\xi)|)$ considering just the P and the R branches. 154
Figure 3.12- Amplitude Modulation as a function of the optical thickness (nd); evaluated by direct calculation of equation (3.2). The reflectivity was fixed as $R = 0.30$. (Amplitude Modulation in arbitrary units)..... 156
Figure 3.13- Amplitude Modulation as a function of the optical thickness (nd); evaluated using the convolution method. The reflectivity was fixed as $R = 0.30$. (Amplitude Modulation in arbitrary units) 156
Figure 3.14- FPI Transmission for $d = 0$ and for $d = 0 + \lambda_0/4$. 157
Figure 3.15-Amplitude Modulation as a function of the Reflectivity (*AM* in arbitrary units)..... 159
Figure 3.16- $G(\nu)$ profile for the CO sensor. 160
Figure 3.17- Amplitude Modulation as a function of R and nd evaluated by direct calculation. (*AM* in arbitrary units) 161
Figure 3.18- $|G(\xi)|$ for the CO sensor. 162
Figure 3.19- Amplitude Modulation as a function R for the CO sensor. (*AM* in arbitrary units)..... 162
Figure 3.20. Trial filter performance for a CO_2 sensor. 165
Figure 3.21- Magnitude of the Fourier Transform of the filters for the CO_2 sensor..... 166
Figure 3.22- Background Amplitude Modulation as a function of the optical thickness. (*AM* in arbitrary units)..... 168
Figure 3.23- Amplitude Modulation as a function of the Concentration. (*AM* in arbitrary units)..... 168
Figure 3.24- Filter performances for a CO sensor. 169
Figure 3.25- Fourier transforms of the filter performances for the CO sensor. 170
Figure 3.26- Background Amplitude Modulation for the CO sensor. (*AM* in arbitrary units)..... 170
Figure 3.27- Filter performances with error tolerances. 172
Figure 3.28- Fourier Transform of the filters shown in figure 3.27..... 173
Figure 3.29- Amplitude Modulation for the CO sensor considering error in the filters. 173
Figure 4.1-FPI placed at image point $(2f)$. 177

Figure 4.2- FPI fringes considering different angles of incidence. $R = 0.30$, $nd = 0.05$ cm. 178

Figure 4.3- Differential of source area viewed by the detector/FPI for a given θ. (Adapted from Dereniak and Boreman 1996 [3]). 180

Figure 4.4- Flux distribution as a function of the solid angle. A differential element of source area ($\mathrm{d}A_s$) is formed per each differential element of solid angle. 182

Figure 4.5- Average spectral FPI transmission profiles per differential element of solid angle. $R = 0.30$, $nd = 0.05$cm, $\theta_{\max} = 0.0624$rad. 183

Figure 4.6- Final FPI transmission fringe pattern over all the angles of incidence. Here $R = 0.30$, $nd = 0.05$cm, $\theta_{\max} = 0.0624$rad. 184

Figure 4.7- Typical FPI transmission fringe pattern for short cavity lengths and different $f/\#$ values. a) cavity length $d = 0$ μm; b) cavity length $d = 1.15$μm. In both cases $R = 0.45$. 185

Figure 4.8- FPI transmission fringes with cavity lengths of 10-50 μm and different $f/\#$ values. a) cavity length $d = 10$μm; b) cavity length $d = 50$μm. 186

Figure 4.9- FPI transmission fringes considering a cavity length $d = 5 \times 10^{-2}$cm and different $f/\#$ values. 187

Figure 4.10- FPI transmission fringes considering a cavity length $d = 0.28$ cm and different $f/\#$ values 188

Figure 4.11- FPI transmission fringes considering a cavity length $d = 0.28$cm and large $f/\#$ values. 189

Figure 4.12- Multiple beam fringes on the FPI mirrors. 190

Figure 4.13- FTIR scan of a Pyrex substrate 0.2 mm thickness coated with a ZnS layer 444 nm. In the small box a detail of the scan shows the SPRF produced on the pyrex substrate. 191

Figure 4.14- FPI with two plane and parallel mirrors coated with a thin film layer. 191

Figure 4.15- FPI fringes for a narrow gap FPI considering the $f/\#$ and SPRF. a) $d = 0$ μm, b) $d = 1.15$μm. 194

Figure 4.16- FPI fringes for a cavity length $d = 10$μm counting the $f/\#$ and SPRF. 195

Figure 4.17- Simulated and measured FPI fringe patterns pondering the $f/\#$, SPRF and $d = 10$μm. a) simulation results, b) Measured FTIR background spectrum with a resolution of 0.5 cm^{-1}. (Arbitrary units). 195

Figure 4.18- Simulated FPI fringe pattern considering $d = 0.05$ cm SPRF and the $f/\#$. 196

Figure 4.19- FTIR measurements for a FPI with $d = 0.045$cm. a) Background FTIR scan with resolution 4 cm^{-1}; b) Background FTIR scan with resolution 2 cm^{-1}..... 196

Figure 4.20- Simulated FPI fringe pattern pondering a $d = 0.29$cm, $f/7$ and the SPRF. 197

Figure 4.21- FTIR background spectrum for a FPI with cavity length $d = 0.29$cm..... 197

Figure 4.22- Simulated FPI fringes; $d = 0.28$cm, CaF_2 substrates 0.2 mm thickness.... 199

Figure 4.23- Simulated FPI fringes; $d = 0.28$cm, CaF_2 substrates 5 mm thickness..... 199

Figure 4.24- FPI with flat and parallel mirrors with AR coatings. 200

Figure 4.25- Simulated FPI fringe pattern for $d = 0.28$cm, CaF_2 substrates 1mm thickness with AR Cryolite layers..... 201

Figure 4.26- Simulated FPI fringe pattern for $d = 0.28$cm, CaF_2 substrates 2mm thickness, with AR Cryolite layers. 201

Figure 5.1- Experimental gas setup..... 203

Figure 5.2- Amplitude modulation as function of the cavity length and f number counting the $f/\#$ effect on the FPI fringes..... 205

Figure 5.3- Amplitude Modulation obtained with both methods, the Direct Numerical Method and the Convolution Method. (Arbitrary Units). 206

Figure 5.4- Measured Filter Response for a CO_2 sensor..... 206

Figure 5.5- Amplitude Modulation as a function of the cavity length and the f number. Here a blackbody converging source was considered..... 208

Figure 5.6- Amplitude Modulation for the CO_2 sensor pondering the blackbody source. a) AM as a function of the f number with $d = 0.28$ cm; b) AM as a function of the cavity length with $f/18$ cm. Gas pathlength $l = 1.4$ cm and $C = 8100$ ppm CO_2..... 209

Figure 5.7- Simulated Blackbody Radiance Spectra..... 209

Figure 5.8- Amplitude Modulation as a function of the cavity length and the f number for the CH_4 sensor. Results obtained by the Direct Numerical Method (upper) and the upper Convolution method (lower). $R = 0.45$ and $C = 50\%$. 211

Figure 5.9- Amplitude Modulation for the CH_4 sensor as a function of the cavity length (b) and the f number (a). 212

Figure 5.10- Measured response of the filter used for the CH_4 gas sensor. 212

Figure 5.11- Function $G(\nu) = L(\nu, 1074\text{K})\, Fil(\nu)\, T(\nu, C)$ and its Fourier transform for the CH_4 sensor for different gas concentrations.....212

Figure 5.12- AM as a function of the reflectivity for the CH_4 sensor with $d = 0.055$ cm and $f/10$. b) AM as a function of the CH_4 concentration for $R_0 = 0.4$.....213

Figure 5.13- Simulated normalized transmission fringe patterns for a FPI with $d = 0.28$ cm, $R = 0.45$ and different f numbers $f/\#$.....214

Figure 5.14- Function $G(\nu) = L(\nu, 1074K)\, Fil(\nu)\, T(\nu, C)$ for the CO_2 sensor and its Fourier transform $G(\xi)$. 215

Figure 5.15- Amplitude Modulation as a function of the reflectivity for the CO_2 sensor. b) AM as a function of the CO_2 concentration for $R_0 = 0.4$ 215

Figure 5.16- Measured filter response used for the CO sensor.....216

Figure 5.17- Simulated Amplitude Modulation AM as a function of the f number and cavity length for the CO sensor with $C = 10000$ and $R = 0.45$. 218

Figure 5.18- Simulated amplitude modulation AM for 10000 ppm CO concentration and $R = 0.45$. a) AM as a function of the f number; b) AM as a function of the cavity length.....219

Figure 5.19- Normalized transmission fringe patterns for FPI with $d = 0.145$ and $R = 0.45$ and different f numbers. 219

Figure 5.20- Function $G(\nu) = L(\nu, 1074K)\, Fil(\nu)\, T(\nu, C)$ for the CO sensor and its Fourier transform $G(\xi)$. 220

Figure 5.21- Amplitude modulation as a function of the reflectivity (left) for $d = 0.145$ cm, $f/12$ and gas pathlength of $l = 1.4$ cm. AM as a function of the concentration at R_0.....220

Figure 5.22- FPI fringe patterns counting the SPRF for a 4mm thickness CaF_2 substrates coated with a ZnS layer of 470nm thickness. 223

Figure 5.23- Measured FPI mirror reflectivity in the region from $2.85 \leq \lambda \leq 6.66$ µm..225

Figure 5.24- Experimental setup of a FPI with a collimated HeNe laser at 1.52 µm. ..226

Figure 5.25- Measured FPI mirror reflectivity at $\lambda \approx 1.52$ µm and $\lambda \approx 632$ nm. 227

Figure 5.26- Simulated FPI fringe pattern for $\lambda \approx 1.5$ µm, $R = 0.305$ and $nd = 0.055$ cm. 228

Figure 5.27- Measured FPI fringe pattern as a function of the cavity length Δd. Here mirrors with $R = 0.305$ were utilised.....228

Figure 5.28- Modulated signal reaching the detector $[\phi(R, n, d, \Delta d, \theta_{\max}, C)]$ as a function of the cavity length scan. The triangular waveform shows the PZT drive signal (arbitrary units). 230

Figure 5.29- Harmonics of the modulated signal reaching the detector as a function of the cavity length. PZT drive signal in arbitrary units..... 231

Figure 5.30- Responsivity for the LTI Q1 pyroelectric detector. Data taken from DIAS Infrared Systems [5]. 234

Figure 5.31- Final output detector response $\phi(R, n, d, t, \theta_{\max}, C)^{\mathrm{V}}$. PZT drive signal in arbitrary units. 234

Figure 5.32- Simulated modulated signal reaching the detector $[\phi(R, n, d, \Delta d, \theta_{\max}, C)]$ as a function of the cavity length scan (Δd) with PZT image effect. a) Cavity length is $d = 0.28\mathrm{cm} + 0.0\mu\mathbf{m}$, b) Cavity length is $d = 0.28\mathrm{cm} + 0.3\mu\mathbf{m}$. The triangular waveform shows the PZT drive signal (arbitrary units). 235

Figure 5.33- Simulated harmonics of the modulated signal $\phi(R, n, d, \Delta d, \theta_{\max}, C)$ reaching the detector as a function of the cavity length (Δd). a) Cavity length is $d = 0.28\mathrm{cm} + 0.0\mu\mathrm{m}$, b) Cavity length is $d = 0.28\mathrm{cm} + 0.3\mu\mathrm{m}$. Here the harmonics present the phase shift. The triangular waveform shows the PZT drive signal (arbitrary units). 236

Figure 5.34- Simulated final output detector response $\phi(R, n, d, t, \theta_{\max}, C)^{\mathrm{V}}$ and its Fourier transform. a) Cavity length is $d = 0.28\mathrm{cm} + 0.0\mu\mathrm{m}$, b) Cavity length is $d = 0.28\mathrm{cm} + 0.3\mu\mathrm{m}$. The triangular waveform shows the PZT drive signal (arbitrary units)..... 237

Figure 5.35- Measured output detector for a CO sensor where the PZT was driven with a 5 Hz triangular waveform with different DC offset (Arbitrary Units). 238

Figure 5.36- Full experimental setup. 239

Figure 5.37- Simulated and Measured Amplitude Modulation for the CH_4 sensor with $R = 0.2$ and gas concentration $C = 50\%$. 240

Figure 5.38- Simulated and Measured amplitude modulation (a) as function of the f number, (b) as function of the cavity length. Here $R = 0.2$ and gas concentration $C = 50\%$..... 240

Figure 5.39- FPI fringe pattern considering the f number effect and $d = 0.055\mathrm{cm}$. 241

Figure 5.40- Simulated and measured Amplitude Modulation as a function of the CH_4 gas concentration..... 242

Figure 5.41- Measured Detector Output for different CH_4 concentration. 242
Figure 5.42- Simulated and Measured Amplitude Modulation for the CO_2 sensor for a gas concentration $C = 500\text{ppm}$ and $l = 38$ cm. 243
Figure 5.43- Simulated and Measured amplitude modulation for 500ppm CO_2 concentration and $l = 38$ cm. 243
Figure 5.44- Simulated and measured Amplitude Modulation as a function of the CO_2 gas concentration. 244
Figure 5.45- Simulated and Measured AM^V for the CO sensor as a function of the f number and cavity length with $C = 10000\text{ppm}$CO and $R = 0.28$. 246
Figure 5.46- Simulated and Measured amplitude modulation for 10000ppm CO concentration. a) cavity length $d = 0.145$cm. b) f number $f/12$. 246
Figure 5.47- Simulated and measured Amplitude Modulation as a function of the CO gas concentration. 247
Figure 5.48- Electronic Interface 248
Figure 5.49- Noise for the LTI Q1 pyroelectric detector. Data taken from DIAS Infrared Systems [5]. 248
Figure 5.50- Frequency dependence of the normalized noise voltage at voltage mode. 251
Figure 5.51- Simulated Amplitude modulation versus CH_4 concentration. 256
Figure 5.52- PSD output for different CH_4 concentrations. PSD time constant $RC = 10$s. 257
Figure 5.53- PSD output for different CH_4 concentrations. PSD time constant $RC = 3$s. 257
Figure 5.54- PSD output for different CH_4 concentrations. PSD time constant $RC = 1$s. 258
Figure 5.55- PSD output for different CO concentrations. PSD time constant $RC = 10$s. 259
Figure 5.56- PSD output for different CO concentrations. PSD time constant $RC = 3$s. 259
Figure 5.57- PSD output for different CO concentrations. PSD time constant $RC = 1$s. 260
Figure 5.58- PSD output for different CO concentrations. $RC = 1$s and $l = 10$cm. 261
Figure 5.59- PSD output for different CO concentrations. $RC = 3$s and $l = 10$cm. 261

Figure 5.60- PSD output for different CO concentrations. $RC = 1$s and $l = 10$cm. 262
Figure 5.61- PSD output for different CO_2 concentrations. $RC = 1$s and $l = 1.4$cm. The legend '0ppm CO_2' refers the concentration in gas cell with pathlength $l = 1.4$. Here the normalized CO_2 background concentration was approximately 1071 ppm. 264
Figure 5.62- PSD output for different CO_2 concentrations. $RC = 3$s and $l = 1.4$cm. The legend '0ppm CO_2' refers the concentration in gas cell with pathlength $l = 1.4$. Here the normalized CO_2 background concentration was approximately 1071 ppm. 264
Figure 5.63- Simulated cross sensitivity of the CH_4 sensor with water vapour. 266
Figure 5.64- Measured CH_4 sensor response. a) 0%CH_4+8%H_2O, (b) 0%CH_4+100%CO_2. 266
Figure 5.65- Measured CH_4 sensor response. a) 5%CH_4+8%H_2O, b) for 5%CH_4+95%CO_2 266
Figure 5.66- Simulated cross sensitivity of the CO sensor for 0%CO with H_2O and with CO_2. 267
Figure 5.67- Simulated cross sensitivity of the CO sensor for 1% CO with H_2O and with CO_2. 268
Figure 5.68- Measured CO sensor response for 0% CO + 8% H_2O and for 0% CO + 100% CO_2. 268
Figure 5.69- Measured CO sensor response for 1% CO + 8% H_2O and for 1% CO + 100% CO_2. 268
Figure 5.70- CO sensor cross sensitivity with N_2O. 269
Figure 5.71- Simulated cross sensitivity of the CO_2 sensor for 300ppm CO_2 with H_2O and with CO. 270
Figure 5.72- Measured CO_2 sensor response for 300ppmCO_2 + 8% H_2O and for 300ppmCO + 1% CO. 270

Declaration of Authorship

I, **EVERARDO VARGAS-RODRIGUEZ**, declare that the thesis entitled:

"Optical Gas Sensors Based on Correlation Spectroscopy Using a Fabry-Perot Interferometer"

and the work presented in it, are my own. I confirm that:

- This work was done wholly or mainly while in candidature for a research degree at this University;
- where any part of this thesis has previously been submitted for a degree or any other qualification at this University or any other institution, this has been clearly stated;
- where I have consulted the published work of others, this is always clearly attributed;
- where I have quoted from the work of others, the source is always given. With the exception of such quotations, this thesis is entirely my own work;
- I have acknowledged all main sources of help;
- where the thesis is based on work done by myself jointly with others, I have made clear exactly what was done by others and what I have contributed myself;
- parts of this work have been published in the publications listed in Appendix A.

Signed:

Date:

Acknowledgements

I would like to thank Prof. Harvey N. Rutt for giving the opportunity to work in this project, for his support, the short but productive meetings where he always listen to me with patient and gave me lots of ideas to resolve the problems that we found during the development of this project. Also I would like to thank the ORC people since all of them where very kind and ease my life during my PhD studies. Special thanks deserve my group partners Chong Yew Lee, Paul Hoy, Angela Swift, and Arun Kannath with who I passed several hours at the lab when both of us were fighting with our experimental problems, but it always was a great time. Thanks also to all my friends outside the ORC which also support me and make my time more enjoyable, especially the members of the MexSoc Society.

I am grateful to my sponsors Mexican Science Council (CONACyT) and the University of Southampton for the scholarships that permitted me carry out my studies.

Finally, I wish to thank my family for their support and encouragement for always trying my best. To my wife, Landy, for all her love, support, patient and her hard working, which always give me the strength to continue even in the most difficult times.

Abbreviation List

AM	Amplitude Modulation
L	Blackbody Spectral Radiance
k	Boltzmann's constant
γ	Collisional broadening coefficient (cm^{-1}/atm)
A_d	Detector Element Area
$f/\#$	F number
FPI	Fabry-Perot Interferometer
FT	Fourier transform
FTIR	Fourier Transform Infrared Spectrophotometer
d	FPI Cavity Length
Δd	FPI Cavity Length Scan
FSR	Free Spectral Range
FWMH	Full Width at Medium High

C	Gas concentration
IR	Infrared
IFT	Inverse Fourier transform
c	Light speed
$\alpha(\nu)$	monochromatic absorption coefficient
Δf	Noise equivalent bandwidth
NEP	Noise Equivalent Power
NDS	Non Dispersive Gas Sensor
D^*	Optical Detector Detectivity
R_v	Optical Detector Responsivity
nd	Optical thickness
Ppb	parts per billion
Ppm	parts per million
PSD	Phase Sensitive Detector
h	Planck's constant
R	Reflectivity
n	Refractive index
J	Rotational quantum number
$E(v, J)$	Ro-vibrational energy level
S/N	Signal to Noise Ratio
Ω	Solid Angle
SPRF	Spectral Parasitic Reflection Fringes
T	Temperature
v	Vibrational quantum number
cm^{-1}	Wavenumber

Chapter 1

1. Gas Sensors.

Gas sensing plays an important role in very different fields such as environmental, medicine, and industrial applications. A precise control of the gas concentration can be vital for security, human health, quality in industrial processes in many other applications. For instance some gases that are commonly monitored are the ‘combustion gases’ such as carbon monoxide (CO), carbon dioxide (CO_2), nitric oxide (NO), nitrogen dioxide (NO_2), sulphur dioxide (SO_2) and water vapour (H_2O). Each one of these presents different risks for our health depending of its concentration in the environment. Probably one of the combustion gases that causes most deaths worldwide is CO and many of these deaths occurs in houses. CO is a colourless, odourless gas, which combines with haemoglobin (Hb) in the blood to form carboxyhaemoglobin (COHb) [1]. Haemoglobin has an affinity 240 times higher for CO than for oxygen which reduces the capacity to carry oxygen [1, 2] which gradually produces acute adverse health effects. At low concentration it causes nausea; headaches and disorientation occur at higher concentrations [3]. Very high concentrations can be life

threatening [1]. The safety standard for CO exposure it is generally 9 ppm for an eight hour average exposure and 20-35 ppm for a one-hour average exposure [2, 3].

Another important combustion gas is Carbon Dioxide (CO_2) which is naturally present in air. It is also produced by human respiration processes [2] where the exhaled mix contains ~3% CO_2. Therefore an unpleasant environment can be a consequence of poor ventilation. CO_2 is also used in many industrial processes; as fertilizer in greenhouses, for carbonation of beverages (it gives the 'fizz' to soft drinks), it is injected in capped bottles to remove oxygen, in breweries and wineries it is produced by the fermentation process. According to the literature the occupational exposure standards for CO_2 are 0.5% averaged over a time weighted period of eight-hours daily considering five working days per week [2, 4], 3% average for a short-term (15 minute) exposure, and 4% as the maximum instantaneous limit considered immediately dangerous to life and health [4]. Any detrimental effects of low-level CO_2 concentration exposure (<0.5%) are reversible [2, 4]. Exposure to concentrations between 0.5 and 3% causes adaptive biochemical changes which may be considered a mild physiological strain [2] such as effects on the breathing rate, this doubles the normal rate at 3% CO_2 and is it four times at 5% CO_2 [4]. According to occupational exposure and controlled atmosphere research CO_2 is hazardous via direct toxicity at levels above 5% [4]. High concentrations of CO_2 (>17%) may cause severe and even fatal poisoning (this poisoning it is called hypercapnia). High concentrations of CO_2 can occur in industry for instance at ice-making factories or even in recreational activities such as diving [5].

Methane (CH_4) is other important gas that should always be monitored in some industries such as mining, oil extraction and landfills. It is explosive between its Lower Explosive Limit (LEL) of 5% methane in air by volume and its Upper Explosive Limit (UEL) of 15% [6]. In coal mines CH_4 can be found at very high concentrations of 80 to 90% and therefore with poor ventilation controls it can be diluted to the explosion limits and ignited by a spark from mining equipment [7]. This is a common accident that claims the life of many miners around the world every year.

In the industry it is not just for safety reasons that it is necessary to keep the concentrations of gases under control but there are many production or quality processes that rely on this monitoring. For instance in the food industry it is necessary to pack the

product under certain concentration of oxygen in order to prevent fast degradation of the product [8]. In combustion processes it is also necessary to monitor the concentration of oxygen to guarantee that the correct amount of combustible it is being used, this helps to save fuel reducing the cost of the process. There is an almost endless list of applications for gas sensors in a very wide diverse fields!. In Table 1.1 some common gases and their concentration ranges of interest for some industrial processes or human health are listed.

Table 1.1- Some common gases and their concentration ranges depending on application

Gas	Application	Concentration Range Usually monitored
CO	Environmental, Human Health	Above the Threshold Limit Value TLV = 30 ppm per 8 hours average exposure [2, 3]
CO_2	Environmental, Human Health,	Above the natural concentration in air 300ppm
		Around the TLV that it is 0.5% per 8 hours average exposure [1, 4].
	Ice Making Factories	This industry uses large amount of CO_2 in their process (>17%).
	Food Industry Packaging quality testing of inert atmosphere (CO_2 or N_2) of packaged foods [8].	0–100 ppm Oxygen or 0–3% Oxygen in N_2 or CO_2 [8]
	Bottled or canned beverages CO_2 fermentation gas recovery/scrubbing for headspace bottling process [8]	0–100 ppm Oxygen in CO_2 [8]
CH_4	Mining, Oil Industry, landfills, etc.	The Lower Explosive Limit (LEL) 5% and Upper Explosive Limit (UEL) 15% [6, 7].
O_2	Steel Manufacturing	Ranges 0-2%, 0-5%, 0-10%, 0-10ppm depending of the process [8].
	Petroleum & Refining	0-1%, 0-2%, 0-5%, 0-25% depending of the process [8].
	Power Generation	0-5% [8]
N_2O	Human Health	Recommended Exposure Limit REL = 50 ppm per 8 hours average exposure [9]

These are some of the reasons that explain the importance of gas sensors. Gas sensors can be classified in different groups depending of their principle of operation. One of these groups is chemical gas sensors which are devices that in contact with a gas or a mixture of gases changes one or more of its physical or chemical properties [10], such as light absorption, electrical conductivity, mass, adsorption, chemical reaction [11]. These changes (called measurands) are measured and quantified directly or indirectly in different ways but commonly as an electrical signal [10, 11]. Hence we can separate chemical gas sensors into two main groups electrochemical and optical sensors. In this thesis we will present the design of an optical gas sensor based on correlation spectroscopy using a Fabry-Perot Interferometer as a modulator, therefore in this work we will focus on this design. However, in the following sections of this chapter we will briefly review some characteristics of various gas sensor designs pointing out some of their advantages and disadvantages. This will help us to visualise the possible advantages and disadvantages of our optical gas sensor design.

1.1. Electrochemical Gas Sensors.

Electrochemical gas sensors are based on the interrelation between the physical or chemical change due to the presence of the gas and an electrical circuit. Electrochemical gas sensors can be classified according to the measurand. There are several types of electrochemical sensors and here we would like just to mention some of the most popular electrochemical sensors such as those based on conductivity, piezoelectricity (mass) and amperometric changes.

1.1.1. Conductivity Gas Sensors.

In this method the change in the material's conductance in the presence of the target gas it is measured. Most of the conductivity gas sensors use as a sensing material a conductive polymer composite (i.e. Polymer-carbon Black), intrinsically conductive polymer (i.e. polyaniline PAni, polypyrrole PPy), metal oxides (i.e. stannic oxide SnO_2, zinc oxide ZnO, and tungsten oxide WO_3) or ceramics (i.e. gamma-hematite γ-Fe_2O_3). The mechanisms that lead to the resistance changes are different for each class of material [11]. For instance in the conductive polymer material some of the gas permeates into the sensing element making it to expand. This increases the polymer's

electrical resistance since there is a reduction of conducting pathways for charge carriers [12]. In the metal oxide sensors there is a change in oxide conductance when it interacts with a gas and the change it is usually proportional to the gas concentration [11]. Conductivity gas sensors are probably the most common electrochemical gas sensors and a wide range of these sensors are readily commercially available [13]. These are employed to detect many different gases such as flammable gases or carbon monoxide in enclosed environments. The advantages of these sensors is that they are completely solid state and therefore have long shelf lives and show little deterioration in use [13], depending on the type of material the response and recovery time can vary from a few seconds up to some minutes. Some of the disadvantages of these sensors are that they can suffer from limited selectivity and sensitivity [13], some of them, especially the metal oxide type, present high power consumption since they require a heater [11, 13], and drift can be observed due to sensor aging especially in polymer composites. Some metal oxide sensors can suffer from 'sensor poisoning' due to irreversible binding of compounds, such as sulphur compounds, to the sensor oxide. In Table 1.2 some examples of conductivity gas sensor are listed mentioning it sensitivity, concentration range, type of sensing material, and some advantages and disadvantages.

1.1.2. Piezoelectric Gas Sensors.

Piezoelectric materials deform when a voltage is applied across them. Here when a oscillating potential is applied near to the resonant frequency of the piezoelectric crystal a stable oscillating circuit it is formed [14]. The degree of deformation is dependant on the piezoelectric and therefore the resonant frequency is a function of the piezoelectric material mass; this principle it is exploited by the piezoelectric gas sensor. The gas sensor is formed by coating a piezoelectric material (usually quartz) with a gas sensitive layer. The sensitive layer will adsorb the analyte increasing the mass and therefore changing the resonant frequency. Thus the frequency change will be related to the gas concentration. Piezoelectric gas sensors are divided into two groups; they are the quartz crystal microbalance (QCMB), also called thickness shear mode (TSM) [14] and the surface acoustic wave (SAW) also called bulk acoustic wave (BAW) [14] sensors. In the SAW sensors a surface wave is produced that travels along the surface in parallel direction to the piezoelectric surface whilst in the QCM sensor a wave is produced that propagates through the bulk of the crystal in a perpendicular direction to the

piezoelectric surface [11, 14-16]. Some advantages of the piezoelectric gas sensors are that they have high sensitivity (in the order of ppm or lower) since these are very sensitive to mass so by adsorbing a small amount of analyte the resonant frequency changes [15]. Moreover they present fast response times and their fabrication cost, especially SAW sensors, can be relatively inexpensive [16]. However these sensors can present poor selectivity since any molecule (other than the analyte) adsorbed by the sensitive layer will change the mass producing a frequency shift [15]. Consequently the sensor produces an incorrect concentration measurement. Moreover as these sensors operate at high frequencies, generally in the range from 10MHz up to some hundreds MHz [16], the electronics required it is relatively more complex than the required for conductivity sensors [11]. Furthermore these sensors also are altered by aging [16]. In Table 1.2 some examples of piezoelectric gas sensors, mentioning their sensitivity concentration range, type of sensing material, and some advantages and disadvantages are listed.

1.1.3. Amperometric Gas Sensors.

The amperometric gas sensors usually contain a liquid electrolyte solution and are therefore not as robust and small as the conductivity or piezoelectric gas sensors, but generally they have higher selectivity and sensitivity [13]. Amperometric gas sensors have been designed in different forms and are significant in commercial terms as the ‘lambda probe’ which is a potentiometric sensor for oxygen that can be found in many modern automobiles [13]. The potentiometric sensor usually has a cell divided by a porous membrane (usually polymer/metal/Nafion® [15, 17]). Here in one part of the cell it is the analyte and in the other part is the electrolyte solution, which is usually an inorganic acid [15]. The analyte must diffuse through the membrane to become dissolved in the internal electrolyte solution and then to a ‘working’ electrode [13]. Here, when an appropriate potential is applied on the reference electrode, the analyte molecules are anodically oxidized or cathodically reduced, resulting in a current change[15]. In Table 1.1 some examples of amperometric gas sensor mentioning their sensitivity concentration range, type of sensing material, and some advantages and disadvantages are listed.

Table 1.2- Examples of Electrochemical Gas Sensors.

Type of Sensor	[Reference]-Sensing Material	Target Gas/ Sensitivity/ Detection Range	Advantages	Disadvantages
Conductivity	[12]-Polymer-carbon black composite	Low vapour pressure gases/ detectable from ppb High vapour pressure gases/ detectable from ppm	Solid state, fast response.	Sensitive to temperature.
Conductivity	[18]- Ceramic (γ-Fe_2O_3)	Isobutane (i-C_4H_{10}) / 0.05-0.5%	Low humidity dependence, operates at room temperature.	Sensitive to temperature.
Conductivity	[19]- Metal Oxide (Tin Oxide)	CO / >600ppm	Small sensing element $10\mu m \times 30\mu m$	Presents Oxygen sensitivity.
Conductivity	[20]- Metal Oxide SNO_2-ZnO	Ethanol (C_2H_5OH) /0-200ppm	Solid State	Present some sensitivity to acetone CH_3COCH_3, CO and NO_2.
Conductivity	[21]- Metal Oxide ZnO	Chlorine gas (Cl_2)/ 0-300ppm	Operates at room temperature.	Temperature sensitive. Slow time response (15s) and recovery (>50s)
Piezoelectric (QCMB, SAW)	[22]- Polymers Polydimethylsiloxane (SE30)	Tetrachloroethene/ detection from 1ppm	High sensitivity	Frequency signals from 80MHz up to 433 MHz.
Piezoelectric (QCMB)	[23]- Gold- 2,2-bithiophene	Acetone, Chloroform	High sensitivity	Sensitive to other molecules
Amperometric	[17]- Electrolyte solution NaOH	Acetaldehyde/ from 12ppb	High Sensitivity	Sensitive to other molecules
Amperometric	[24]- Electrolyte solution H_2SO_4	Carbon Monoxide (CO) / detects from <1ppm	High sensitivity.	Slow time response >15s

1.2. Optical Gas Sensors.

The principle of operation of optical gas sensors is based on detecting changes due to the interaction between electromagnetic radiation and the gas. Spectroscopy studies the interaction between electromagnetic radiation and matter (atoms, molecules, atomic or molecules ions, solids) [25]. Both oscillating magnetic and electric fields of the electromagnetic radiation can interact with matter and give rise to different energy transitions. Table 1.3 summarises the region of the spectrum and the types of energy transitions observed there. Each type of energy transitions has its applications; for instance nuclear spin resonance it is used in magnetic resonance imaging (MRI) machines widely employed in medicine. X rays produced by bremsstrahlung (German for braking radiation) are utilized in medical X-ray machines. Here as we are interested in sensors monitoring the interaction of the electric field of the electromagnetic radiation with a gas therefore we will concentrate in this kind of interaction.

Table 1.3-Types of energy transitions on each region of the electromagnetic spectrum [26]

Region of the Spectrum	**Interacting Field**	**Type of Energy Transitions**
RF	Magnetic Field	Nuclear Spin Resonance Electronic Spin Resonance
Microwave	Electric and/or Magnetic	Rotational
Infrared	Electric	Vibrational, Rotational-Vibrational (ro-vibrational)
UV/Vis	Electric	Electronic
X-rays	Electric [27]	Electronic [28]

1.2.1. Interaction of light with molecules.

In this interaction light can be absorbed, emitted or scattered. In a very simple description we can say that light is absorbed when a radiated photon has enough energy to excite a molecule or atom to pass from a state of low energy (E_0) to a state of higher

energy (E_1) (Figure 1.1a). Hence the photon transfers its energy to the molecule or atom. The photon must have energy $E = h\nu = E_1 - E_0$ to produce the transition, where h is the Planck constant and ν is the frequency of the photon.

Stimulated light emission occurs when a photon of light stimulates an excited atom or molecule to decay from an initial high energy state (E_1) to a state of lower energy (E_0) (Figure 1.1b). Hence a photon is emitted which has energy $E = h\nu = E_1 - E_0$ and it will be in phase with the incident photon [29]. This means that under this process light amplification can occur since the incident and the emitted waves add constructively. In thermodynamic equilibrium at any temperature the majority of molecules or atoms populate the lower energy states (ie $N_{E_0} > N_{E_1}$ where N is the number of molecules or atoms) [30]. It means that the total number of elementary absorption events is larger than emission events. Consequently the incident radiation is absorbed. Hence in order to produce an stimulated emission it is necessary to force a temporary situation where more of the molecules or atoms populate the higher energy levels rather than the lower level (ie $N_{E_0} < N_{E_1}$), it is called population inversion [30]. To produce the population inversion an external source of energy is required to populate a specific upper energy level. This energy is commonly called the *pump energy* [30]. Some common external sources of *pumping energy* are intense light sources (such as flash lamp and lasers) and electricity (ie high voltage pulses) [31]

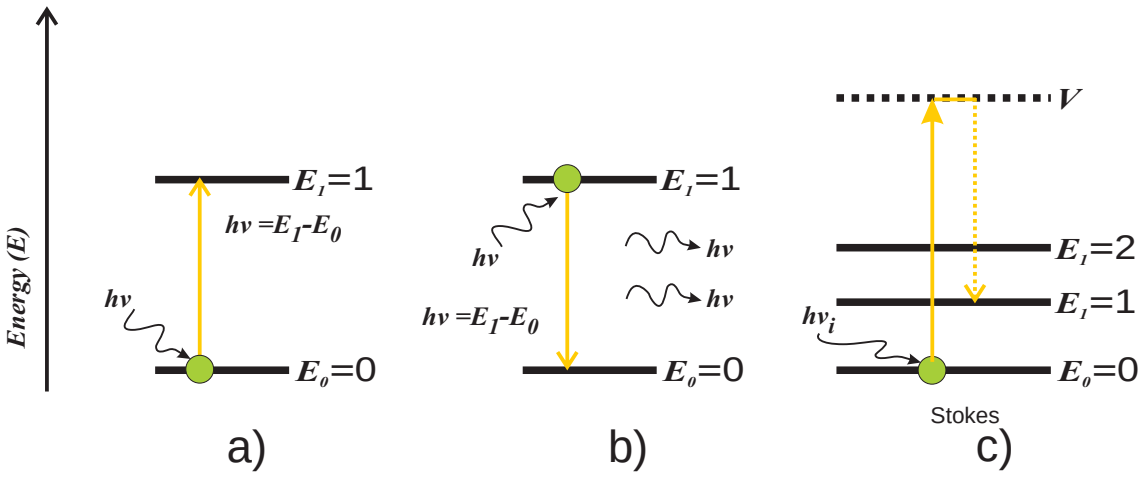

Figure 1.1- Transitions (a) absorption, (b) stimulated emission and (c) scattering.

When a photon of light is incident on a molecular or atomic sample it can be scattered. Basically we can consider two types of scattering, Rayleigh and Raman.

Another type of scattering is known as Brillouin scattering which involves the interaction of photons with acoustic phonons; as this type of interaction is out of the scope of this work therefore we will not discuss with more detail this issue. In Rayleigh scattering some photons rebound in the molecular sample with no exchange of energy, therefore the scattered light has the same wavelength as the incident light [32]. In Raman scattering the scattered light will have either longer or a shorter wavelength than the incident light. When the emitted photon has longer wavelength the process is called Stokes Raman scattering and when the emitted photon has shorter wavelength the process is called anti-Stokes Raman scattering [32]. Here it is necessary that the incident photon do not have the exact energy $E = h\nu$ to excite a molecule to make a transition to another stable state. Consequently if the incident photon has energy $E = h\nu_i$ it will excite the molecule to transit to a virtual state. Finally a transition from the virtual level to a new stationary state takes place with the emission of a photon (Figure 1.1c). When the atom or molecule transits from the virtual state to a state of lower energy, than its initial state, the emitted photon will have higher energy than the incident photon and therefore an anti-Stokes Raman transition occurs. In similar way if the atom or molecule transits from the virtual state to a stable state of higher energy the emitted photon will have lower energy than the incident photon giving rise to a Stokes transition (Figure 1.1c).

Molecules and atoms have a set of electronics states, and for each electronic state there is a set vibrational state and for each vibrational state there is a set of rotational states [33]. These are called energy levels. Each molecule will have a set of unique transitions forming a unique absorption, emission or scattering spectrum. Moreover there are specific rules that determine if a transition it is allowed or forbidden (selection rules) and these are not the same for all molecules. Furthermore it is necessary to calculate the intensity of each transition which requires more detailed study of the spectroscopy area. Consequently in order to evaluate an absorption, emission or scattered spectrum it is necessary to review in detail its spectroscopic characteristics. Since it is a complex and very wide area of study here we just review very briefly the principles of the ro-vibrational transitions occurring in the mid infrared region (MIR).

1.2.1.1 Mid Infrared ro-vibrational transitions

In the process that gives rise to vibrational transitions, absorption or emission, the interaction is usually between the molecule and the electric field [34]. In the infrared ro-vibrational transitions due to Raman scattering are possible; however these transitions are extremely weak in the gas phase [34] so they will be not considered here. The allowed ro-vibrational transitions are different for each molecule and they depend on characteristics such as the type of molecule and its symmetry. Molecules are classified as linear molecules, symmetric tops, spherical tops, and asymmetric tops.

Linear molecules have all their atoms arranged in a straight line (Figure 1.2). Here three axes may be set, the axes a and b as shown in figure and the axis c is perpendicular to these axes. Therefore the main moments of inertia of a linear molecule are $I_A = 0$ and $I_B = I_c$. Symmetric tops are molecules whose moments of inertia are $I_B = I_C \neq I_A$ such as NH_3. Spherical tops are molecules with moments of inertia $I_B = I_B = I_A$ such as CH_4. Asymmetric top molecules have moments of inertia $I_B \neq I_B \neq I_A$ to this group belongs H_2O.

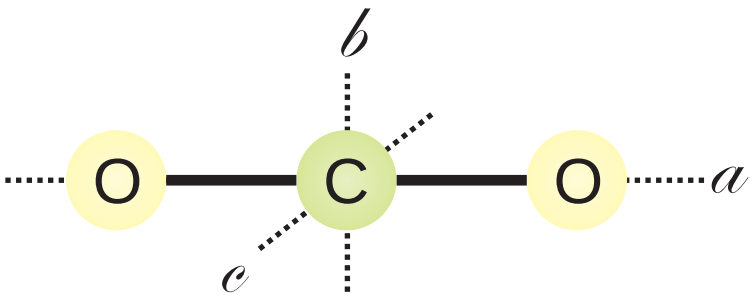

Figure 1.2- Linear molecule.

Here if a photon of light with energy E_p is incident on a molecule, this may be excited to transit from a ro-vibrational state (v, J) to another ro-vibrational energy state (v', J') of higher energy. Thus the incident photon E_p must have energy

$$E_p = E(v', J') - E(v, J). \tag{1.1}$$

where v is the vibrational quantum number, J is the rotational quantum number (both can have only values 0, 1, 2, 3, …). The energy of each ro-vibrational level $E(v, J)$ is given by the sum of rotational and vibrations energy. Evaluation of these energies varies

for each molecule depending on the type of molecule and requires the use of different mathematical models. The simplest case is for linear molecules therefore for simplicity here we will define just the ro-vibrational energy for a linear molecule considering it as a rigid rotor. This will be reviewed with more detail in chapter 2. In mid infrared spectroscopy it is useful to use the frequency ν in wavenumber units (cm^{-1}) rather than energy. Energy can be converted into wavenumbers as follows $\nu = E/hc$. Thus the frequency that a photon must have to excite a ro-vibrational transition in a linear molecule can be rewritten as

$$\nu_p = \left(v' + \frac{1}{2}\right) h\omega_{\text{osc}} + BJ\left(J'+1\right) - \left(v + \frac{1}{2}\right) h\omega_{\text{osc}} + BJ\left(J+1\right) \tag{1.2}$$

ω_{osc} the oscillation frequency and B is called the rotational constant. For the rigid rotor $\omega_{\text{osc}} = \mu^{1/2}\left(2\pi c k^{1/2}\right)^{-1}$ and $B = h/(8\pi^2 I_B c)$ where μ is the reduced mass of the system and c is the speed of light. Moreover, transitions will only occur if this satisfies the selection rules for the combined motion, which are

$$\Delta v = v' - v = \pm 1 \text{ and } \Delta J = J' - J = \pm 1$$

By applying the selection rules to equation (1.2) the frequency of the ro-vibrational transition can be evaluated. Hence it is possible to say that energy of the incident photon E_p to excite a transition it is given by

$$\nu_p = h\omega_{\text{osc}}\Delta v + n2BJ\left(J+1\right) \tag{1.3}$$

where $n = \pm 1, \pm 2, \pm 3, \pm 4, ...$ Equation (1.3) tells us that there is a set of ro-vibrational transitions which frequencies are evenly separated by $2BJ(J+1)$ cm^{-1}. In figure 1.3a the ro-vibrational spectrum of Carbon Monoxide (CO) is shown and it is seen that the transitions present a regular spacing.

Up to here the molecule was considered as a rigid rotator; however real molecules are not exactly rigid rotators, which will modify the frequency of the transitions. For instance the real ro-vibrational lines are not equidistant since the rotational constant B is

slightly different for each ro-vibrational level ($B \neq B'$). Furthermore the intensities are different for each transition (Figure 1.3a).

Here we have seen that linear molecules have spectra with regular separation between the transitions. However in some specific absorption bands of linear molecules (ie the bending mode of CO_2) a strong peak at the band centre can appear, called the Q branch, in this case the selection rule $\Delta J = 0$ applies. Furthermore other molecules do not have a spectrum with regular spacing between the ro-vibrational lines and many molecules can have spectra with very complex distribution of transitions; for instance the ro-vibrational transitions of water vapour (H_2O) and methane (CH_4) shown in figure 1.3. Therefore in order to evaluate the ro-vibrational spectrum of a molecule it is necessary to consider many more parameters related with the molecule such as symmetry, point group, dipole moment which determine if a band is infrared active, and it is necessary to evaluate the intensity of each transition of the ro-vibrational spectrum. For the moment we will not discuss this any further but in Chapter 2 we present in detail the spectroscopic theory required to evaluate the ro-vibrational absorption spectra of linear molecules and the asymmetric tops (CO, CO_2, N_2O and H_2O).

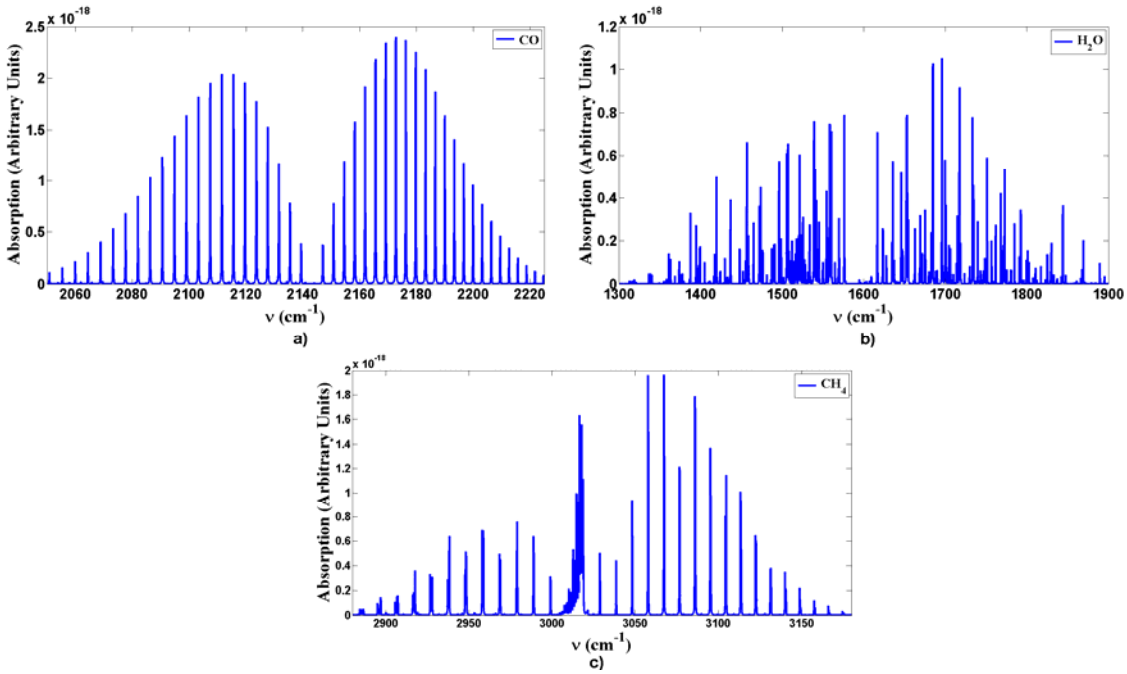

Figure 1.3- Ro-vibrational absorption spectra. a)CO, b)H_2O and c) CH_4.

1.2.2. Types of Optical Gas sensors

Optical gas sensors measure the changes in light when it interacts with the molecules, these changes as mentioned above are absorption, emission or scattering. There are several gas sensor setups and different applications and therefore several ways to classify them. In a very general way we can classify the optical gas sensors as dispersive and non dispersive.

1.2.2.1 Dispersive Optical Gas Sensors

Dispersive gas sensors are instruments that use a prism or diffraction grating to disperse a spectrally broadband source (i.e. Figure 1.4). Each one of the constituent 'coloured' beams (different frequency) is focussed onto a detector and its intensity is recorded. To change the 'colour' focused into the detector the grating or prism is rotated. Here by recording the intensities of each 'colour' the rotation-vibration spectra is obtained. Therefore, these instruments resolve the spectrum since both the frequency and intensity of the transitions are determined. This kind of gas sensors is widely used in analytical laboratory instruments such as most of the UV/VIS spectrophotometers. There is a wide range of these instruments currently available on the market with a diverse variety of ranges. Moreover the sample it is not limited to gases; it can be solid or liquid.

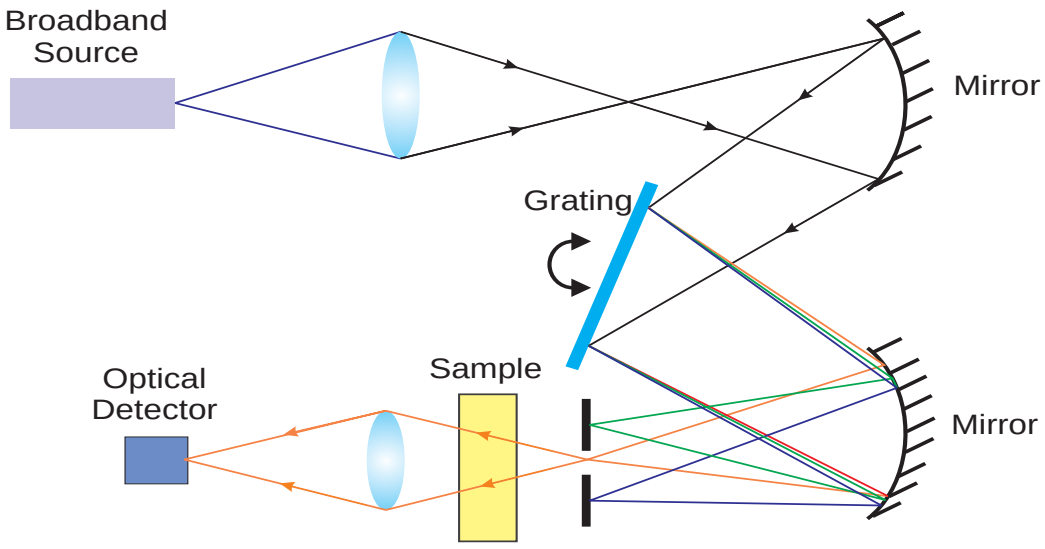

Figure 1.4- Dispersive Gas Sensor.

1.2.2.2 Non-Dispersive Optical Gas Sensors

In non dispersive gas sensors all the ‘colours’ which constitute the broadband source reach the detector at the same time (Figure 1.5). The simplest Non-Dispersive gas sensor (NDS) cannot resolve the spectrum since at the same time all wavelengths reach the detector and therefore it is nither possible to determine at which frequency a transition occurs nor its intensity. Commercially there are several gas sensors that measure the concentration of a specific gas which are based on the non-dispersive principle such as Guardian Plus a CO_2 detector by Edinburgh Instruments [35], the 400 IR CO_2 by Digital Control Systems [36] and the Carbocap CO_2 sensor by Vaisala Instruments [37]. In these examples the magnitude of the detector output is a function of the gas concentration.

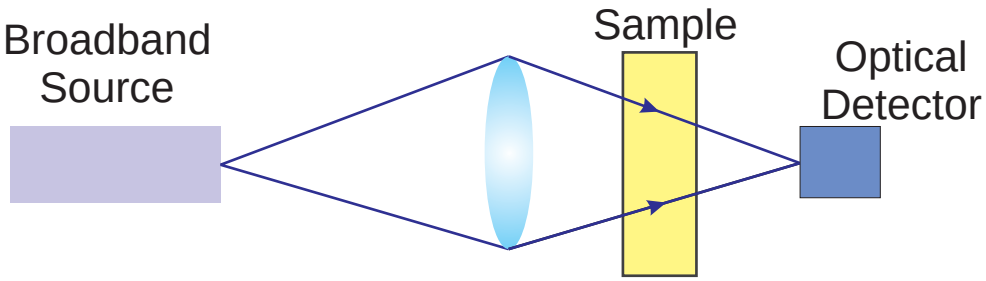

Figure 1.5- Non-Dispersive gas sensor.

As stated above the simplest Non-dispersive sensor (NDS) cannot resolve the spectrum directly. However by doing some modifications to the basic NDS setup it is possible to resolve the spectrum without using dispersive elements. An example of this is the Fourier Transform Infrared Spectrophotometer (FTIR) in which the broadband beam is passed through a Michelson interferometer before it reaches the detector. One of the interferometer mirrors it is scanned producing an intensity change of the beam reaching the detector which it is recorded. Therefore after the mirror scan is completed an interferogram it is obtained. By evaluating the Fourier transform of this interferogram the spectrum is resolved. These instruments are probably the most common analytical instrument for molecular spectroscopy in the infrared region.

Both types of spectrophotometers, dispersive and non-dispersive are powerful tools for molecular spectroscopy. However they are generally bulky and expensive since they use specialised optics, calibration, dedicated computer, etc. Consequently the utilisation

of these instruments to just monitor the concentration of a gas it is not cost-effective. Therefore in this work we will focus on optical gas sensor that can be utilised to measure a gas concentration.

1.3. Optical Gas sensors as concentration monitors

Optical gas sensors represent another technique to measure the gas concentration. In the literature different setups have been proposed to monitor the concentration of several molecules in their gas phase. Each gas sensor setup has its possible applications, its advantages and disadvantages; here let us review briefly some of these.

1.3.1. NDS Optical Gas sensor as concentration monitor

Probably the simplest setup consists in passing a light beam through a cell containing the gas sample (analyte) and the transmitted light is measured by an optical detector (Figure 1.6a). From the changes in the measured transmitted light the gas concentration can be determined. This is possible since as the concentration of the target gas increases (the gas cell pressure remains constant i.e. 1atm) the light absorption is stronger. It is important to recall that the total transmission of light through a gas path length is described by the Beer-Lambert law given by

$$T(\nu) = \exp\left[-lC\alpha(\nu)\right] \tag{1.4}$$

where l is the gas cell path length, C is the gas concentration and $\alpha(\nu)$ is the monochromatic absorption coefficient which describes the frequencies where the transitions occurs (usually called line positions) and their intensities. Thererfore as C increases the transmission $T(\nu)$ at certain frequencies decreases. These sensors usually use a bandpass filter to limit the operating frequency range (generally covering the frequencies where the most intense transitions occur). Consequently the overall transmission reaching the detector will be maximum when the target concentration it is zero and it will start to decrease as the gas concentration increases. These sensors are usually called Non-Dispersive Gas Sensors and several designs based on this principle of operation can be found either in literature. Moreover many of these are commercially available; for instance in Table 1.4 some examples are given. Apart from the simple

design presented in figure 1.6 there are various modified setups which can increase the minimum detectable concentration (sensitivity) and their ability to 'identify' if the absorption are due to the analyte or if they are due to some other molecule (selectivity). We will discuss this further in a later section.

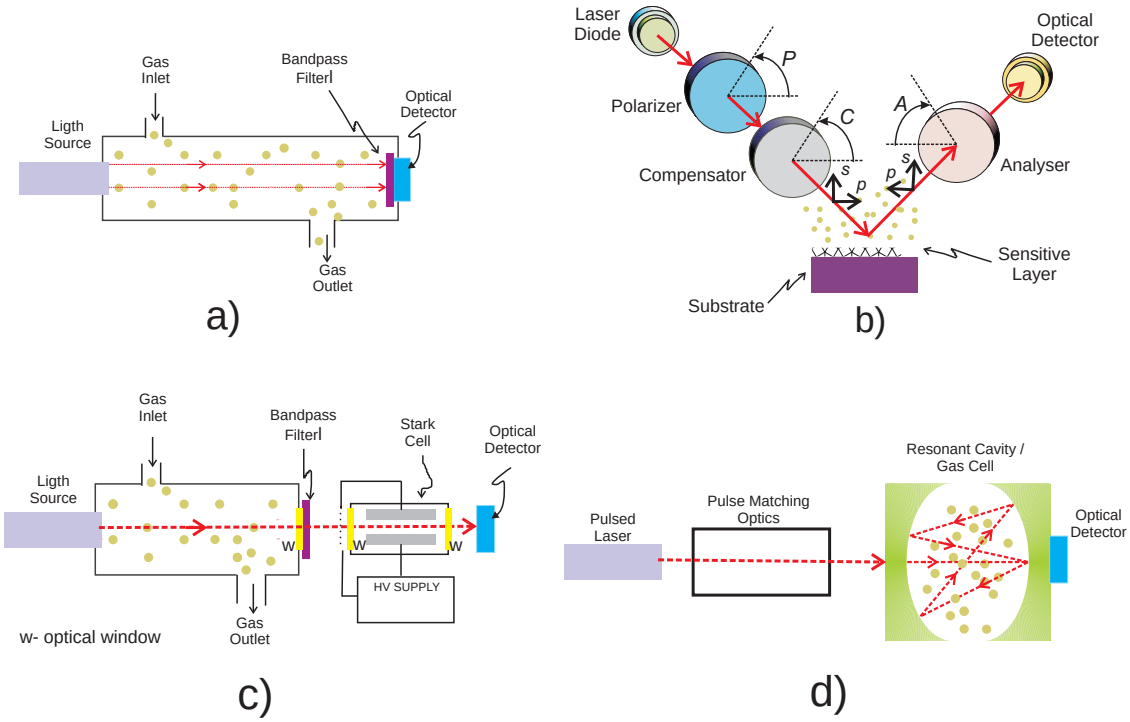

Figure 1.6- Setup of some optical gas sensor for concentration monitoring. a) basic NDR sensor; b) Ellipsometric gas sensor (redraw from Wang et al [38]); c) Gas sensor based on the Stark modulation; d) Optical gas sensor based cavity ring-down spectroscopy (redraw from O'Keefe and Deacon [39]).

1.3.2. Optical Gas Sensors based on Ellipsometry

Gas sensors based on ellipsometry can be described as a mixture of an electrochemical gas sensor with an optical gas sensor. In these sensors a polarised light beam reaches the sensing layer at an oblique angle of incidence. The sensing layer is deposited on a substrate and when it interacts with the analyte some of their physical properties changes such as thickness and refractive index [40]. These physical property changes in the sensitive layer will modify the polarization on the reflected beam (Figure 1.6). Therefore by measuring the changes in the complex reflectance ratio the gas concentration can be determined. The complex reflectance ratio is defined by $\tilde{\rho} = \tilde{R}_p / \tilde{R}_s$ where $\tilde{R}_p$ is the complex reflection coefficient for parallel polarized light (p-direction) and $\tilde{R}_s$ is the coefficient for perpendicular polarized light (s-direction) [38,

41]. These sensors have as their main advantage their high sensitivity to the target molecule or analyte [40] however their main disadvantage is the susceptibility to absorb species other than the analyte [41]. In Table 1.4 some gas sensors based on ellipsometry found in literature are listed including their application and concentration range where available.

1.3.3. Optical Gas Sensors based on the Stark Effect.

In these sensors two gas cells are required; one is called the measurement cell and the second one is a special cell called the Stark cell (Figure 1.6c). As the analyte flows through the measurement gas cell therefore when the light beam passes through the measurement gas cell the corresponding absorptions at certain frequencies will appear. The Stark cell it is a special cell because it has two electrodes to which a high voltage can be applied. Furthermore the gas cell it is filled with a certain amount of the analyte gas and it will remain sealed during the measurement. By applying a high voltage in the electrodes cell a spectroscopic effect called the Stark effect it is observed, which is due to the interaction of a static field with a rotating molecules which has an electric dipole moment [42]. This effect causes the absorption lines of the spectrum to shift by an amount depending on the extent of the interaction between the applied field E and the dipole moment μ of the molecule. Furthermore the Stark effect forms a characteristic spectral pattern of 'lobe components' which can be exploited to determine the J value of a line [42].

The spectral shift due to the Stark effect is approximately given by [42]

- $\Delta\nu = 0.50344 E_z \mu_c \dfrac{2KM}{J(J+1)(J+2)}$ for symmetric top molecules
- $\Delta\nu = 0.25345 \dfrac{E_z^2 \mu_c^2}{B} \dfrac{3M^2(8J^2+16J+5) - 4J(J+1)^2(J+2)}{J(J+1)(J+2)(2J-1)(2J+1)(2J+3)(2J+5)}$
  for linear and asymmetric molecules.

This shift can be utilized experimentally to induce modulation. Here when the applied field is equal to zero the absorptions of the Stark cell will match in frequency with the absorptions occurred at the measurement gas cell, making them stronger. When a high voltage is applied to the electrodes to provide a high field in [43] the Stark effect

shifts the absorptions lines, in the Stark cell, and therefore the total transmission changes. Now if the high voltage is applied in the form of rectangular pulses the detector will produce a modulated AC signal output. The amplitude of this AC signal will change when the concentration of the measurement gas cell changes. These sensors have high selectivity since the modulator is the absorption lines of the same gas as the analyte. Their main disadvantage is the high voltage levels required to produce the shift which can be in the order of kV [42, 43]. In Table 1.4 some examples of gas sensors based on the Stark effect are mentioned.

1.3.4. Optical gas sensors based cavity ring-down spectroscopy.

In ring down cavity spectroscopy a pulse of light it is coupled into a high-finesse optical cavity, formed by two or more highly reflecting mirrors aligned to form a stable optical cavity [44]. Here a small portion of the coupled light beam is outcoupled each transit cycle [39] (Figure 1.6d). The decay rate in the outcoupled light beam is determined by the total cavity loss including the absorption of the analyte [39]. The decay rate is a direct measure of losses within the cavity including the losses due to the absorption of the gas species. As the losses due to the mirror surfaces are known the gas absorption can be derived from the time decay [44]. A main advantage of these systems is their high sensitivity to the target molecule since the ring-down cavity acts as a multipass absorption cell. Therefore the roundtrip path length for a transit cycle is very large compared to effective longitudinal path length [39]. Now thinking of gas concentration monitors the ring down cavity sensors can be to some extent not cost effective since their setups are more complex than the non-dispersive gas sensors. In Table 1.4 some examples of these sensors are given including their target molecule and sensitivity range.

The gas sensor setups described above are just some examples of the many different options for optical gas concentration monitoring. However for the sake of the discussion from here we will concentrate on Non-Dispersive gas sensor for concentration monitoring, operating in the mid infrared since our project it is related with this technique.

Table 1.4-Characteristics of different Optical gas sensors for concentration monitoring.

Type of Sensor	Reference	Target Gas/ Sensitivity/ Detection Range	Advantages	Disadvantages
NDS	Edinburgh Instruments [35], model Guardian Plus	Either CO_2 (0-3000ppm) or CH_4 (0-100%) (other ranges available)	Good accuracy $\pm 2.5\%$ of range Very low sensitivity to water vapour	
NDS	Digital Control Systems [36], 400 IR CO_2.	CO_2 (0-20%)	High accuracy $\pm 5\%$ of reading	
Ellipsometric	Wang et al [38]	Methanol (15-50ppm), ethanol (6-19 ppm), and 2-propanol (4-13ppm).	High sensitivity	Takes a few minutes for recover after a measurement. Sensitive to source instability.
Ellipsometric	Zangooie et al [45]	Acetone (12-1500ppm)	High Sensitivity	Long recovery times after measurement >2min.
Elipsometric	Guo et al [46]	Halothane vapour (0.35%-35%)	High Sensitivity	
Stark	Dakin et al [43]	Water vapour (>1.2%)	Good sensitivity and selectivity	High Voltage required 2KV
Ring down Cavity	Spece et al [44]	Carbon Dioxide (1.3-2000ppm)	High sensitivity	Complex setup
Ring down Cavity	Kosterev et al [47]	Nitric Oxide (≥ 0.7 ppb)	Very High Sensitivity	Complex setup
Ring down Cavity	Manne et al [48]	Ammonia (≥ 50 ppb)	Very High sensitivity.	Complex setup

1.4. NDS Optical Gas sensors as concentration monitors

Non Dispersive gas sensors are probably the most popular optical technique to monitor the gas concentration especially in the mid infrared (MIR). These systems are usually simple, with just a few components (Figure 1.6a) which simplifies their operation and maintenance. Moreover most of the gases have their strongest absorption bands (called fundamental bands) in the MIR with wavelengths region from 2 to 8 μm; for instance CO, CO_2, and CH_4 absorbs at 4.7, 4.3 and 3 μm respectively. Nitrogen (N_2) and Oxygen (O_2) the most important constituents of air do not have infrared active absorption bands. When an EM wave in the IR wavelengths irradiates a molecule the electric field acts on the charge distribution in the molecule. The IR absorption will occur if the oscillating electric field changes the molecule charge distribution, increasing or reducing the dipole moment [42]. Thus symmetric bonds such as those of homonuclear molecules do not absorb infrared radiation [26]. This issue it is addressed with more detail in Chapter 2.

Various very different arrangements have been proposed for NDS Optical Gas sensors used as concentration monitors. One possible way to classify these sensors is by the number of sources, gas cells and filters that they use. Some of the basic and simplest possible configurations are

- *Single-beam Single-wavelength,*
- *Single-beam Dual-wavelength,*
- *Tuneable Absorption Spectroscopy (TAS).*

Here we will review some of these typical gas sensors configurations. But first let us mention the basic characteristics of the most common sources and detectors employed by MIR-NDS sensors

1.4.1. NDS Basic Components

For gas concentration monitors based on NDS operating in the MIR the common sources are blackbodies, Light emitting diodes (LED) and lasers. Detectors can be either thermal detectors (pyroeletcric, bolometers, etc) or photon detector (ie MCT, InAs, etc.). The selection of each of these components depends on the sensor application, such as gas concentration range to be monitored, restrictions in power consumption, instrument portability, etc.

1.4.1.1 Sources for MIR-NDS

As stated above the most common light sources for MIR-NDS are thermal sources, LEDs and lasers. Each of these has very different characteristics such as spectral profile, emitted power, level of power consumption, etc. Therefore let us review some of the basic characteristics of these sources.

1.4.1.1.1 Blackbody Sources

These probably are the most commonly utilized sources for MIR-NDS since there is a very wide range of them on the market. These sources are relatively simple, for instance a coiled resistance wire filament or a tungsten filament, they are fairly inexpensive and they radiate a considerable amount of power. The blackbody spectral radiance in terms of power $[\mathrm{Watts}/\left(\mathrm{cm}^2-\mathrm{sr}\right)]$ is given by [49]

$$L=\frac{2hc^2\nu^3}{\exp\left(\frac{hc\nu}{kT}\right)-1}\mathrm{d}\nu \tag{1.5}$$

where h is the Planck's constant $(h=6.626076\times10^{-34}\ \mathrm{m^2Kg/s})$, c is the light speed in vacuum $(c=2.997921\times10^{10}\ \ \mathrm{cm/s})$, k is the Boltzmann's constant $(k=1.3806586\times10^{-23}\ \mathrm{m^2Kg\ s^{-2}K^{-1}})$, ν is the frequency in wavenumbers, and T is the absolute source temperature. It is important to recall that $1\ \mathrm{Watt}=1\ \mathrm{m^2Kg/s^3}$. Consequently a hotter source radiates more power (Figure 1.7). Some of the main advantages of these sources are: a) emitted power over a wide spectral region, b) usually they do not require complex electric supply for operation, c) their life time is reasonably

large (around 3 years) and d) they do not require frequent calibration. The main limitation of these sources is their relatively high power consumption which can limit their use in portable instruments. In Table 1.5 we list some thermal emitters that are commercially available including some of their characteristics.

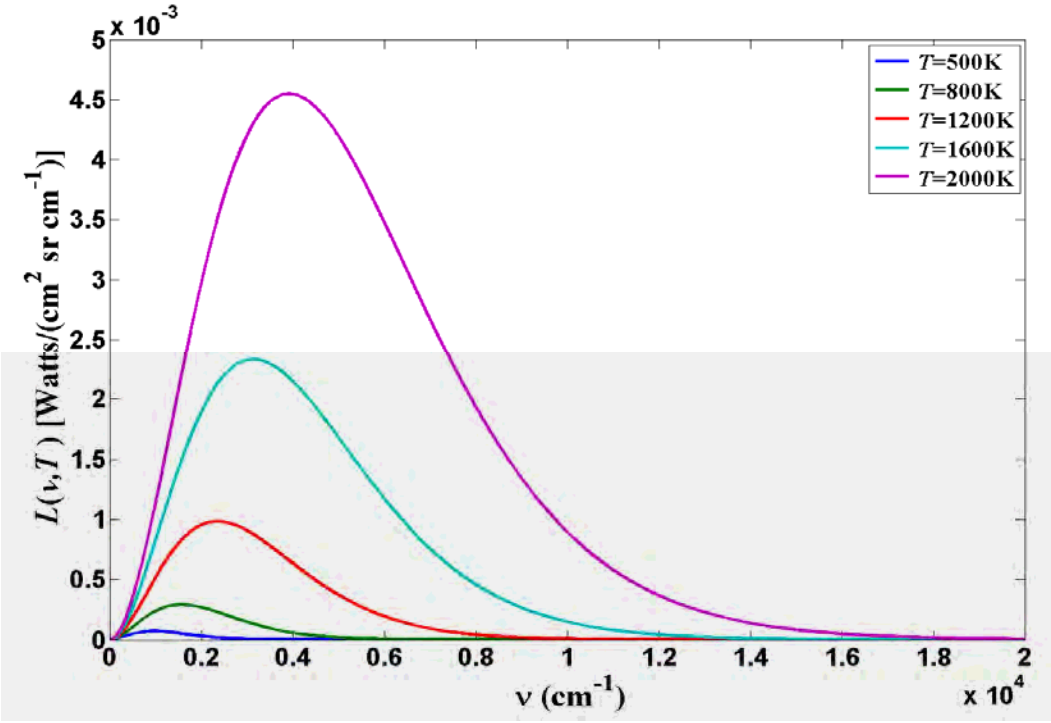

Figure 1.7- Spectral radiance of a blackbody at different temperatures.

1.4.1.1.2 Light Emitting Diodes LED

LEDs are another source option for MIR-NDS, these are small with low power consumption and their time response it is of the order of 10^{-9} s. These sources emit over a narrow spectral region and their power emission is relatively small in the order of μWatt. LEDs usually consume less power than thermal sources which can make them more suitable for portable instruments; however their application suitability can be limited by their lower power emission. Moreover LEDs spectral profiles are usually affected by temperature and current fluctuations. These fluctuations produce a spectral shift of the emission profile (Figure 1.8). These shifts should be taken into consideration when designing a MIR-NDS since it is necessary to analyse how much these possible shifts affect the overall sensor response. In Table 1.5 some examples of MIR-LEDs with some of their characteristics that are commercially available are listed.

1.4.1.1.3 Lasers

Lasers represent another source option for MIR-NDS, especially the semiconductors lasers. Lasers can have multiple longitudinal multimode or single mode emissions. Spectrally these emission modes can be very narrow (narrow line width) in the order of a very small fraction of a wavenumber (Figure 1.9). Using some laser characteristics it is possible to tune the emission modes, this means shift spectrally the emissions modes. For instance, in a semiconductor laser the emission mode can be shifted by changing the temperature of the laser 'chip' [50]. Usually for gas sensing the most used are the single mode lasers, since it is possible to tune the mode exactly to the frequency where one transition of the target gas occurs, in a later section we review this technique with more detail. Solid state lasers have power outputs in the order of mW (quantum cascade lasers). These lasers are sensitive to temperature fluctuations and as a consequence their spectral emission profile can shift (Figure 1.9b). The main advantages of the solid state lasers are their small size, high power emission and very narrow bandwidth. The main disadvantage is that they need more sophisticated temperature and current drivers to keep them operating at the correct wavelength.

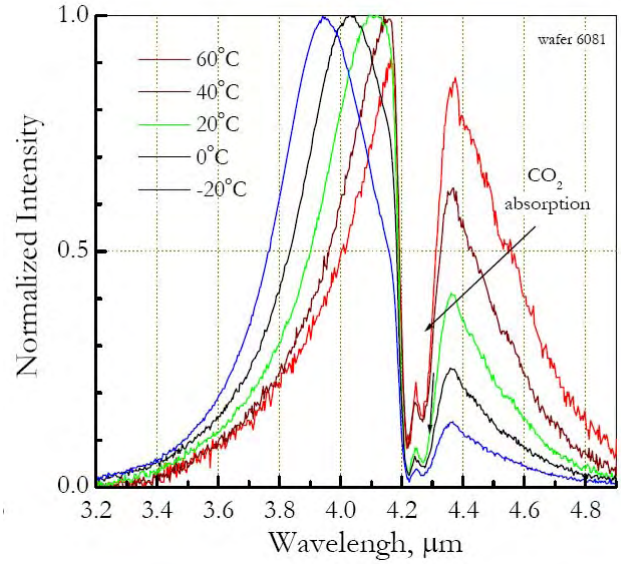

Figure 1.8- Emission spectral profile for a LED with peak emission at $\lambda = 4.2$µm. Graphic taken from Ioffe LED LTd.

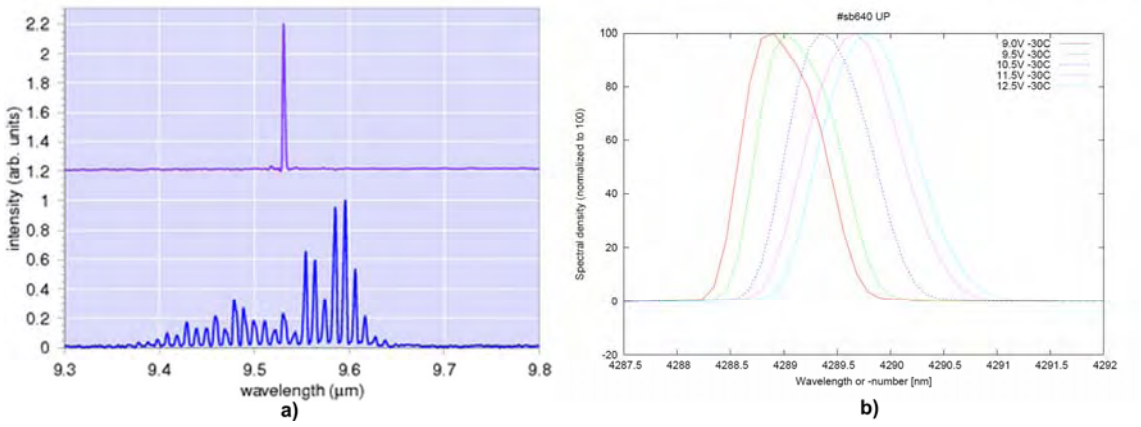

Figure 1.9- Spectral Emission Laser a) Multimode (bottom) and single mode (top) laser. b) Spectral emission profile of a quantum cascade laser DFB electrically tuned along the wavelength. Graphs taken from (a) nanonoplus GmbH and (b) Alpes Lasers SA.

Table 1.5- Examples of sources that can be used in NDS gas sensors.

Type of Source	Model and Supplier	Temperature / radiated power	Driver requirements	Source Area	Modulated	Wavelength region
Thermal	IR-12 by Scitec Instruments.	$T = 1074$K	DC 4.5 V at 1.8 A (8 watts)	3.5×3.5 mm^2	Steady	All MIR
Thermal	CS-IR-20 by Boston Electronics	$T = 1100$K	DC 5V at 0.8 A (4 watts)	1.5×3.5 mm^2	Steady	All MIR
Thermal	IR-55 by HawkEye Technologies	$T = 1023$K	DC or AC 6.4V at 0.135A (0.9watts)	1.5×1.5 mm^2	Pulsed	2 - 20µm
LED	LED42SC by Ioffe LED LTd	70 µWatt / 25 µWatt	0.4V @ 1A / 0.3 @ 0.2A	$\oslash = 3.3$ mm	Pulsed / CW	3.8 - 4.4 µm (FWMH)
LED	LED47SC by Ioffe LED LTd	25 µWatt / 5 µWatt	0.9V @ 1A / 0.25 @ 0.2A	$\oslash = 3.3$ mm	Pulsed / CW	4.4 – 5.0 µm (FWMH)
LED	LED30SC by Ioffe LED LTd	250 µWatt / 50 µWatt	0.4V @ 1A / 0.26 @ 0.2A	$\oslash = 3.3$ mm	Pulsed / CW	2.8 – 3.1 µm (FWMH)
Laser (QC-DBF)	sb640 UP by Alpes Lasers SA	0.5 mW @ 15ºC	12.5V @ 1.26A		Pulsed	2322 cm^{-1} (4.304 µm) with FWMH ≈1 cm^{-1}
Laser (QC-DBF)	Sbcw1428 UP by Alpes Lasers SA	2.7 mW @ -20ºC	12.7V @ 0.45A		CW	2305 cm^{-1} (4.338 µm) with FWMH <1 cm^{-1}
Laser (QC-DFB)	nanoplus 9.5µm	1 mW @ <260K	6.2A	8×20 µm^2	Pulsed	9.55µm

Note: FWMH is for Full Width at Medium High

QC-DBF is for Quantum Cascade Distributed Feedback Laser

1.4.1.2 Detectors for MIR-NDS

Optical detector can be classified as a photon-detectors and thermal detectors. *Photon-detectors* are materials or devices that detect light by a direct interaction of the radiation with the electronic system of the material [51]. Hence in photodetectors the radiation is absorbed by the electronic system causing changes in the electrical properties [51]. In *Thermal detectors* the radiation is absorbed by the lattice, causing heating of the lattice [51]. The change in the lattice temperature causes a change in the electronic system which consequently causes changes in the electrical properties [51]. Some of the physical parameters that can change in the detectors are resistance (bolometers), polarization (pyroelectric), voltage (thermocouple), mechanical displacement (Golay Cell) [49].

There are some figures of merit which are utilisable to characterize and quantify the response of detectors. Some of the typical figures of merit usually stated in the detector's datasheets are detectivity (D^*), responsivity, and Noise Equivalent Power (NEP) (which it is indeed a 'defect' function rather than a merit function, the smaller it is better). The NEP is the minimum radiant power incident on the detector that yields a signal to noise ratio equal to one [49] which can be expressed as

$$\frac{S}{N} = \frac{R_v \phi}{g_d} = \frac{R_v \mathrm{NEP}}{g_d} = 1 \tag{5.6}$$

where R_v is the detector responsivity, ϕ is the incident radiated power, and g_d is the detector noise (current or voltage). The responsitivity is the amount of output seen per watt of radiant incident power [49]. Thus the product $R_v \phi$ represents the detector output signal (g_o) in term of voltage or current. Therefore the NEP can be rewritten as [49]

$$\mathrm{NEP} = \frac{g_d}{R_v} = \frac{\phi}{g_o / g_d} \tag{5.7}$$

The detectivity D^* is the signal to noise ratio when 1 Watt of incident power is incident on the detector with an area of $A = 1$ cm^2 and 1 Hz noise equivalent bandwidth $(\Delta f = 1\,\mathrm{Hz})$. Therefore higher is better. The detectivity in terms of NEP is given by

$$D^* = \frac{\sqrt{A_d \Delta f}}{\mathrm{NEP}} \tag{1.8}$$

These are the basic figures of merit of the detectors however there are others parameters that must be considered such as the time response, ie how much time they need to respond to any change in the radiant incident power. For instance the thermal detectors are much slower than photon detectors. Also it is important to point out that the figures of merits D^*, R_v and NEP are functions of temperature and frequency (Figure 1.10) so these are not flat and therefore the frequency of operation must be considered when selecting a detector. Due to the fast time response and high detectivity in the MIR photon-detectors are the best option, however before selecting a detector it is necessary to consider that some of these must be cooled down (Figure 1.10). This can be a limitation in designing a portable MIR-NDS system. Hence the selection of the best detector will depend on the application requirements such as portability, concentration range to be measured which will determine the D^*, R_v and NEP required for the application, etc.

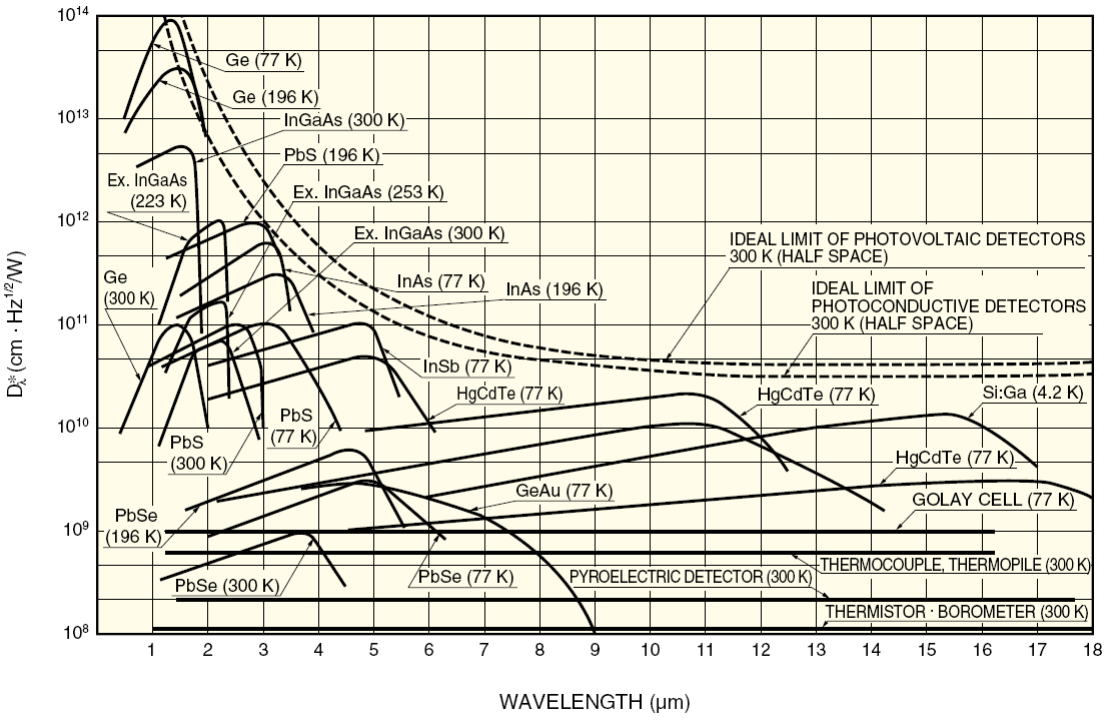

Figure 1.10- Spectral response D^* for different detectors. Graph taken from Hamamatsu [52]

1.4.2. NDS Single-Beam Single-Wavelength

These sensors have just one source (*Single-Beam*), one detector and one band pass filter (*Single-Wavelength*) (Figure 1.6). These sensors are probably the simplest optical gas sensor for concentration monitoring. The band pass filter passes the frequencies at which the vibration-rotation absorptions of the target molecule absorb (Figure 1.11). This prevents the sensor from detecting ro-vibrational absorptions due to other molecules. For instance in figure 1.11 the frequencies at which CO absorbs are passed by the filter whilst the frequencies at which CO_2 and H_2O absorbs are attenuated. Thus the overall transmission through the gas cell is given by

$$I = \int_{\nu_1}^{\nu_2} S(\nu)\, T(\nu)\, Fil(\nu)\, \mathrm{d}\nu \tag{1.9}$$

where $S(\nu)$ is the spectral source profile, $T(\nu)$ is the transmission through the gas pathlength described by the Beer Lambert law (equation 1.4), $Fil(\nu)$ is the spectral response of the band pass filter.

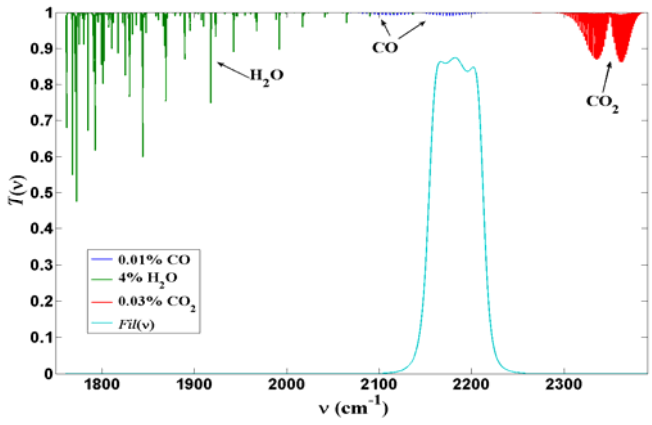

Figure 1.11- Simulated ro-vibrational spectra of CO, CO_2 and H_2O and a typical spectral band pass filter response. Here $S(\nu) = 1$.

As the concentration of the target molecule increases in the gas cell the ro-vibrational absorptions get stronger. Thus considering that the target molecule is mixed in air and that air it is flowing through the cell, so the cell's pressure is 1atm. Therefore as the gas concentration increases the overall transmission I is reduced. Consequently the changes in I are directly related to the target gas concentration. The main advantages of this

design is the simple optical design. However these sensors can present limited selectivity since the overall transmission I is affected by all the absorptions occurring within the range of frequencies passed by the filter. It can be a problem since other molecules (we can call them 'foreign' molecules just to differentiate them from the target molecule) can have ro-vibrational transitions in this filter band pass range. Therefore if the concentration of 'foreign' molecules increases their absorption will be stronger. Consequently the overall transmission will be modified every time that the concentration of the 'foreign' molecules changes. For instance in figure 1.12 we show how the ro-vibrational absorption spectra of CO_2 becomes stronger with the concentration, and in Figure 1.12b we see how some rovibrational lines of H_2O overlap the CO absorptions. Therefore in this case if the target molecule is CO the sensor will present some degree of sensitivity to water vapour.

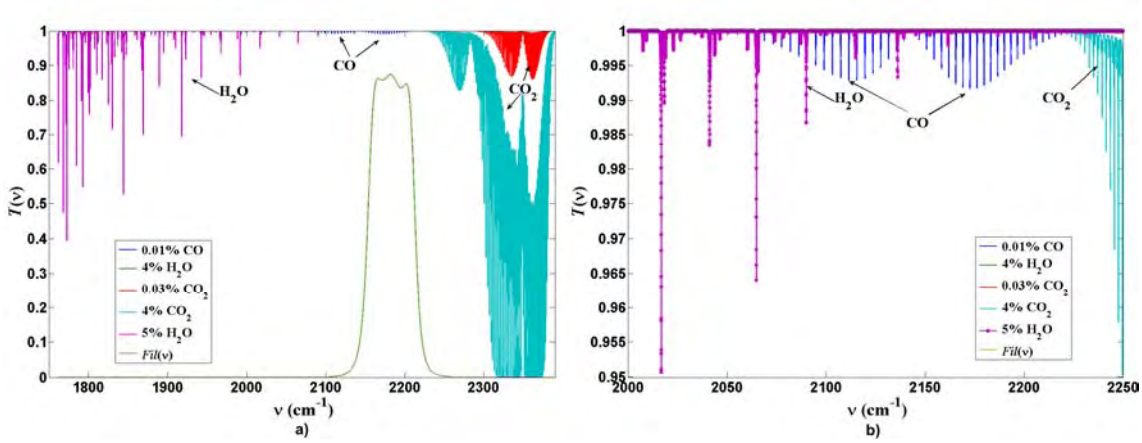

Figure 1.12- Simulated ro-vibrational spectra of CO, CO_2 and H_2O showing the changes of increasing the CO_2 concentration and H_2O. b) Detail showing how the H_2O absorptions overlap the CO absorptions. Here $S(\nu) = 1$

Many sensors using this design have been proposed in the literature and indeed many commercial sensors use this design. The technique can be applied to detect gases whose absorption bands are practically free of 'foreign' absorptions. For instance in normal air CO_2 can be a very good target for this design since in the region where its fundamental ro-vibrational band occurs, in the region of the 2250 cm^{-1}, the absorptions due to other 'foreign' molecules are very weak. Furthermore another problem that can affect the sensor performance is source instability, which will produce a change in the total transmission. Some examples of CO_2 sensor using this design are those presented by ref

[35, 53]. In Table 1.6 some examples of commercial NDS single-beam single wavelength sensors are listed.

1.4.3. NDS Single-Beam Dual-Wavelength

Single-Beam Dual-Wavelength can be achieved in very different ways. The simplest can be by using a single source (*Single Beam*) and two identical detectors with two different filters (*Dual-Wavelength*). Here the filters form two channels, the measurement and the reference channels. Thus the overall transmission for the measurement channel will be given by

$$I_1 = \int_{\nu_1}^{\nu_2} S(\nu)\, T(\nu)\, Fil_1(\nu)\, \mathrm{d}\nu \tag{1.10}$$

and for the reference channel

$$I_2 = \int_{\nu_2}^{\nu_2} S(\nu)\, T(\nu)\, Fil_2(\nu)\, \mathrm{d}\nu \tag{1.11}$$

The sensor response is then given by the relationship between I_1 and I_2 which can expressed as $I = I_1/I_2$. This design has the advantage that it only uses one source which can be helpful to reduce the error due source drift or a constant change in power $[aS(\nu)]$. These variations are cancelled since both channels are affected in the same proportion. Here the main limitation of this type of sensors is that reference channel must cover a spectral region close to the measurement channel where any other molecule absorbs or that these absorptions are very weak. However it is also necessary that the measurement channel is free of absorptions due to molecules other than the target. This is because if there is absorption in the reference channel the sensor response will be changed so that $I = I_1/aI_2$; If there is absorption due to 'foreign' molecules in the measurement channel therefore the sensor response will change to $I = bI_1/I_2$. In Table 1.6 some examples of this type of sensors are provided.

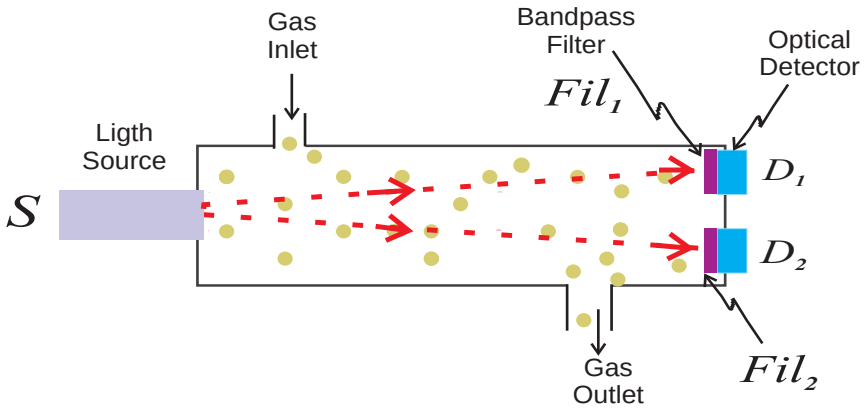

Figure 1.13- Optical Gas sensor with *Single-Beam Dual-Wavelength*.

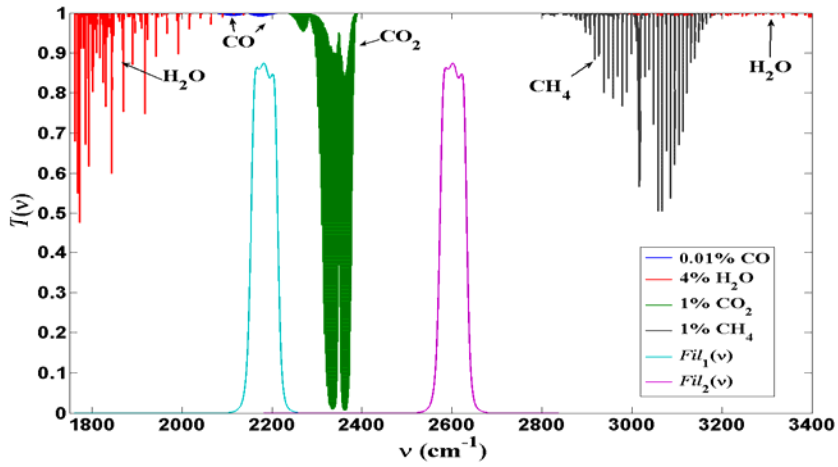

Figure 1.14- Simulated ro-vibrational spectra of CO, CO_2 and H_2O . The measurement channel it is defined by $Fil_1(\nu)$ and the reference channel by $Fil_2(\nu)$.

1.4.4. NDS, Tuneable Absorption Spectroscopy (TAS).

Another technique applied to measure the gas concentration consists in resolving one or more rotational lines of the spectroscopic spectrum of the target molecule by using a Laser [54]. Here it is important to mention that this technique satisfies the non dispersive gas sensor principle. However it is a special case, ie. it resolves the spectrum, and in literature it is considered as a separate sensor category from NDS.

The gas concentration measurement based on the TAS technique can be implemented by several ways. The simplest case is called *TAS line-locked mode* [55] which consists in tuning the laser emission frequency to match a single ro-vibrational line (Figure

1.15). In these systems the overall transmission of the laser beam through the gas pathlength will change depending on the gas concentration. The overall transmission is given by

$$I = \int_{\nu_1}^{\nu_2} L(\nu)T(\nu)\mathrm{d}\nu \tag{1.12}$$

where $L(\nu)$ is the laser emission profile and $T(\nu)$ is the transmission through the gas pathlength. In this setup as the laser emission is very narrow the overall transmission I will be very sensitivity to any change in the absorption of the target ro-vibrational line. According to equation (1.12) when there is a zero target concentration the overall transmission will be maximum and as gas concentration rises the overall transmission will be reduced.

Another way to implement the TAS technique is by tuning or scanning the narrow width laser emission along a relatively wide frequency region, where the target absorption spectrum occurs [56]. This method permits us to resolve the absorption spectrum of the target molecule. This technique is often applied when very low concentrations need to be measured, usually in the order of ppb, or as well to detect very weak ro-vibrational transitions. Two of the main advantages of the TAS technique are both high sensitivity to the target molecule and that using it the target absorption spectra can be resolved. However the technique is limited by several factors for instance these systems require more specialized equipment such as the laser, dedicated instrumentation such as a laser temperature controller, current drive controllers, etc. Moreover some semiconductors lasers must be cooled down for operation, which means that the system will require frequent maintenance. Furthermore for normal gas concentration monitoring of trace gases such as CO_2, CO or CH_4 probably this technique it is not cost effective compared with standard NDS. In Table 1.6 some examples of TAS sensors systems are provided.

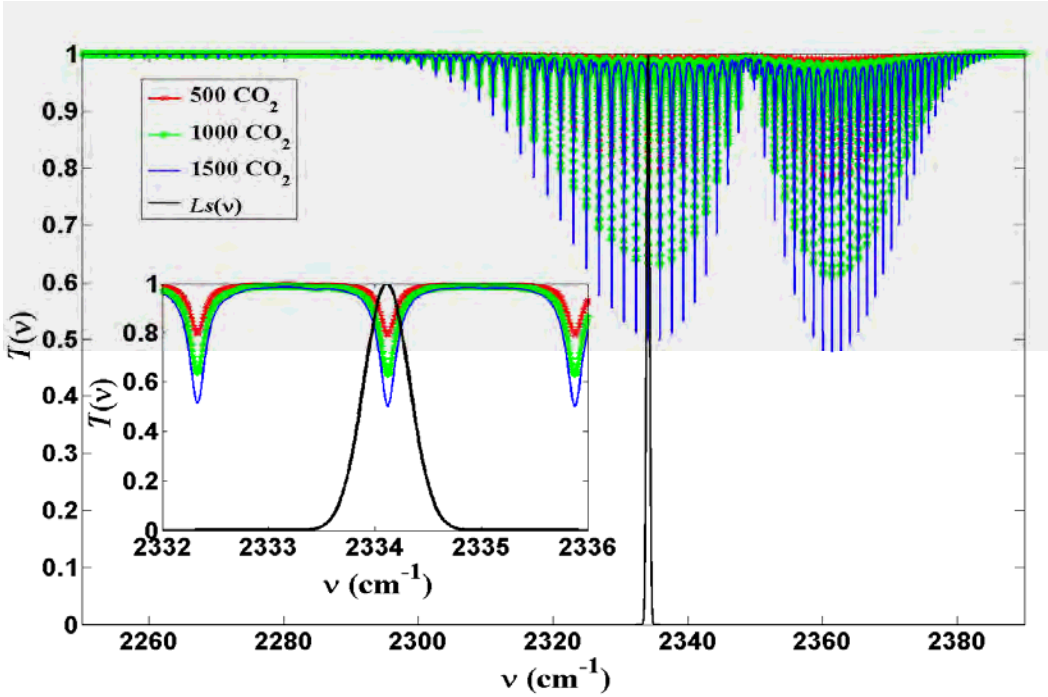

Figure 1.15- Ideal laser emission tuned to match a single ro-vibrational of CO_2. For clarity the spectral region close to the narrow laser emission and the ro-vibrational transition are shown in the inset.

Table 1.6-Characteristics of different Optical gas sensors for concentration monitoring.

Type of Sensor	Reference	Target Gas/ Sensitivity/ Detection Range	Advantages	Disadvantages
Single-Beam Single-Wavelength	Edinburgh Instruments [35], AirCheck IP65	CO_2 (0-3000ppm) (other ranges available)	Very low sensitivity to water vapour	Not portable instrument
Single-Beam Single-Wavelength	Zhang et al [53]	CO_2 (0-3%)	Very low sensitivity to water vapour	Not portable instrument
Single-Beam Dual-Wavelength	Model 400 CO2 by Digital Control Systems [36].	Either CO_2 (0-3000ppm) or CH_4 (0-100%) (other ranges available)	Very low sensitivity to water vapour	Temperature compensation system required to compensates for thermal shifts due to gas law effects.
Single-Beam Dual-Wavelength	MyCO_2 by Edinburgh Instruments [35].	CO_2 (0-2000ppm) (other ranges available)	Very low sensitivity to water vapour	Not portable instrument power consumption 6 Watts
TAS	Roller et al [57].	Nitric Oxide (min 1.5 ppb)	Very high sensitivity	Cryogenic temperatures
TAS	TGA100A by Campbell Scientific, Inc.[58]	Nitrous Oxide (min 1.5 ppb) Methane (min 7 ppb) Ammonia (min 6 ppb)	Very high sensitivity	Cryogenic temperatures
TAS	Menzel [59].	Nitric Oxide NO (min 3ppb)	Very high sensitivity	Cryogenic temperatures

1.5. NDS based on Cross Correlation Spectroscopy

The cross-correlation spectrometer was first described by Goody in 1968 [60]. Before analyse this spectrometer let us to recall that a cross correlation of two real valued functions it is defined by

$$f \star g = \int_{-\infty}^{\infty} f(\tau)\, g(t+\tau)\, \mathrm{d}\tau. \tag{1.13}$$

In this operation the function $g(\tau)$ is shifted along the τ axis and the integral must be evaluated for each t value. Therefore the cross correlation result will be a function of shift represented by t. In the theoretical Goody's cross correlation spectrometer [60] the absorption spectra of the target gas must be shifted along the wavenumber axis. Mathematically this concept can be easily understandable however in practice it is impossible to shift the absorption spectra as required by the cross correlation function. However Goody proposed a conceptual spectrometer [60] to get an 'experimental simulation' of two point spectral shift. This cross correlation spectrometer was very simple (figure 1.16) since it consisted in basically a two arms arrangement with two gas cells (the reference and the measurement cells). In this arrangement the chopper-mirror alternately passes the light through the arms. Prior to the light entering the two arm arrangement it passes by the measurement cell which contains the target gas which can be mixed with others gases. Moreover in one of the two arms a reference cell is placed which contains a volume of pure target gas or a mixture of pure target gas and non absorbing gas (ie N_2 for infrared). When light follows the arm 2, it is passed by the measurement cell thence reflected by the chopper/mirror to Mirror M2 which reflects the light into the reference cell and afterwards it is passed to the detector. Here the overall transmission it is given by

$$I(\Delta\nu_1) = \int_{\nu_1}^{\nu 2} S_1(\nu) Fil(\nu) A(\nu) T_1(\nu) T_2(\nu + \Delta\nu_1) \mathrm{d}\nu, \tag{1.14}$$

where $A(\nu)$ is the light transmission through the measurement cell considering just gases other than the target, $T_1(\nu)$ is the transmission through measurement cell considering just the target gas, and $T_2(\nu + \Delta\nu_1)$ is the transmission through the

reference cell. Here the ro-vibrational line positions of $T_1(\nu)$ and $T_2(\nu + \Delta\nu_1)$ occurs exactly at the same frequency since they are due to the same molecule (the target) and therefore this simulates in practice a spectral shift of $\Delta\nu_1 = 0$ cm^{-1}.

Moreover when light it is passed through the arm 1, here it is first passed through the reference cell, subsequently is passed by the chopper/mirror and travels to Mirror M1 which reflects this to the chopper/mirror which reflects the light to the detector. Therefore the transmission $T_2(\nu + \Delta\nu_2) = 1$ since light no passes the reference cell. This can be conceptually interpreted as a shift of the target absorption spectrum of the reference cell by $\Delta\nu_2 = \infty$ cm^{-1}, which means that all the transitions of the target molecule in the reference cell are now at infinity $T_2(\nu + \infty) = 1$. Consequently this simple conceptual spectrometer setup permits to experimentally have two discrete absorption spectrum shifts $\Delta\nu_1 = 0$ cm^{-1} and $\Delta\nu_2 = \infty$ cm^{-1}. Therefore this device allows the conceptual experimental performance of a cross correlation function. The overall transmission through the arm 2 it is given by

$$I(\Delta\nu_2) = \int_{\nu_1}^{\nu 2} S_1(\nu) Fil(\nu) A(\nu) T_1(\nu) T_2(\nu + \Delta\nu_2) \mathrm{d}\nu. \tag{1.15}$$

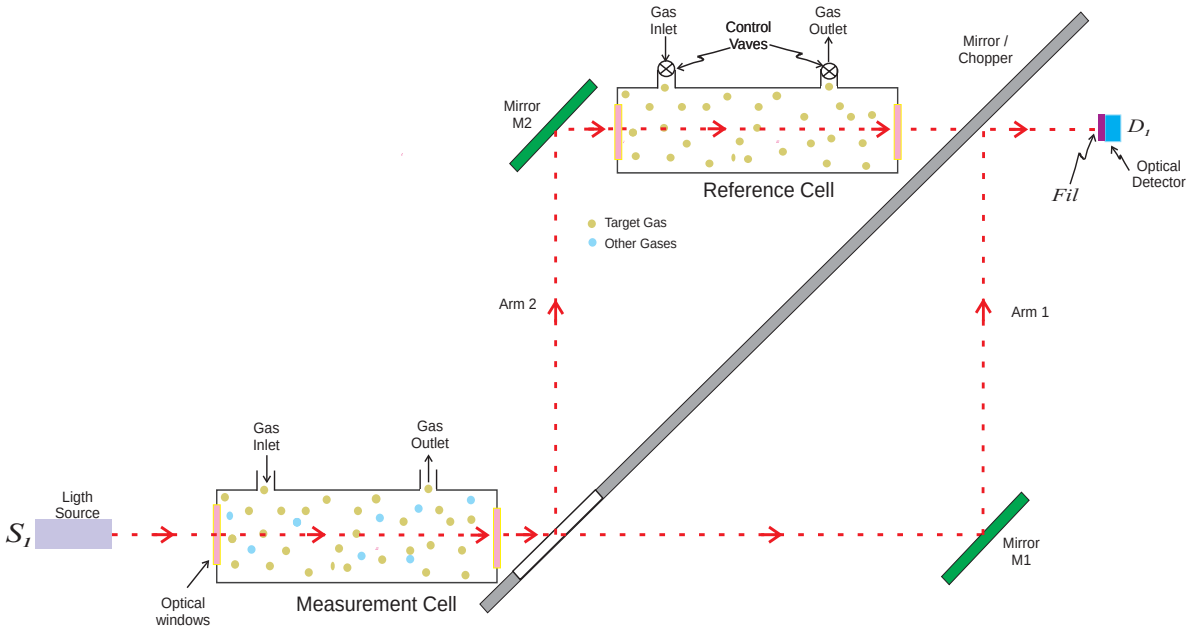

Figure 1.16- Goody's Cross-Correlation Gas Sensor Setup [60].

For instance in figure 1.17 we show the simulated absorption spectrum due to the presence of CO_2 in the measurement cell $T_1(\nu)$ (in this example CO_2 is the target gas). Here we are assuming that in the gas cell there is also water vapour and carbon monoxide. The absorptions of this mixture are described by $A(\nu)$. Moreover the transmission spectra due to the absorptions of CO_2 in the reference cell are represented by $T_2(\nu + \Delta\nu)$. Here for clarity we simulate the shifts $\Delta\nu_1 = 0$ cm^{-1} and $\Delta\nu_2 = 180$ cm^{-1}. In the first case, $\Delta\nu_1 = 0$ cm^{-1} the frequencies where the transitions occur are exactly the same as where the absorptions of $T_1(\nu)$, in the second case when $\Delta\nu_2 = 180$ cm^{-1} all the transitions of CO_2 are shifted far away from the filter's bandpass region of and therefore in this region $T_2(\nu) = 1$. In practice it is impossible to shift the absorption spectra as shown in figure 1.17, however as stated above by using the conceptual Goody's spectrometer is possible to simulate in practice that the reference cell absorption spectrum is shifted to infinity.

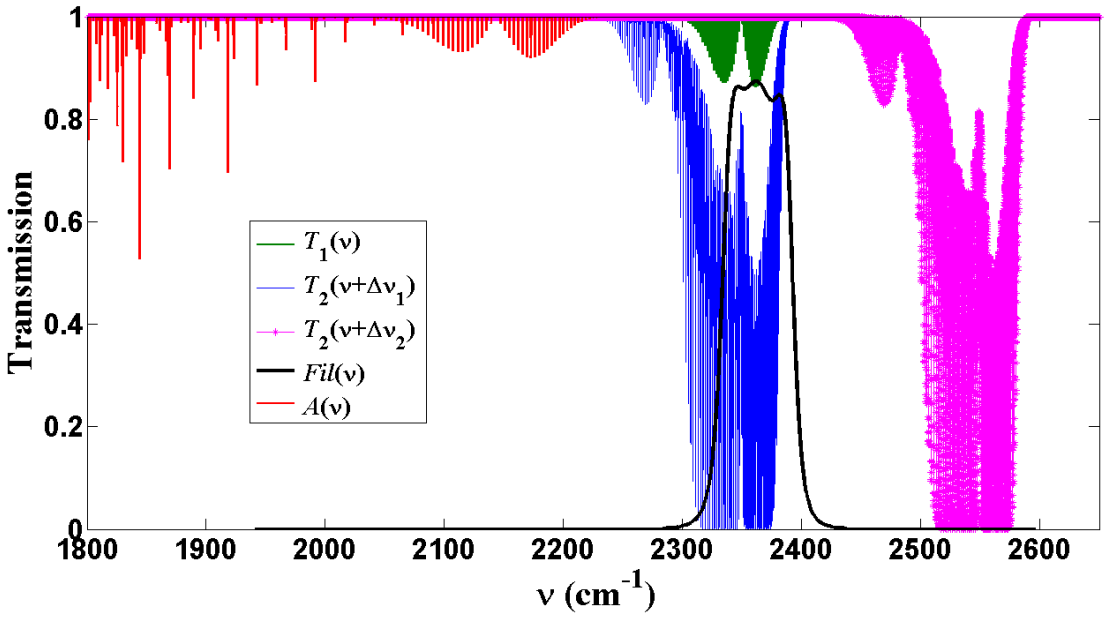

Figure 1.17- Ro-vibrational transmission spectra of a target molecule shifted along the wavenumber axis as required by the cross correlation function.

The main advantage of the Goody cross-correlation spectrometer is that the sensor will present very high selectivity to the target gas. This is because the cross correlation between spectra of different gases is very small. This can be shown if we consider that the source profile it is flat over the bandpass filter region and if the absorptions of gases

other than the target do not change. This allow us to rewrite equations (1.14) and (1.15) as

$$I(\Delta\nu_1) = \int_{\nu_1}^{\nu 2} S_1(\nu)\mathrm{d}\nu \int_{\nu_1}^{\nu 2} Fil(\nu)\mathrm{d}\nu \int_{\nu_1}^{\nu 2} A(\nu)\mathrm{d}\nu \int_{\nu_1}^{\nu 2} T_1(\nu)T_2(\nu+\Delta\nu_1)\mathrm{d}\nu. \tag{1.16}$$

and

$$I(\Delta\nu_2) = \int_{\nu_1}^{\nu 2} S_1(\nu)\mathrm{d}\nu \int_{\nu_1}^{\nu 2} Fil(\nu)\mathrm{d}\nu \int_{\nu_1}^{\nu 2} A(\nu)\mathrm{d}\nu \int_{\nu_1}^{\nu 2} T_1(\nu)T_2(\nu+\Delta\nu_2)\mathrm{d}\nu. \tag{1.17}$$

Thus the average difference between $I(\Delta\nu_1)$ and $I(\Delta\nu_2)$, also called depth modulation, can be expressed as

$$D_m = \frac{2\left[I(\Delta\nu_2) - I(\Delta\nu_1)\right]}{I(\Delta\nu_2) + I(\Delta\nu_1)} = \frac{2\left[\int_{\nu_1}^{\nu 2} T_1(\nu)T_2(\nu+\Delta\nu_2)\mathrm{d}\nu - \int_{\nu_1}^{\nu 2} T_1(\nu)T_2(\nu+\Delta\nu_1)\mathrm{d}\nu\right]}{\int_{\nu_1}^{\nu 2} T_1(\nu)T_2(\nu+\Delta\nu_2)\mathrm{d}\nu + \int_{\nu_1}^{\nu 2} T_1(\nu)T_2(\nu+\Delta\nu_1)\mathrm{d}\nu} \tag{1.18}$$

The result of this approach, equation (1.18), it is very important since it shows that the depth modulation is independent of absorptions due to other gases.

There are many other experimental setups to simulate the Goody cross-correlation spectrometer for instance the arrangement proposed by Dakin et al [43, 61] which it is shown in figure 1.18. Here the same simulated cross correlation is obtained as in Goody's setup. The main advantage of this design is that it eliminates the chopper/reflector which it is replaced by two identical intermittent sources which are synchronized and complementary, the drive control sequence for the sources is shown in figure 1.18. Hence when source (S_1) it is turned on the source S_2 it is in the off state, therefore the overall transmission at detector D_1 it is given by equation (1.16) with $\Delta\nu_1 = 0$ cm^{-1}. Moreover when the source S_2 is in the on state and source S_1 is in the off state the overall transmission is given by equation (1.17) with $\Delta\nu_2 = \infty$ cm^{-1}. The detector D_2 was used by the authors for calibration purposes.

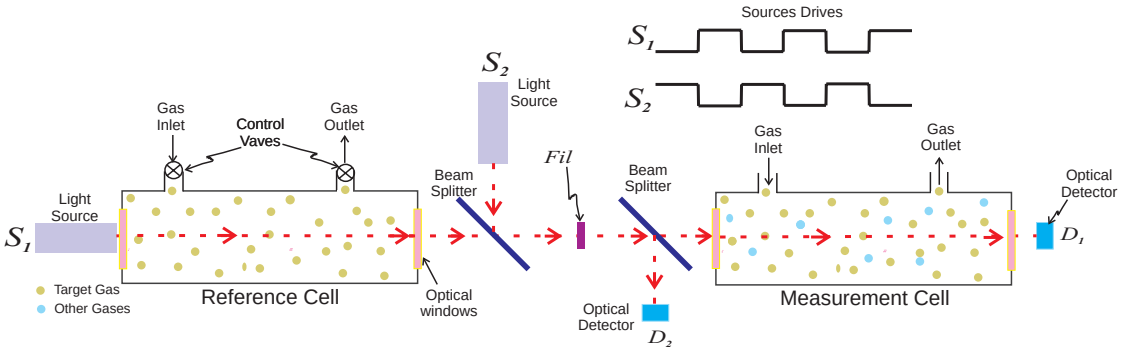

Figure 1.18- Dakin's Cross-Correlation Gas Sensor Setup [43, 61].

The main advantage of sensors based on the cross correlation principle as defined by Goody it is that these are practically insensitive to absorptions due to molecules other than the target gas, as described by equation (1.18). Obviously this approach will have some limits, for instance if the absorptions due to other molecules are very strong within the bandpass filter region saturation can be observed and therefore a serious reduction in the overall transmission will be produced which can produce a large error in the sensor response. The main disadvantage of these sensor setups is that they need two gas cells and one of them, the reference cell, must be sealed to avoid the leakage of the reference gas which will produce incorrect readings.

Before continuing it is important to mention that NDS gas sensors presented above can be adapted to introduce optical fibres into the designs. NDS fibre gas sensors can also be classified into one of the several groups of NDS sensors that we have mentioned above. One of the main advantages of using optical fibre in NDS sensors is that the measurement cell can be in a remote place or in an 'unfriendly' environment. Hence an optical fibre can be installed to avoid a person having to go to the measurement place every time that the measurement must be taken. For instance Dakin et al [43, 61] as well as the bulk cross correlation setup shown in figure 1.18 they presented in the same paper exactly the same device but modified to allow the use of optical fibres. In this work we will not discuss any further the DNS fibre gas sensors since it is not within the scope of this project. Instead we will concentrate on other types of cross correlation spectroscopy which is the main topic of our project, the NDS-based on Fabry-Perot Cross Correlation Spectroscopy.

1.6. NDS-based on Fabry-Perot Cross Correlation Spectroscopy.

As was stated in previous section the cross correlation spectroscopy as defined by Goody [60] is between the spectra of an unknown mixture $A(\nu)T_1(\nu)$, contained in the measurement cell, and the spectra of the target gas $T_2(\nu)$, which is contained in the reference cell. To implement the cross correlation function the transmission spectra of the target gas must be shifted along the wavenumbers axis $T_2(\nu + \Delta\nu)$. Here, the shifted function contains the information about the line positions of the ro-vibrational transitions. However as was mentioned above it is practically impossible to shift the ro-vibrational transitions as required and therefore this must be carry out by means of indirect conceptual methods which can simulate the cross correlation. The simplest experimental setups (i.e. Goody's spectrometer) were presented in the previous section and their main disadvantage is that they need two gas cells and one of them must be sealed (the reference cell). Another technique to 'experimentally simulate' the cross correlation as defined by Goody [60] is by using a Fabry-Perot Interferometer (FPI). This technique eliminates the requirement of the sealed gas cell.

The FPI is an instrument formed by two flat or spherical mirrors which produces a set of spectral transmission fringes [62]. The simplest FPI it is that formed by two parallel and flat mirrors (Figure 1.19). The transmission fringe profile it is described by the Airy formula given by [62]

$$I_{FP}\left(\nu, R, n, d, \Delta d\right) = \frac{1}{1 + \dfrac{4R}{\left(1-R\right)^2}\sin^2\left(\dfrac{4\pi n(d+\Delta d)\nu}{2}\right)} \tag{1.19}$$

where R is the mirror reflectivity, nd is optical thickness of the FPI, and ν is the frequency. Furthermore, another important parameter that needs to be defined here is the separation between two consecutive FPI fringes which is known as the Free Spectral Range (FSR) which, in terms of wavenumbers it is given by [62]

$$\mathrm{FSR} = \frac{1}{2nd}. \tag{1.20}$$

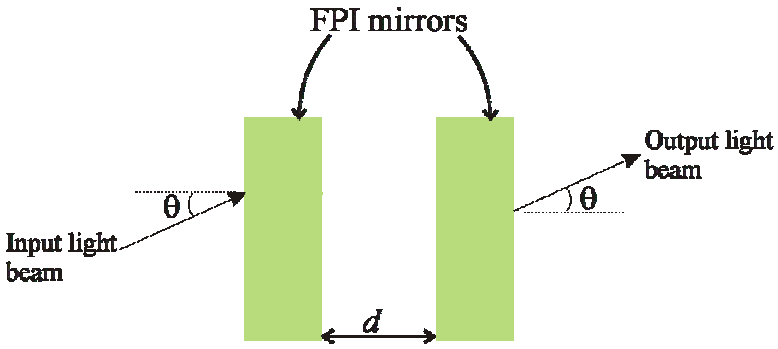

Figure 1.19- Plane Fabry-Perot Interferometer

By selecting a specific cavity length value (d) it is possible to match the FPI transmission fringes with some ro-vibrational absorption lines of a molecule. As the FPI fringes are equidistant and symmetric therefore the ro-vibrational transitions that we can match with the FPI must have almost equidistant separation. This is the case of most diatomic and linear molecules (CO, CO_2, N_2O, etc.) and some transitions of symmetric top and spherical tops (ie CH_4). For instance in figure 1.20 the absorption spectra of CH_4 at $\lambda_0 \approx 3$ µm it is presented, and the cavity length of the FPI it is selected to match the FPI fringes with some ro-vibrational lines of CH_4.

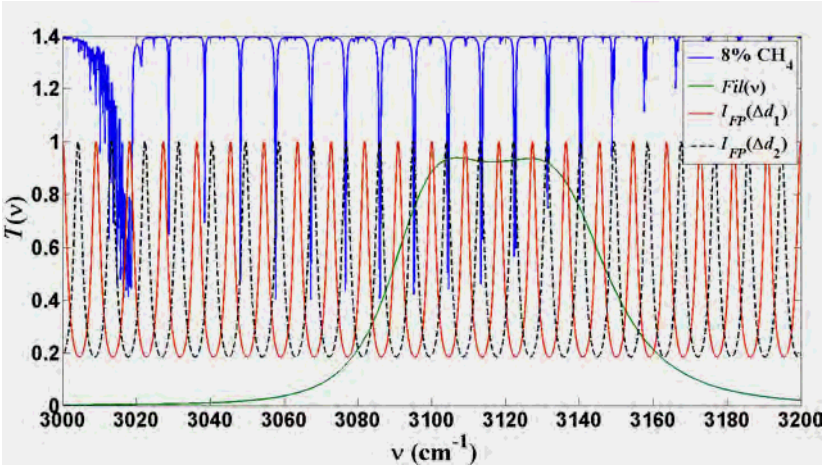

Figure 1.20- FPI transmission fringes matched with CH_4 rotational lines here $d = 0.055$ cm^{-1}. A slight change in the cavity length $d + \Delta d$ shifts the FPI fringes along the wavenumber axis. The CH_4 spectrum is shifted up 0.4 units for clarity.

To match the ro-vibrational lines the cavity length of the FPI must be approximately $d = 1/(2\overline{\Delta\nu})$ where $\overline{\Delta\nu}$ is the average separation between the ro-vibrational line

positions. For instance for a diatomic or linear molecule the FPI cavity length must be $d \approx 1/[2(2B)]$ assuming that the lines are almost equidistant with $2B$ separation as defined by equation (1.3). Furthermore it is possible to spectrally shift the FPI fringes by changing the optical thickness by Δd. To shift one FPI fringe over one FSR we need to vary the optical thickness by one half of the reference wavelength $(n\,(d-\Delta d) = nd - \lambda_0/2)$. This property can be exploited to obtain a cross correlation function.

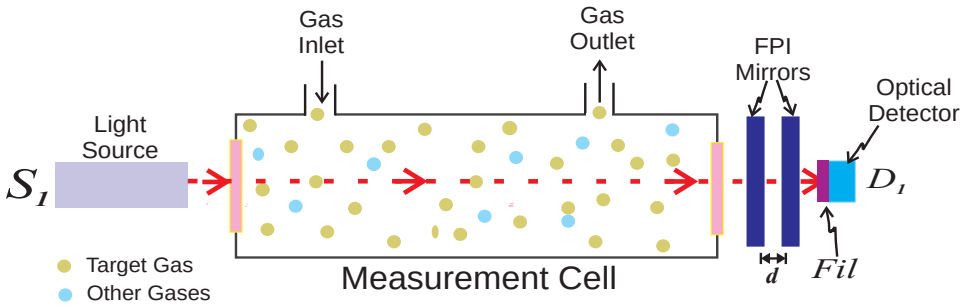

Figure 1.21- NDS Gas sensor setup based with an FPI.

A simple NDS gas sensor design with a FPI it is presented in figure 1.21, which is basically a *Single-Beam Multiple-Wavelength* design. The overall transmission in this setup it is given by

$$I_D\,(R, n, d+\Delta d) = \int_0^\infty I_{FP}\,(\nu, R, n, d+\Delta d)\,T\,(\nu)\,Fil\,(\nu)\,S\,(\nu)\mathrm{d}\nu \qquad (1.21)$$

By scanning the separation between the two FPI mirrors $d+\Delta d$ a cross correlation function it is obtained. This can be applied to conceptually simulate a gas sensor based on cross correlation as defined by Goody. The difference in this approach is that the reference transmission spectrum of the target gas is replaced by the FPI transmission fringe pattern and it is really shifted over the wavenumber axis experimentally. Hence the FPI must have almost the same separation between its transmission fringes as the separation of the ro-vibrational lines (Figure 1.20). This allows us to simulate practically the Goody's cross correlation principle. Here the main advantage is the elimination of the sealed reference cell which is replaced by a FPI. Several gas sensors using this technique can be found in literature and references [63-66] are some examples.

1.6.1. NDS gas sensors with Fabry-Perot Interferometers that do not satisfy the Correlation Spectroscopy principle.

There are some cases where sensors using a FPI can not be considered as based on cross correlation spectroscopy as defined by Goody. By selecting a very narrow cavity length broad FPI fringes are formed with a very large FSR. Thence if the cavity length is scanned by $d + \Delta d$ the wide fringes of the FPI transmission fringes are shifted along the wavenumbers axis. This is indeed a cross correlation operation however the shifted function (FPI transmission fringe pattern) does not have any information about the separation of the ro-vibrational transitions of the target gas. Here the condition to simulate the Goody cross correlation principle it is not satisfied and therefore these FPIs can not be utilised to design a sensor based on cross correlation spectroscopy. However these FPIs can be used to design other interesting sensor setups. Here two main cases can be identified which we have called the medium gap FPI and the narrow gap FPI.

1.6.1.1 The medium gap FPI

The medium gap FPI has a cavity length for which a wide fringe covers completely or partially a particular target absorption band. When the cavity length is scanned the wide fringe is shifted to another spectral region where ideally no other molecule absorbs. For instance in figure 1.22 we show the FPI transmission fringe pattern assuming a medium cavity length. Here when the cavity length scan $\Delta d = 0$ the FPI fringe illuminates one branch of the CH_4 and at some point of the cavity length scan (Δd_2) the FPI fringe is shifted to a spectral regions where any other molecule absorbs. This is in fact the same concept as the *Single-Beam Dual-Wavelength* presented in section 1.4.3

Several sensors using this concept can be found in literature, for instance the CO_2 sensor presented by Carlson 1997 [67] which is now commercially available (see Vaisala Instruments Catalog 2005 [37]). See also the ethylene (C_2H_4) gas sensor proposed by Saari *et al* 1998 [68]. Another good example of this type of sensor is the CO_2/H_2O sensor described by Noro *et al* [69], here the separation between two consecutive FPI fringes is fixed to be very large allowing just one wide fringe which at some point illuminates the H_2O absorption band and then the same FPI fringe is shifted

to cover the CO_2 absorption band. In all these cases the FPI is utilisable to produce a wide FPI fringe which is shifted along the wavenumber axis.

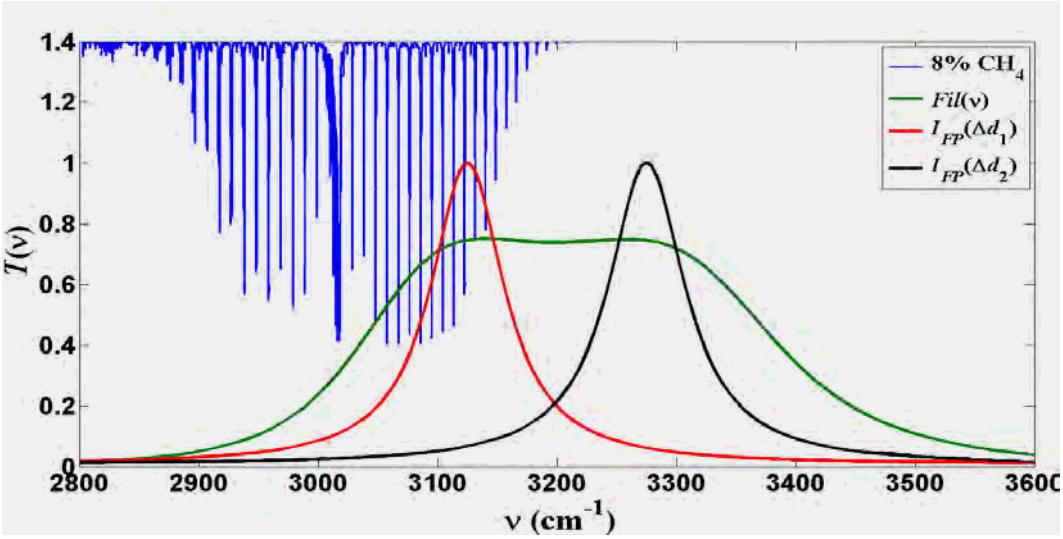

Figure 1.22- Simulated wide FPI fringe for a CH_4 medium gap sensor. The CH_4 absorption spectrum is shifted up 0.4 units for clarity. FPI cavity length $d = 5 \times 10^{-4}$ cm.

1.6.1.2 The narrow gap FPI gas sensor

Another exclusion case is when the FPI cavity length approaches zero, $d = 0$ and is scanned by one quarter of the reference wavelength $d + \lambda_0/4$. Consequently the spectral FPI transmission fringes will be extremely wide with a very large FSR. Ideally, at the initial point $d = 0$ cm the FPI transmission fringe pattern is flat, over the filter bandpass region, and equal to one (ON state). After the FPI cavity length scan has reached $\Delta d = \lambda_0/4$ cm the FPI transmission drops to a minimum (OFF state), here again there are no spectral fringes over the filter bandpass region (Figure 1.23), the minimum value will depend on the mirror reflectivity. This kind of modulation is quite similar to a mechanical chopper since we have basically two operational states ON and OFF as with the mechanical chopper. This type of modulation can be a convenient replacement for source modulation since this can help to avoid problems with the source stability and its recovery time. Moreover it is important to mention that this type of modulator it is not limited only to gas sensing and it is possible to use this FPI modulator in a wide range of applications.

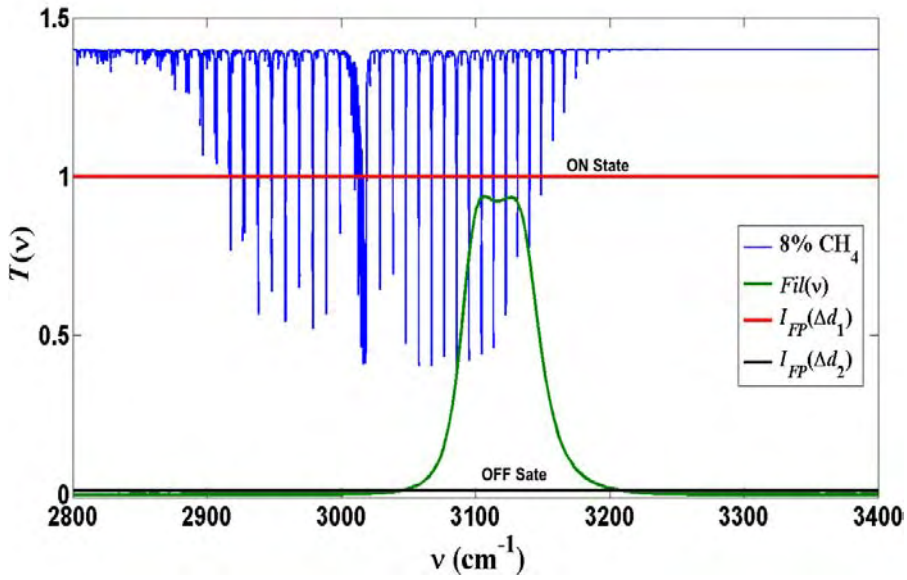

Figure 1.23- Simulated narrow gap FPI modulator with $d = 0$ µm. For ON state $\Delta d_1 = 0$ µm and for the OFF state $\Delta d_2 = 3.3/4$ µm. For clarity the CH_4 absorption band is shifted up 0.4 units.

1.7. Optical Gas sensors based on Micromachined Fabry-Perot Interferometers (MFPI).

Technology used for the fabrication of Micro-Electro-Mechanical-Systems (MEMS) devices is developing very fast and now it is possible to integrate within the same device micro-mechanical, micro-optical, and micro-electronic elements. The MEMS tunable FPI (MFPI) has gained attention and several works aiming at the integration of MFPIs can be found in literature (see Table 1.7). Furthermore, with current MEMS technology it is possible to integrate within the same MEMS device both the MFPI and the optical detector. For instance Vaisala Instruments [37, 67] offers commercially a CO_2 detector which has a medium gap MFPI which also integrates the optical detector. Another good example of commercial MFPI is the tunable FPI filter offered by Infratec GmbH [70]. Most of the MFPIs that can be found in the literature have a medium gap, which means that the cavity length of the FPI is just of few microns (1 to 30 µm) also in most of them the reflectivity of the FPI mirrors it is generally $R \leq 0.95$ (Table 1.7). As was stated before in section 1.4.3 the NDS gas sensors based on *Single-Beam Dual-Wavelength* design, which can be reached with a medium gap FPI, are reliable to detect some molecules. Here, the use of an MFPI is very convenient since it can help to considerably reduce the size and power consumption of the sensor.

Table 1.7- Some relevant MFPI's devices and their applications.

Reference	Application	Reflectivity, Cavity length
Wang et al 2004 [71]	Pressure sensing	
Heredero et al 2003 [72]	DC and AC electrical current measurements	$d = 36\,\mu m$, $R \approx 0.3$
Zuo et al 1997 [73]	Condenser microphone	
Li et al 2001 [74]	Condenser microphone	
Yamashita et al 1998 [75]	Infrared gas sensing	
InfraTec GmbH 2006 [70]	Infrared tunable band pass filter.	
Grasdepot et al 1996 [76], Alause et al 1997 [77]	Infrared gas sensing.	$d = 0.7 \rightarrow 2\,\mu m$, $R \approx 0.3$
Calaza et al 2004 [78]	Infrared gas sensing	$d = 1\,\mu m$, $R \approx 0.99$
Correia et al 1999 [79]	Microspectrometer with integrated photodiode and tuning over the entire visible spectral range with high spectral resolution.	$d = 1.2\,\mu m$, $R > 0.9$
Clift et al [80]	Monochromator. d=20 µm, $\mathscr{R}$>0.9	$d = 20\,\mu m$, $R > 0.9$
Noro et al 2002 [69]	MIR H_2O and CO_2 gas sensor	$d = 3.4\,\mu m$
Carlson 1997 [67] and Vaisala Instruments, Saari 1998 [37]	MIR CO_2, H_2O, or C_2H_4, gas sensor. MFPI integrated with optical detector.	
Srivastava et al 2004 [81]	Infrared Tunable filter.	$d = 0.7 \rightarrow 2\,\mu m$, $R > 0.9$
Jerman et al 1998 [82]	Tunable filter centred at $\lambda_0 = 1.5\,\mu m$	$d = 3.5\,\mu m$, $R > 0.95$
Blomiberg et al 1997 [83]	Infrared Tunable filter	$R > 0.9$
Patterson 1997 [84]	Micro-Mechanical FPI filter for operation in the 700-900 nm wavelength region with integrated photodetector.	$d = 1 \rightarrow 6.27\,\mu m$, $R \approx 0.3$
Neumann et al [85]	Infrared Tunable filter.	$d = 1.5 \rightarrow 2.5\,\mu m$, $R > 0.9$

1.8. Potential applications of MFPIs for cross correlation spectroscopy.

Practically all the current MFPIs found in literature can be exployed as modulators to design a *Single-Beam Dual-Wavelength* gas sensor. However the use of MFPI in gas sensors based on cross correlation spectroscopy has been not widely analysed. As was stated before the technique of cross correlation spectroscopy has potential use for detecting with high selectivity molecules with very well defined rotational lines such as CO_2, CO, CH_4, etc. They are practically insensitive to molecules other than the target molecule which is the main advantage of this technique.

We think that it is possible to fabricate MFPIs with wide cavity length using the same technology currently utilised to fabricate the medium gap MFPI ($d = 1$ to 30 μm). Obviously some issues will require further research, for instance how implement the longer spacers required in the new MFPI. As MEMS integration is very expensive it is compulsory to model very carefully the response of the wide gap FPI gas sensor. For instance it is necessary to determine the optimal parameters of the FPI such as reflectivity and cavity length. Furthermore we need to define the source characteristics, optics (lens, windows, etc), detector characteristics (detectivity, element area, etc), FPI mirror clear apertures, etc.

1.9. Thesis Outline.

In this work we present an analysis of the gas sensor design based on cross correlation spectroscopy with a wide cavity length FPI. Here we present some mathematical models to represent the system response. Depending on the source characteristics two cases can be defined when light reaching the FPI is collimated and when it is converging. When light it is collimated all rays reaching FPI will have the same angle of incidence. In contrast when the light reaching the detector is converging the rays reaching the detector have different angle of incidence. These source characteristics will change the FPI transmission fringe pattern response and therefore the overall sensor response will be affected. All these issues are reviewed in this work and the theoretical predictions are confirmed with experimental results.

In order to correctly simulate the gas sensor based on cross correlation spectroscopy with a MFPI it is required to have precise information about the spectroscopic absorption spectra of the target molecule. This information can be easily obtained from dedicated databases such as HITRAN 2004 [86]. This database contains a comprehensive list of line positions and intensities of the rotational lines for different molecules and different wavelength regions. Although it is simpler to use the information given by HITRAN to obtain the line positions and intensities of the ro-vibrational transitions for many molecules we think that it is useful to review how these line positions and intensities are evaluated, for molecules of importance to this thesis. Evaluation of these can provide us with very useful knowledge such as understanding the type of molecule, the molecule symmetry and selection rules, effects of other rotational constants in the line position of diatomic and linear molecules. Moreover this review is helpful to understand the evaluation of the line intensities, and how these are affected by temperature and pressure. Updated spectroscopic constants can easily be introduced as they become available, temperature and pressure effects are more completely modelled, and various spectroscopic effects (such as 'hot bands' etc) can readily be 'turned on and off' to understand their effect, as compared to simple use of HITRAN extracts. Therefore in Chapter 2 we review briefly some basic spectroscopic definitions and some mathematical models which can be used to compute the line position and intensities for CO_2, CO, N_2O and H_2O. However all the information presented in Chapter 2 is not new, here we make a compilation from many literature sources which is convenient to quickly learn the basic spectroscopic characteristics of the relevant molecules and as well to quickly reproduce their absorption spectra. Due to time limitation we did not simulate the CH_4 spectrum and we use directly the values listed in HITTRAN 2004 [86].

In chapter 3 we analyse the case when the FPI is illuminated with a collimated beam. In this chapter the novel analytical method to evaluate very rapidly the wide gap gas sensor response as a function of the gas concentration is presented, we called this *the convolution method*. Furthermore, using this analytical method the optimal FPI cavity length can be easily obtained. Moreover the method helped us to determine more rapidly the optimum FPI mirror reflectivity. Furthermore during the wide gap design it was observed that for some band pass filters the sensitivity of the gas sensors was

seriously affected for low gas concentration. This bandpass filter issue it is also underlined by our *convolution method* and it is also described in Chapter 3.

In chapter 4 the case when the FPI is illuminated with a converging beam is analysed. In this chapter a mathematical model capable of calculating the FPI fringe pattern considering a converging beam is presented. Here a blackbody source was considered. Using this mathematical model it is shown that the FPI transmission fringe pattern is strongly affected by long cavity length values for non-collimated beams. Possible solutions to minimize the effect of the degraded FPI fringe pattern are proposed, however some penalties have to be paid such as higher source power requirement. In this case it is important to keep in mind that in addition to the FPI fringe pattern produced by the two FPI mirrors others FPI fringe patterns can be produced by internal reflection within the mirrors substrates. For clarity in this thesis we called these internal mirror reflections *spectral parasitic reflection fringes (SPRF)*. These parasitic reflections can produce strong undesirable effects which interfere with the main FPI fringe pattern (produced by the two mirrors). In Chapter 4 a mathematical model which takes into account the *spectral parasitic reflection fringes (SPRF)* and the converging beam is presented. Here it is shown that the *SPRF effects* are even stronger for long cavity lengths. This effect should be seriously considered in the design of gas sensor based on cross correlation spectroscopy with a wide gap MFPI since this factor can compromise the device functionality. In this chapter some possible solutions to reduce the *SPRF effects* are presented. For instance is shown that for a FPI that does not require miniaturization thicker mirror substrates can reduce the *SPRF effects*. This is not a practical solution for a real MFPI for this case the *SPRF effects* can be reduced using antireflection coatings on the FPI mirrors substrates.

In Chapter 5 we present the results obtained with a proof of principle bench top experiment. Here we employed a converging blackbody source with different cone angles. In this section it is shown that the experimental results are in good agreement with the simulated results obtained by numerical evaluation. This proves that a FPI with small clear apertures (ie 1×1 mm^2) and with a converging blackbody source can be used to design a gas sensor based on cross correlation spectroscopy with very high selectivity to the target gas and practically negligible sensitivity to other molecules. Our

experimental setups were built with bulk optical components to provide a proof of principle experiment since the fabrication of one MEMS structure is really expensive!

1.10. References

1. T. W. Pelham, L. E. Holt, and M. A. Moss, Exposure to carbon monoxide and nitrogen dioxide in enclosed ice arenas, *Occup. Environ. Med.* **59**(4), p. 224-233., 2002

2. W. J. Fisk, R. K. Spencer, D. T. Grimsrud, F. J. Offermann, *et al.*, *INDOOR AIR QUALITY CONTROL TECHNIQUES Radon, Formaldehyde, Combustion Products*, 1987

3. B. Levesque, E. Dewailly, R. Lavoie, and D. Prud'Homme, Carbon monoxide in indoor ice skating rinks: evaluation of absorption by adult hockey players, *Am J Public Health* **80**(5), p. 594-598, 1990

4. R. P. Hepple and S. M. Benson, A Review of Human Health and Ecological Risks due to CO_2 Exposure, *American Geophysical Union, Spring Meeting*, 2001

5. P. Halpern, Y. Raskin, P. Sorkine, and A. Oganezov, Exposure to extremely high concentrations of carbon dioxide: A clinical description of a mass casualty incident, *Annals of Emergency Medicine* **43**(2), p. 196-199, 2004

6. Landfill Gas Primer An Overview for Environmental Health Professionals Department of Health and Human Services Agency for Toxic Substances and Disease Registry Division of Health Assessment and Consultation 2001, 2001

7. M. T. Parra, J. M. Villafruela, F. Castro, and C. Mendez, Numerical and experimental analysis of different ventilation systems in deep mines, *Building and Environment* **41**(2), p. 87-93, 2006

8. S. Akbar, P. Dutta, and C. Lee, High-Temperature Ceramic Gas Sensors: A Review, *International Journal of Applied Ceramic Technology* **3**(4), p. 302-311, 2006

9. NIOSH, Controlling Exposures to Nitrous Oxide During Anesthetic Administration, *The National Institute for Occupational Safety and Health* **NIOSH ALERT: 1994**(DHHS (NIOSH) Publication No. 94-100), 1994

10. NOSE-II, *On chemical gas sensors*, http://www2.nose-network.org/ (last accessed; 30/01/2007).

11. K. Arshak, E. Moore, G. M. Lyons, J. Harris, *et al.*, A review of gas sensors employed in electronic nose applications, *Sensor Review* **24**, p. 181-198, 2004

12. B. C. Muñoz, G. Steinthal, and S. Sunshine, Conductive polymer-carbon black composites-based sensor arrays for use in an electronic nose, *Sensor Review* **19**, p. 30-30, 1999

13. R. Knake, P. Jacquinot, A. W. E. Hodgson, and P. C. Hauser, Amperometric sensing in the gas-phase, *Analytica Chimica Acta* **549**(1-2), p. 1-9, 2005

14. K. J. Albert, N. S. Lewis, C. L. Schauer, G. A. Sotzing, *et al.*, Cross-Reactive Chemical Sensor Arrays, *Chem. Rev.* **100**(7), p. 2595-2626, 2000

15. H. Bai and G. Shi, Gas Sensors Based on Conducting Polymers, *Sensors* **7**, p. 267-307, 2007

16. H. T. Nagle, R. Gutierrez-Osuna, and S. S. Schiffman, The how and why of electronic noses, *IEEE Spectrum* **35**(9), p. 22-31, 1998

17. R. Knake and P. C. Hauser, Portable instrument for electrochemical gas sensing, *Analytica Chimica Acta* **500**(1-2), p. 145-153, 2003

18. Y. Nakatani, M. Matsuoka, and Y. Iida, γ-Fe_2O_3 Ceramic Gas Sensor, *Components, Hybrids, and Manufacturing Technology, IEEE Transactions on [see also IEEE Trans. on Components, Packaging, and Manufacturing Technology, Part A, B, C]* **5**(4), p. 522-527, 1982

19. M. Heule and L. J. Gauckler, Miniaturised arrays of tin oxide gas sensors on single microhotplate substrates fabricated by micromolding in capillaries, *Sensors and Actuators B: Chemical* **93**(1-3), p. 100-106, 2003

20. K.-W. Kim, P.-S. Cho, S.-J. Kim, J.-H. Lee, *et al.*, The selective detection of C_2H_5OH using SnO_2-ZnO thin film gas sensors prepared by combinatorial solution deposition, *Sensors and Actuators B: Chemical* **123**(1), p. 318-324, 2007

21. D. R. Patil and L. A. Patil, Room temperature chlorine gas sensing using surface modified ZnO thick film resistors, *Sensors and Actuators B: Chemical* **123**(1), p. 546-553, 2007

22. K. Bodenhofer, A. Hierlemann, G. Noetzel, U. Weimar, *et al.*, Performances of Mass-Sensitive Devices for Gas Sensing: Thickness Shear Mode and Surface Acoustic Wave Transducers, *Anal. Chem.* **68**(13), p. 2210-2218, 1996

23. M. Giannetto, V. Mastria, G. Mori, A. Arduini, *et al.*, New selective gas sensor based on piezoelectric quartz crystal modified by electropolymerization of a molecular receptor functionalised with 2,2'-bithiophene, *Sensors and Actuators B: Chemical* **115**(1), p. 62-68, 2006

24. Y. Chao, S. Yao, W. J. Buttner, and J. R. Stetter, Amperometric sensor for selective and stable hydrogen measurement, *Sensors and Actuators B: Chemical* **106**(2), p. 784-790, 2005

25. C. Mansfield, *An Investigation into the Viability of an Infrared Diagnostic Instrument for Measurement of CO_2 Isotope Ratios in Breath*, in *Optoelectronics Research Centre*. 2000, University of Southampton: Southampton.

26. D. Pavia, G. Lampman, and G. Kriz, *Introduction to Spectroscopy*, 3rd, Thomson Learning, 2001

27. F. Jalilehvand, X-ray Absorption Spectroscopy (XAS), *University of Calgary*,

28. J. Inczedy, T. Lengyel, and A. M. Ure, *Compendium on Analytical Nomenclature*, *Definitive Rules 1997*, 3rd, International Union of Pure and Applied Chemistry Analytical Chemistry Division, 1997

29. O. Svelto and D. C. Hanna, *Principles of Lasers*, 4th Edition, Plenum Press, 1998

30. H. Abramczyk, *Introduction to Laser Spectroscopy*, Elsevier, 2005

31. A. Yariv, *Optical Electronics in Modern Communications*, 5th, Oxford University Press, 1997

32. J. M. Hollas, *High Resolution Spectroscopy* 2nd Edition, John Wiley & Sons, 1998

33. G. Herzberg, *The Spectra and Structures of Simple Free Radicals*, *An Introduction to Molecular Spectroscopy*, 1st, Cornell University Press, 1971

34. J. M. Hollas, *Modern Spectroscopy*, 3rd Edition, John Wiley & Sons, 1996

35. Edinburgh_Instruments_Ltd. 2006. http://www.edinst.com (last accessed 15/02/2006);

36. Digital_Control_Systems_Inc. 2006. http://www.dcs-inc.net/model400.htm (last accessed 15/02/2006);

37. Vaisala-Instruments, Vaisala CARBOCAP sensor technology for stable carbon dioxide measurement, *Vaisala Instruments Catalog 2005*, p. 86-87, 2005

38. G. Wang, H. Arwin, and R. Jansson, An optical gas sensor based on ellipsometric readout, *Sensors Journal, IEEE* **3**(6), p. 739-743, 2003

39. A. O'Keefe and D. A. G. Deacon, Cavity ring-down optical spectrometer for absorption measurements using pulsed laser sources, *Review of Scientific Instruments* **59**(12), p. 2544-2551, 1988

40. H. Arwin, Is ellipsometry suitable for sensor applications?, *Sensors and Actuators A: Physical* **92**(1-3), p. 43-51, 2001

41. D. Beaglehole and H. K. Christenson, Vapor adsorption on mica and silicon: entropy effects, layering, and surface forces, *J. Phys. Chem.* **96**(8), p. 3395-3403, 1992

42. H. W. Kroto, *Molecular Rotation Spectra*, John Wiley & Sons, Ltd, 34-42, 1975

43. J. P. Dakin, H. O. Edwards, and B. H. Weigl, Latest developments in gas sensing using correlation spectroscopy, *Proceedings of SPIE* **2508**, 1995

44. T. G. Spence, C. C. Harb, B. A. Paldus, R. N. Zare, *et al.*, A laser-locked cavity ring-down spectrometer employing an analog detection scheme, *Review of Scientific Instruments* **71**(2), p. 347-53, 2000

45. S. Zangooie, R. Bjorklund, and H. Arwin, Vapor sensitivity of thin porous silicon layers, *Sensors and Actuators B: Chemical* **43**(1-3), p. 168-174, 1997

46. S. Guo, R. Rochotzki, I. Lundstrom, and H. Arwin, Ellipsometric sensitivity to halothane vapors of hexamethyldisiloxane plasma polymer films, *Sensors and Actuators B: Chemical* **44**(1-3), p. 243-247, 1997

47. A. A. Kosterev, A. L. Malinovsky, F. K. Tittel, C. Gmachl, *et al.*, Cavity ringdown spectroscopic detection of nitric oxide with a continuous-wave quantum-cascade laser, *Applied Optics* **40**(30), p. 5522-9, 2001

48. J. Manne, O. Sukhorukov, W. Jager, and J. Tulip, Pulsed quantum cascade laser-based cavity ring-down spectroscopy for ammonia detection in breath, *Applied Optics* **45**(36), p. 9230-7, 2006

49. E. L. Dereniak and G. D. Boreman, *Infrared Detectors and Systems*, USA, John Wiley and Sons Inc., 1996

50. Sacher-Lasertechnik-Group, *Principles of Diode Lasers*, http://data.sacher-laser.com/techdocs/podl.pdf (last accessed; 1/05/2007).

51. R. L. Petritz, Fundamentals of Infrared Detectors, *Proceedings of the IRE* **47**(9), p. 1458-1467, 1959

52. Hamamatsu-Corporation, *Characteristics and Use of Infrared detectors*, http://sales.hamamatsu.com/assets/applications/SSD/ (last accessed; 8/04/2007).

53. G. Zhang, J. Lui, and M. Yuan, Novel carbon dioxide gas sensor based on infrared absorption, *Optical Engineering* **39**(8), p. 2235-2240, 2000

54. J. Hodgkinson and R. Tatam. *Optical Gas Sensors*. 2005. <http://www.cranfield.ac.uk/soe/cpoe/ndir.htm> (last accessed 14/02/2006);

55. G. J. Fetzer, A. S. Pittner, W. L. Ryder, and D. A. Brown, Tunable diode laser absorption spectroscopy in coiled hollow optical waveguides, *Applied Optics* **41**(18), p. 3613-21, 2002

56. E. D. Hinkley, A. R. Calawa, P. L. Kelley, and S. A. Clough, Tunable-Laser Spectroscopy of the ν_1 Band of SO_2, *Journal of Applied Physics* **43**(7), p. 3222-3224, 1972

57. C. Roller, K. Namjou, J. D. Jeffers, M. Camp, *et al.*, Nitric oxide breath testing by tunable-diode laser absorption spectroscopy: application in monitoring respiratory inflammation, *Applied Optics* **41**(28), p. 6018-29, 2002

58. Cambel-Scientific-Inc., *TGA100A Trace Gas Analyzer System*, http://www.campbellsci.com/tga100a (last accessed; 9/04/2007).

59. L. Menzel, A. A. Kosterev, R. F.Curl, F. K. Tittel, *et al.*, Spectroscopic detection of biological NO with a quantum cascade laser, *Appl. Phys. B* **72**, p. 859-863, 2001

60. R. Goody, Cross-Correlating Spectrometer, *J. Opt. Soc. Am. B* **58**(7), p. 900-908, 1968

61. J. P. Dakin, M. J. Gunning, P. Chambers, and Z. J. Xin, Detection of gases by correlation spectroscopy, *Sensors and Actuators B: Chemical* **90**, p. 124-131, 2003

62. M. Born and E. Wolf, *Principles of Optics*, 3rd Edn Great Britain, Pergamon Press, 1965

63. J. P. Dakin, Review of Fibre Optic Gas Sensors, *The Plessey Company PLC*, 1988

64. W. Jin, G. Stewart, B. Culshaw, S. Murray, *et al.*, Absorption measurement of methane gas with a broadband ligth and interferometric signal processing, *Optics Letters* **18**, p. 1364-1366, 1993

65. A. Mohebati and T. A. King, Remote detection of gases by diode laser spectroscopy, *Journal of Modern Optics* **35**, p. 319-324, 1998

66. J. J. Barrett and S. A. Myers, New Interferometric Method for Studying Periodic Spectra Using a Fabry-Perot Interferometer, *J. Opt. Soc. Am.* **61**(9), p. 1246-1251, 1971

67. H. Carlson, CARBOCAP - new carbon dioxide sensor electrically tuneable interferometer for infrared gas analysis, *Sensor Review* **17**(4), p. 304-306, 1997

68. H. Saari, J. Antila, M. Blomberg, R. Mannila, *et al.*, VTT AUTOMATION Miniaturised Gas Sensor on the Basis of Micromachined Fabry-Perot Interferometer, 1998

69. M. Noro, K. Suzuki, N. Kishi, H. Hara, *et al.*, CO2/H2O gas sensor with a MEMS Fabry-Perot filter, *2002 IEEE/LEOS International Conference on Optical MEMS* 2002

70. InfraTec-GmbH, TIF 100 Tunable, micromachined, electrostatic actuated band pass filter for the MIR region,

71. W. Wang, R. M. Lin, D. G. Guo, and T. T. Sun, Development of a novel Fabry–Perot pressure microsensor, *Sensors and Actuators A* **116**, p. 59–65, 2004

72. R. L. Heredero, J. L. Santos, R. F. d. Caleya, and H. Guerrero, Micromachined low-finesse Fabry-Perot interferometer for the measurement of DC and AC electrical currents, *Sensors Journal IEEE* **3**(1), p. 13-18, 2003

73. Q. Zou, Z. Li, and L. Liu, Theoretical and experimental studies of single-chip-processed miniature silicon condenser microphone with corrugated diaphragm, *Sensors and Actuators A: Physical* **63**(3), p. 209-215, 1997

74. X. Li, R. Lin, H. Kek, J. Miao, *et al.*, Sensitivity-improved silicon condenser microphone with a novel single deeply corrugated diaphragm, *Sensors and Actuators A: Physical* **92**(1-3), p. 257-262, 2001

75. K. Yamashita, A. Murata, and M. Okuyama, Miniaturized infrared sensor using silicon diaphragm based on Golay cell, *Sensors and Actuators A: Physical* **66**(1-3), p. 29-32, 1998

76. F. Grasdepot, H. Alause, W. Knap, J. P. Malzac, *et al.*, Domestic gas sensor with micromachined optical tunable filter, *Sensor and Actuators B* **35-36**, p. 377-380, 1996

77. H. Alause, F. Grasdepot, J. P. Malzac, W. Knap, *et al.*, Micromachined optical tunable filter for domestic gas sensors, *Sensor and Actuators B* **43**, p. 18-23, 1997

78. C. Calaza, L. Fonseca, M. Moreno, S. Marco, *et al.*, A surface micromachining process for the development of a medium-infrared tuneable Fabry-Perot interferometer, *Sensor and Actuators A* **113**(1), p. 39-47, 2004

79. J. H. Correia, M. Bartek, and R. F. Wolffenbuttel, Bulk-micromachined tunable Fabry–Perot microinterferometer for the visible spectral range, *Sensors and Actuators A* **76**, p. 191–196, 1999

80. D. J. Clift, S. R. Mallinson, and J. H. Jerman. *A Miniature Fabry-Perot Interferometer with a Corrugated Silicon Diaphragm Support*. ICSensors. (last accessed;

81. R. Srivastava, U. G. Shenoy, S. R. Forrest, S. Chinnayelka, *et al.*, Bulk micromachining of a MEMS tunable Fabry-Perot interferometer: effect of residual silicon on device performance, *J. Microlith., Microfab., Microsyst.* **3**(4), p. 579-588, 2004

82. J. H. Jerman and S. R. Mallinson, A Miniature Fabry-Perot Interferometer Fabricated Using Silicon Micromachining Techniques, *THO215-4 IEEE* p. 16-18, 1998

83. M. Blomiberg, O. Rusanen, K. Keranen, and A. Lehto, A Silicon Microsystem - Miniaturised Infrared Spectrometer, *TRANSDUCERS '97 1997 International Conference on Solid-state Sensors and Actuators*, Chicago: 1997

84. J. D. Patterson, Micro-Mechanical Voltage Tunable Fabry-Perot Filters Formed in (111) Silicon, *NASA Technical Paper 3702*, 1997

85. N. Neumann, M. Heinze, S. Kurth, and K. Hiller. *A Tunable Fabry-Perot-Interferometer for 3 - 4.5 µm Wavelength with Bulk Micromachined Reflector Carrier*. www.infratec.de/sensorik/publications_en.shtml/, (last accessed 21/02/2006);

86. L. S. Rothman, D. Jacquemart, A. Barbe, D. C. Benner, *et al.*, The HITRAN 2004 molecular spectroscopic database, *Journal of Quantitative Spectroscopy and Radiative Transfer* **96**(2), p. 139-204, 2005

Chapter 2

2. High resolution spectroscopic modelling.

As the gas sensor design requires accurate information about the molecular absorption line positions and intensities, it was necessary to simulate some absorption spectra of our target gases such as CO_2 at 4.3 μm, and CO at 4.7 μm. Currently there are some dedicated databases which contain information such as line positions, line intensity, width of the lines, temperature correction parameters, etc. One of these databases which is accepted widely as a standard is HITRAN (High Resolution Transmission) database [1-5] which has spectroscopic information about many molecules including CO, CO_2, N_2O, CH_4, and H_2O. Using this information it is possible reproduce the infrared absorption spectrum of the molecules and therefore it is possible to start the sensor design. However, we think that it is worthwhile to give a brief review of the basic spectroscopic concepts to understand better some behaviour of the absorption spectra, for instance to know why and how the spectra is affected by temperature and by changes in pressure. Therefore in this chapter we present a recompilation from different sources of the mathematical models used to reproduce the

line position, line intensities, line shapes, and widths of our target molecules (CO_2 at 4.3 μm, N_2O at 4.6 μm and CO 4.7 μm).

In order to simulate accurately our gas sensors it is necessary to consider that there may be absorption bands of other molecules occurring very close to our target absorption bands. For instance an absorption band due to H_2O occurs close to the fundamental band of CO at 4.7 μm. Hence these absorptions are relevant since these can introduce some cross sensitivity errors in our sensors response. Cross sensitivity is the error produced by the presence of absorption lines of a different molecules (interfering lines) occurring very close to the absorptions lines of our target molecule. When the gas sensor can not 'identify' the presence of interfering absorptions it produces a response as if the absorptions are due to the target gas and therefore a false alarm is generated. This is a typical problem within gas sensors since for instance we do not want a CO sensor that responds to water vapour! As some important absorption bands of water vapour occurs very close to the absorption bands of CO, CO_2 and CH_4 therefore we need to reproduce some H_2O absorption bands using accurate spectroscopic models. The absorption spectrum of water vapour at 6.2 μm is of relevance for the CO and CO_2 sensors, since this absorption band can produce cross sensitivity errors in these sensors. In the same way, the absorption spectrum of water vapour at 2.7 μm is needed to properly predict the CH_4 sensor response at 3 μm. The spectroscopic models of CO_2, CO, and N_2O will be discussed in section 2.1 since they have very similar characteristics and practically the same theory is applicable for the three molecules. Finally, in section 2.2 the mathematical models used to reproduce the water vapour spectra are presented. The water vapour models are presented in a different section since these models are very different to those utilised for the linear and diatomic molecules presented in section 2.1.

2.1. Absorption Spectra for diatomic and linear molecules.

In this section for simplicity let us present firstly the simple spectroscopic model employed to simulate the absorption spectra of carbon dioxide (CO_2) molecule. This is a linear molecule and has a strong absorption spectrum in the region of 4.3 μm. The

second spectroscopic model to be presented is for the N_2O molecule, which is also a linear molecule and therefore simple to reproduce. This molecule has a very weak absorption spectrum at 4.6 μm. This absorption spectrum is needed to evaluate the cross sensitivity tables of the CO_2 and CO detectors. Finally, we will present the spectroscopic model used to simulate the absorption spectrum of carbon monoxide (CO), which is a diatomic molecule. This molecule has a weak absorption spectrum in the region of 4.7 μm. The spectroscopic model of CO is also very simple and generally speaking is similar to the CO_2 and N_2O spectroscopic models.

2.1.1. Carbon Dioxide Absorption Model

Evaluation of the CO_2 spectrum can be developed in three steps, the first consists in evaluating the line positions, which requires information such as the symmetry, types of bands, symmetry effect, and selection rules. The second step consists in evaluating the line intensities. Finally the last step is to build the CO_2 absorption spectrum and here it is necessary to know the line widths and shapes. All these points are presented briefly in this section.

2.1.1.1. Symmetry elements and operations

The molecule's nuclear configuration determines the symmetry of the molecule. A molecule may have one or several symmetry elements such as a plane of symmetry, a centre of symmetry, or an axis of symmetry [6]. To each symmetry element corresponds a symmetry operation. This is a coordinate transformation such as reflection or rotation that will produce a configuration of the nuclei indistinguishable from the original one [6]. There are several possible elements of symmetry which depends of the atoms molecule arrangement. The elements of symmetry related to a linear molecule are the *centre of symmetry* and the ∞-*fold axes*. A molecule is designated as linear because its atoms are arranged in a straight line such as CO_2, and N_2O.

A molecule has a *centre of symmetry* if the coordinates of all the particles of the molecule, expressed in the Cartesian system with the origin at the centre of mass, are change in sign $(x \to -x, y \to -y, z \to -z)$ an equivalent equilibrium configuration of the molecule is achieved [7, 8]. This symmetry operation is called reflection or

inversion at the centre [6, 7]. For instance $^{12}C^{16}O_2$ is a molecule which has this symmetry element (Figure 2.1).

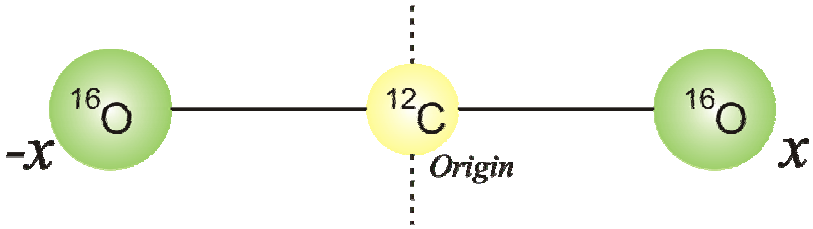

Figure 2.1- Molecule with a centre of symmetry

A molecule has *p-fold axis* of symmetry, where $p = 1, 2, 3, ...,$ if by rotation operation by an angle $360°/p$ about the axis a configuration indistinguishable from the original one is obtained [6]. Linear molecules can have some particular cases of the *p-fold* axis element. A two fold axis C_2 is present when a rotation of 180° about the axis will transform the molecule into itself (Figure 2.2a). Another element of symmetry in linear molecules is the infinite fold axes of symmetry (∞-*fold axes*) where by a rotation of $360°/\infty$ will transform the molecular configuration into an indistinguishable one [6] (Figure 2.2b). An example of a molecule having this type of symmetry is $^{17}O\,^{12}C^{16}O$.

In general a molecule can have several symmetry elements and by combination of these systems of higher symmetry are obtained [6]. However not all the symmetry elements combination are possible but only certain ones. A possible combination of symmetry operations that leaves at least one point unchanged is called a point group [6]. Just a limited number of such point groups exist and any molecule must belong to one of these. Linear molecules belong to either the $D_{\infty h}$ or $C_{\infty \nu}$ point groups.

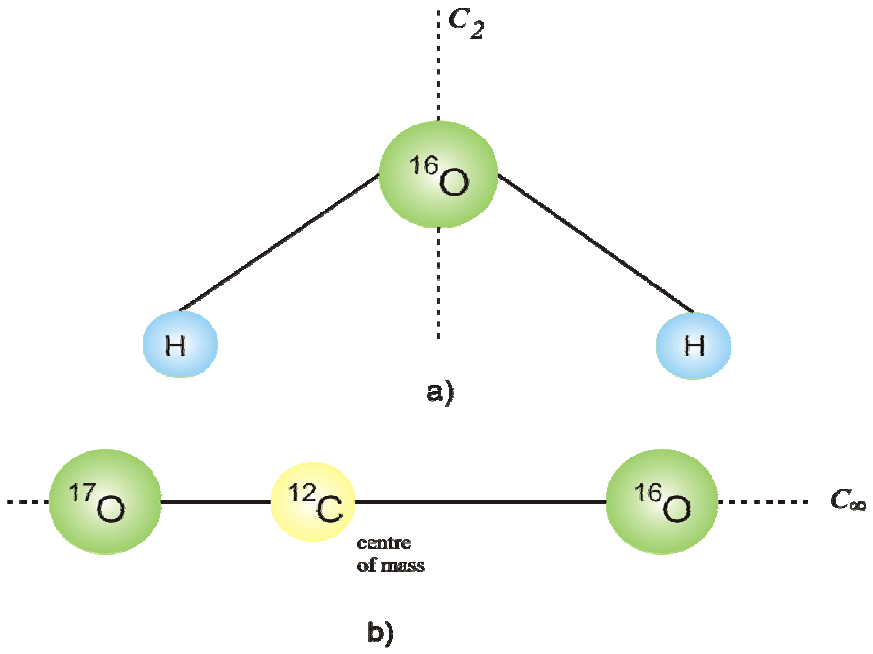

Figure 2.2- Molecules with a *p-fold axes.* a) Molecule with a C_2*-fold* axis; b) Molecule with a ∞*-fold axes.*

The $D_{\infty h}$ point group has an ∞*-fold axis* (C_∞), and infinite number C_2's perpendicular to the C_∞ axis, an infinite number of planes trough the C_∞ axis, and it has a centre of symmetry [6]. All homonuclear diatomic molecules and symmetrical linear molecules such as $^{12}C^{16}O_2$ belong to this group.

The $C_{\infty\nu}$ point group has an ∞*-fold axis* (C_∞) and an infinite number of planes trough the C_∞ axis [6]. For instance the $^{17}O\,^{12}C^{16}O$ molecule belongs to this group; also all the heteronuclear diatomic molecules belong to this group.

2.1.1.2. Line position at high resolution

The total vibrational rotational energy in wavenumbers for CO_2 is given by

$$E_{v+r}(v+J) = G_v + BJ(J+1) - DJ^2(J+1)^2 + HJ^3(J+1)^3, \qquad (2.1)$$

where, G_v is the vibrational term value, B is the rotational constant, D is the centrifugal distortion constant, and H is the constant due to anharmonicity [6, 9]. The value of the

spectroscopic constants will depend on the molecule isotopic variant and the selected transition.

The total energy change in a transition will be given by

$$\begin{aligned}\Delta E_{v+r}\left(v+J\right) = \left(G'_v - G''_v\right) + B'J'\left(J'+1\right) - D'J'^2\left(J'+1\right)^2 + H'J'^3\left(J'+1\right)^3 \\ - B''J''\left(J''+1\right) + D''J''^2\left(J''+1\right)^2 - H''J''^3\left(J''+1\right)^3\end{aligned} \tag{2.2}$$

where the single prime denotes the upper levels, and the double prime denotes the lower levels [9]. The factor $\left(G'_v - G''_v\right)$ is called the band centre and it will be represented by $\overline{\nu_0}$. The P branch, where $J' = J'' - 1$, is defined by

$$\begin{aligned}\Delta E_{v+r}\left(v,J\right) = \mathrm{P}\left(v,J\right) = \overline{\nu_0} + B'J''\left(J''-1\right) - D'J''^2\left(J''-1\right)^2 + H'J''^3\left(J''-1\right)^3 \\ - B''J''\left(J''+1\right) + D''J''^2\left(J''+1\right)^2 - H''J''^3\left(J''+1\right)^3\end{aligned} \tag{2.3}$$

for the R branch where $J' = J'' + 1$ we have

$$\begin{aligned}\Delta E_{v+r}\left(v,J\right) = \mathrm{R}\left(v,J\right) = \overline{\nu_0} + B'\left(J''+1\right)\left(J''+2\right) - D'\left(J''+1\right)^2\left(J''+2\right)^2 \\ + H'\left(J''+1\right)^3\left(J''+2\right)^3 - B''J''\left(J''+1\right) + D''J''^2\left(J''+1\right)^2 - H''J''^3\left(J''+1\right)^3\end{aligned} \tag{2.4}$$

and the Q branch where $J' = J''$ is given by

$$\begin{aligned}\Delta E_{v,J}\left(v,J\right) = \mathrm{Q}\left(v,J\right) = \overline{\nu_0} + B'J''\left(J''+1\right) - D'J''^2\left(J''+1\right)^2 + H'J''^3\left(J''+1\right)^3 \\ - B''J''\left(J''+1\right) + D''J''^2\left(J''+1\right)^2 - H''J''^3\left(J''+1\right)^3\end{aligned} \tag{2.5}$$

Basically these relationships give the line positions and the band centre, but further considerations are needed to obtain the spectrum. For instance, it is important to know the symmetry characteristic of the molecule in order to know the selections rules, and therefore determine if the Q branch is present or not.

2.1.1.3. Types of Infrared bands

Vibrational bands are classified as parallel or perpendicular according to their vibrational angular momentum and corresponding quantum number *l*. Energy states in which $l = 0, 1, 2, 3, ...$ are classified in species, or term symbols, as of type Σ, Π, Δ,

$\Phi, ...$ respectively. Furthermore, the components M_x, M_y and M_z of the dipole moment of the molecule $\mathbf{M}$ have their own symmetry properties and therefore these have a designated specie. In the infrared the selection rules allow only vibrational transitions for which the components M_x and M_y are of specie Π_u and M_z is of specie ${\Sigma_u}^+$ (the subscript u is dropped for the point group $C_{\infty\nu}$ [6]). It implies that

$$\Delta l = 0, \pm 1, \qquad \Sigma^+ \nleftrightarrow \Sigma^-, \qquad g \nleftrightarrow g, \qquad u \nleftrightarrow u.$$

And only rotational transitions for which

$$\Delta J = 0, \pm 1, \qquad + \nleftrightarrow -, \qquad s \nleftrightarrow a.$$

Therefore, according to these rotation-vibrational selection rules, three types of infrared bands of linear molecules can occur [6, 9]:

(*i*) Transitions for which $l = 0$ and $\Delta l = 0$. These bands are called parallel bands and give $\Sigma - \Sigma$ transitions. These bands only allow $\Delta J = \pm 1$, and they have only P and R branches (they do not have a Q branch). For these the dipole moment M_z has specie ${\Sigma_u}^+$. Some fundamental bands belong to this type of bands for instance the fundamental band of the antisymmetric stretching ν_3 mode of CO_2.

(*ii*) Transitions for which $\Delta l = \pm 1$. These are called perpendicular bands, and give $\Pi - \Sigma$, $\Delta - \Pi, ...$ transitions. In these bands $\Delta J = 0, \pm 1$,, and therefore they have P, R and Q branches. In these bands M_x and M_y have specie Π_u while $M_z = 0$. These bands can be either fundamental or overtone bands. For instance, the fundamental band of the bending ν_2 mode of CO_2 belongs to this type of transitions.

(*iii*) Transitions for which $l \neq 0$ and $\Delta l = 0$. These are parallel bands, and give $\Pi - \Pi$, $\Delta - \Delta, ...$ type transitions. These bands allow $\Delta J = 0, \pm 1$ and therefore they have P, R and Q branches. For these bands only $M_z \neq 0$ so the Q branch is weak. The hotbands of CO_2 are examples of these types of bands. Hotbands can be observed when an appreciable number of molecules are in the first, second, or so

on vibrational states. The population of these vibrational states increases with temperature.

In conclusion, the vibrational angular momentum and the dipole moment are very important since these determine the basic form of the absorption band i.e. determines when the Q branch is present. Taking into account the rotation-vibrational selection rules, in the case of the CO_2 spectrum at 4.3 μm, where the fundamental band of the ν_3 mode occurs, just bands of type (*i*) and (*iii*) occurs. For the N_2O spectral region at 4.6 μm which is related with our project just bands of types (*i*) and (*iii*) are considered. Finally, it is possible to say that the fundamental bands of CO occurring at 4.7 μm are bands of type (*i*).

2.1.1.4. Symmetry effects

Only certain energy levels are allowed for isotopomers belonging to the $D_{\infty h}$ point group restricting the number of transitions. By symmetry the ***vibrational energy levels*** are classified as symmetric or anti-symmetric with respect to the centre of symmetry. Symmetric levels are described as even and their term symbol is labelled with the subscript g. Similarly, anti-symmetric levels are described as odd and their term symbols are labelled with the subscript u. Only transitions between states of opposite symmetry are allowed $(g \leftrightarrow u)$, i.e.$\Sigma_g \rightarrow \Sigma_u$ and $\Pi_g \rightarrow \Pi_u$, the rest of the transitions are forbidden i.e. $g \nleftrightarrow g$, $u \nleftrightarrow u$ [6, 9].

Rotational energy levels are classified in a similar manner, each level has either $(+)$ or $(-)$ parity. In the case of the fundamental band, the even numbered rotational levels have $(+)$ parities, and the odd numbered levels have $(-)$ parities. Furthermore, each rotational level has assigned a symmetry (s) for symmetric level and (a) for the antisymetric level. Furthermore, even J rotational levels of specie Σ_g are classified as symmetric (s), and odd J levels as anti-symmetric (a), and vice versa for the specie Σ_u. Symmetry properties for rotational energy levels only allow transitions between levels of opposite parity and are forbidden to take place between levels of dissimilar symmetry [6]

$$(+) \leftrightarrow (-), (+) \nleftrightarrow (+), (-) \nleftrightarrow (-)$$

$$(s) \nleftrightarrow (a), (a) \leftrightarrow (a), (s) \leftrightarrow (s)$$

Due to symmetry considerations, in the $D_{\infty h}$ group the anti-symmetric rotational levels of the lower state do not exist. For instance, for the fundamental ν_3 band of $^{12}C^{16}O_2$, which is $(\Sigma_g \rightarrow \Sigma_u)$, all transitions which would originate in odd rotational J levels of Σ_g are absent, so that the lower rotational number J'' have values of 0, 2, 4, 6,… as a consequence [6].

Rotational energy level classification for Bands of types (*ii*) and (*iii*) have further considerations. Hotbands $\Pi_g \rightarrow \Pi_u$, and $\Delta_g \rightarrow \Delta_u$ of CO_2 are some examples. In these bands, each rotational level (J) is divided into two sublevels called ***e*** and ***f*** due l type doubling. Each of these sublevels will have parity $(+)$ or $(-)$ depending whether J is even or odd. In addition, rotational sublevels, ***e*** and ***f***, are also symmetrical (s) and anti-symmetrical (a) with respect to the centre of symmetry. These levels follow the selections rules defined previously. The ***e***-levels parities and symmetry designations are determined by $(-1)^{J+1}$, and vice versa for the ***f***-levels. The symmetry properties remain the same as discussed below, with the symmetric levels (s) and the anti-symmetric levels (a) of species Π_g or Δ_g corresponding to levels of positive and negative parity respectively, while the reverse is the case for the upper vibrational level Π_u or Δ_u. Considering CO_2 isotopomers of the $D_{\infty h}$ group undergoing $\Pi_g \rightarrow \Pi_u$ transitions, all anti symmetric rotational levels of the lower state are again absent. This produces a spectrum in which rotational levels of odd numbered J and even numbered J posses a single transition line originating from ***e***-level and ***f***-level respectively. The opposite is true from transition of type $\Delta_g \rightarrow \Delta_u$ [9].

2.1.1.5. Ro-vibrational Line Strength

Line positions and the selection rules were defined previously and using these information we proceed to evaluate the ro-vibrational line strengths. The basic formula utilised to obtain the line strength of each ro-vibrational line is given by

$$S_{v+r} = \left(\frac{\Delta E_{v+r}}{\overline{\nu_0}}\right) \frac{S_v^0 L_{J''l} E_{J''} F_{J''}}{Q_R} \left[1 - \exp\left(\frac{hc\Delta E_{v+r}}{kT}\right)\right], \qquad (2.6)$$

where, ΔE_{v+r} is the line position (2.2), $\overline{\nu_0}$ is the band centre, $L_{J''l}$ are the Hönl-London factors, S_v^0 is the rotationless band strength in units of $\left[\mathrm{cm}^{-1}/\left(\text{molecule-cm}^{-2}\right)\right]$ at 296K, $E_{J''}$ is the lower level rotational energy, $F_{J''}$ is the Herman Wallis Factor, Q_R is the rotational partition function, and T is the temperature [3, 10, 11].

The assumption that transition probability is constant is not correct, due to a rotational dependence associated with the number of degenerate energy levels available in a transition's upper state. This is accounted for by Hönl-London Factors which give the number of participating rotational levels at a given J'', the sum of which in each branch represents its proportion of total rotational line degeneracy, i.e. $2J+1$ [9]. For the fundamental and the hotband bands of the isotopomer modelled the Hönl-London Factors are given by

$$L_{J''l}^{\mathrm{R}} = \frac{(J''+1+l)(J''+1-l)}{J''+1} \tag{2.7a}$$

$$L_{J''l}^{\mathrm{P}} = \frac{(J''-1-l)(J''-l)}{J''} \tag{2.7b}$$

$$L_{J''l}^{\mathrm{Q}} = \frac{(2J''+1)\,l^2}{J''(J''+1)} \tag{2.7c}$$

where, the superscript R, P and Q denotes the respective branch [10].

Effects from the interaction of rotation and vibration are taken into account by the Herman-Wallis coefficients required to accurately describe line-strength. For R and P branches the Herman-Wallis factor are defined by

$$F_{J''} = \left(1 + a_1 m + a_2 m^2 + a_3 m^3\right)^2, \tag{2.8a}$$

where, m is equal to $-J''$ in the P branch and $J''+1$ in the R branch. For the Q branch the Herman-Wallis factors are given by

$$F_{J''} = \left(1 + b_2 m^2\right)^2; \tag{2.8b}$$

where, m is equal J''. In both cases (2.8a) and (2.8b) the Herman Wallis coefficients are a_1, a_2, a_3, and b_2 [9, 10]. The Herman-Wallis coefficients used to simulate the spectroscopic models for the different CO_2 isotopomers are presented in Table 2.2 to Table 2.4.

The rotational energy of the lower level it is given by

$$E_{J''} = \exp\left[-\frac{B''hcJ''\left(J''+1\right)}{kT}\right] \tag{2.9}$$

where, c is the velocity of light, h is the Planck's constant, k is Boltzmann's constant, and T is the temperature.

Line intensities reflect the populations of the initial level so the higher the population of the lower level stronger will be the absorption line intensity originating from this level. The ***population of a rotational level*** is related to the rotational partition function Q_R. It is a normalizing factor required to give a constant band intensity as the intensity distribution of the rotational lines changes with temperature. For diatomic and linear molecules at ordinary temperatures it is given by [6]

$$Q_R = \sum_J \left(2J+1\right)\exp\left[-\frac{BJ\left(J+1\right)hc}{kT}\right] \tag{2.10}$$

If the nuclear spin is neglected. According to Herzberg 1945 [6] the direct summation given by (2.10) is required for very low temperatures. For normal temperatures Herzberg [6] recommended the use of the following expansion

$$Q_R = \frac{kT}{hcB} + \frac{1}{3} + \frac{1}{15}\frac{hcB}{kT} + \frac{4}{315}\left(\frac{hcB}{kT}\right)^2 + \frac{1}{315}\left(\frac{hcB}{kT}\right)^3 + \ldots \tag{2.11}$$

However, for a small B and large T the rotational partition function, which is the case of CO_2, can be evaluated using the classical expression [6] given by

$$Q_R = \frac{kT}{hcB}. \tag{2.12}$$

The rotationless band strength value $S_v^0(T)$, for each transition is given by [10]

$$S_v^0(T) = \frac{8\pi^3 10^{-36}}{3hc} \frac{\overline{\nu_0} I_a}{g_j Q_v(T)} \exp\left(-\frac{hcG_v''}{kT}\right) |R_v|^2, \tag{2.13}$$

where, I_a is the natural isotopic abundance, G_v'' is the vibrational energy of the lower state, T is the temperature. ***The population distribution of the vibrational levels*** is related to the vibrational partition function$g_j Q_v(T)$. As the temperature will affect the total internal partition function, $Q = g_j Q_v(T) Q_R(T)$, it should be recalculated for a given T. The evaluation of the total internal partition sum can be easily obtained using the following approximation [12]

$$Q(T) = a + bT + cT^2 + dT^3, \tag{2.14}$$

where constants a, b, c and d for a range temperature from 70 to 400 K are listed in Table 2.1. Finally, the $S_v^0(T)$ values, for $T = 296$ K, corresponding to several CO_2 bands due to different isotopomers are given on Table 2.2-2.4.

Table 2.1- Polynomial coefficients of $Q(T)$ for the range 70-400 K. [12]

Isotopomer	a	b	c	d
$^{12}C^{16}O_2$	-2.1995	9.6751x10^{-1}	-8.0827x10^{-4}	2.8040x10^{-6}
$^{13}C^{16}O_2$	-3.8840	1.9263	-1.6058x10^{-3}	5.8202x10^{-6}
$^{16}O\,^{12}C^{18}O$	-4.7289	2.0527	-1.7421x10^{-3}	6.0748x10^{-6}

2.1.1.6. Absorption Line Shape

Description of the line position and line intensity given previously, do not give any information about the shape of the line. Transitions do not occur at one precise frequency, but rather they have a measurable width and specific shape [9]. The precise line shape depends on the some parameters, such as the pressure and temperature. For

normal pressure (1 atm) the line shape has a Lorentzian profile, this is true for homogeneously broadened lines [13] and is defined by

$$f_L(\nu_0) = \frac{\frac{\gamma}{\pi}}{(\nu_0 - \Delta E_{v+r})^2 + \gamma^2}. \tag{2.15}$$

In a homogeneous mechanism the principal contribution to the line width in gases are the collisional broadening γ (cm^{-1}/atm) which is proportional to pressure [13]. The Lorentzian profile is valid to describe the line shape in the infrared region of atmospheric molecules at normal pressure [14]. However for low pressures it is no longer true since now the line broadening mechanism is both homogeneous and heterogeneous. The heterogeneous line broadening in gases is associated with the Doppler effect [14]. This gives rise to the Gaussian line shape described by

$$f_G(\nu_0) = \frac{1}{\delta\sqrt{\pi}} \exp\left[-\left(\frac{\nu - \nu_0}{\delta}\right)^2\right] \tag{2.16}$$

where the Doppler line width it is given by $\delta = (2kT/m)^{1/2}(\nu/c)$ where m is the molecular weight. In the infrared region and considering low pressure the line widths are governed by both the homogeneous and the heterogeneous contributions. Therefore the resultant line shape is given by a convolution of the Gaussian and the Lorentzian contributions, this shape is known as the Voigt line shape [13]. According to [14] the Voigt shape occurs when $\gamma(P/\delta) < 1$. In our compilations we will consider as a valid the Lorentzian line shape, since our target region is mid infrared at 1 atm.

The line shape of CO_2 is being described by the normalized Lorentzian function [15]. The coefficient γ is independent of vibrational transition and differs for each ro-vibrational transition. The air broadening coefficient for CO_2 at 296K are given by a polynomial in terms of J'' [10]

$$\gamma = \begin{cases} 0.09489 & J'' = 1 \\ 0.09259 - 1.749 \times 10^{-3} J'' + 4.236 \times 10^{-5} J''^2 - 3.6793 \times 10^{-7} J''^3 & 2 \le J'' \le 45 \\ 0.039313 + 1.7806 \times 10^{-3} J'' - 3.7746 \times 10^{-5} J''^2 + \\ + 2.957 \times 10^{-7} J''^3 + 7.9569 \times 10^{-10} J''^4 & 46 \le J'' \le 121 \end{cases} \tag{2.17}$$

The final ro-vibrational absorption band is formed by the performing the overall sum of the products of the line-strength times the Lorentzian function of each absorption line [9].

There are several notation formats to express the absorption bands. In the older literature it is common to find that the absorption state of CO_2 were expressed as $\nu_1\nu_2{}^l\nu_3$, where the number of excited quanta associated with the particular vibration mode are ν_1, ν_2 and ν_3; l is the vibrational angular moment quantum number. The notation employed by the HITRAN database [2] to represent the CO_2 absorption bands is $\nu_1\nu_2 l\nu_3$r. These notations are practically the same the only difference is the r in the HITRAN notation. r is an integer called the ranking number and it is unity for the highest vibrational energy level of a Fermi resonating group. Therefore, the fundamental band due to the ν_3 vibration mode of CO_2 is expressed as $00001 \rightarrow 00011$ in HITRAN notation. Similarly, one of the CO_2 hotbands is expressed as $01101 \rightarrow 01111$ in HITRAN notation. The spectroscopic constants for all the bands modelled are given in Table 2.2 to Table 2.4, here bands are presented using the HITRAN notation. These tables contain the band centres, the Herman Wallis coefficients and the rotationless band strengths for each one of the modelled isotopomers. A simulated absorption spectrum for CO_2 at 4.3 μm is shown in figure 2.3.

Table 2.2- Spectroscopic constants for $^{12}C^{16}O_2$ transitions [4, 10].

Transition	**Band Centre**	$S_\nu^0 \times 10^{-22}$	B''	$D'' \times 10^{-7}$	$H'' \times 10^{-13}$	B'	$D' \times 10^{-7}$	$H' \times 10^{-13}$	a_1	a_2	a_3	b_2
00001-00011	2349.14291	916076	0.39021889	1.33338	0.077	0.38714135	1.32998	0.088	-0.00014	0	0	0
01101-01111e	2336.63231	70417	0.39063900	1.35295	0.099	0.38759250	1.34768	0.149	-0.00032	0	0	0
01101-01111f	2336.63231	70417	0.39125464	1.36088	0.149	0.38819027	1.35761	0.172	-0.00032	0	0	0
02201-02211e	2324.14068	2632	0.39166676	1.37452	-3.605	0.38863604	1.36021	-3.407	-0.00015	0	0	0
02201-02211f	2324.14068	2632	0.39166676	1.38022	0.148	0.38863604	1.37396	0.173	-0.00015	0	0	0
10002-10012	2327.43246	1717	0.39048223	1.57098	2.173	3.8750292	1.57357	1.981	-0.00008	0	0	0
10001-10011	2326.59761	1021	0.39018888	1.14919	1.1492	0.38706302	1.41183	1.803	-0.00015	0	0	0
11102-11112e	2315.23473	147	0.39074498	1.49447	1.005	0.38778212	1.48514	4.360	-0.00017	-0.144	0	0
11102-11112f	2315.23473	147	0.39169032	1.56357	1.163	0.38870505	1.56314	1.266	-0.00017	-0.144	0	0
03301-03311e	2311.66758	105	0.39237834	1.40009	-1.562	0.38937642	1.38853	-1.349	-0.00012	-0.015	0	0
03301-03311f	2311.66758	105	0.39237834	1.40009	-1.179	0.38937642	1.38853	-1.005	-0.00012	-0.015	0	0
11101-11111e	2313.77268	72.3	0.39040962	1.25853	0.906	0.387364478	1.24083	0.849	-0.00014	-0.002	0	0
11101-11111f	2313.77268	72.3	0.39133390	1.21099	0.451	0.38823509	1.20080	0.362	-0.00014	-0.002	0	0

Table 2.3- Spectroscopic constants for $^{13}C^{16}O_2$ transitions [4, 10]

Transition	**Band Centre**	$S_\nu^0 \times 10^{-22}$	B''	$D'' \times 10^{-7}$	$H'' \times 10^{-13}$	B'	$D' \times 10^{-7}$	$H' \times 10^{-13}$	a_1	a_2	a_3	b_2
00001-00011	2283.48711	9286	0.39023754	1.33346	0.151	0.38727344	1.32916	0.170	-0.00013	0	0	0
01101-01111e	2271.75989	771.6	0.39061133	1.35489	0.497	0.38768022	1.34923	0.585	-0.00015	0	0	0
01101-01111f	2271.75989	771.6	0.39124542	1.36377	0.305	0.38829411	1.35938	0.280	-0.00015	0	0	0
02201-02211e	2260.04908	33.7	0.39161360	1.32714	-0.634	0.38869955	1.32077	0	-0.00013	0.012	0	0
02201-02211f	2260.04908	33.7	0.39161360	1.38798	-0.256	0.38869955	1.38420	0	-0.00013	0.012	0	0
10002-10012	2261.90969	19.5	0.39091592	1.58290	2.406	0.38803647	1.57716	2.349	-0.00014	-0.005	0	0
10001-10011	2262.84815	11.6	0.38971769	1.20251	2.207	0.38672378	1.19863	2.111	-0.00014	0.017	0	0
11102-11112e	2250.69406	1.81	0.39096282	1.49053	0	0.38801702	1.30863	0	0	0	0	0
11102-11112f	2250.69406	1.81	0.39221550	1.56117	0	0.38914170	1.54833	0	0	0	0	0
03301-03311e	2248.35587	1.43	0.39228792	1.38603	-1.128	0.38940346	1.37467	-0.864	-0.00012	0.095	0	0
03301-03311f	2248.35587	1.43	0.39228792	1.38603	-0.039	0.38940346	1.37467	0.221	-0.00012	0.095	0	0
11101-11111e	2250.60467	0.897	0.39005116	1.27429	0.318	0.38713084	1.26068	0.641	-0.00014	-0.013	0	0
11101-11111f	2250.60467	0.897	0.39091846	1.23846	1.829	0.38794439	1.23446	2.096	-0.00014	-0.013	0	0

Table 2.4- Spectroscopic constants for $^{16}O^{12}C^{18}O_2$ transitions [4, 10].

Transition	**Band Centre**	$S_\nu^0 \times 10^{-22}$	B''	$D'' \times 10^{-7}$	$H'' \times 10^{-13}$	B'	$D' \times 10^{-7}$	$H' \times 10^{-13}$	a_1	a_2	a_3	b_2
00001-00011	2332.11231	3686	0.36818450	1.18701	-0.015	0.36528675	1.18424	0.014	-0.00032	0	0	0
01101-01111e	2319.73770	289	0.36860192	1.20678	0.186	0.36573112	1.20268	0.217	-0.00013	0.006	0	0
01101-01111f	2319.73770	289	0.36915324	1.20692	-0.285	0.36626757	1.20380	-0.0296	-0.00013	0.006	0	0
02201-02211e	2307.38300	11.4	0.3695641	1.24872	-3.814	3.6670707	1.23511	-3.705	-0.00012	0.016	0	0
02201-02211f	2307.38300	11.4	0.3695641	1.23158	0.603	0.36670707	1.22499	0.444	-0.00012	0.0016	0	0

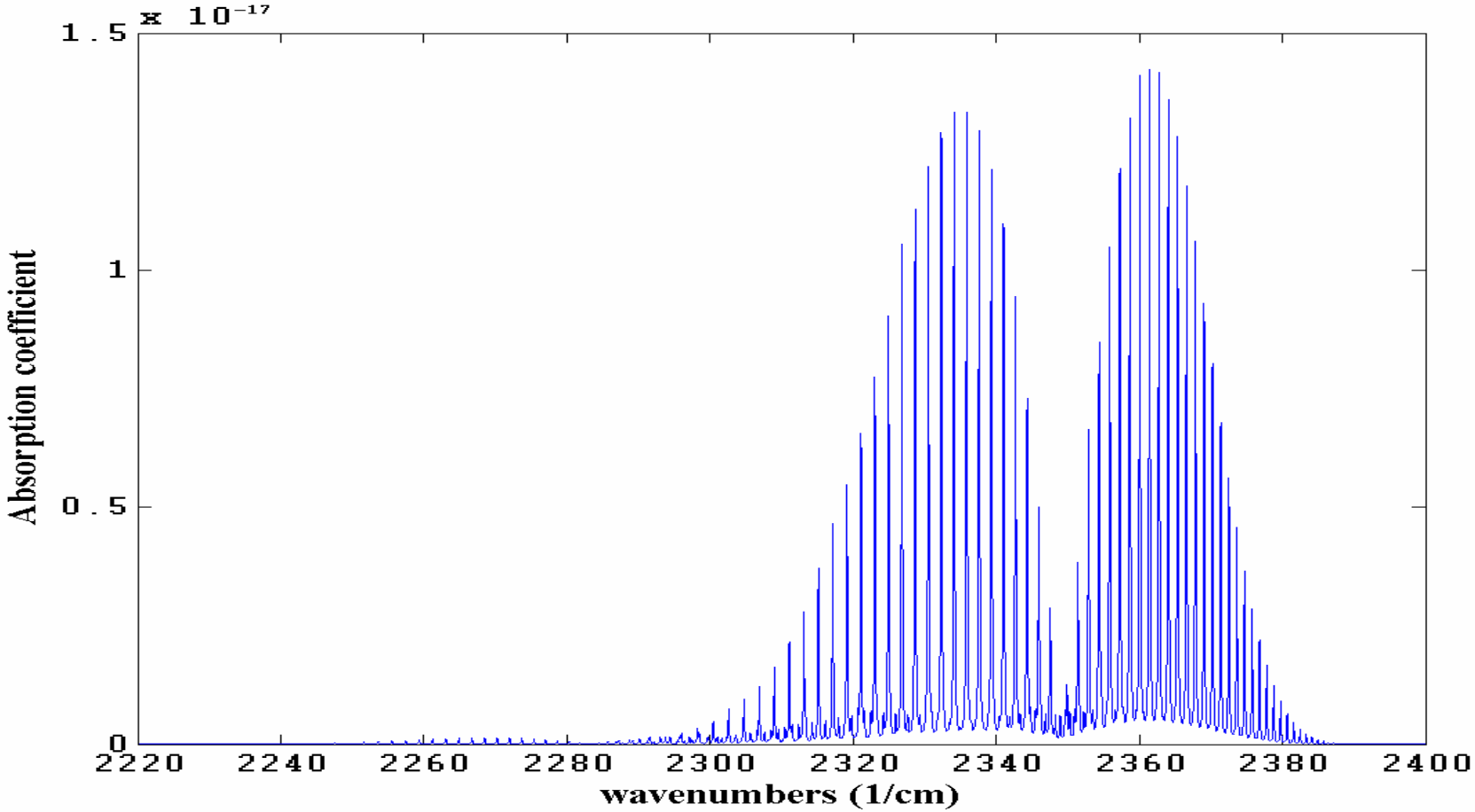

Figure 2.3- Simulated absorption spectrum of CO_2. This spectrum includes several bands due to $^{12}C^{16}O_2$, $^{13}C^{16}O_2$ and $^{16}O^{12}C^{18}O$ isotopomers.

2.1.1.7. Validation of the CO_2 model.

In order to validate our simulated spectrum of CO_2 we compare our computed results with those listed in the HITRAN 2004 database [1]. According to the HITRAN database the difference between the measured line position and the computed line position is in the order of 0.0001 cm^{-1} for most of the ro-vibrational lines of the strongest fundamental band of the CO_2 in the region of the 4.3 μm [1, 3]. In the same way the computed lines reported by HITRAN present an error around 6% for the same absorption bands [1, 3]. Here we require to evaluate how close are our computed line positions and intensities with those provided by HITRAN in order to be sure that our data have good level of confidence. Firstly, in this section we evaluate the difference between the calculated line positions and those listed in HITRAN. Here we will call to this difference the *residual difference*. Secondly, we evaluate the error in the line intensity. Here we just present the result obtained for the fundamental bands of the three most abundant isotopomers $^{12}C^{16}O_2$, $^{13}C^{16}O_2$ and $^{16}O\ ^{12}C^{18}O$. The residual difference in line position for the fundamental bands $00011 \leftarrow 00000$ of the $^{12}C^{16}O_2$ and $^{13}C^{16}O_2$ isototopomers is in the order of $\leq 5 \times 10^{-5}$ cm^{-1} for $J \leq 50$ (Fig. 2.2 and 2.3 respectively). The $00011 \leftarrow 00000$ band of the $^{16}O\ ^{12}C^{18}O$ isotopomer has even much lower residual difference in the order of $\leq 5.06 \times 10^{-7}$ for $J \leq 80$ (Fig. 2.4). The deviation in the line position is mainly due to precision errors in the constants D and H since the deviation increases as J increase. It can be appreciated with the fundamental band $^{16}O^{12}C^{18}O$ where the deviation is practically negligible meaning that all the rotational constants for this band are more accurate than is needed for our purposes.

Furthermore, considering that the residual difference in the ro-vibrational line positions for the $00011 \leftarrow 00000$ band of $^{12}C^{16}O_2$ is $\leq 1 \times 10^{-5}$ cm^{-1} for $J \leq 80$ and these ro-vibrational lines have in average a FWMH of 0.14 cm^{-1}; therefore we can say that our model deviates by $1/14,000^{\text{th}}$ of a typical ro-vibrational line width for this band when $J \leq 80$. The deviation is even much lower, in the order of $1/280,000^{\text{th}}$, for the fundamental band of $^{16}O\ ^{12}C^{18}O$. In the next chapter it will be shown that the separation of two rotation lines is of great importance in our project. In average the separation of the ro-vibrational lines of the $^{12}C^{16}O_2$ fundamental band is around 1.8 cm^{-1} for the P branch and 1.3 cm^{-1} for the R branch when $J \leq 40$. Hence the deviation of the

computed line position is around $1/28,000^{\text{th}}$ of the separation between two consecutive ro-vibrational lines.

These deviations are very small and for our application they are negligible. In our particular case in order to simulate our sensor with sufficient accuracy we build a wavenumber axis using an interval of 0.01 cm^{-1} which is $1/16^{th}$ of the line width and around $1/160^{th}$ of the separation of two consecutive ro-vibrational lines. This wavenumber interval is much larger than the residual difference in line position between our computed values and the HITRAN values. It means that using a 0.01 cm^{-1} interval in the wavenumber axis the evaluated line positions are the same as those given by HITRAN and therefore the residual differences will not affect the final CO_2 spectrum. A wavenumber axis with a 0.01 cm^{-1} interval is good enough to reproduce an accurate CO_2 spectrum which can be used to simulate our gas sensors which are based mainly in the separation of the ro-vibrational lines.

The line intensity error (%) of our calculated values and those listed in the HITRAN 2004 for the fundamental bands of of $^{12}C^{16}O_2$ and $^{13}C^{16}O_2$ and $^{16}O\ ^{12}C^{18}O$ are presented in figures 2.5-2.7. Here it can be seen that the error is around 0.01% for $J \leq 80$, which is very small. This error is mainly due to precision errors in the rotational constants and in the Herman-Wallis Factors coefficients. However the errors are quite small and this will not introduce a significant error in the simulation of our gas sensor.

According to HITRAN 2004 the total accumulated strength of the fundamental bands of the three most abundant isotopomers $^{12}C^{16}O_2$, $^{13}C^{16}O_2$ and $^{16}O^{12}C^{18}O$ is $928291.4 \times 10^{-22}\ \mathrm{cm}^{-1}/(\mathrm{molecule} - \mathrm{cm}^{-2})$ at 296K for $J \leq 110$. In our simulation we are including the fundamental bands of these three isotopomers considering ro-vibrational lines up to $J \leq 80$ and the overall accumulated strength is 928288.3×10^{-22} $\mathrm{cm}^{-1}/(\mathrm{molecule} - \mathrm{cm}^{-2})$. This represents the 99.9996% of the total strength obtained from HITRAN up to $J \leq 110$. Therefore, if we consider that our model has an error of 0.01% and that just the 99.9996% of the total strength is taken into account we find that our model has an accuracy of around 99.9896 %. Furthermore we need to consider that the HITRAN line intensities have an error of around 6% therefore our computed line intensities have an accuracy of 93.999624% with respect to the real measured intensities [1-3]. This led us to consider that the model presented in the previous section to

calculate the line intensities for CO_2 is sufficiently accurate. Finally, in Table 2.5 a comparison between calculated line position and intensities with respect to HITRAN 2004 of some ro-vibrational lines are presented, at 296K the strongest ro-vibrational line is at $J = 16$, here can be observed that the deviations are very small.

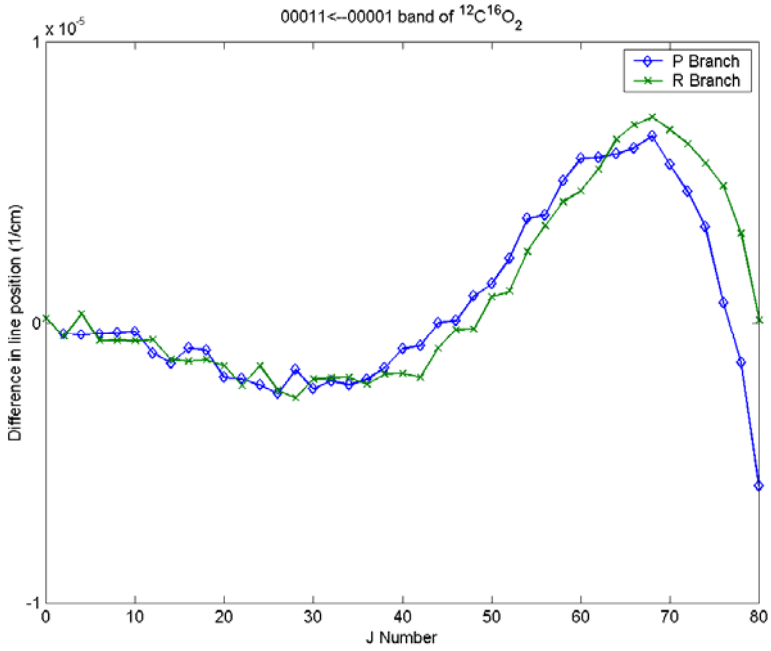

Figure 2.4- Residual difference in line position between our calculated positions and HITRAN 2004 for the $00011 \leftarrow 00000$ of $^{12}C^{16}O_2$.

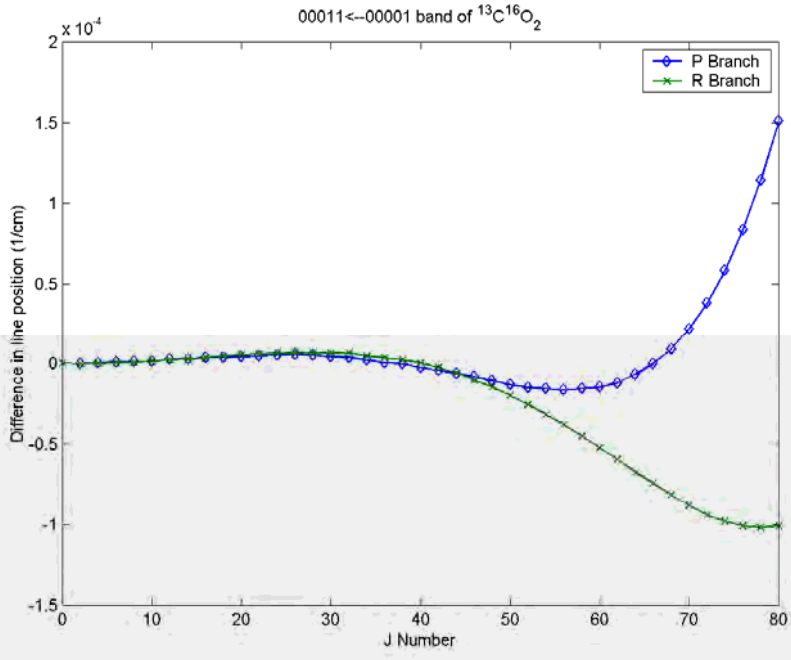

Figure 2.5- Residual difference in line position between our calculated positions and HITRAN 2004 for the $00011 \leftarrow 00000$ of $^{13}C^{16}O_2$.

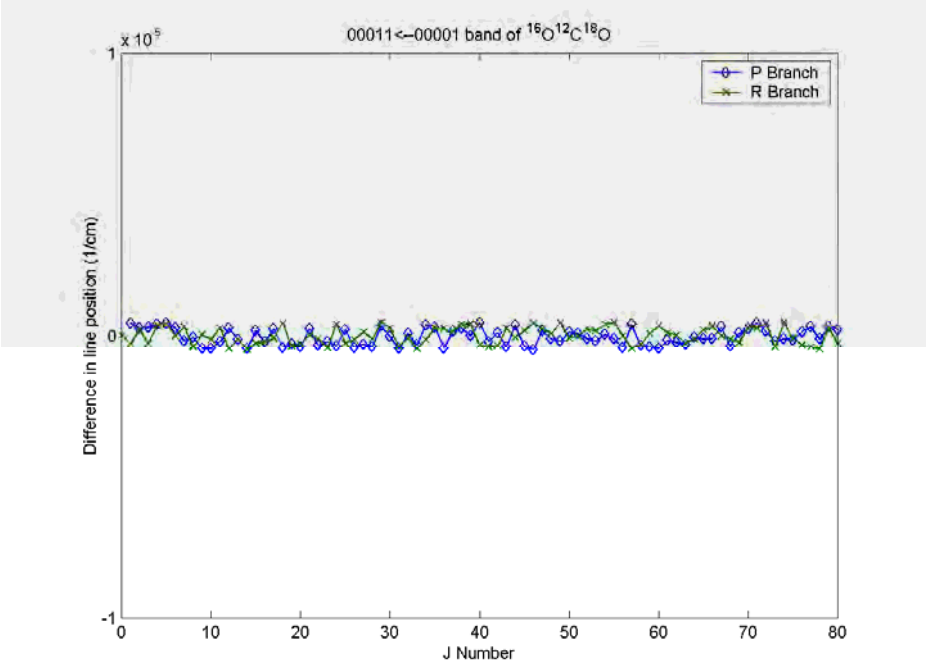

Figure 2.6- Residual difference in line position between our calculated positions and HITRAN 2004 for the $00011 \leftarrow 00000$ of $^{16}O^{12}C^{18}O_2$.

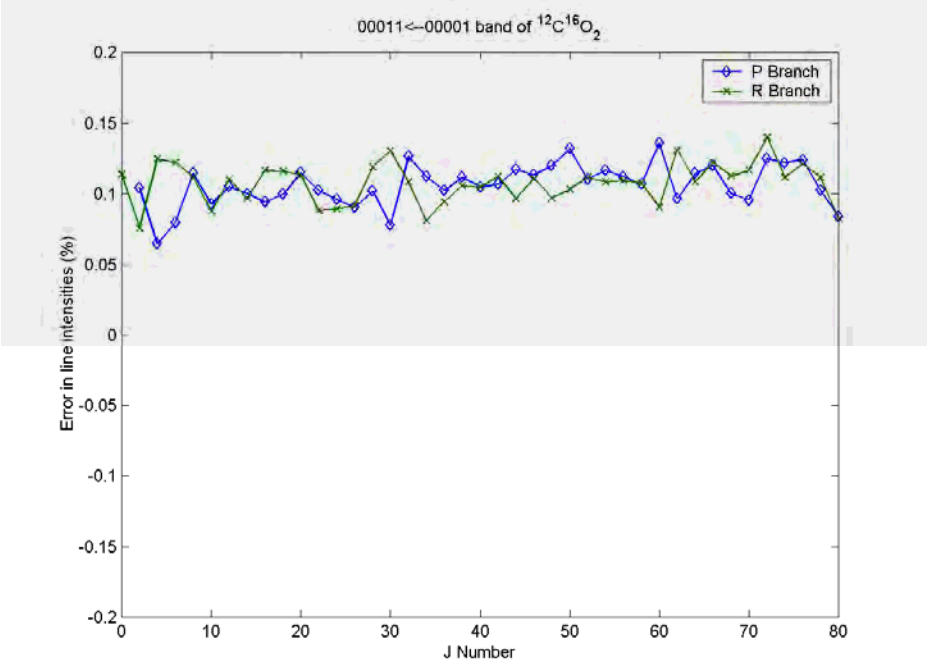

Figure 2.7- Error in Line intensities between HITRAN 2004 and the computed values 2004 for the $00011 \leftarrow 00000$ of $^{12}C^{16}O_2$.

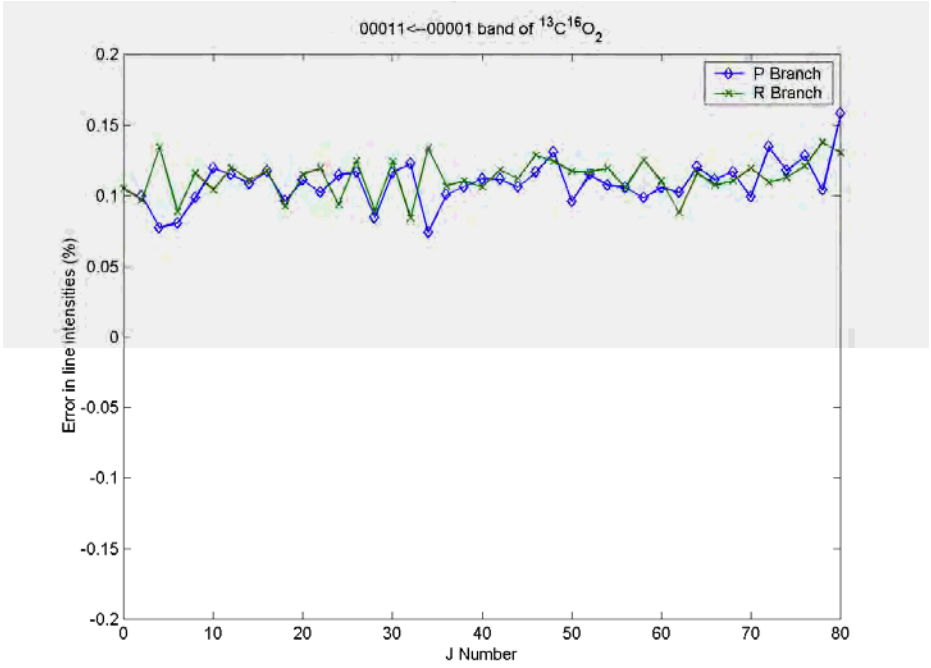

.

Figure 2.8- Error in Line intensities between HITRAN 2004 and the computed values 2004 for the $00011 \leftarrow 00000$ of $^{13}C^{16}O_2$.

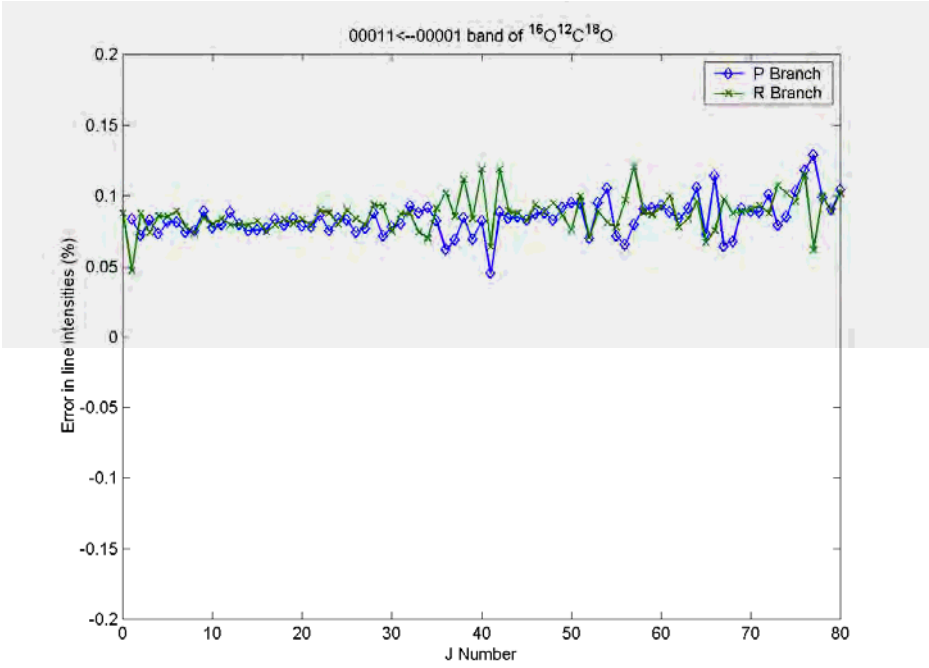

Figure 2.9- Error in Line intensities between HITRAN 2004 and the computed values 2004 for the $00011 \leftarrow 00000$ of $^{16}O^{12}C^{18}O_2$.

Table 2.5- Some calculated line position and intensities versus HITRAN 2004, for the 00011 ← 00000 of $^{12}C^{16}O_2$.

J		R Brach		P Brach	
		Calculated	HITRAN	Calculated	HITRAN
12	Line Position	2358.727368	2358.727369	2339.372389	2339.37239
	Intensity	$3.3617x10^{-18}$	$3.358x10^{-18}$	$3.0992x10^{-18}$	$3.096x10^{-18}$
14	Line Position	2360.109127	2360.109128	2337.658143	2337.658185
	Intensity	$3.50139x10^{-18}$	$3.498x10^{-18}$	$3.2632x10^{-18}$	$3.260x10^{-18}$
16	Line Position	2361.466077	2361.466078	2335.91954	2335.919541
	Intensity	$3.5281x10^{-18}$	$3.524x10^{-18}$	$3.3151x10^{-18}$	$3.312x10^{-18}$
18	Line Position	2362.798194	2362.798195	2334.156485	2334.156486
	Intensity	$3.453x10^{-18}$	$3.449x10^{-18}$	$3.2652x10^{-18}$	$3.262x10^{-18}$
20	Line Position	2364.105453	2364.105455	2332.369045	2332.369047
	Intensity	$3.29173x10^{-18}$	$3.288x10^{-18}$	$3.0992x10^{-18}$	$3.125x10^{-18}$

2.1.2. Nitrous Oxide Spectroscopic Model

N_2O is a linear molecule so all the theory needed to evaluate the line positions and strengths is the same as that used for modelling CO_2. Here, just some special properties of this molecule, such is the symmetry effects, must be considered. In section 2.1.1.4 the symmetry effects for linear molecules were discussed, and it was said that if a molecule is symmetric with zero nuclear spin then only certain energy levels are allowed. For instance, in the fundamental band of the $^{12}C^{16}O_2$ isotopomer, which has a centre of inversion, all transitions originating in odd rotational levels are absent due to symmetry constraints. In the case of N_2O, it is a molecule of the form $X-X-Y$ which has two identical nuclei but not the symmetry of the point group $D_{\infty h}$ therefore no statistical difference between the even and odd rotational levels is present [6], which implies that all rotational levels are present in the spectrum.

N_2O has three important absorption bands at 588.8, 1284.90 and 2223.75 cm^{-1} increasing in intensity in that order. None of these bands can be interpreted as an overtone or combination band, thus they are the three infrared active fundamental bands [6]. Because of the spectral region involved with the project the bands at 1284.90 and 2223.75 cm^{-1} were simulated. In this section the 588.8 band is not presented since this

band is irrelevant for the gas sensor simulation. However this band can be reproduced using the same mathematical model presented in this section and it is only necessary to use another set of spectroscopic constants for this particular band.

The vibration-rotation energy expression of this linear molecule can be expressed in terms of effective parameters B, D, H as

$$E_{(v+r)} = BJ(J+1) - DJ^2(J+1)^2 + HJ^3(J+1)^3 + LJ^4(J+1)^4, \qquad (2.18)$$

this equation is the same as the utilised in the carbon dioxide model (2.1), the only difference is that here a new high order term (L) is introduced. The $^{14}N_2{}^{16}O$, $^{14}N^{15}N^{16}O$, $^{15}N^{14}N^{16}O$, $^{14}N^{14}N^{18}O$, and $^{14}N^{14}N^{17}O$ isotopomers were included in the model. The effective parameters for the two first isotopomers used in the simulation are given in Table 2.6. In these tables we employ the vibration-state notation given by [16] which has the form $v_1v_2lv_3$ where l is the vibrational angular momentum quantum number. The same notation is used in the HITRAN database [2].

The strength of the infrared absorption lines at frequency ν can be evaluated using equation (2.6). The differences for N_2O are the Herman-Wallis and Hönl-London factors that for CO_2 were given in section 2.1.1.5. Here, it is necessary to modify these expressions in order to obtain the correct line strength values. For N_2O the Hönl-London factors are expressed [17] as

$$L = \begin{cases} \dfrac{m^2 - l^2}{|m|} & \Delta J = \pm 1, \Delta l = 0 \\ \dfrac{l^2(2J+1)}{J(J+1)} & \Delta J = 0, \Delta l = 0 \\ \dfrac{(m+z)(m+z+1)}{|m|} & \Delta J = \pm 1, \Delta l = \pm 1 \\ \dfrac{(2J+1)(J-z)(J+z+1)}{J(J+1)} & \Delta J = 0, \Delta l = \pm 1 \end{cases} \qquad (2.19)$$

where $z = |l''|(|l'| - |l''|)$, and $m = J'' + 1$ for the R branch and $m = -J$ for the P branch. The double prime denotes the lower level and the single prime the upper level.

The Herman-Wallis (F factor) expression is given [17, 18] by

$$F = \left[1 + a_1 m + a_2 J'\left(J' + 1\right)\right]^2, \tag{2.20}$$

where a_1 and a_2 are the Herman-Wallis coefficients, these coefficients are given in Table 2.6.

The air broadening coefficients needed to evaluate the line shape were taken from [19]. Moreover Toth 1993 [20] gives a list of self broadening coefficients as a function of the pressure, which can be useful in cases when the pressure varies. A simulated spectrum of nitrous oxide is shown in figure 2.10.

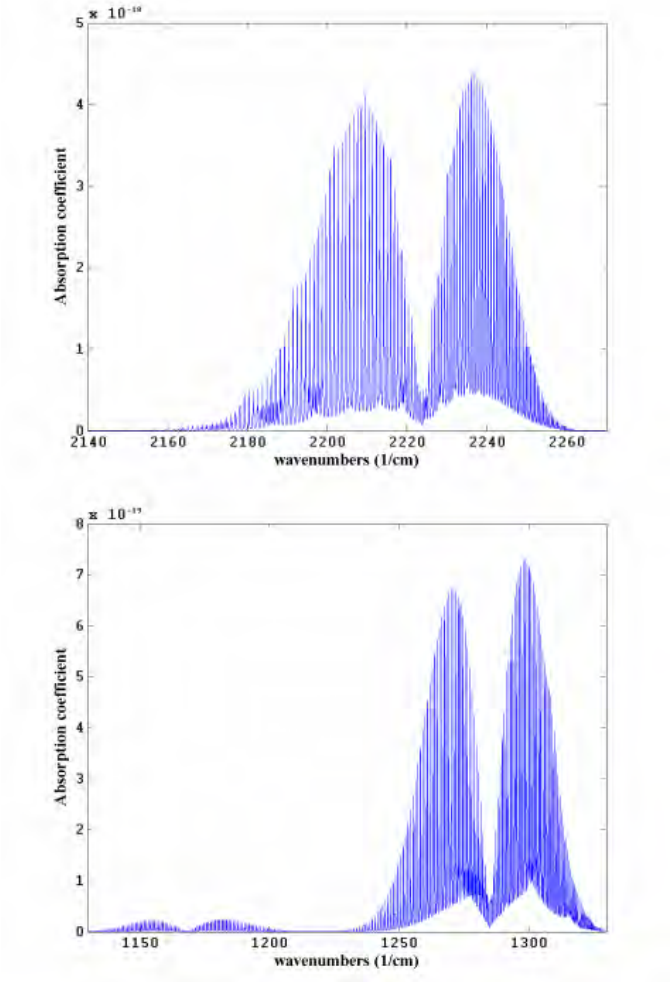

Figure 2.10- Simulated absorption spectra of N_2O. In the lower figure, the strong band shown is due to the fundamental band $1000 \leftarrow 0000$ centred at 1284.90 cm^{-1}; while the weaker band is due to the overtone 0200-000. In the upper figure the strong absorptions are due to the $0001 \leftarrow 0000$ band centred at 2223.7 cm^{-1}.

Table 2.6- Spectroscopic constants for $^{14}N_2{}^{16}O$ and $^{14}N^{15}N^{16}O$ transitions

Band	**Band Centre**	B''	$D''\times10^{-7}$	H'' $\times10^{-13}$	L'' $\times10^{-18}$	B'	D' $\times10^{-7}$	$H'\times10^{-13}$	L' $\times10^{-18}$	a_1 $\times10^{-4}$[c]	a_2 $\times10^{-5}$[c]	$\|R\|$[c]
$^{14}N_2{}^{16}O$												
1000-0000	1284.90336[a]	0.419011[a]	1.760919[a]	-0.1652[a]	0	0.41725509[a]	1.72619[a]	1.2632[a]	1.8527	-0.09	0	1.336×10^{-1}
1110e-0110e	1291.49786[a]	0.419177[a]	1.783245[a]	-0.1714[a]	0	0.41746475[a]	1.74899[a]	1.1382[a]	0	-0.44	-0.64	1.366×10^{-1}
1110f-0110f	1291.49786[a]	0.419969[a]	1.793030[a]	-0.1766[a]	0	0.41837307[a]	1.72005[a]	2.2462[a]	0	-1.48	-0.36	1.368×10^{-1}
0001-0000	2223.75677[b]	0.419011[a]	1.760919[a]	-0.1652[a]	0	0.41555951[b]	1.75467[b]	-0.1362[b]	0	-0.23	0	2.477×10^{-1}
0111e-0110e	2209.52473[b]	0.419177[a]	1.783245[a]	-0.1714[a]	0	0.41577089[b]	1.77578[b]	-0.1116[b]	0	-0.59	0.23	2.454×10^{-1}
0111f-0110f	2209.52473[b]	0.419969[a]	1.793030[a]	-0.1766[a]	0	0.41654792[b]	1.78722[b]	-0.1557[b]	0	-0.38	0.39	2.450×10^{-1}
0200-0000	1168.13230[a]	0.419011[a]	1.760919[a]	-0.1652[a]	0	0.41992097[a]	2.49236[a]	29.6362[a]	0	-0.01	2.48	2.570×10^{-2}
$^{14}N^{15}N^{16}O$												
1000-0000	1280.35412[c]	0.418981[a]	1.763264[a]	0.0000[a]	0	0.41712730[b]	1.754555[b]	0.472[a]	0.472	0.00	0	1.364×10^{-1}
1110e-0110e	1284.75756[c]	0.419108[a]	1.785830[a]	0.0000[a]	0	0.41727313[b]	1.773906[b]	0.000[a]	0	-1.29	0.83	1.33×10^{-1}
1110f-0110f	1284.75756[c]	0.419918[a]	1.794460[a]	0.0000[a]	0	0.41816523[b]	1.760323[a]	0.000[a]	0	-0.19	0.90	1.34×10^{-1}
0001-0000	2177.65681[c]	0.418981[a]	1.763264[a]	0.0000[a]	0	0.41565409[b]	1.756773[b]	0.1254[b]	0.1254	0.77	0.22	2.414×10^{-1}
0111e-0110e	2164.16440[c]	0.419108[a]	1.785830[a]	0.0000[a]	0	0.41582475[b]	1.776541[b]	0.0000[b]	0	2.36	-0.39	2.470×10^{-1}
0111f-0110f	2164.16440[c]	0.419918[a]	1.793030[a]	0.0000[a]	0	0.41661910[b]	1.787460[b]	0.0000[b]	0	1.87	0.00	2.440×10^{-1}
0200-0000	1144.33338[c]	0.418981[a]	1.794460[a]	0.0000[a]	0	0.41992172[a]	2.845420[a]	66.796[a]	66.796	-2.07	2.58	1.690×10^{-2}

[a] Values taken from Toth 1986 [18]; [b] Values taken from Toth 1991 [21]; [c] Values taken from Toth 1993 [20].

2.1.2.1. Validation of the N_2O model.

In order to validate our simulated spectrum of N_2O we compared our simulated result with the HITRAN 2004 [1] database. According to the HITRAN database the difference between the measured line position and the computed line position is in the order of 0.0001 cm^{-1} or better for most of the ro-vibrational lines of the strongest bands of the N_2O [1, 3]. In the same way the computed lines reported by HITRAN present an error around 2-5% for the same absorption bands [1, 3]. Here we require to evaluate how close are our computed line positions and intensities with those provided by HITRAN in order to be sure that our data have good level of accuracy. In this section the evaluated residual difference between the computed line position and those listed in HITRAN for the fundamental bands of $^{14}N^{14}N^{16}O$ and $^{14}N^{15}N^{16}O$ which occur at 2220 cm^{-1} are presented. The residual difference for the fundamental bands $0001 \leftarrow 0000$ of $^{14}N^{14}N^{16}O$ and $^{14}N^{15}N^{16}O$ is in the order of $\leq 10 \times 10^{-5}$ cm^{-1} for $J \leq 60$ (figure 2.11 and 2.12). These residual differences in line positions is around a factor of 10 lower than the obtained for CO_2 since the constants B, D, H and L have a greater precision. The average FWMH of one ro-vibrational line of the $0001 \leftarrow 0000$ $^{14}N^{14}N^{16}O$ is 0.15 cm^{-1} for $J \leq 40$, therefore our model deviates by $1/15,000^{th}$ of a typical rotational line width.

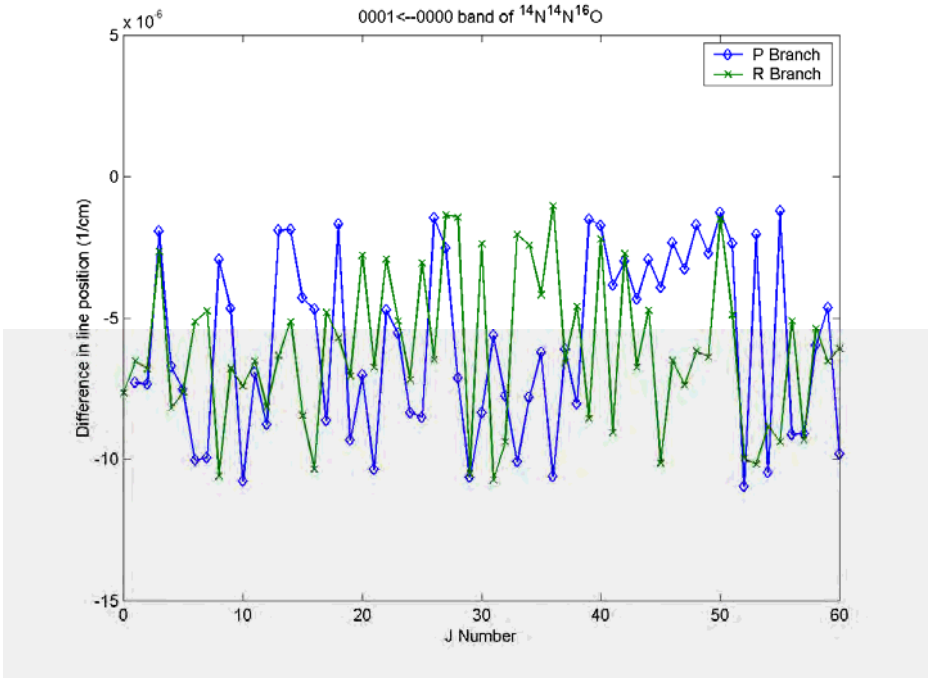

Figure 2.11- Residual difference in line position between our calculated positions and HITRAN 2004 for the $0001 \leftarrow 0000$ of $^{14}N^{14}N^{16}O$.

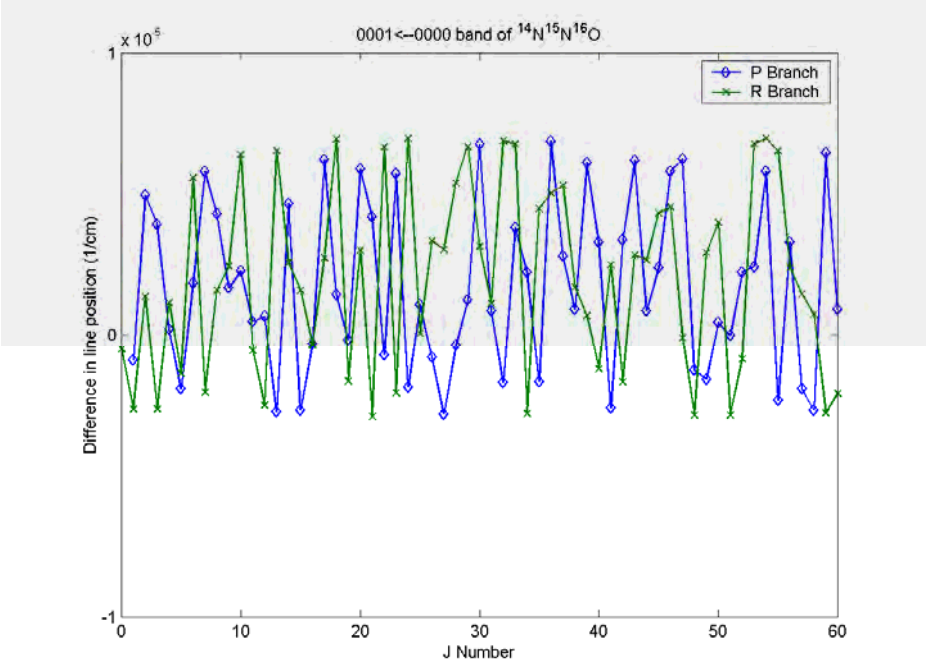

Figure 2.12- Residual difference in line position between our calculated positions and HITRAN 2004 for the $0001 \leftarrow 0000$ of $^{14}N^{15}N^{16}O$.

The deviation of the computed line position with respect to the line width is really small, and this deviation is around 5 times lower when it is compared with the separation of the ro-vibrational lines. On average the separation of the ro-vibrational lines of the $0001 \leftarrow 0000$ of $^{14}N^{14}N^{16}O$ is around 0.6 cm^{-1} for the R branch and 0.97 cm^{-1} for the P branch when $J \leq 40$. Therefore the deviation of the computed line position is around $1/60{,}000^{th}$ of the separation between two consecutive ro-vibrational lines of the R branch. In order to simulate our sensor with sufficient accuracy we build a wavenumber axis using an interval of 0.01 cm^{-1} which is $1/15^{th}$ of the line width and around $1/60^{th}$ of the separation of two consecutive ro-vibrational lines for the R branch for $J \leq 40$. Using this interval the deviation of our computed line position, respect to HITRAN 2004, do not affect the final spectrum of $^{14}N^{14}N^{16}O$. The accuracy is clearly good enough to reproduce a spectrum sufficiently accurate to simulate our gas sensors.

The line intensity error (%) between our calculated values and those listed in the HITRAN 2004 for the fundamental bands of $^{14}N^{14}N^{16}O$ and $^{14}N^{15}N^{16}O$ are presented in figure 2.13 and figure 2.14. Here it can be seen that the error is around ≤ 0.4 for $J \leq 60$. However, the errors are small enough so as not introduce a significant error in the simulations of our gas sensor. In our simulation we are including all ro-vibrational

lines with $J \leq 60$ and according to our simulation at 296K all these lines have an accumulated intensity of 499026.9×10^{-22} cm^{-1}/(molecule cm^{-2}). According to HITRAN 2004 the accumulative intensity for the ro-vibrational lines with $J \leq 92$ is equal to 499668.1×10^{-22}. Therefore, our model covers around the 99.87%, or practically all the total band strength of the $0001\leftarrow0000$ band of $^{14}N^{14}N^{16}O$. Therefore, considering the that our model has an error of 0.04% and that just the 99.87% of the total strength is taken into account we see that our model has an accuracy of around 99.83 %. Now if we consider that the HITRAN line intensities have a maximum average error of 5% this lead us to say that our simulated spectra have an accuracy of 94.8385%. Hence the model presented in previous section, to calculate the line intensities for N_2O, is sufficiently accurate, and therefore it is good enough to guarantee precise simulations of our gas sensor. Finally, in Table 2.7 a comparison between calculated line positions and intensities with respect to HITRAN 2004 of some ro-vibrational lines are presented, at 296K the strongest ro-vibrational line is at $J = 15$ here can be observed that the deviations are very small.

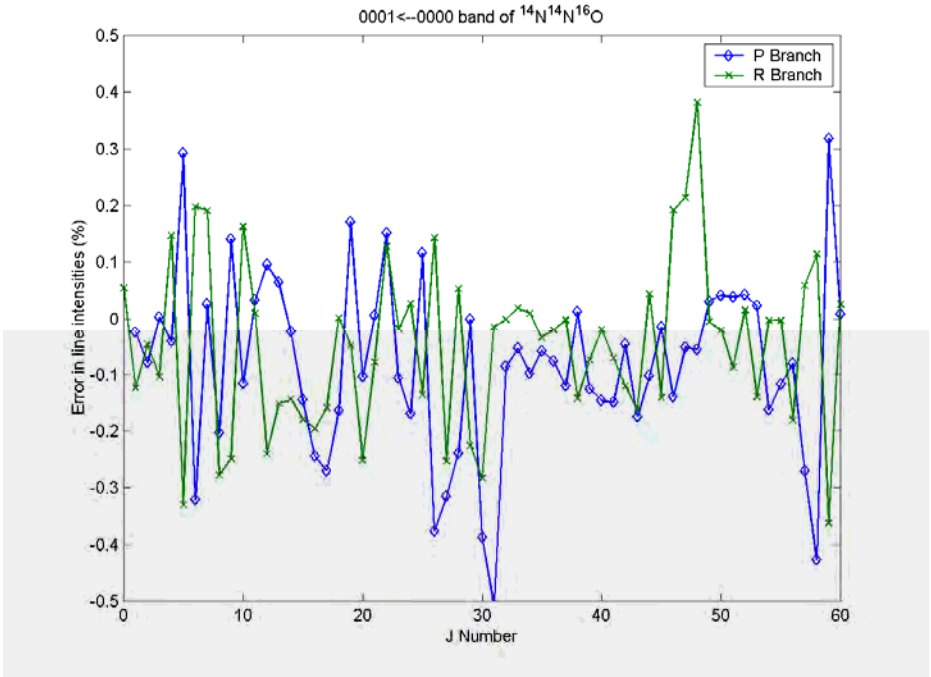

Figure 2.13- Error in Line intensities between HITRAN 2004 and the computed values 2004 for the $0001 \leftarrow 0000$ of $^{14}N^{14}N^{16}O$.

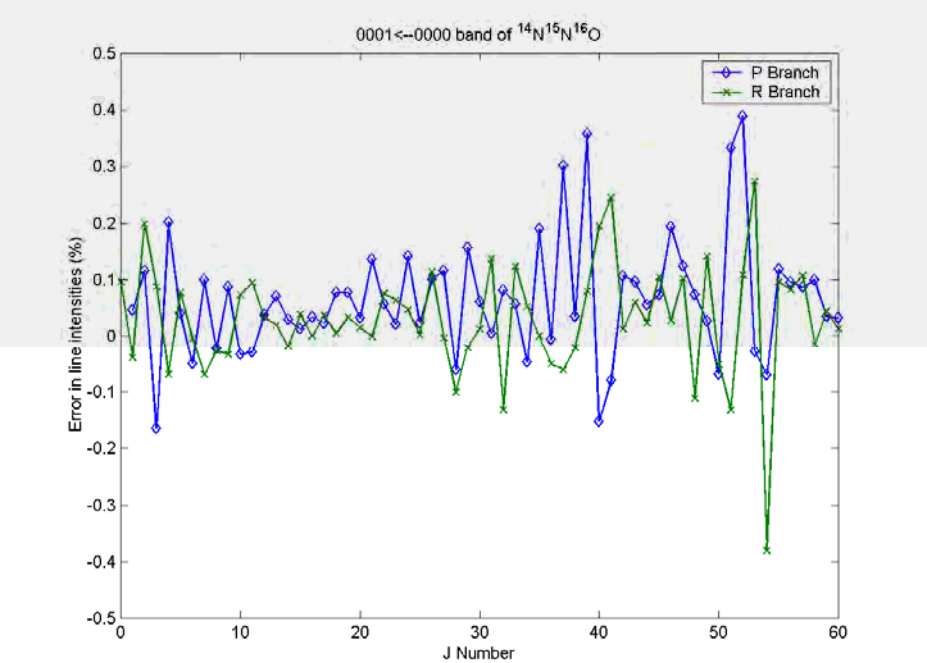

Figure 2.14- Error in Line intensities between HITRAN 2004 and the computed values 2004 for the $0001 \leftarrow 0000$ of $^{14}N^{15}N^{16}O$.

Table 2.7- Some calculated line position and intensities versus HITRAN 2004, for the $0001 \leftarrow 0000$ of $^{14}N^{14}N^{16}O$.

J		R Brach		P Brach	
		Calculated	HITRAN	Calculated	HITRAN
13	Line Position	2234.762354	2234.76236	2212.325608	2212.32561
	Intensity	9.86307×10^{-19}	9.878×10^{-19}	9.0778×10^{-19}	9.072×10^{-19}
14	Line Position	2235.496395	2235.4964	2211.398238	2211.39824
	Intensity	9.98471×10^{-19}	9.999×10^{-19}	9.2308×10^{-19}	9.233×10^{-19}
15	Line Position	2236.223472	2236.22348	2210.464026	2210.46403
	Intensity	1.0022×10^{-18}	1.004×10^{-18}	9.3006×10^{-19}	9.314×10^{-19}
16	Line Position	2236.94358	2236.94359	2209.522975	2209.52298
	Intensity	9.97941×10^{-19}	9.999×10^{-19}	9.2913×10^{-19}	9.314×10^{-19}
17	Line Position	2237.656715	2237.65672	2208.575091	2208.5751
	Intensity	9.86236×10^{-19}	9.878×10^{-19}	9.2081×10^{-19}	9.233×10^{-19}

2.1.3. Carbon Monoxide Spectroscopic Model

In this section the spectroscopic model utilised to reproduce the CO spectrum at 4.7 μm is presented. Here, the line positions, intensities and line shape are computed in a similar manner to the CO_2 and N_2O models. The CO line positions are evaluated by using the Dunham formula given by [22]

$$E(v,J)=\sum_{kl}Y_{kl}\left(v+\frac{1}{2}\right)^{k}\left[J(J+1)\right]^{l}, \tag{2.21}$$

where v represents the quantum vibrational number, and Y_{kl} are the Dunham coefficients. The complete set of Dunham coefficients used in our simulations were taken from Farrenq et al 1991[23] and are listed in Table 2.8

The carbon monoxide line intensities can be calculated using the next formula which is a simplified version of formulae given by [24, 25]

$$S(T)=\frac{8\pi^{3}10^{-36}}{3hc}\frac{I_{a}\nu}{Q(T)}\exp\left(-\frac{hcG_{\nu}''}{kT}\right)\exp\left(-\frac{E_{r}''}{kT}\right)\left[1-\exp\left(\frac{hc\nu}{kT}\right)\right]H_{n}(v)\,F(v,J'')\,|R_{\nu}|^{2} \tag{2.22}$$

$Q(T)$ is the total internal partition sum, G_{ν}'' is the energy of the lower vibrational level, E_{r}'' is the energy of the lower rotational level, I_a is the isotopic abundance, $|R_{\nu}|^{2}$ is the squared rotationless dipole moment, $H_n(v)$ are the Honl-London Factors and $F(v,J'')$ are the Herman Wallis Factors.

The total internal partition function was evaluated using a simple approach given [24] by

$$Q(T)=Q(297.36)\left(\frac{T}{297.36}\right) \tag{2.23}$$

With

$$Q\left(297.36\right)=\begin{cases}107.91 & {}^{12}\mathrm{C}^{16}\mathrm{O} & T<500\mathrm{K}\\ 112.86 & {}^{13}\mathrm{C}^{16}\mathrm{O} & T<500\mathrm{K}\\ 113.26 & {}^{12}\mathrm{C}^{18}\mathrm{O} & T<500\mathrm{K}\end{cases}$$

In section 2.1.1.5 the Hönl-London factors and the Herman Wallis were explained in detail. Here, the Herman-Wallis factors expression were calculated using the relationship [25]

$$F_n\left(v,m\right)=\sum_{i=0}^{6}\sum_{j=0}^{3}{g_{ij}}^{n}m^i v^j; \tag{2.24}$$

where v is the vibrational quantum number and m is a running index given by

$$m=\frac{J'\left(J'+1\right)-J''\left(J''+1\right)}{2} \tag{2.25}$$

The coefficients ${g_{ij}}^{n}$ are listed in Table 2.9. The Honl-London factors were evaluated using the following formula [25]

$$H_n\left(v\right)=\sum_{i=0}^{9}{h_i}^{n}v^i, \tag{2.26}$$

the ${h_i}^{n}$ coefficients for the 1-0 fundamental band are given in Table 2.9.

The line shape is described by the normalized Lorentzian function (2.13), which depends of the air broadening coefficients (see section 2.1.1.6). For CO these coefficients were taken from [26]. A plot of the simulated CO spectrum at 4.7 μm is shown in figure 2.15; this plot includes the fundamental bands (1-0) of $^{12}C^{16}O$, $^{13}C^{16}O$, and $^{12}C^{18}O$ isotopomers.

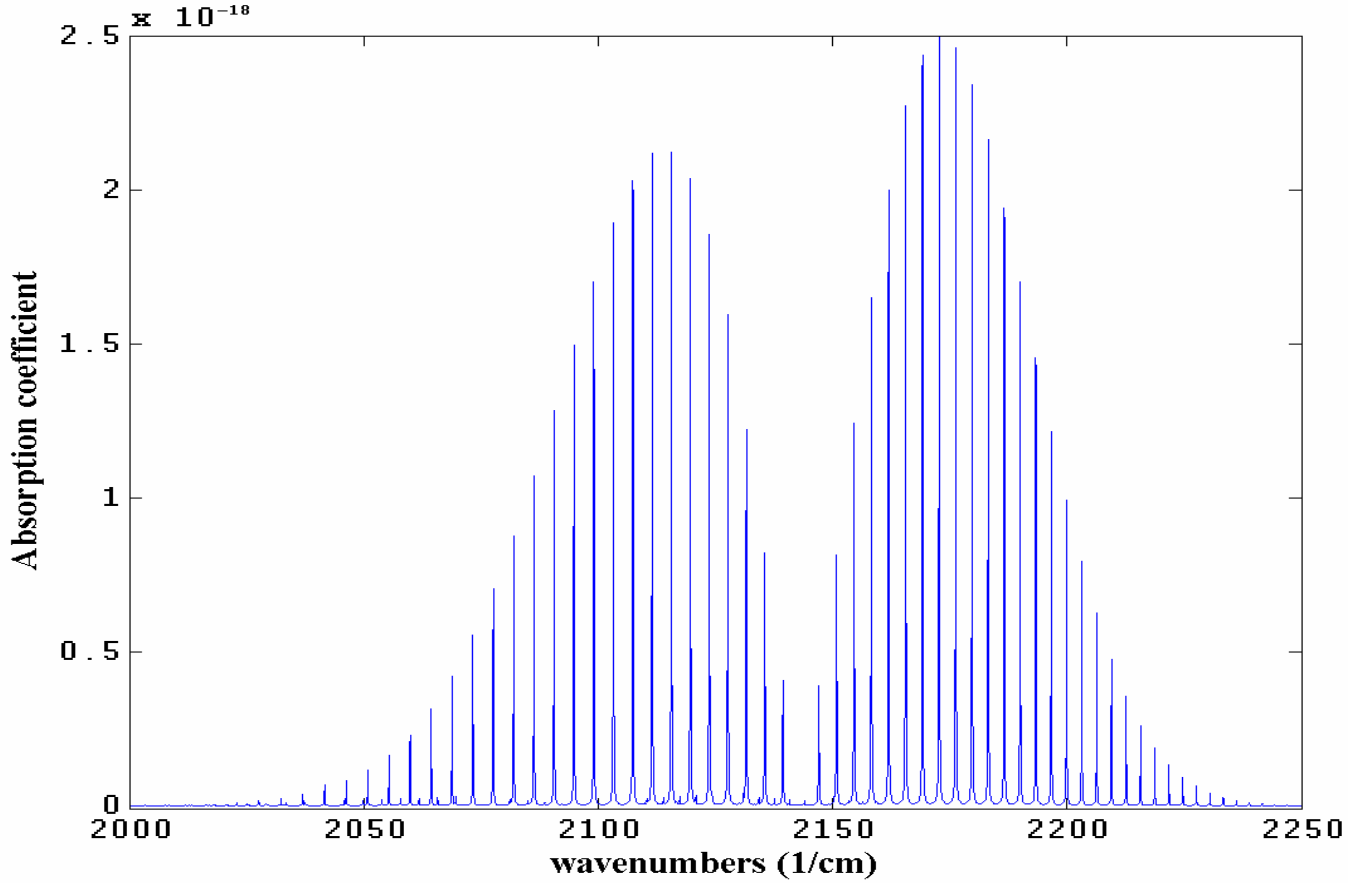

Figure 2.15- Simulated CO absorption spectrum at 4.7 μm. This plot includes the 1-0 fundamental bands of the $^{12}C^{16}O$, $^{13}C^{16}O$, and $^{12}C^{18}O$ isotopomers.

Table 2.8- Dunham Coefficients Y_{kl} [23].

$^{12}C^{16}O$							
k \ ***l***	**0**	**1**	**2**	**3**	**4**	**5**	**6**
0	0	1.931280985	$-0.6121615183\times10^{-5}$	$0.5884905033\times10^{-11}$	$-0.3615785745\times10^{-16}$	$-0.4555298526\times10^{-22}$	$-0.151964150\times10^{-26}$
1	2169.812670	-0.017504392	$0.1034922952\times10^{-8}$	$-0.1428653277\times10^{-12}$	$-0.7405801298\times10^{-18}$	$-0.5922257515\times10^{-23}$	0
$^{13}C^{16}O$							
0	0	1.846151725	$-0.5593901826\times10^{-5}$	$0.5140386572\times10^{-11}$	$-0.3019101986\times10^{-16}$	$-0.3635889807\times10^{-22}$	$-0.115945471\times10^{-26}$
1	2121.439026	-0.01635976671	$0.9246022661\times10^{-9}$	$-0.1220091918\times10^{-12}$	$-0.6045838445\times10^{-18}$	$-0.4621580733\times10^{-23}$	0
$^{12}C^{18}O$							
0	0	1.839113877	$-0.5551151313\times10^{-5}$	$0.5081809481\times10^{-11}$	$-0.2973317238\times10^{-16}$	$-0.3567098022\times10^{-22}$	$-0.113318022\times10^{-26}$
1	2117.397251	-0.01626640228	$0.9158136642\times10^{-9}$	$-0.1203886604\times10^{-12}$	$-0.5942790712\times10^{-18}$	$-0.4525486860\times10^{-22}$	0

Table 2.9- $g_{ij}{}^{n}$ and $h_{i}{}^{n}$coefficients needed for the fundamental bands of CO. [25].

$h_i{}^1$			
i	**$^{12}C^{16}O$**	**$^{13}C^{16}O$**	**$^{12}C^{18}O$**
0	1	1	1
1	-0.46983	-0.13884×10^{-2}	-0.13919×10^{-2}
2	0.54506×10^{-1}	-0.17167×10^{-3}	-0.16629×10^{-3}
3	0.13275×10^{-3}	-0.12586×10^{-5}	-0.27044×10^{-5}
4	0.10692×10^{-4}	0.97746×10^{-7}	0.35548×10^{-6}
5	-0.12119×10^{-5}	-0.17236×10^{-7}	-0.44971×10^{-7}
6	0.57580×10^{-7}	0.12038×10^{-8}	0.29867×10^{-8}
7	-0.16334×10^{-8}	-0.49605×10^{-10}	-0.11527×10^{-9}
8	-0.16334×10^{-10}	0.10749×10^{-11}	0.23420×10^{-11}
9	-0.54474×10^{-13}	-0.94714×10^{-14}	-0.19336×10^{-13}

$g_{ij}{}^1$			
i	**$^{12}C^{16}O$**	**$^{13}C^{16}O$**	**$^{12}C^{18}O$**
0	1	1	1
1	0.19027×10^{-3}	0.18715×10^{-3}	0.18689×10^{-3}
2	0.70112×10^{-5}	0.67064×10^{-5}	0.66819×10^{-5}
3	-0.21784×10^{-7}	-0.20339×10^{-7}	-0.20230×10^{-7}
4	-0.82485×10^{-11}	-0.73902×10^{-11}	-0.76315×10^{-11}
5	-0.20811×10^{-12}	-0.18781×10^{-12}	-0.18337×10^{-12}
6	-0.83958×10^{-16}	-0.77479×10^{-16}	-0.41659×10^{-16}

2.1.3.1. Validation of CO model.

In order to validate our simulated spectrum of CO we compared our simulated result with the HITRAN 2004 database [1]. According to the HITRAN database the difference between the measured line position and the computed line position is in the order of 0.0001 cm^{-1} for most of the ro-vibrational lines of the strongest fundamental bands of the CO in the region of 4.7 μm [1, 3]. In the same way the computed lines reported by HITRAN present an error around 3-6% for the same absorption bands [1, 3]. Here we require to evaluate how close are our computed line positions and intensities with those provided by HITRAN in order to be sure that our data have good level of accuracy. In this section the residual difference in line positions between the calculated values and HITRAN are presented, here just for the relevant fundamental bands $(1 \leftarrow 0)$ of $^{12}C^{16}O$ and $^{13}C^{16}O$. The residual difference in line positions for the fundamentals bands $(1 \leftarrow 0)$ of $^{12}C^{16}O$ and $^{13}C^{16}O$ is in the order of $\leq 4 \times 10^{-5}$ cm^{-1} for $J \leq 50$ (Fig. 2.16 and 2.17). The average FWMH of one ro-vibrational line of the $(1 \leftarrow 0)$ of $^{12}C^{16}O$ and is around 0.10 cm^{-1} for $J \leq 40$, therefore our model deviates by $1/2{,}500^{th}$ of a typical ro-vibrational line width.

The deviation of the computed line position with respect to the line width is very small, and this deviation is around 30 times lower when it is compared with the separation of the ro-vibrational lines. On average the separation of the ro-vibrational lines of $(1 \leftarrow 0)$ band of $^{12}C^{16}O$ for $J \leq 40$ is around 3.05 cm^{-1} for the R branch and 4.50 cm^{-1} for the P branch. Thus the deviation of the computed line position is around $1/76{,}250^{th}$ of the separation between two consecutive ro-vibrational lines of the R branch. In order to simulate our sensor with sufficient accuracy we build a wavenumbers axis using an interval of 0.01 cm^{-1} which is $1/10^{th}$ of the line width and around $1/305^{th}$ of the separation of two consecutive ro-vibrational lines for the R branch for $J \leq 40$. Using this interval the deviation of our computed line position, respect to HITRAN 2004, do not affect the final spectrum of $^{12}C^{16}O$. The accuracy is more than good enough to reproduce a spectrum sufficiently accurate to simulate our gas sensors which are based mainly in the separation of the ro-vibrational lines.

The line intensity error (%) between our calculated values and those listed in the HITRAN 2004 for the fundamental bands of $(1 \leftarrow 0)$ of $^{12}C^{16}O$ and $^{13}C^{16}O$ is around

$\leq 0.2\%$ for $J \leq 50$ (Fig. 2.18 and 2.19). The errors are small enough so as not introduce a significant error in the simulations of our gas sensor. In our simulation we are including all ro-vibrational lines with $J \leq 50$ and according to our simulation at 296K all these lines have an accumulated intensity of 99666.6×10^{-22} cm^{-1}/(molecule cm^{-2}) at 296K. According to HITRAN 2004 the accumulative intensity for the ro-vibrational lines with $J \leq 60$ is equal to 99685.3×10^{-22} cm^{-1}/(molecule cm^{-2}) at 296K. Therefore, our model covers around the 99.98% of practically the total band strength of the $1 \leftarrow 0$ band of $^{12}C^{16}O$. Therefore assuming that our model has an error of 0.02% and that just the 99.98% of the strength is considered we see that our model has an accuracy of around 99.96%. Furthermore considering that line intensities in HITRAN have an average error of around 5% therefore our compute line intensities have an accuracy of around 94.962%. This lead us to conclude that the model presented in the previous section to calculate the line intensities for CO is sufficiently accurate, and therefore it is good enough to guarantee precise simulations of our gas sensor. Finally, in Table 2.10 a comparison between calculated line position and intensities with respect to HITRAN 2004 of some ro-vibrational lines are presented, at 296K the strongest ro-vibrational line is at $J = 8$, here can be observed that the deviations are very small.

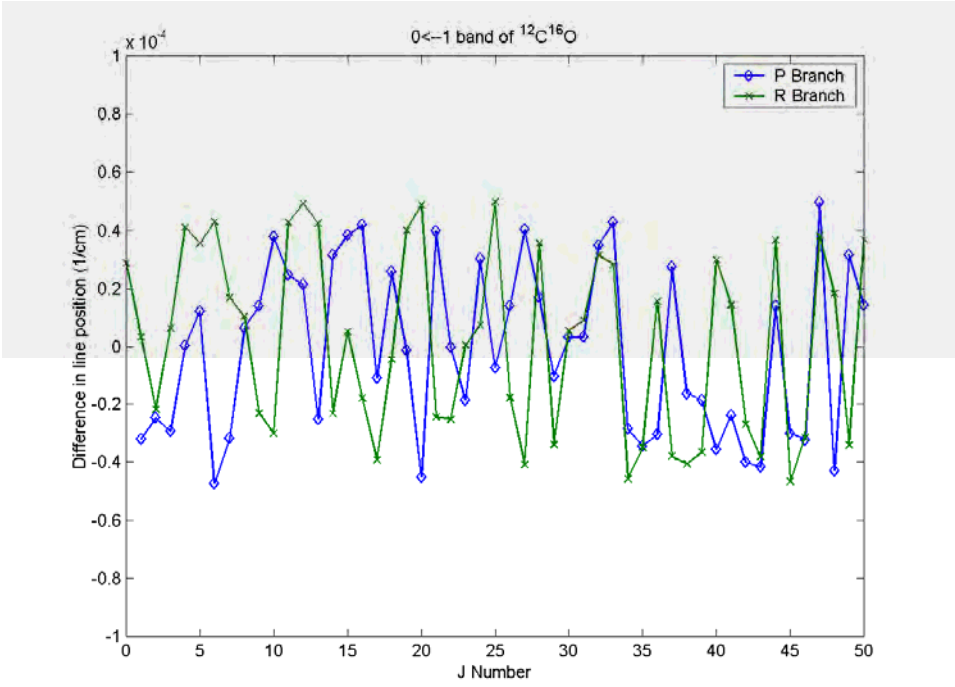

Figure 2.16- Residual difference in line position between our calculated positions and HITRAN 2004 for the $1 \leftarrow 0$ of $^{12}C^{16}O$.

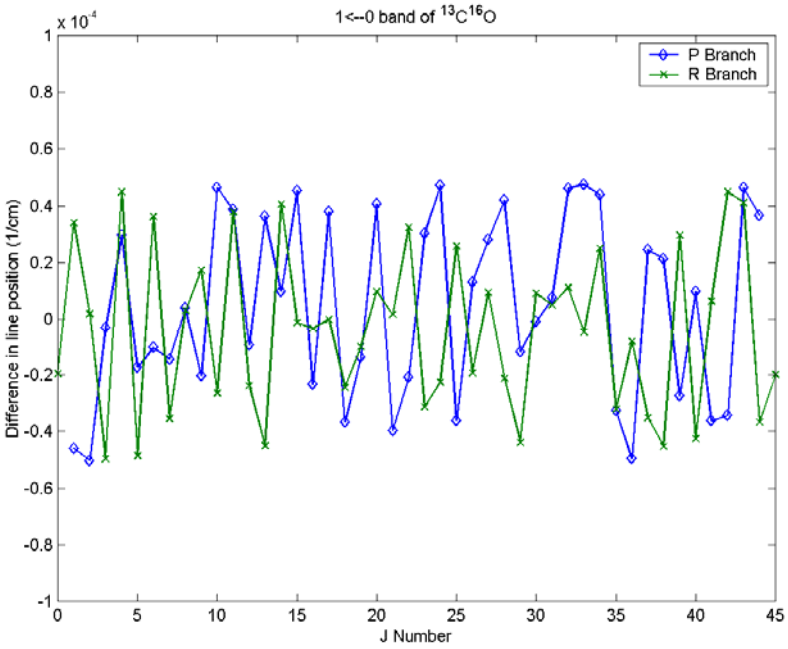

Figure 2.17- Residual difference in line position between our calculated positions and HITRAN 2004 for the $1 \leftarrow 0$ of $^{13}C\,^{16}O$.

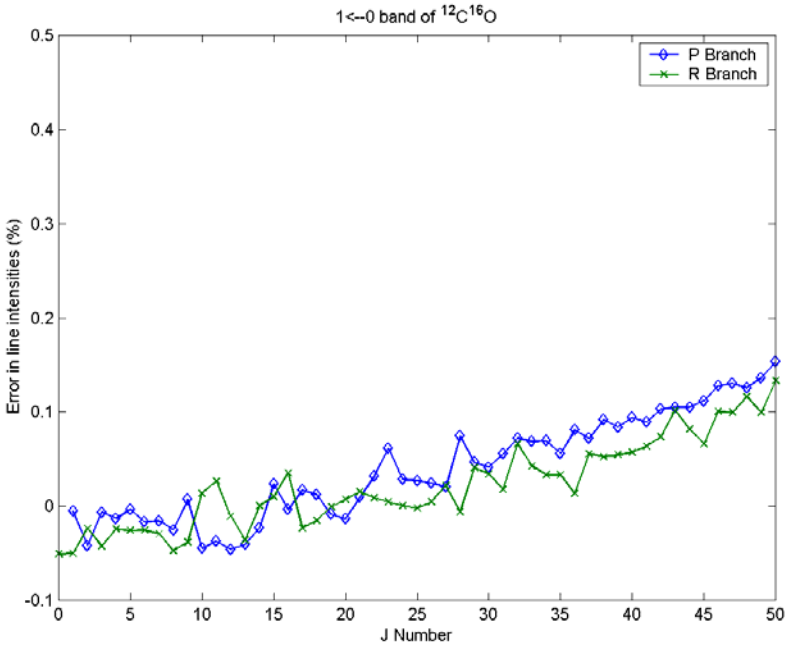

Figure 2.18- Error in Line intensities between HITRAN 2004 and the computed values 2004 for the $1 \leftarrow 0$ of $^{12}C\,^{16}O$.

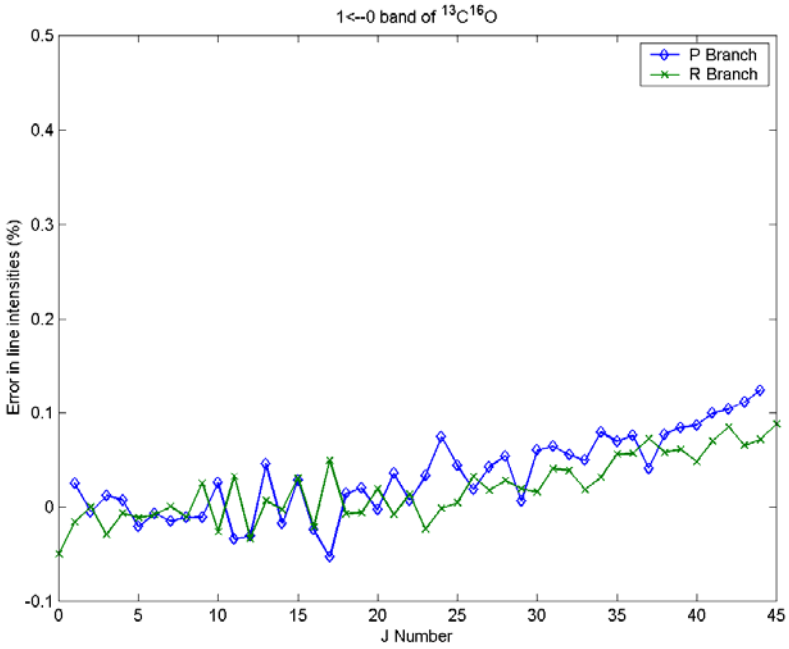

Figure 2.19- Error in Line intensities between HITRAN 2004 and the computed values 2004 for the $1 \leftarrow 0$ of $^{13}C\,^{16}O$.

Table 2.10- Some calculated line position and intensities versus HITRAN 2004, for the $1 \leftarrow 0$ of $^{12}C\,^{16}O$.

J		R Brach		P Brach	
		Calculated	**HITRAN**	**Calculated**	**HITRAN**
6	**Line Position**	2169.197943	2169.1979	2119.68095	2119.681
	Intensity	4.439×10^{-19}	4.44×10^{-19}	3.708×10^{-19}	3.709×10^{-19}
7	**Line Position**	2172.758817	2172.7588	2115.6289	2115.629
	Intensity	4.460×10^{-19}	4.46×10^{-19}	3.788×10^{-19}	3.789×10^{-19}
8	**Line Position**	2176.28351	2176.2835	2111.543007	2111.543
	Intensity	4.329×10^{-19}	4.33×10^{-19}	3.721×10^{-19}	3.722×10^{-19}
9	**Line Position**	2179.771877	2179.7719	2107.423214	2107.4232
	Intensity	4.073×10^{-19}	4.08×10^{-19}	3.531×10^{-19}	3.531×10^{-19}
10	**Line Position**	2183.22377	2183.2238	2103.269738	2103.2697
	Intensity	3.724×10^{-19}	3.72×10^{-19}	3.249×10^{-19}	3.250×10^{-19}

2.2. Water vapour Spectroscopic Models

Water, H_2O is an important molecule because it is ubiquitous in gas samples in real-life applications and has strong absorption lines in the regions of interest. Therefore, it is vital to have an accurate model of its spectrum. The calculation to generate the rotation-vibration energy levels of H_2O is very difficult as it is an asymmetric top molecule and it is particularly complicated due to specific problems related with large motions of the hydrogen atoms which lead to huge centrifugal distortion effects [27]. Moreover numerous vibration-rotation resonances strongly perturb the line positions and intensities [28].

The rotational level J of an asymmetric top molecule has $2J+1$ rotational sublevels [7]. Each rotational sublevel of an asymmetric top molecule it is represented by three quantum numbers JK_aK_c. In older literature it is the representation $JK_{-1}K_{+1}$ is also frequently found which is basically the same; in this work we will use the first notation. The number K_a runs from 0 to J while the number K_c from $-J$ to 0. Another notation found in older literature, which can be very useful in some cases, represents each rotational sublevel by J_τ where $-J \leq \tau \leq J$ and $\tau = K_a + K_c$.

There are several different methods to calculate the rotational energy levels and intensities of H_2O. The simplest method to calculate the energy levels it is based on a Hamiltonian due to J. K. G. Watson [11, 29, 30]. This method is able to fit the energy levels of H_2O up to J and $K_a < 13$ approximately [27, 28, 31]; for higher values of K_a the model starts to diverge rapidly. In our specific case we need to simulate two H_2O spectra one in the region of the 6.25 μm and the second one at 2.7 μm. These are needed to correctly predict the cross sensitivity of the CH_4, CO and CO_2 detectors with water vapour. In these detectors weak absorptions produced by very highly excited rotational levels will not affect seriously the cross sensitivity calculations when normal temperatures are assumed. For instance, consider a CO detector were the target rotational lines are those belonging to the fundamental R branch where the operational spectral range is 2100-2220 cm^{-1}. In this region the strongest absorptions of H_2O are due to transitions originated from energy levels with $J''=7,\ K_a''=6$ and $J''=8,\ K_a''=7$. Furthermore, within this spectral range other transitions such as transitions with $J''=8,\ K_a''=8$, and $J''=9,\ K_a''=7$ of H_2O occur in the same

spectral range, but these which are 10 times weaker than transitions originating in $J'' = 7, \quad K_a'' = 6$ and in $J'' = 8, \quad K_a'' = 8$. Moreover the H_2O ro-vibrational lines are even weaker in the spectral range where the P branch of the fundamental band of CO lies. Therefore a model which fits the ro-vibrational lines of the H_2O up to $J'' \leq 13, \quad K_a'' \leq 11$ is good enough to simulate our CO detector. As ro-vibrational lines with $J'' > 13, \quad K_a'' > 11$ are very weak at room temperature (296K) in our application we will consider them as negligible. Therefore, the Watson Hamiltonian is appropriate to calculate the energy levels since this model fits well energy levels up to $J'' \leq 13, \quad K_a'' \leq 11$, which is enough for our application. In section 2.2.1 the spectroscopic model used to simulate the water vapour spectrum at 6.25 μm it is reviewed.

It is important to mention that more recent methods than the Watson Hamiltonian can be found in the literature which are much powerful and can fit much better highly excited rotational levels of H_2O (up to $J'' \leq 24$), for instance the methods proposed by Couderth [32, 33] and Starikov [34]. Highly excited levels are of importance in certain cases, for example when high temperatures are considered. These methods [32-34] are more complicated than the basic Watson Hamiltonian .

To evaluate the cross sensitivity of the methane sensor (CH_4) with water vapour we need to reproduce the H_2O absorption spectrum at 2.7 μm. This spectrum is a triad, which means that three H_2O absorptions bands occur very close together and furthermore these bands are interacting with each other forming a very complex spectrum. To reproduce this spectrum we utilised the mathematical model proposed by Flaud and Camy-Peyret [35] which is based on the Watson Hamiltonian, it is presented in section 2.2.2.

2.2.1. The ν_2 Absorption Band of $H_2{}^{16}O$.

In this section we describe the method used to reproduce the H_2O absorption spectrum the bending mode ν_2 at 6.25 μm represented as $010 \leftarrow 000$. The vibrational state 010 it is also represented as $v = 1$ and the state 000 as $v = 0$. Evaluation of the absorption band can be divided in four steps. In the first step the energy levels are be evaluated; here we will use the Watson Hamiltonian which fits well rotational energy

levels up to $J'' \leq 13, \quad K_a'' \leq 11$. The second step consists in the evaluation of the line intensities which will be carried out using the method and data provided by references [27, 28, 31, 35, 36]. Finally to form the absorption spectrum the broadening coefficients are required to evaluate the line widths, here we will use the broadening coefficients kindly provided by R. A. Toth [37]. These steps are described in the following sections and also the constants, operators and matrix elements required to reproduce the spectrum are presented.

2.2.1.1. The Watson Hamiltonian, A reduction

Energy levels for the bending mode ν_2 of H_2O can be evaluated by [28]

$$H^{vv} = E_v + H_r^v \tag{2.27}$$

where E_v is the vibrational energy of the state v and H_r^v is the rotational Watson Hamiltonian of type A reduction [38] of the state v. E_v is given as the band centre if vibrational resonances do not affect the sate v as in the case of mode ν_2; the values of E_1 and E_0 required for the evaluation of this band are listed in Table 2.14.. The reduced Watson Hamiltonian (H_r^v) it is very convenient for calculation of the energy levels of an asymmetric top molecule since its resulting matrix elements are evaluated in a basis of a symmetric-top wavefunctions $|JK\rangle$ instead of the asymmetric wavefunctions $|JK_aK_c\rangle$ [30]. The matrix elements are given by $\langle JK''|H_r^v|JK'\rangle$ and are non zero when $\Delta K = K' - K'' = 0, \pm 2$ [38] forming a tridiagonal matrix. The energy levels are obtained by diagonalizing the resultant matrix. The Hamiltonian H_r^v it is defined by equations (2.28a)-(2.28f) [7]. In these equations $\langle P\rangle$ is the total angular momentum and $\langle P_Z\rangle$, $\langle P_X\rangle$, and $\langle P_Y\rangle$ are the components of the total angular momentum over the respective axis. $\langle P_{XY}\rangle$ represents the relation between the X and Y components given by $\langle P_X - P_Y\rangle$. The constants *A*, *B*, *C* are the principal rotational constants of the molecule, and the rest of the parameters, i.e. H_J, Δ_J, P_J, etc, are the centrifugal constants. Finally to evaluate the matrix elements the total angular momentum $\langle P\rangle$ and its components $\langle P_Z\rangle$ and $\langle P_{XY}\rangle$ must be defined. These definitions are given in equations (2.29a)-(2.29f) [7].

$$H_r^v = H_r^{v(2)} + H_d^{v(4)} + H_d^{v(6)} + H_d^{v(8)} + H_d^{v(10)} \tag{2.28a}$$

$$H_r^{v(2)} = \left(\frac{B^v + C^v}{2}\right) P^2 + \left(A^v - \frac{B^v + C^v}{2}\right) (P_Z)^2 + \left(\frac{B^v - C^v}{2}\right) (P_{XY})^2 \tag{2.28b}$$

$$\begin{aligned} H_d^{v(4)} = &- \Delta_J^v P^4 - \Delta_{JK}^v P^2 (P_Z)^2 - \Delta_K^v (P_Z)^4 - 2\delta_J^v P^2 (P_{XY})^2 \\ &- \delta_K^v \left[(P_Z)^2 (P_{XY})^2 + (P_{XY})^2 (P_Z)^2\right] \end{aligned} \tag{2.28c}$$

$$\begin{aligned} H_d^{v(6)} = &H_J^v P^6 + H_{JK}^v P^4 (P_Z)^2 + H_{JK}^v P^2 (P_Z)^2 + H_K^v (P_Z)^6 + 2h_J^v P^4 (P_{XY})^2 \\ &+ h_{JK}^v P^2 \left[(P_Z)^2 (P_{XY})^2 + (P_{XY})^2 (P_Z)^2\right] + h_K^v \left[(P_Z)^4 (P_{XY})^2 + (P_{XY})^2 (P_Z)^4\right] \end{aligned} \tag{2.28d}$$

$$\begin{aligned} H_d^{v(8)} = &L_J^v P^8 + L_{JJK}^v P^6 (P_Z)^2 + L_{JK}^v P^4 (P_Z)^4 + L_{KKJ}^v P^2 (P_Z)^6 + L_K^v (P_Z)^8 \\ &+ 2l_J^v P^6 (P_{XY})^2 + l_{JK}^v P^4 \left[(P_Z)^2 (P_{XY})^2 + (P_{XY})^2 (P_Z)^2\right] \\ &+ l_{KJ}^v P^2 \left[(P_Z)^4 (P_{XY})^2 + (P_{XY})^2 (P_Z)^4\right] + l_K^v \left[(P_Z)^6 (P_{XY})^2 + (P_{XY})^2 (P_Z)^6\right] \end{aligned} \tag{2.28e}$$

$$\begin{aligned} H_d^{v(10)} = &P_J^v P^{10} + P_{JJK} P^8 (P_Z)^2 + P_{JK}^v P^6 (P_Z)^4 + P_{KJ}^v P^4 (P_Z)^6 + P_{KKJ}^v P^2 (P_Z)^8 \\ &+ P_K^v (P_Z)^{10} + 2p_J^v P^8 (P_{XY})^2 + p_{JJK}^v P^6 \left[(P_Z)^2 (P_{XY})^2 + (P_{XY})^2 (P_Z)^2\right] \\ &+ p_{JK}^v P^4 \left[(P_Z)^4 (P_{XY})^2 + (P_{XY})^2 P_Z{}^4\right] + p_{KKJ}^v P^2 \left[(P_Z)^6 (P_{XY})^2 + (P_{XY})^2 (P_Z)^6\right] \\ &+ p_K^v \left[(P_Z)^8 (P_{XY})^2 + (P_{XY})^2 (P_Z)^8\right] \end{aligned} \tag{2.28f}$$

$$\langle JK \left| P^{2n} \right| JK \rangle = J^n (J+1)^n \tag{2.29a}$$

$$\langle JK \left| P_Z^{2n} \right| JK \rangle = K^{2n} \tag{2.29b}$$

$$\langle JK \left| P^{2n} P_Z^{2n} \right| JK \rangle = J^n K^{2n} \tag{2.29c}$$

$$\langle JK \left| P^{2n} \left(P_X^{2n} - P_Y^{2n}\right) \right| JK \pm 2 \rangle = -\frac{1}{2} J^n (J+1)^n f_\pm (J, K) \tag{2.29d}$$

$$\begin{aligned} &\langle JK \left| P^{2n} \left[P_Z^{2m} \left(P_X^{2n} - P_Y^{2n}\right) + \left(P_X^{2n} - P_Y^{2n}\right) P_Z^{2m}\right] \right| JK \pm 2 \rangle \\ &= -\frac{1}{2} J^n (J+1)^n \left[K^2 + (K \pm 2)^2\right] f_\pm (J, K) \end{aligned} \tag{2.29e}$$

$$f_\pm (J, K) = \left\{\left[J (J+1) - K (K \pm 1)\right] \left[J (J+1) - (K \pm 1) (K \pm 2)\right]\right\}^{1/2} \tag{2.29f}$$

where $m, n = 0, 1, 2, \ldots$

2.2.1.2. Energy Levels

The energy matrix for a given J in a basis of a symmetric-top wavefunctions $|JK\rangle$ is a square matrix of order $2J+1$ since $-J \leq K \leq J$ [39]. By means of Wang's transformation this matrix can be partitioned into four independent matrices labelled $\mathbf{E}^+$, $\mathbf{E}^-$, $\mathbf{O}^+$ and $\mathbf{O}^-$ which have a new symmetry basis $|JK\gamma\rangle$ [38, 39]. These submatrices are also a tridiagonal and are defined by [39]

$$\mathbf{E}^{\pm}_{K',K} = \begin{bmatrix} E_{0,0} & \sqrt{2}E_{0,2} & 0 & 0 & \dots \\ \sqrt{2}E_{0,2} & E_{2,2} & E_{2,4} & 0 & \dots \\ 0 & E_{2,4} & E_{4,4} & E_{4,6} & \dots \\ 0 & 0 & E_{4,6} & E_{6,6} & \dots \\ \vdots & \vdots & \vdots & \vdots & \ddots \end{bmatrix}, \tag{2.30a}$$

$$\mathbf{O}^{\pm}_{K',K} = \begin{bmatrix} E_{1,1} \pm E_{-1,1} & E_{1,3} & 0 & 0 & \dots \\ E_{1,3} & E_{3,3} & E_{3,5} & 0 & \dots \\ 0 & E_{3,5} & E_{5,5} & E_{5,7} & \dots \\ 0 & 0 & E_{5,7} & E_{7,7} & \dots \\ \vdots & \vdots & \vdots & \vdots & \ddots \end{bmatrix}. \tag{2.30b}$$

The submatrix $\mathbf{E}^-$ has exactly the same elements as $\mathbf{E}^+$, except that the first column and the first row of $\mathbf{E}^{\pm}_{K',K}$ are eliminated in the case of the $\mathbf{E}^-$ submatrix. In these submatrices labels E and O denotes even and odd K values respectively whilst the + and - refers to even and odd γ [39]. Wang's representation permits us to reduce the size of the original Hamiltonian matrix, since it is divided into four matrices of similar size, roughly $(2J+1)/4$. The matrix elements of the Wang's submatrices are given by $E_{K'',K'} = \langle JK''\gamma'' | H_r^v | JK'\gamma' \rangle$. Here, the energy levels are obtained by diagonalization of the submatrices $\mathbf{E}^+$, $\mathbf{E}^-$, $\mathbf{O}^+$, and $\mathbf{O}^-$. When a matrix is diagonalized two matrices are obtained, one contains the eigenvalues and the other contains the eigenvectors; from these the eigenvalues are the energy levels. The resulting energy levels of $\langle H_r^v \rangle$ are labelled and sorted according to their quantum numbers J, K_a, K_c. There are basically two ways to sort and label the energy levels; the first way is using the notation JK_aK_c where K_a runs from 0 to J, and K_c from J to 0. The second way is to represent the level as J_τ, where $\tau = K_a - K_c$, here τ runs from $-J$ to J, so the levels are labelled as J_{-J}, J_{-J+1},…,J_J. Here the label J_{-J} is assigned to the lower energy level for a given J

in contrast J_J is assigned to the higher energy level. Thus if the energy levels are sorted in increasing energy the corresponding label will be in increasing assigned in an increasing τ [40].

Finally, the Hamiltonian employed to calculate the energy levels of the ν_2 band is the same as the described in equation (2.28a) just with the inclusion of two additional terms expressed by [27]

$$H_r^v = H_r^v + H_d^{v(4)} + H_d^{v(6)} + H_d^{v(8)} + H_d^{v(10)} + Q_K^v {P_Z}^{12} + R_K^v {P_Z}^{14}; \quad (2.31)$$

The constants for the two states (000) and (010) are listed in Table 2.14, and the operators involved are defined in equations (2.29a)-(2.29f).

2.2.1.3. Selection Rules and Line Positions.

In the last section, to evaluate the energy levels the asymmetric rotational wave functions $|JK_aK_c\rangle$ was expanded in an adapted symmetry wave functions $|JK\gamma\rangle$. However, this expansion is not enough to calculate the line positions and the line intensities since this does not include the asymmetric vibrational wave function. The asymmetric vibration rotation wavefunction of an asymmetric level $|vJK_aK_c\rangle$ can be expanded into a symmetry adapted basis using the following expansion [28]

$$|vJK_aK_c\rangle = \sum_v \sum_K C_K^v |v\rangle |JK\gamma\rangle \quad (2.32)$$

where, v is the vibrational level $|v\rangle = |v_1v_2v_3\rangle$, C_K^v are the coefficients of the respective eigenvector. For the ν_2 band $|0\rangle = |000\rangle$ is the ground state and $|1\rangle = |010\rangle$ is the upper state. In this representation each vibration-rotation wave function of a level $|vJK_aK_c\rangle$ has an overall symmetry type $\Gamma = A_1, A_2, B_1, B_2$. (Table 2.11) [28]

The symmetry type (Γ) is important since it defines the selection rules and therefore the allowed transitions. The allowed transitions $\Gamma'' \leftrightarrow \Gamma'$ are $A_1 \leftrightarrow A_2$ or $B_1 \leftrightarrow B_2$, where Γ'' represents the symmetry of the lower level, whilst Γ' the symmetry of the upper level. Depending of the dipole moment component two types of bands can occur

which are called A, and B types (Table 2.12). The allowed changes in J, K_a, and K_c, between the lower and upper level, will depend of the specific band type as shown in Table 2.12. The $010 \leftarrow 000$ H_2O band (the ν_2 bending mode) belongs to the band type B [7], therefore using Table 2.12 the line positions of the band can be computed.

Table 2.11- Adapted Symmetry types of vibrational-rotational levels [28].

v_3	K_a	K_c	Γ
e	*e*	*e*	A_1
e	*e*	*o*	B_2
e	*o*	*o*	A_2
e	*o*	*e*	B_1

Table 2.12- Selection Rules [28]

Band type	**Change in** v_3	ΔJ	$\Gamma'' \leftrightarrow \Gamma'$	**Dipole moment Component** (μ_Z')	**Change in** $K_a K_c$
A	$e \leftrightarrow o$	0, ±1	$A_1 \leftrightarrow A_2$ or $B_1 \leftrightarrow B_2$	(μ_A')	*ee* ↔ *eo* or *oo* ↔ *oe*
B	$e \leftrightarrow e$ or $o \leftrightarrow o$			(μ_B')	*ee* ↔ *oo* or *oe* ↔ *eo*

The adapted symmetry (Γ) is defined as the product of a vibrational symmetry times the rotational symmetry $\Gamma = \Gamma_v \times \Gamma_r$. The rotational adapted symmetry Γ_r is helpful to determine in which matrix $\mathbf{E}^+$, $\mathbf{E}^-$, $\mathbf{O}^+$, and $\mathbf{O}^-$ of the Wang's representation a specific asymmetric vibration-rotation energy level (v, J, K_a, K_c) can be found as shown in Table 2.13. In these tables even levels are represented by *e*, while odd levels by *o*.

Table 2.13- Symmetry Type Γ_r of the rotational function $|JK\gamma\rangle$ [28, 41]

J	K_aK_c	γ	Γ_r	**Name of the Basis**
e	*e e*	+	A_1	$\mathbf{E}^+$
	o e	+	A_2	$\mathbf{O}^+$
	e o	-	B_1	$\mathbf{E}^-$
	o o	-	B_2	$\mathbf{O}^-$
o	*e o*	+	B_2	$\mathbf{E}^+$
	o o	+	B_1	$\mathbf{O}^+$
	e e	-	A_1	$\mathbf{E}^-$
	o e	-	A_2	$\mathbf{O}^-$
$\|JK\gamma\rangle = \frac{1}{\sqrt{2}}\left(\|J \quad K\rangle + \gamma\|J \quad -K\rangle\right) \quad K > 0, \quad \gamma = \pm 1$				
$\|J0\rangle = \|J0\rangle$				

2.2.1.4. Line Intensities

In the absence of an external field the line intensity is expressed by [33]:

$$S\left(T,\nu_0\right)=\frac{8\pi^3}{3hc}\frac{g_a 10^{-43}}{Q\left(T\right)}\nu_0 \exp\left(\frac{-hcE_A}{kT}\right)\left[1-\exp\left(\frac{-hc\nu_0}{kT}\right)\right]R_A^B \qquad (2.33)$$

where $S\left(T,\nu_0\right)$ is the line intensity in [cm^{-1}/(molecule-cm^{-2})], $Q\left(T\right)$ is the total partition function at temperature T, g_A is the degeneracy of the lower level that is set equal to 1 when K_a+K_c is even, otherwise it will be set equal to 3 [33], E_A is the energy of the lower level, ν_0 is the line position of the transition, and R_A^B is the vibration-rotation dipole moment matrix element connecting the lower state *A* with the upper state *B*. For the band due to (000) and (010) states of H_2O R_A^B can be written as [27]:

$$R_A^B=\langle A\left|\mu_Z{}'\right|B\rangle=\langle v''J''K_a{}''Kc''\left|\mu_Z{}'\right|v'J'K_a{}'K_c{}'\rangle \qquad (2.34)$$

where v represents the vibrational level. The double dashed variables are related to the lower level, and the single dashed to the upper level. Equation (2.34) is expressed as a function of asymmetric wave functions. Therefore, it needs to be represented in a

symmetric adapted basis using the expansion described by (2.32). Here by substitution of (2.32) into (2.34) the dipole moment for the $010 \leftarrow 000$ band R_A^B can be rewritten as [27]

$$R_A^B = \left| \sum_{K''} \sum_{K'} C_{K''}^{0*} C_{K'}^{1} \langle v'' J'' K'' \gamma'' \left| {}^1\mu_z{}' \right| v' J' K' \gamma' \rangle \right|, \tag{2.35}$$

where $C_{K''}^{0*}$ and $C_{K'}^{1}$ are the eigenvectors coefficients of the lower and the upper energy levels respectively. These eigenvectors are obtained after diagonalizing the Hamiltonian matrix as was stated before.

To evaluate the complete value of R_A^B it is necessary to calculate the transformed transition moment operator $\langle v'' J'' K'' \gamma'' \left| {}^1\mu_z{}' \right| v' J' K' \gamma' \rangle$. This operator can be evaluated by using the following expansion [35]

$$\langle 0 J'' K'' \gamma'' \left| {}^1\mu_z{}' \right| 1 J' K' \gamma' \rangle = \sum_j {}^1\mu_j{}' \langle {}^1A_j \rangle, \tag{2.36}$$

where ${}^1\mu_j{}'$ are numerical coefficients and ${}^1A_j$ are the matrix elements. In early papers [27, 35] just 8 coefficients and operators were listed $(j = 1 \ldots 8)$. But recently R. A. Toth [31, 36] presented new calculations considering up to 19 operators $(j = 1 \ldots 19)$. The latter helps us to fit better the weak transitions, which can not be exactly calculated with the set of 8 constants. Therefore we utilised the 19 operators and coefficients given by [31], listed in Table 2.14 and Table 2.15 respectively, to evaluate the dipole moment R_A^B for each transition.

Finally, in order to evaluate the full spectrum as a function of wavenumber (Figure 2.20) we need to know the air broadening coefficients. Some experimental evaluations of these parameters are available, such are those measured by Toth 2000, HITRAN 2003 [5, 42], etc. In our case we worked with a latest parameter set which was kindly provided by Toth 2004 [37].

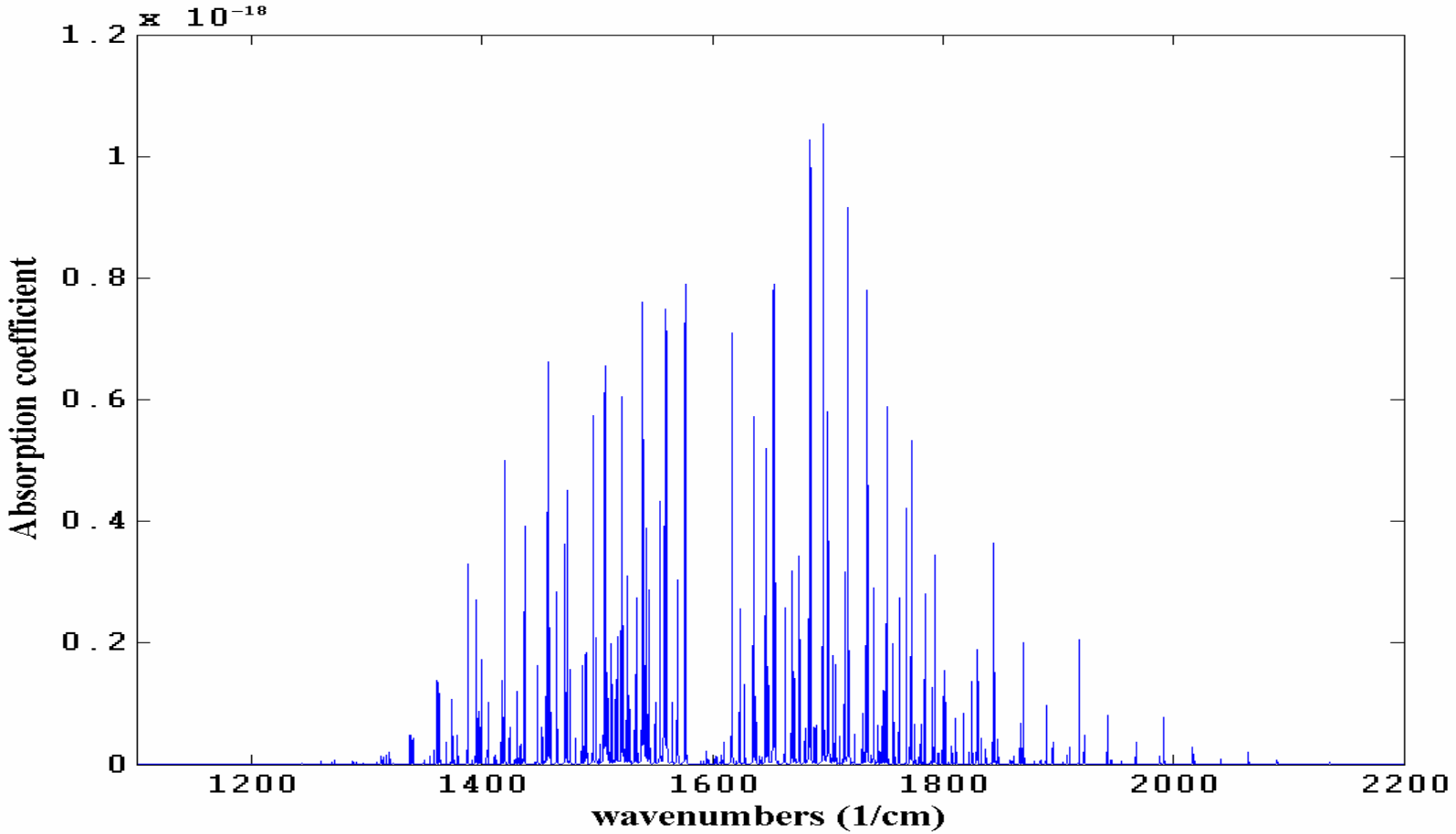

Figure 2.20- Simulated $010 \leftarrow 000$ band of water vapour (the ν_2 bending mode). Monochromatic absorption coefficient (1/molecules-cm^{-2}).

Table 2.14- Vibration-Rotation Energy Level Parameters of the (000) and (010) states of $H_2{}^{16}O$ [27]

Constant	$v = 0(000)$	$v = 1(010)$
E_v	0.00000×10^{0}	1.59474×10^{3}
A	2.78807×10^{1}	3.11284×10^{1}
B	1.45217×10^{1}	1.46876×10^{1}
C	9.27746×10^{0}	9.12913×10^{0}
Δ_J	1.24894×10^{-3}	1.39537×10^{-3}
Δ_{JK}	-5.76550×10^{-3}	-7.60530×10^{-3}
Δ_K	3.25199×10^{-2}	5.75564×10^{-2}
δ_J	5.08380×10^{-4}	5.78790×10^{-4}
δ_K	1.30070×10^{-3}	3.76620×10^{-3}
H_J	4.50610×10^{-7}	6.11800×10^{-7}
H_{JK}	-1.92100×10^{-6}	2.88200×10^{-6}
H_{KJ}	-1.37000×10^{-5}	-4.49540×10^{-5}
H_K	1.22810×10^{-4}	3.53476×10^{-4}
h_J	2.25660×10^{-7}	2.91170×10^{-7}
h_{JK}	-4.21000×10^{-7}	0.00000×10^{0}
h_K	2.39580×10^{-5}	8.42630×10^{-5}
L_{JJK}	8.66000×10^{-10}	0.00000×10^{0}
L_{JK}	-3.68100×10^{-8}	0.00000×10^{0}
L_{KKJ}	1.29150×10^{-7}	8.08900×10^{-8}
L_K	-6.49600×10^{-7}	-2.19190×10^{-6}
l_{JK}	6.17000×10^{-10}	3.37100×10^{-9}
l_K	-1.54100×10^{-7}	-4.30700×10^{-7}
P_{KKJ}	6.81000×10^{-12}	0.00000×10^{0}
P_K	2.39900×10^{-9}	1.05940×10^{-8}
p_K	1.70400×10^{-10}	8.91400×10^{-10}
Q_K	-6.49000×10^{-12}	-3.15780×10^{-11}
R_K	7.65000×10^{-15}	4.07100×10^{-14}

Table 2.15- Operators and Matrix elements of the Dipole Moment for B-Type band of water vapour [31, 41]

j	n	$\langle J''K''\|A'(j)\|J'K'\rangle/\langle J''K''\|\Phi(x)\|J' \quad K''+\Delta K\rangle$
1	1	1
2	1	$J'(J'+1)+J''(J''+1)$
3	1	$K'^2+K''^2$
4	1	$K'^2-K''^2$
5	1	$K'^2-K''^2-2m$
6	1	$(K'^2-K''^2)(K'^2-K''^2-2m)$
7	1	$J''(J''+1)-2m(m-1)+(2m-1)K''\Delta K-K''^2-1$
8	3	$[(J'-K''\Delta K-1)(J'-K''\Delta K-2)(J'+K''\Delta K+2)(J'+K''\Delta K+3)]^{1/2}$
9	1	$K'^2\,J'(J'+1)-K''^2\,J''(J''+1)$
10	1	$K'^4-K''^4$
11	1	$(K'^2-K''^2)\cdot[J'(J'+1)+J''(J''+1)]$
12	1	$K'^2\,(J'^2+J')^2$
13	1	K'^6
14	1	K'^4
15	1	$K'^2\,J'(J'+1)$
16	1	$K'^6-K''^6$
17	1	$J'(J'+1)$ if m=0 and $J''=K_c''$ or $J'=K_c'$, otherwise 0
18	1	$J'(J'+1)$ if m=0 and $J''=K_c''$ or $J'=K_c'-1$, otherwise 0
19	1	$J'(J'+1)$ if m=0 and $J''=K_c''$ or $J'=K_c'$, otherwise 0

$$\langle J''K''\,|\Phi(x)|\,J' \quad K''+\Delta K\rangle = \begin{cases} \frac{1}{2}\left[\frac{(2J''+1)(J''-K''\Delta K)(J''+K''\Delta K+1)}{J''(J''+1)}\right]^{1/2} & \Delta J=0 \\ \frac{-\Delta J\Delta K}{2}\left[\frac{(m+K\Delta K)(m+1+K\Delta K)}{J''(J''+1)}\right]^{1/2} & \Delta J=\pm 1 \end{cases}$$

$$\Delta J = J'-J''=0,\pm 1 \qquad m=[J'(J'+1)-J''(J''+1)]/2,$$

$$K'-K''=n\Delta K \qquad\qquad \Delta K=\pm 1$$

Table 2.16- Dipole Moment Coefficients ${}^{1}\mu_j'$ of the (010)-(000) band of H_2O. [31]

	Ranges		
J	**839.643-1399.204 cm^{-1}**	**1403.462-1799.616 cm^{-1}**	**1801.324-2568.790 cm^{-1}**
1	1.30132×10^{-1}	1.29532×10^{-1}	1.30545×10^{-1}
2	5.48191×10^{-5}	1.48163×10^{-5}	7.46634×10^{-6}
3	5.9159×10^{-4}	5.31372×10^{-5}	-2.2411×10^{-4}
4	-5.7257×10^{-3}	-6.9870×10^{-3}	-6.3232×10^{-3}
5	-1.86242×10^{-4}	-3.01150×10^{-4}	-1.44108×10^{-4}
6	-4.83242×10^{-5}	-3.61126×10^{-5}	-1.7076×10^{-5}
7	2.1242×10^{-4}	5.78202×10^{-5}	1.44180×10^{-5}
8	-4.2685×10^{-5}	-1.8513×10^{-5}	-1.3921×10^{-5}
9	-1.2124×10^{-5}	-1.1954×10^{-5}	-3.20561×10^{-7}
10	6.7434×10^{-5}	2.2891×10^{-5}	1.8710×10^{-5}
11	1.0816×10^{-5}	4.27192×10^{-6}	5.35375×10^{-7}
12	-2.26814×10^{-9}	1.0064×10^{-9}	-3.68166×10^{-9}
13	-1.1540×10^{-7}	3.99398×10^{-8}	6.1443×10^{-9}
14	-5.3424×10^{-6}	-4.20189×10^{-6}	1.9229×10^{-6}
15	2.04112×10^{-6}	-8.75744×10^{-6}	2.41181×10^{-7}
16	-3.5453×10^{-7}	-1.32918×10^{-8}	-6.92104×10^{-8}
17	9.715×10^{-5}	4.8159×10^{-5}	-1.34518×10^{-5}
18	1.9155×10^{-5}	3.1122×10^{-5}	-7.9577×10^{-6}
19	5.59727×10^{-5}	2.2241×10^{-5}	1.0126×10^{-5}

2.2.2. The $2\nu_2$, ν_1 and ν_3 Bands of $H_2{}^{16}O$.

The H_2O absorption spectrum at 2.7 μm is formed by three interacting absorption bands. These bands are due to 3 vibrational states (020), (100) and (001) of $H_2{}^{16}O$. This spectrum is more difficult to simulate than the H_2O spectrum $010 \rightarrow 000$ at 6.25 μm presented in the previous section. In the $2\nu_2$, ν_1 and ν_3 bands strong Fermi and Coriolis interactions exist between the three bands, which increases the complexity required to reproduce their absorption spectrum. The Fermi resonance occurs when two or more vibrational levels of the same symmetry have nearly the same energy [7] which makes that energy levels 'repel' each other, increasing the separation between these energy levels [6, 7]. The vibrational levels (020) and the (100) have the same symmetry Γ_a (Table 2.18). If the motion of the particle is referred to a uniform rotating coordinate system the centrifugal and the Coriolis accelerations should be taken into account. These accelerations are due to apparent centrifugal and Coriolis forces whose magnitudes are $F_{cen} = mr\omega^2$ and $F_{Coriolis} = 2mv_\alpha\omega \sin\varphi$ respectively [6]. Where m is the mass of the particle, v_α is the apparent velocity respect to the moving coordinate system, r is the distance from the axis of rotation, ω the angular velocity of the coordinate system with respect to a fixed coordinate system, and φ the angle between the axis of rotation and the direction of v_α. The Coriolis 'force' occurs only for a moving particle and it is directed at right angles to the direction of motion and right angles to the axis of rotation. The effect of the Coriolis 'force' is generally larger than the effect due to the centrifugal force since the velocity due to vibration v_α is generally much larger than that due to rotation $r\omega$. The Coriolis contribution can be significant when two or more vibrational states v and v' have nearly the same energy $E_v \approxeq E_{v'}$ since the rotation vibration coupling can be large [7].

The model proposed by Flaud and Camy-Peyret [41] evaluates the energy levels of each state 020, 100, and 001 taking into consideration the Fermi type interactions between the (020) and (100) states and the Coriolis interaction between the three vibrational state (020), (001) and (100). In this work we employed this model to evaluate the line positions for these bands. Furthermore the line intensities were evaluated using the model proposed by Flaud and Camy-Peyret [35], this method it also presented in this section.

2.2.2.1. Hamiltonian Matrix, and Energy Levels.

The Hamiltonian proposed by Flaud and Camy-Peyret [41] takes into account the interaction between the three states (001), (100) and (020) of $H_2{}^{16}O$. This matrix Hamiltonian if formed by 3 x 3 blocks. The diagonal blocks contain the rotational part of each state neglecting interaction with other states; these blocks are of Watson A type Hamiltonian (v-diagonal operator). The off diagonal blocks contain the operators that take into account the interaction between the 3 states. The Hamiltonian matrix for the three interacting states it is represented as

$$\mathbf{H} = \begin{bmatrix} \mathbf{H}_{22} & \mathbf{H}_{23} & \mathbf{H}_{24} \\ \mathbf{H}_{32} & \mathbf{H}_{33} & \mathbf{H}_{34} \\ \mathbf{H}_{42} & \mathbf{H}_{43} & \mathbf{H}_{44} \end{bmatrix} \tag{2.37}$$

where the sub-index 2 is for the vibrational (020) state, the 3 for (100) and the 4 for the (001) state. The diagonal blocks $\mathbf{H}_{22}$, $\mathbf{H}_{33}$, and $\mathbf{H}_{44}$ correspond to the rotational parts of each state neglecting interaction between them. The off diagonal blocks contain the interactions between the states, for example the block $\mathbf{H}_{32}$ contains the Fermi type interaction between the (100) and (020) states.

Since the diagonal blocks are of Watson A type Hamiltonian, therefore their matrix elements are given by

$$\begin{aligned} \mathbf{H}_r^v = {} & E_v + \frac{(B^v + C^v)\,P^2}{2} + \left(A^v - \frac{B^v + C^v}{2}\right) {P_Z}^2 + \frac{B^v - C^v}{2} {P_{XY}}^2 \\ & - \Delta_J^v P^4 - \Delta_{JK}^v P^2 {P_Z}^2 - \Delta_K^v {P_Z}^4 - 2\delta_J^v P^2 {P_{XY}}^2 - \delta_K^v \left[{P_Z}^2 {P_{XY}}^2 + {P_{XY}}^2 {P_Z}^2\right] \\ & + H_J^v P^6 + H_{JK}^v P^4 {P_Z}^2 + H_{KJ}^v P^2 {P_Z}^4 + H_K^v {P_Z}^6 + 2h_J^v P^4 {P_{XY}}^2 \\ & + h_K^v \left[{P_Z}^4 {P_{XY}}^2 + {P_{XY}}^2 {P_Z}^4\right] + L_{KKJ}^v P^2 {P_Z}^6 + L_K^v {P_Z}^8 \\ & + l_K^v \left[{P_Z}^6 {P_{XY}}^2 + {P_{XY}}^2 {P_Z}^6\right] + P_K^v {P_Z}^{10} \end{aligned} \tag{2.38}$$

Where the index v corresponds to the vibrational state $v = v_1 v_2 v_3$; here equation (2.36) is basically the definition of the Watson Hamiltonian, as given in (2.31), which was used to evaluate the energy levels for the absorption spectrum of the ν_2 mode at 6.25 μm. The only difference between these two Hamiltonians is the number of resonance terms that are required. Using Wang's transformation the adapted symmetry of the Watson Hamilnian $|JK\rangle$ is expanded to $|JK\gamma\rangle$ and furthermore the Watson blocks are

split into four submatrices $\mathbf{E}^{+}$, $\mathbf{E}^{-}$, $\mathbf{O}^{+}$, and $\mathbf{O}^{-}$ of symmetry $\Gamma = A_1, A_2, B_1, B_2$. To evaluate the matrix elements the symmetric rigid rotor definitions for the $\langle P^2 \rangle$, $\langle {P_Z}^2 \rangle$, and $\langle {P_{XY}}^2 \rangle$ operators can be employed, these are given by equations (2.29a) to (2.29f).

The off diagonal blocks' matrix elements are given by

$$\mathbf{H}_{32} = h_{32} + h'_{32}{P_Z}^2 + h''_{32}P^2 + h'''_{32}{P_{XY}}^2, \tag{2.39}$$

$$\mathbf{H}_{43} = h_{43}\left(P_X P_Z + P_Z P_X\right), \tag{2.40}$$

$$\mathbf{H}_{42} = h_{42}\left(P_X P_Z + P_Z P_X\right). \tag{2.41}$$

To evaluate these matrix elements a few extra operator definitions, such as $\langle P_X P_Z + P_Z P_X \rangle$, are required. Furthermore as there are other allowed changes in K, such those connecting the Coriolis blocks $\mathbf{H}_{42}$, $\mathbf{H}_{43}$ which require more operator definitions. The operators needed to evaluate the matrix elements of the off diagonal blocks can be expressed as

$$\langle J'' K'' \gamma \left| {P_{XY}}^2 \right| J' \quad K \pm 2 \quad \gamma' \rangle = \langle J'' \quad K \left| {P_{XY}}^2 \right| J' \quad K'' \pm 2 \rangle, \quad K'' \geq 1, \gamma''\gamma' = +1 \tag{2.42}$$

$$\langle J'' \quad 1 \quad \gamma'' \left| {P_{XY}}^2 \right| J' \quad 1 \quad \gamma' \rangle = \frac{\gamma'' + \gamma'}{2} \langle J'' \quad 1 \left| {P_{XY}}^2 \right| J' \quad -1 \rangle, \quad K'' = 1, \gamma''\gamma' = +1 \tag{2.43}$$

$$\langle J'' K'' \gamma'' \left| P_X P_Z + P_Z P_X \right| J' \quad K'' \pm 1 \quad \gamma' \rangle = \langle J'' K'' \left| P_X P_Z + P_Z P_X \right| J' K'' \pm 1 \rangle, \quad K'' \geq 1, \gamma''\gamma' = -1 \tag{2.44}$$

$$\langle J'' \quad 0 \left| P_X P_Z + P_Z P_X \right| J' \quad 1 \quad \gamma' \rangle = \frac{1 - \gamma'}{\sqrt{2}} \langle J'' \quad 0 \left| P_X P_Z + P_Z P_X \right| J'' \quad 1 \rangle, \quad \gamma''\gamma' = -1 \tag{2.45}$$

$$\langle J'' \quad 1 \quad \gamma'' \left| P_X P_Z + P_Z P_X \right| J' \quad 0 \rangle = \frac{1 - \gamma''}{\sqrt{2}} \langle J'' \quad 1 \left| P_X P_Z + P_Z P_X \right| J' \quad 0 \rangle, \quad \gamma''\gamma' = -1 \tag{2.46}$$

$$\langle J'' K'' \gamma'' \left| P_X P_Z + P_Z P_X \right| J' \quad K'' \pm 1 \quad \gamma' \rangle = \frac{K' + K''}{2} \langle J'' K'' \left| P_X \mp i P_Y \right| J' K' \rangle, \quad \gamma''\gamma' = -1 \tag{2.47}$$

$$\langle J'' \quad K'' \left| P_X \mp i P_Y \right| J' \quad K'' \pm 1 \rangle = \sqrt{J''\left(J''+1\right) - K'\left(K' \pm 1\right)} \tag{2.48}$$

All operator definitions, excepting (2.47), were taken from [28]. The operator definition given in (2.47) can be found in [43]. The energy levels of the three states are given by eigenvalues of the block Hamiltonian matrix expressed in (2.37). The rotational constants needed to evaluate the matrix diagonal blocks (Watson-Hamiltionian) are given in Table 2.20. The coupling constants required to evaluate the off diagonal blocks are given in Table 2.21. Finally, some useful sketches showing how the Hamiltonian submatrices are filled and their dimensions, depending of the *J* and level parity are shown in figures 2.21-2.23.

2.2.2.2. Selection Rules

The vibrational-rotational asymmetric wave functions $|v_1 v_2 v_3 J K_a K_c\rangle$ need to be expanded in an adapted symmetric basis $|v_1 v_2 v_3\rangle|JK\gamma\rangle$. Using the adapted symmetry basis, expressed by the Wang's representation, the full Hamiltonian given in (2.35) splits into 4 submatrices $\mathbf{E}^+$, $\mathbf{E}^-$, $\mathbf{O}^+$, and $\mathbf{O}^-$ each one of order $(3/4)(2J+1)$ [41]. To each matrix corresponds one type of symmetry $\Gamma = A_1, A_2, B_1, B_2$. The possible Γ symmetries for a C_{2v} molecule are listed in Table 2.18.

The symmetry type Γ is related to the vibrational symmetry type Γ_v and to the rotational adapted symmetry type Γ_r since $\Gamma = \Gamma_v \times \Gamma_r$. The symmetry type Γ_v of the vibrational state v it is given in Table 2.18 while the symmetry type of the rotational level Γ_r it is given in Table 2.19. In these tables *e* denotes an even level whilst *o* an odd level. The allowed transitions depend on the adapted symmetry type as $\Gamma'' \leftrightarrow \Gamma'$; these transitions are $A_1 \leftrightarrow A_2$ or $B_1 \leftrightarrow B_2$, where Γ'' represents the symmetry of the lower level, whilst Γ' the symmetry of the upper level. Basically, these rules are the same as for the bending mode ν_2 which was explained in section before, see Table 2.12. Here, bands $2\nu_2$ and ν_1 are of type B, whilst the ν_3 band is of type A [7]. Finally by using the appropriate selection rules (Table 2.12) the line positions of the 3 bands can be computed.

Table 2.17- Symmetry Types of vibration rotation-levels. After [28, 41]

$\Gamma\left(\lvert v_1 v_2 v_3 J K_a K_c\rangle\right)$			
v_3	K_a	K_c	Γ
e	*e*	*e*	A_1
o	*o*	*e*	
e	*o*	*o*	A_2
o	*e*	*o*	
e	*o*	*e*	B_1
o	*e*	*e*	
e	*e*	*o*	B_2
o	*o*	*o*	

Table 2.18- Symmetry type Γ_v of the vibrational function $\lvert v\rangle$. After [28]

v_3	Γ_v
e	A_1
o	B_1

Table 2.19-Symmetry type Γ_r of the rotational function $\lvert JK\gamma\rangle$. After [28]

J	K	γ	Γ_r	Name and dimension of the basis
$2p$	*e*	+	A_1	$\mathbf{E}^+(p+1)$
$p>0$	*o*	+	A_2	$\mathbf{O}^+(p)$
	e	-	B_2	$\mathbf{E}^-(p)$
	o	-	B_1	$\mathbf{O}^-(p)$
$2p-1$	*e*	+	B_2	$\mathbf{E}^+(p)$
$p>1$	*o*	+	B_1	$\mathbf{O}^+(p)$
	e	-	A_1	$\mathbf{E}^-(p-1)$
	o	-	A_2	$\mathbf{O}^-(p)$
$\lvert JK\gamma\rangle = \frac{1}{\sqrt{2}}(\lvert JK\rangle + \gamma\lvert J \quad -K\rangle), \quad K>0, \gamma=\pm 1$				
$\lvert J \quad 0\rangle = \lvert J \quad 0\rangle$				

Table 2.20- Constants used to fit the 3 vibrational states (020), (100) and (001). After [41]

Constant	$v = 2(020)$	$v = 3(100)$	$v = 4(001)$
E_v	3.156215x10^{3}	3.652474x10^{3}	3.7559295x10^{3}
A	3.558672x10^{1}	2.712217x10^{1}	2.6648050x10^{1}
B	1.484154x10^{1}	1.430477x10^{1}	1.4431302x10^{1}
C	8.974480x10^{0}	9.104570x10^{0}	9.1381670x10^{0}
Δ_J	1.58040x10^{-3}	1.233000x10^{-3}	1.3054900x10^{-3}
Δ_{JK}	-1.04880x10^{-2}	-5.387400x^{-3}	-5.6561000x10^{-3}
Δ_K	1.09919x10^{-01}	3.023000x10^{-2}	2.8584000x10^{-2}
δ_J	6.75200x10^{-04}	4.998700x10^{-4}	5.3817000x10^{-4}
δ_K	8.71700x10^{-03}	1.240500x10^{-3}	1.3261000x10^{-3}
H_J	9.19000x10^{-07}	4.402000x10^{-7}	6.0220000x10^{-7}
H_{JK}	1.08400x10^{-05}	0.000000x10^{0}	0.0000000x10^{0}
H_{KJ}	-9.90300x10^{-05}	-1.418000x10^{-5}	-1.4992000x10^{-5}
H_K	1.04529x10^{-03}	1.001600x10^{-4}	8.4070000x10^{-5}
h_J	4.22700x10^{-07}	2.331000x10^{-7}	3.0870000x10^{-7}
h_{JK}	4.01000x10^{-06}	0.000000x10^{0}	1.0650000x10^{-6}
h_K	2.32600x10^{-04}	2.166000x10^{-5}	2.2660000x10^{-5}
L_K	-7.87000x10^{-06}	-2.696000x10^{-7}	-1.5877000x10^{-7}
l_K	-1.28600x10^{-06}	0.000000x10^{0}	0.0000000x1^{00}
P_K	3.07700x10^{00}	0.000000x10^{0}	0.0000000x10^{0}

Table 2.21- Coupling Constants. After [41].

h_{32}	47.873
h'_{32}	-0.1791
h''_{32}	-1.627x10^{-2}
h'''_{32}	-1.860x10^{-3}
h_{43}	-0.31881
h_{42}	-8.530x10^{-2}

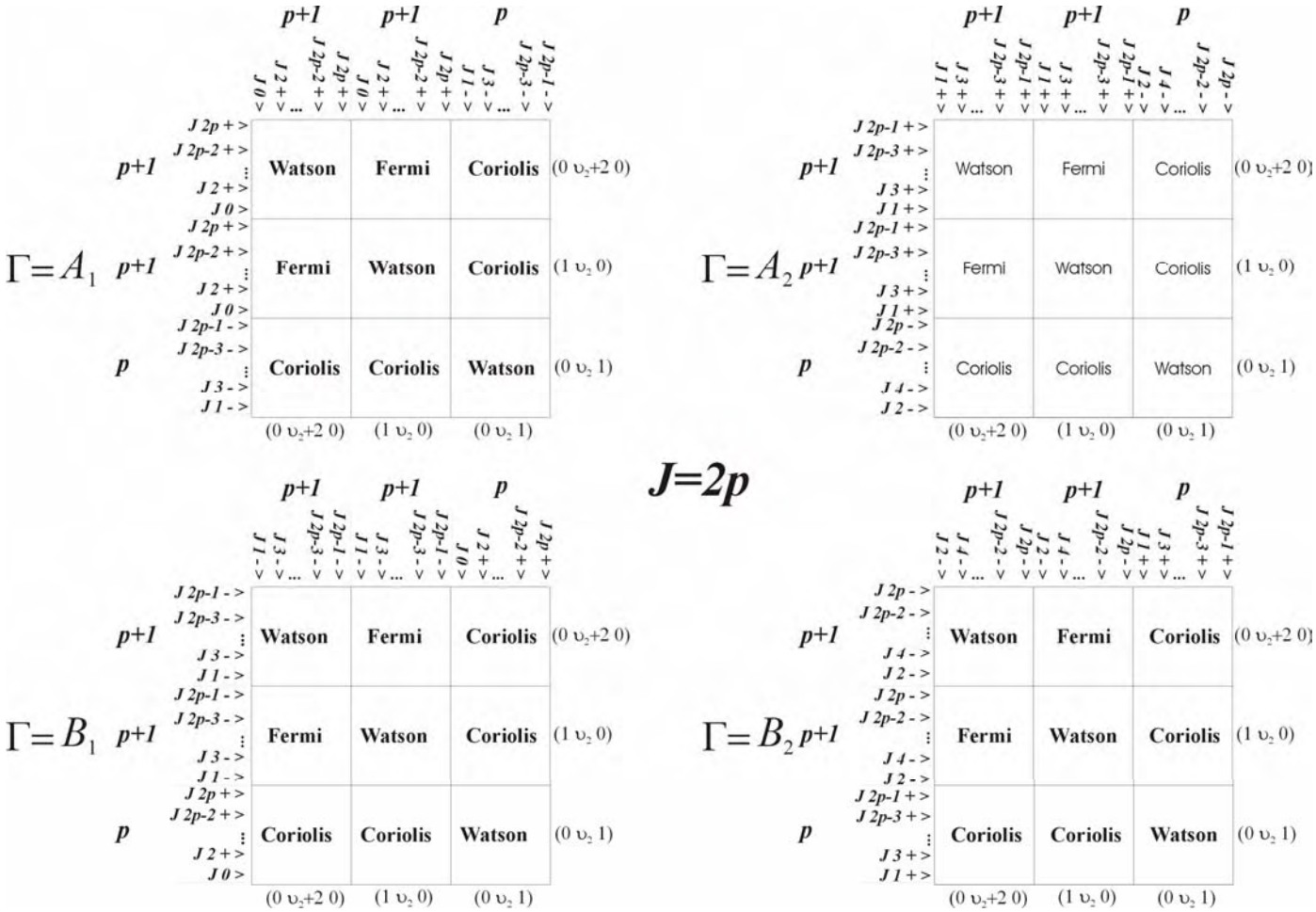

Figure 2.21- Hamiltonian submatrices for an even J level [28]

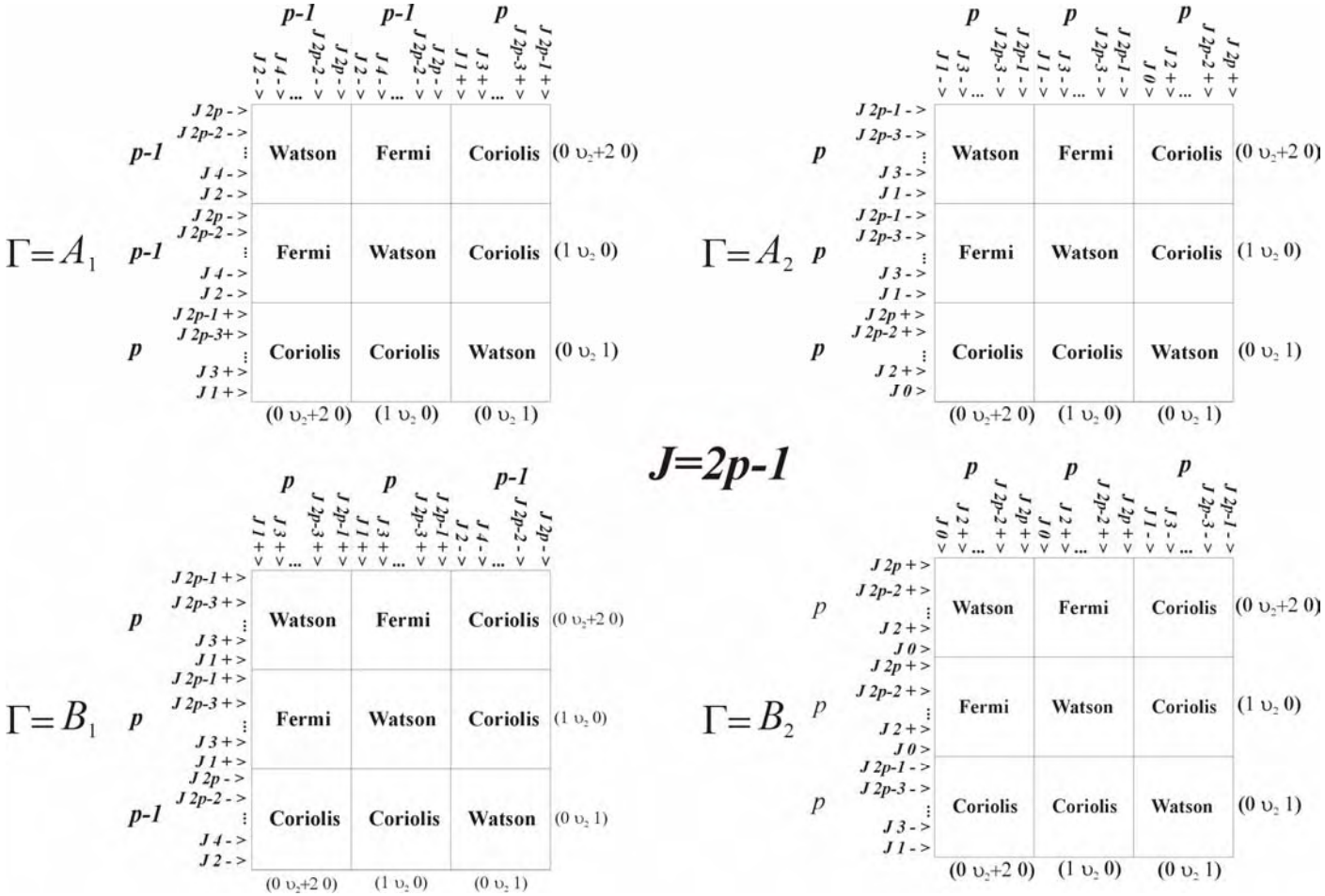

Figure 2.22- Hamiltonian submatrices for an odd J level [28].

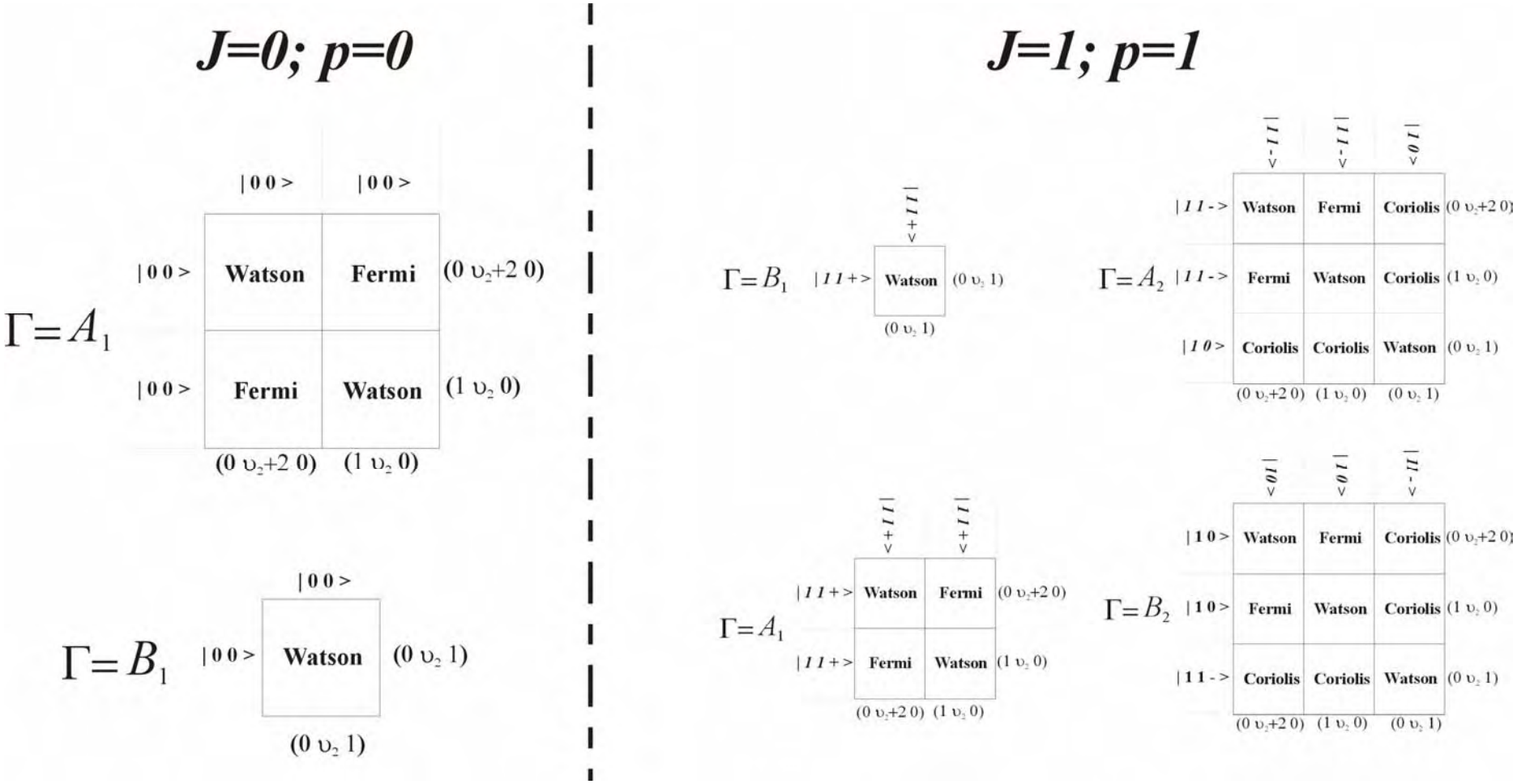

Figure 2.23- Hamiltonian submatrices for special cases of *J* level [28].

2.2.2.3. Line Intensities for the $2\nu_2$, ν_1, and ν_3 bands of $H_2{}^{16}O$.

The method to evaluate the line intensities for the 3 bands is basically the same as the used previously in section 2.2.1.4 to evaluate the ν_2 band. Some modifications in the formulae must be made in order to properly fit the three bands. The line intensity can be evaluated using equation (2.33) and for clarity let us recall it here

$$S(T,\nu_0)=\frac{8\pi^3 g_a 10^{-43}}{3hcQ(T)}\nu_0 \exp\left(\frac{-hcE_A}{kT}\right)\left[1-\exp\left(\frac{-hc\nu_0}{kT}\right)\right]R_A^B \quad (2.49)$$

The parameter's definitions are identical as those given in section 2.2.1.4 excepting the vibration-rotation dipole moment matrix element $\left(R_A^B\right)$ connecting the lower state A with the upper state B, that for the three interacting states is defined by [35]

$$R_A^B=\sum_a\sum_b 3|\langle A|\mu_z|B\rangle|^2. \quad (2.50)$$

The last equation can be expanded as in the case of the ν_2 band in a symmetric adapted basis. Here, R_A^B for the three interacting bands $2\nu_2$, ν_1, and ν_3 considering no external field, can be expanded as

$$R_A^B=\left|\sum_{v=2,3,4}\sum_k\sum_{k'} C_k^{0*}C_{k'}^v\langle J''K''\gamma''|{}^v\mu_z'|J'K'\gamma'\rangle\right|^2. \quad (2.51)$$

In this expansion the wavefunctions $|v_1v_2v_3JK_aK_c\rangle$ were represented in adapted symmetry basis $|v\rangle|JK\gamma\rangle$, where $|0\rangle|000\rangle$, $|2\rangle|020\rangle$, $|3\rangle|100\rangle$, and $|4\rangle|001\rangle$. C_k^{0*} and $C_{k'}^v$ are the eigenvectors coefficients for the ground state (000) and for the 3 interacting states respectively. These eigenvectors are obtained by diagonalization of their respective Hamiltonian matrices. The ${}^v\mu_z'$ is a sum of rotational operators given by [35]

$${}^v\mu_z'=\sum_j {}^v\mu_j'{}^vA_j \quad (2.52)$$

where ${}^{v}A_j$ are matrix elements (Table 2.22) and ${}^{v}\mu'_j$ are numerical constants (Table 2.23); Furthermore, the matrix direction cosine elements required to evaluate ${}^{v}A_j$ are listed in Table 2.24.

Finally to reproduce the absorption spectrum the air broadening coefficients are required. We utilised the coefficients given in the Hitran 2004 database [1]. The simulated absorption spectrum considering of the three interacting modes $2\nu_2$, ν_1, and ν_3 it is shown in Figure 2.24.

Table 2.22- ${}^{v}A_{j}$ matrix elements for the $2\nu_2$, ν_1, and ν_3 bands. [35].

Δv_3 even, $v = (020), (100)$		
j	***n***	$\langle J''K''\,|{}^{v}A_{j}|\,J'K'\rangle / \langle J''K''\,|\Phi(x)|\,J'K'\rangle$
1	1	1
2	1	$J'\left(J'+1\right)+J''\left(J''+1\right)$
3	1	$K'^{2}+K''^{2}$
4	1	$K'^{2}-K''^{2}$
5	1	$K'^{2}-K''^{2}-2m$
6	1	$\left(K'^{2}-K''^{2}\right)\left(K'^{2}-K''^{2}-2m\right)$
7	1	$J''\left(J''+1\right)-2m\left(m-1\right)+\left(2m-1\right)K''\Delta K-K''^{2}-1$
8	3	$\left[\left(J'-K''\Delta K-1\right)\left(J'-K''\Delta K-2\right)\left(J'+K''\Delta K-2\right)\left(J'+K''\Delta K+3\right)\right]^{-1/2}$
$\Delta J = J' - J'' = 0, \pm 1;\ m = \dfrac{J'\left(J'+1\right)-J''\left(J''+1\right)}{2};\ K'-K''=n\Delta K;\ \Delta K = \pm 1$		

Δv_3 odd, $v = (001)$		
j	***n***	$\langle J''K''\,|{}^{v}A_{j}|\,J'K'\rangle / \langle J''K''\,|\Phi(z)|\,J'K'\rangle$
1	0	1
2	0	$J'(J'+1)+J''(J''+1)$
3	0	$2K^{2}$
4	0	$\Delta J''\left[0.5(1+\Delta J)+J''\right]$
5	0	$\begin{cases} 2\left[J''\left(J''+1\right)-K''^{2}\right]-1 & \text{if } \Delta J = 0 \\ -\left(1+2K^{2}\right) & \text{if } \Delta J = \pm 1 \end{cases}$
6	2	$\begin{cases} \Delta K\left[\left(J''-K''\Delta K-1\right)\left(J''+K''\Delta K+2\right)\right]^{1/2} & \text{if } \Delta J = 0 \\ \Delta K\left(m-K''\Delta K-1\right)\left[\left(m+K''\Delta K+2\right)\right]^{1/2} & \text{if} \Delta J = \pm 1 \end{cases}$
7	2	$\begin{cases} 2(K''+\Delta K)\left[\left(J''-K''\Delta K-1\right)\left(J''+K''\Delta K+2\right)\right]^{1/2} & \text{if } \Delta J = 0 \\ 2\left(K''+\Delta K\right)\left[\left(m-K''\Delta K-1\right)\left(m+K''\Delta K+2\right)\right]^{1/2} & \text{if } \Delta J = \pm 1 \end{cases}$
8	2	$\begin{cases} 2(K''+\Delta K)\left[\left(J''-K''\Delta K-1\right)\left(J''+K''\Delta K+2\right)\right]^{1/2} & \text{if} \Delta J = 0 \\ -2\Delta K\left(m-1-K''\Delta K\right)\left[\left(m-K''\Delta K-1\right)\left(m+K''\Delta K+2\right)\right]^{1/2} & \text{if} \Delta J = \pm 1 \end{cases}$
$\Delta J = J' - J'' = 0, \pm 1;\ m = \dfrac{J'\left(J'+1\right)-J''\left(J''+1\right)}{2};\ K'-K''=n\Delta K;\ \Delta K = \pm 1$		

Table 2.23- Constants of the transformed transition moment operators ${}^{v}\mu'_{j}$. [35].

j	**Type B Bands** ${}^{v}\mu'_{j}$		**Type A Band** ${}^{v}\mu'_{j}$
	$v=2(020)$	$v=3(100)$	$v=4(001)$
1	0.005815	-0.015323	0.06869
2	$0.195\text{x}10^{-5}$	0	0
3	0	0	0
4	$-0.397\text{x}10^{-4}$	$0.13633\text{x}10^{-2}$	$-0.1146\text{x}10^{-2}$
5	$0.2277\text{x}10^{-4}$	$-0.5133\text{x}10^{-3}$	0
6	$-0.508\text{x}10^{-5}$	0	$0.500\text{x}10^{-3}$
7	$-0.373\text{x}10^{-5}$	0	0
8	0	0	$0.381\text{x}10^{-4}$

Table 2.24- Matrix Elements of the direction cosines used to evaluate ${}^{v}A_{J}$. [35].

ΔJ	$\langle J'' \quad K'' \lvert \Phi(\alpha) \rvert J+\Delta J \quad K''+\Delta K'' \rangle$	
	$\Delta K=0\,(\alpha=z)$	$\Delta K=\pm 1\,(\alpha=x)$
0	$K''\left[\dfrac{2J''+1}{J''(J''+1)}\right]^{1/2}$	$\dfrac{1}{2}\left[\dfrac{(2J''+1)(J''-K''\Delta K)(J''+K''\Delta K+1)}{J''(J''+1)}\right]^{1/2}$
± 1	$\left(\dfrac{m^2-K''^2}{\lvert m\rvert}\right)^{1/2}$	$\dfrac{-\Delta J\Delta K}{2}\left[\dfrac{(m+K\Delta K)(m+1+K\Delta K)}{J''(J''+1)}\right]^{1/2}$
$m=\begin{cases}-J'' & \Delta J=-1\\ J''+1 & \Delta J=+1\end{cases}$		

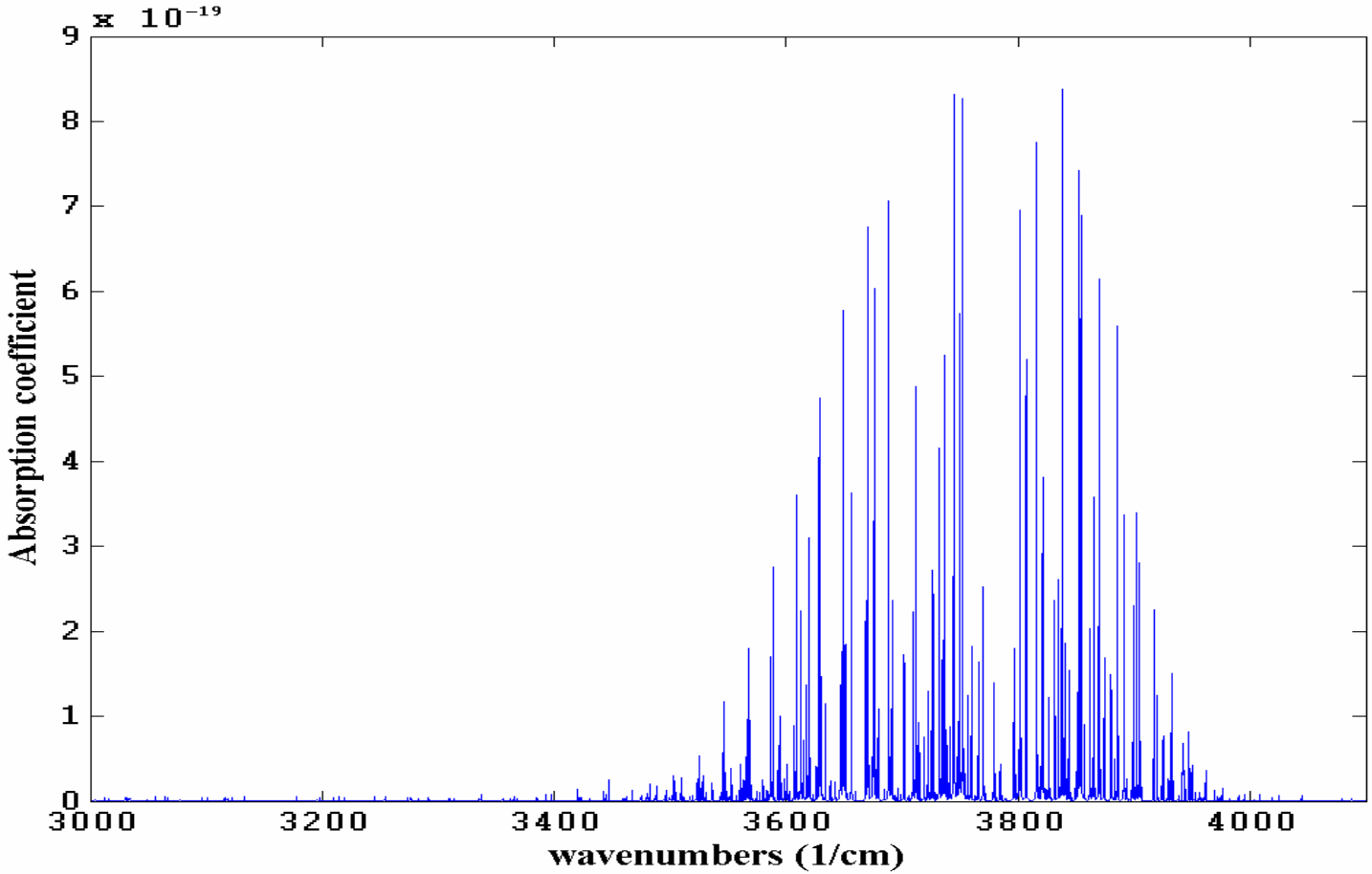

Figure 2.24- Absorption spectrum of the $2\nu_2$, ν_1, and ν_3 bands of $H_2{}^{16}O$.

2.2.3. Validation of the H_2O model.

In order to validate our simulated spectrum of H_2O the computed line positions and intensities were compared with the values listed the HITRAN 2004 database [1]. According to the HITRAN database the difference between the measured line position and the computed line position is in the order of 0.0004 cm^{-1} for most of the ro-vibrational lines of H_2O in the region of 1400 cm^{-1} [1, 3]. In the same way the computed lines reported by HITRAN present an error around 8% for the absorption bands $010 \leftarrow 000$ [2, 31]. Here we require to evaluate how close are our computed line positions and intensities with those provided by HITRAN in order to be sure that our data have good level of accuracy.

The first parameter that it is necessary to review is the residual difference between the computed line position and the line position listed in HITRAN for the fundamental band ν_2 of $H_2{}^{16}O_2$. The residual difference is in the order of ≤ 0.03 cm^{-1} for $J'' \leq 5$ (figure 2.25) and it is slightly larger for few ro-vibrational lines originated from highly exited $J'' = 8 \text{ and } 9$ where the residual difference is ≤ 0.05 cm^{-1} (figure 2.26). The lines with larger residual errors are transitions originating in energy levels with high $J'' > 9$ and $K_a'' > 9$ which are also very weak transitions. In average the FWMH of the ro-vibrational lines is 0.14 cm^{-1} for $J'' \leq 9$ and $K_a'' \leq 9$ [1]. The strongest line of the band ν_2 of $H_2{}^{16}O_2$ at 296K is $4,1,4 \leftarrow 3,0,3$ which presents a residual difference of 0.014 cm^{-1} in comparison with HITRAN 2004; therefore this line deviates $1/10^{th}$ of the FWMH. In contrast the line with the larger residual difference is $10,10,0 \leftarrow 9,9,1$ which presents a residual error of 0.05 cm^{-1}, so this line deviates around $1/3^{th}$ of the FWMH. However this line is very weak in comparison with the $4,1,4 \leftarrow 3,0,3$ which is 4.039×10^5 times stronger. Therefore in our model the ro-vibrational lines which present slightly larger deviations are also very weak, so these lines do not represent a big problem since these will not introduce considerable errors in the simulation of the full spectrum.

A better fit could be made using ro-vibrational constants with greater precision in the four and fifth decimal digit of the constant used to simulate the spectrum. Many of the published constants just have 2 or 3 decimal digits and the mathematical model is very sensitive to small variations in these constants. Furthermore, HITRAN 2004 uses more

complicated mathematical models and also more accurate constants to fit the energy levels with highly excited $J'' \leq 10$. However for our application the model presented in the previous section is sufficiently accurate to fit the lines $J'' \leq 9$ and $K_a \leq 9$ which are of interest for simulate our gas sensors. Lines with $J'' > 9$ are very weak at 296K and therefore we consider that these lines introduce a practically negligible error in our gas sensor simulation. Furthermore, our gas sensor is quite sensitive to the separation between two consecutive ro-vibrational lines of CO, CO_2, N_2O and CH_4 which are our molecules targets. The separation of two consecutive ro-vibrational lines, of these target molecules, is considerably large and very well defined. Therefore a very small deviation in the line position of some H_2O ro-vibrational lines, such as the line $10,10,0 \leftarrow 9,9,1$, will not produce significant changes in the calculation of the cross sensitivity tables.

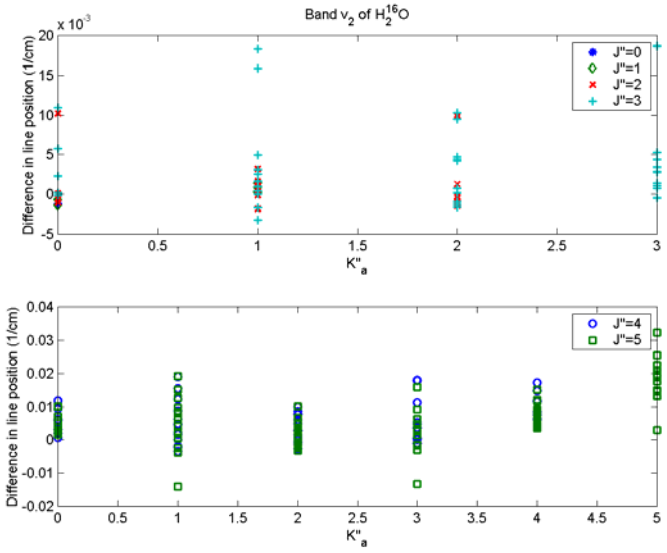

Figure 2.25- Difference in line position between our calculated positions and HITRAN 2004 for the ν_2 of $H_2{}^{16}O$ considering up to $J'' \leq 5$.

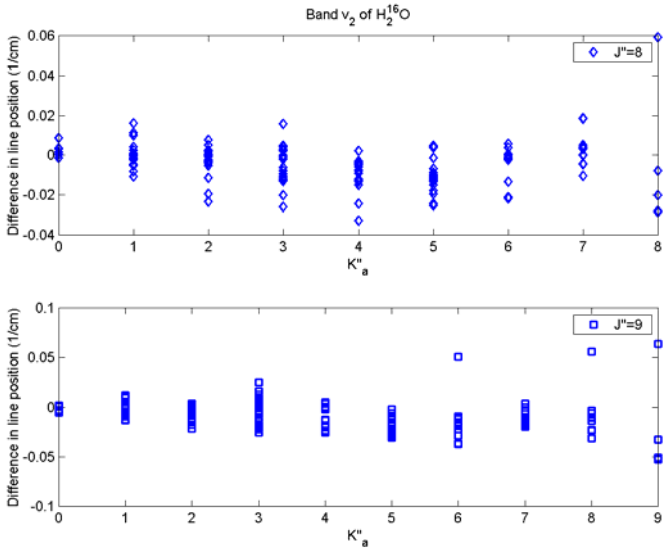

Figure 2.26- Difference in line position between our calculated positions and HITRAN 2004 for the ν_2 of $H_2{}^{16}O$ for $J'' = 8$ and $J'' = 9$.

The line intensity error (%) of our calculated values and those listed in the HITRAN 2004 for the fundamental ν_2 band of $H_2{}^{16}O_2$ is around $\leq 0.04\%$ for $J'' \leq 5$ (figure 2.27). This error is slightly higher for ro-vibrational lines originated from highly exited J'' for instance some lines with $J'' = 8 \text{ and } 9$ present an error larger than 1% (figure 2.28). The line intensity error will increase with J'' however due to our application constraints we considered just lines with $J'' \leq 9$ and $K_a'' \leq 9$ where the error is small enough. Lines with $J'' > 9$ are very weak and therefore will not introduce significant error in the final spectrum. In our simulation we have that the total strength is 106435.1×10^{-22} cm^{-1}/(molecule cm^{-2}) for $J'' \leq 9$ and $K_a'' \leq 9$ at 296K. According to HITRAN 2004 the $H_2{}^{16}O_2$ ν_2 band has an intensity of 107116.6×10^{-22} considering $J'' \leq 20$ and $K_a'' \leq 13$. It means that in our model covers approximately the 99.36% and the total accumulated strength of the fundamental band. Therefore, considering that our simulated results have an average line intensity error of 0.04% and that just the 99.36% of the total band strength is take into account we have that our model has an accuracy of around 99.32%. As the simulated model has less than 1% error in comparison with HITRAN 2004 therefore we consider that the model presented in previous section to calculate the line intensities for the ν_2 band of H_2O is sufficiently accurate, and therefore it is good enough to guarantee precise simulations of our gas sensor. Indeed as the line intensities reported in HITRAN have an uncertainty of around 8% therefore our computed

spectrum has an accuracy of around 91.37%. Similar results are obtained for the $2\nu_2$, ν_1, and ν_3 bands which is reasonable since we employed a similar method to evaluate the line position and intensities.

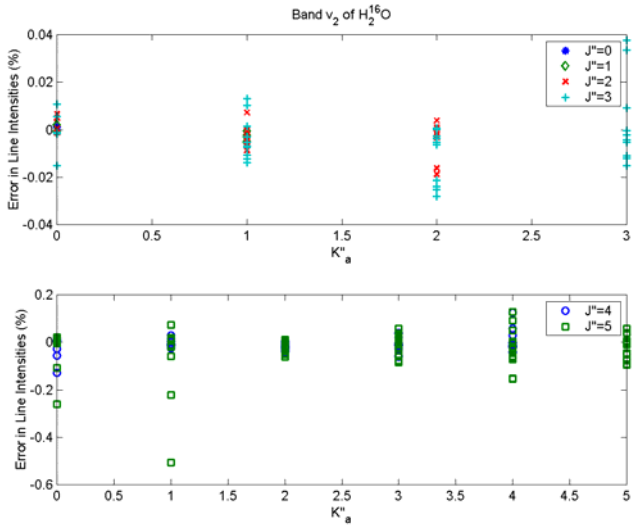

Figure 2.27- Error in Line intensities between HITRAN 2004 and the computed values for the ν_2 of $H_2{}^{16}O$ considering up to $J'' \leq 5$.

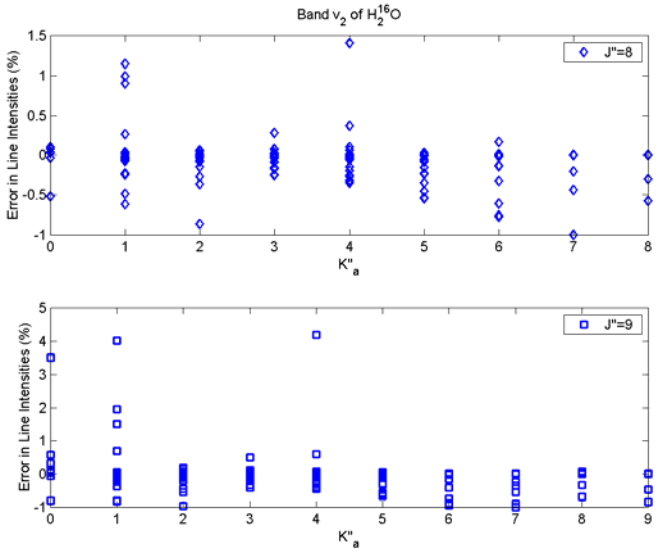

Figure 2.28- Error in Line intensities between HITRAN 2004 and the computed values for the ν_2 of $H_2{}^{16}O$ for $J'' = 8$ and $J'' = 9$.

2.3. References

1. L. S. Rothman, D. Jacquemart, A. Barbe, D. C. Benner, *et al.*, The HITRAN 2004 molecular spectroscopic database, *Journal of Quantitative Spectroscopy and Radiative Transfer* **96**(2), p. 139-204, 2005

2. L. S. Rothman, C. P. Rinsland, A. Goldman, S. T. Massie, *et al.*, The HITRAN Molecular Spectroscopic Database and Hawks (HITRAN Atmospheric Workstation): 1996 Edition, *Journal of Quantitative and Radiative Transference* **60**, p. 665-710, 1998

3. L. S. Rothman, R. R. Gamache, A. Goldman, L. R. Brown, *et al.*, The HITRAN database: 1986 edition, *Applied Optics* **26**, p. 4058-4077, 1987

4. L. S. Rothman, R. R. Gamache, R. H. Tipping, C. P. Rinsland, *et al.*, The HITRAN Molecular Database: Editions of 1991 and 1992, *Journal of Quantitative and Radiative Transference* **48**, p. 469-507, 1992

5. L. S. Rothman, A. Barbe, D. C. Benner, L. R. Brown, *et al.*, The HITRAN molecular spectroscopic database: edition of 2000 including updates through 2001, *Journal of Quantitative and Radiative Transference* **82**, p. 5-44, 2003

6. G. Herzberg, *Molecular Spectra and Molecular Structure, Vol II Infrared and Raman Spectra of Polyatomic Molecules*, USA, Van Nostrand Reinhold Company International, 1945

7. W. Gordy and R. L. Cook, *Microwave Molecular Spectra*, 331-344, 1984

8. N. B. Colthup, L. H. Daly, and S. E. Wiberly, *Introduction to Infrared and Raman Spectroscopy*, Third Edition, United States of America, 109-112, 1990

9. C. Mansfield, *An Investigation into the Viability of an Infrared Diagnostic Instrument for Measurement of CO_2 Isotope Ratios in Breath*, in *Optoelectronics Research Centre*. 2000, University of Southampton: Southampton.

10. L. S. Rothman, R. L. Hawkins, R. B. Wattson, and R. R. Gamache, Energy Levels, Intensities, and Linewidths of Atmospheric Carbon Dioxide Bands, *Journal of Quantitative and Radiative Transference* **48**, p. 537-566, 1992

11. J. K. G. Watson, Centrifugal Corrections for Asymmetric Top Molecules, *Journal of Chemical Physics* **45**, p. 1360-1361, 1966

12. R. R. Gamache, R. L. Hawkins, and L. S. Rothman, Total Internal Partition Sums in the Range 70-3000 K: Atmospheric Linear Molecules, *Journal of Molecular Spectroscopy* **142**, p. 205-219, 1990

13. G. Duxbury, *Infrared Vibration-Rotation Spectroscopy from Free radicals to the infrared sky*, England, John Wiley & Sons LTD, 2000

14. R. A. McClatchey, W. S. Benedict, S. A. Clough, D. E. Burch, *et al.*, AFCRL Atmospheric Absorption Line Parameters Compilation, *Air Force Cambridge Research Laboratories, Enviromental Research Papers No. 434*, 1973

15. R. S. Eng and A. W. Mantz, Tunable Diode Laser Spectroscopy of CO2 in the 10 to 15 μm Spectral Region-Lineshape and Q-Branch Head Absorption Profile, *Journal of Molecular Spectroscopy* **74**, p. 331-344, 1979

16. R. A. Toth, N_2O vibration-rotation parameters derived from measurements in the 900-1090 and 1580-2380- cm^{-1} regions, *J. Opt. Soc. Am. B* **4**(3), p. 357-374, 1987

17. R. A. Toth, Line strengths of N_2O in the 1120-1440 cm^{-1} region, *Applied Optics* **23**(11), p. 1825-1834, 1984

18. R. A. Toth, Frequencies of N_2O in the 1100-1440 cm^{-1} region, *J. Opt. Soc. Am. B* **3**(10), p. 1263-1281, 1986

19. N. Lacome, A. Levy, and G. Guelachvili, Fourier transform measurement of self-, N2-, and O2-broadening of N2O lines: temperature dependence of linewidths, *Applied Optics* **23**, p. 425-435, 1984

20. R. A. Toth, Line strengths (900-3600 cm^{-1}), self-broadened linewidths, and frequency shifts (1800-2360 cm^{-1}) of N_2O, *Applied Optics* **32**(36), p. 7326-7365, 1993

21. R. A. Toth, Line-frequency measurements and analysis of N_2O between 900 and 4700 cm^{-1}, *Applied Optics* **30**(36), p. 5289-5320, 1991

22. J. L. Dunham, The Energy Levels of a Rotating Vibrator, *Physical Review* **41**(6), p. 721, 1932

23. R. Farrenq, G. Guelachvili, A. J. Sauval, N. Grevesse, *et al.*, Improved Dunham Coefficients for CO from Solar lines of High Rotational Excitation, *Journal of Molecular Spectroscopy* **149**, p. 375-390, 1991

24. C. J. Chackerian, G. Guelachvili, and R. H. Tipping, CO 1-0 Band Isotopic Lines as Intensity Standars, *Journal of Quantitative Spectroscopy and Radiative Transfer* **30**, p. 107-112, 1983

25. C. J. Chackerian and R. H. Tipping, Vibration-Rotational and Rotational Intensities for CO Isotopes, *Journal of Molecular Spectroscopy* **99**, p. 431-449, 1983

26. Q. Zou and P. Varanasi, New Laboratory data on the spectral line parameters in the 1-0 and 2-0 bands of 12C16O relevant to atmospheric remote sensing, *Journal of Quantitative Spectroscopy and Radiative Transfer* **75**, p. 63-92, 2002

27. C. Camy-Peyret and J.-M. Flaud, Line positions and intensities in the ν2 band of H216O, *Molecular Physics* **32**, p. 523-537, 1976

28. J. M. Flaud, C. Camy-Peyret, and R. A. Toth, *Water Vapour Line Parameters from Microwave to Medium Infrared*, Pergamon Press, 1981

29. J. K. G. Watson, Determination of Centrifugal Distortion Coefficients of Asymetric-Top Molecules, *Journal of Chemical Physics* **46**, p. 1935-1949, 1967

30. J. K. G. Watson, Determination of Centrifugal Distortion Coefficients of Asymmetric-Top Molecules. III Sextic Coefficents, *Journal of Chemical Physics* **48**(10), p. 4517-4524, 1968

31. R. A. Toth, Water Vapor Measurements between 590 and 2582 cm^{-1}: Line Positions and Strengths, *Journal of Molecular Spectroscopy* **190**, p. 379-396, 1998

32. L. H. Coudert, Analysis of the Rotational Levels of Water and Determination of the Potential Energy Function for the Bending ?2 Mode, *Journal of Molecular Spectroscopy* **165**, p. 406-425, 1994

33. L. H. Coudert, Analysis of the Line Positions and the Line Intensities in the ν2 Band of the Water Molecule, *Journal of Molecular Spectroscopy* **181**, p. 246-273, 1997

34. V. I. Starikov, S. A. Tashkun, and V. G. Tyuterev, Description of Vibration-Rotation Energies of Nonrigid Triatiomic Melecules Using the Generating Function Method, Bending States and Second Triad of Water, *Journal of Molecular Spectroscopy* **151**, p. 130-147, 1992

35. J. M. Flaud and C. Camy-Peyret, Vibration-Rotation Intensities in H2O-Type Molecules Application to the 2ν2, ν1, and ν3 Bands of $H_2{}^{16}O$, *Journal of Molecular Spectrsocopy* **55**, p. 278-310, 1975

36. R. A. Toth, ν2 band of $H_2$16O: line strengths and transition frequencies, *J. Opt. Soc. Am. B* **8**(11), p. 2236-2255, 1991

37. R. A. Toth, private communication, 2004

38. J. K. G. Watson, Aspects of Quartic and Sextic Centrifugal Efects on Rotational Energy Levels, *Vibrational Spectra and Structure* **6**, p. 1-89, 1977

39. G. W. King, R. M. Hainer, and P. C. Cross, The Asymmetric Rotor I. Calculation and Symmetry Classification of Energy Levels, *The Journal of Chemical Physics* **11**(1), p. 27-42, 1943

40. H. W. Kroto, *Molecular Rotation Spectra*, John Wiley & Sons, Ltd, 34-42, 1975

41. J. M. Flaud and C. Camy-Peyret, The interacting States (020), (100) and (001) of H216O, *Journal of Molecular Spectroscopy* **51**, p. 142-150, 1974

42. R. A. Toth, Air- and N_2-Broadening Parameters of Water Vapor: 604 to 2271 cm^{-1}, *Journal of Molecular Spectroscopy* **201**, p. 218-243, 2000

43. L. H. Coudert and J. T. Hougen, Analysis of the Microwave and Far Infrared Spectrum of the Water Dimer, *Journal of Molecular Spectroscopy* **139**(2), p. 259-277, 1990

Chapter 3

3. Optimal system parameters.

There are several ways to design gas sensors based on correlation spectroscopy that uses a Fabry-Perot Interferometer (FPI) as a modulator. One simple sensor configuration that has been used in the literature for some time consists in illuminating the FPI with a collimated beam [1-4]; a simple set up of this type is shown in Figure 3.1. The design of this type of sensor requires determination of the optimal FPI basic parameters such as the reflectivity (R) of the mirrors, and the optical thickness (nd) which is the separation between the two FPI mirrors. In addition to the FPI parameters we need to review the effect of introducing a band pass filter that allows transmission of just the light whose wavelengths match the target molecule absorption bands. Therefore, an optimisation procedure is required to find all these optimal system parameters. The simplest optimisation procedure evaluates numerically the response of the system for different values of R and nd. Although this procedure is very simple to implement it is numerically inefficient and time consuming. Therefore, in this chapter we present a new analytical approach based on the Fourier transform which is capable of determining the

optimal R and nd parameters. Additionally, this method gives guidance on the choice of optimised filters band pass shapes.

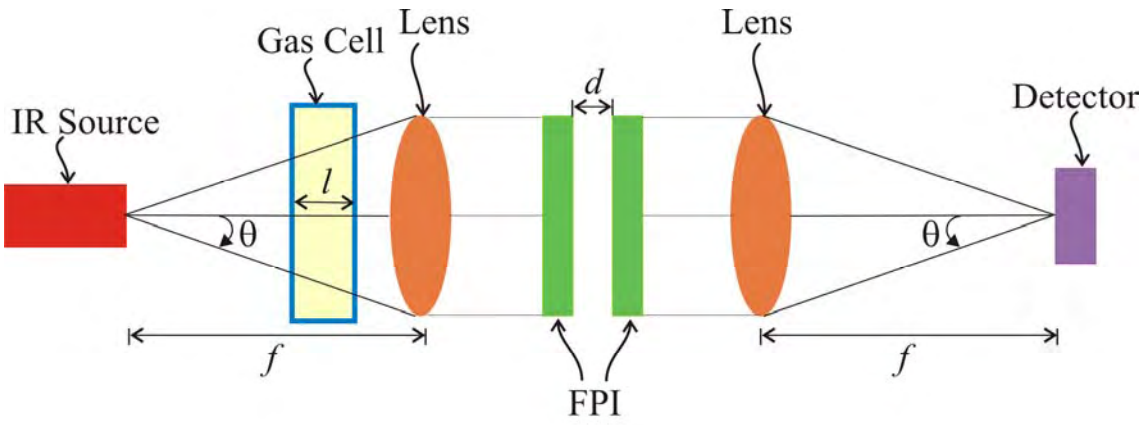

Figure 3.1- Basic configuration of a gas sensors based on correlation spectroscopy that use a Fabry-Perot Interferometer (FPI) as a modulator.

3.1. System Mathematical Model

In the gas sensor shown in figure 3.1 the transmission fringe pattern produced by the FPI is used to modulate the infrared beam arriving at the pyroelectric sensor. Firstly, in order to modulate the beam, the FPI's fringes are matched with very well defined ro-vibrational absorption lines of the target molecule (Figure 3.2a). Well-resolved absorption lines with Lorentzian line shapes are characteristic of most diatomic and linear molecules; for example, CO_2, CO, N_2O, and some specific absorptions bands of symmetric top and spherical top molecules such as NH_3, CH_4 at one atmosphere pressure. Secondly, the FPI's fringes are shifted along the wavenumber axis (Figure 3.2b); this shift is obtained by scanning the cavity length of the FPI from 0 to $\lambda_0/2$ [5]. Consequently, the transmission through the system changes as the FPI's fringes are shifted along the wavenumber axis, producing the beam modulation.

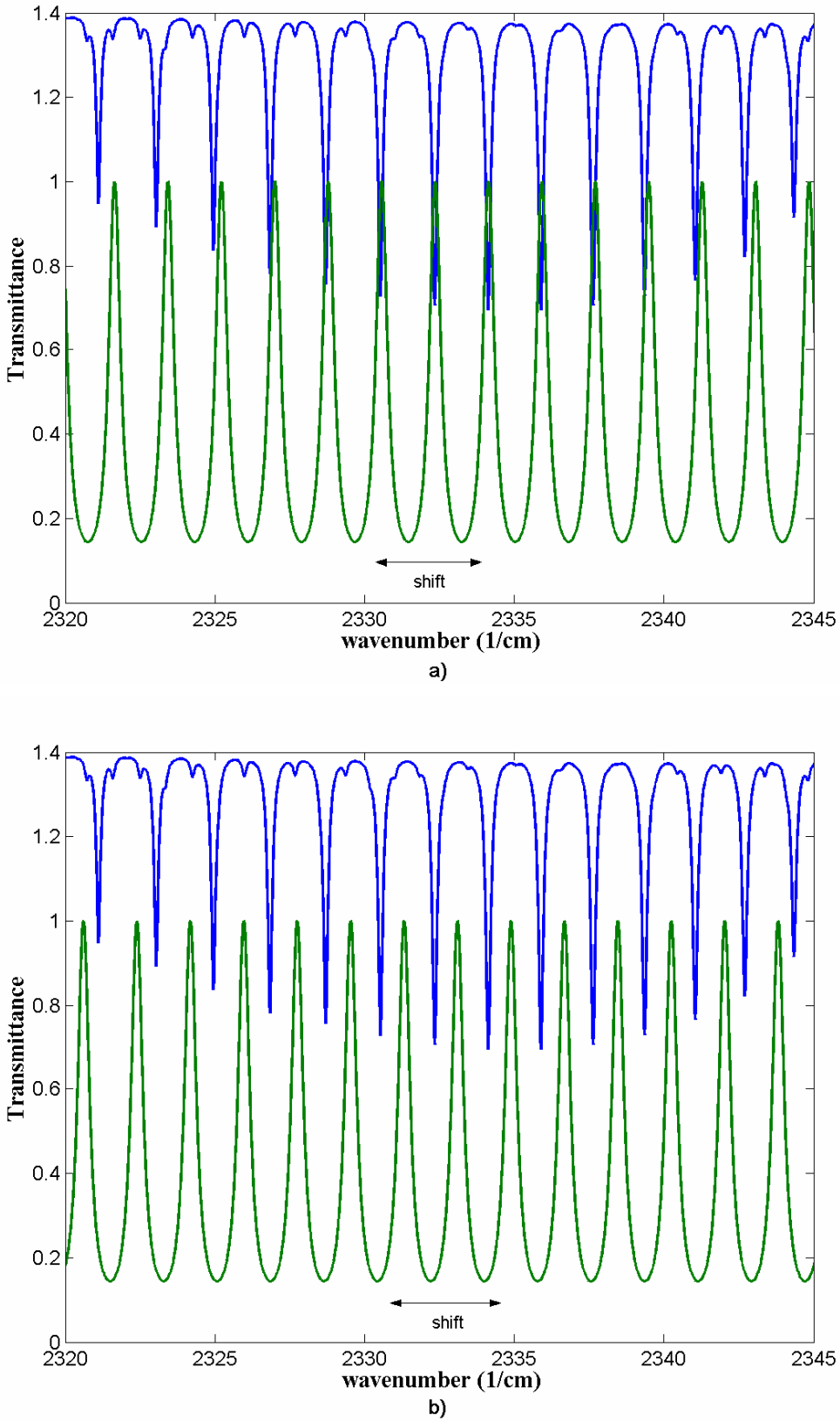

Figure 3.2- FPI's fringes and ro-vibrational lines due to CO_2. a) Absorption lines are matched to the FPI's fringes. b) FPI's fringes shifted along the wavenumber axis. The CO_2 spectrum is shifted up 0.4 units for clarity.

The transmission through the system it is given approximately by

$$I_D(\Delta d) = \int_0^{\infty} I_{FP}(\nu, d, \Delta d)\, T(\nu)\, Fil(\nu)\, S(\nu) \mathrm{d}\nu \tag{3.1}$$

where ν is the frequency expressed in wavenumbers (1/cm), $I_{FP}(\nu, d)$ describes the FPI fringe pattern, the filter transmission is given by $Fil(\nu)$ and the infrared source spectral profile is defined by $S(\nu)$. As the cavity length is scanned the FPI fringes are shifted along the wavenumbers axis; therefore, a value of $I_D(\Delta d)$ will be obtained for each change in the cavity length (Δd). For instance, the function $I_D(\Delta d)$ obtained by scanning the value of the FPI cavity length as $0 \leq \Delta d \leq \lambda_0/2$ it is shown in figure 3.3. In this example, to obtain $I_D(\Delta d)$, we considered the set of ro-vibrational CO_2 absorption lines and the set of FPI fringes presented in figure 3.2 and for simplicity $Fil(\nu)$ and $S(\nu)$ were assumed to be equal to unity. Finally, we would like to define the *amplitude modulation* AM as the difference between the maximum and the minimum values of $I_D(\Delta d)$ represented as $AM = I_D(\Delta d)_{\max} - I_D(\Delta d)_{\min}$.

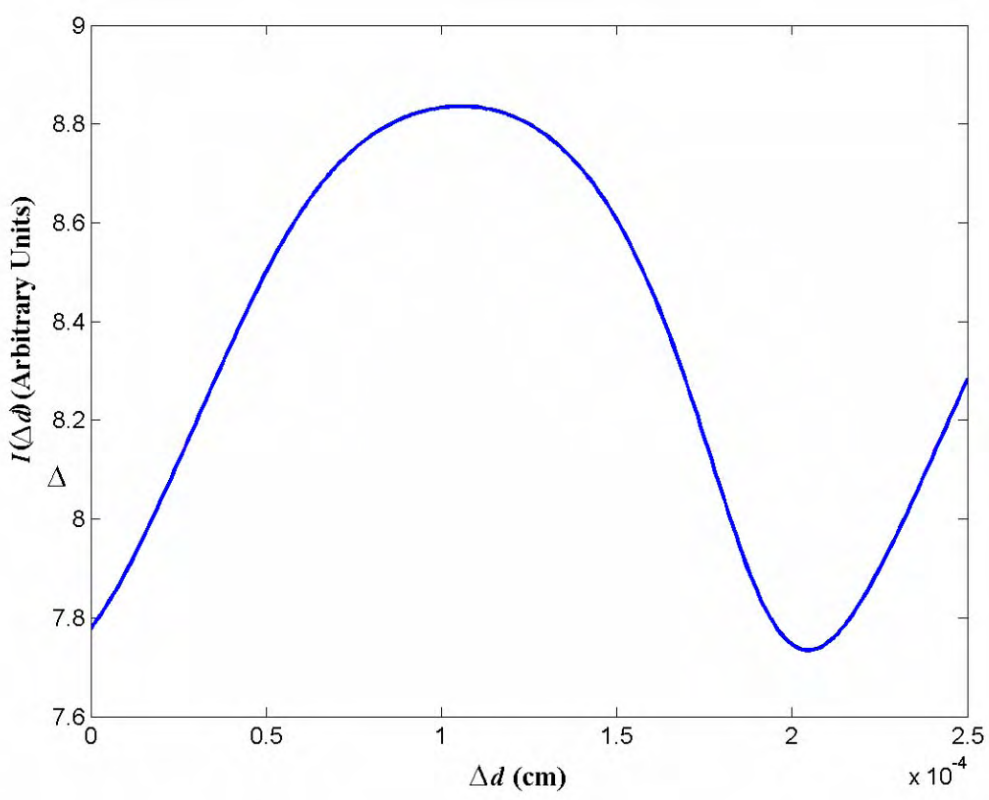

Figure 3.3- Simulated transmission through the system as a function of the cavity length Δd.

The transmission through the system $I_D(\Delta d)$ was described by equation (3.1) in a simplified form, but it is necessary to consider more parameters to have the complete system description. A more comprehensive system response is given by

$$I_D(R,n,d,\Delta d) = \int_0^\infty I_{FP}(\nu,R,n,d,\Delta d)\,T(\nu)\,Fil(\nu)\,S(\nu)\mathrm{d}\nu \qquad (3.2)$$

where d is the FPI cavity length, R is the reflectivity and n is the refractive index of the medium between the FPI's mirrors, and Δd represents cavity length scan. The amplitude of the sensor signal $I_D(R,n,d,\Delta d)$ is directly related to the gas concentration. Hence the amplitude modulation (AM) of the infrared signal reaching the sensor can be expressed as

$$AM = I_D(R,n,d,\Delta d)_{\max} - I_D(R,n,d,\Delta d)_{\min}. \qquad (3.3)$$

The sensor response $I_D(R,n,d,\Delta d)$ depends on several parameters which increases the complexity of the sensor design. Therefore, an optimisation procedure is needed to assure the best performance of the system. This procedure must search for the value of the parameters R, d, n, Δd, and $Fil(\nu)$ that guarantee the maximum amplitude modulation (AM), and the minimum background amplitude modulation possible. In equation (3.3) the amplitude modulation is defined and here $T(\nu) \neq 1$ when the target gas is present. A special case of the amplitude modulation is when the concentration of the target gas is zero in the gas pathlength, so $T(\nu) = 1$. This special case of AM it is called here the 'background amplitude modulation'. Ideally the background amplitude modulation should be zero, however most of the sensors produce small background amplitude modulation. This non-zero background modulation is mainly due to the shifting of the Fabry-Perot fringes which produce very small variations in the amount of transmitted light. Therefore it is important to guarantee that our sensor produces the minimal background amplitude modulation response.

The simplest optimisation procedure consists in evaluating equation (3.2) for all the possible value combinations of the parameters R, d, n, Δd, and $Fil(\nu)$. However, this procedure is time consuming, since it takes a long time to compute all the possible combinations of R (from 0 to 1), nd (from 0 to ∞), and Δd (from 0 to $\lambda_0/2$), since

each point involves integration over a rapidly varying function of frequency. Furthermore, the same procedure should be carried out for each filter shape $Fil(\nu)$. Moreover, this procedure does not give information about what *kind* of filter will produce the lowest background amplitude modulation. Hence after the optimization procedure it is carried out taking into account different filters the background amplitude modulation values are compared between themselves to determine which filter produces the lowest value background modulation. Therefore the direct numerical method is very simple to implement, nevertheless, it is a very slow procedure and gives little 'insight' into the sensor.

Here, to avoid direct numerical evaluation of equation (3.2) a new simple method based on the Fourier transform is presented in the next sections. This method permits evaluation of $I_D(R,n,d,\Delta d)$ in a more efficient form than the direct numerical method. Moreover, the optimum cavity length d can be determined easily from the Fourier transforms involved in the method. Furthermore it will be shown that the optimum R can be determined more efficiently (faster) with the convolution method avoiding the direct numerical evaluation of equation (3.2). Additionally the convolution method also gives guidance on choosing the best band pass filter to reduce the background amplitude modulation.

3.2. Definition of the Mathematical Model Functions.

The system response $I_D(R,n,d,\Delta d)$ described in equation (3.2) depends on four functions $I_{FP}(\nu,R,n,d,\Delta d)$, $T(\nu)$, $Fil(\nu)$ and $S(\nu)$. Here, $I_{FP}(\nu,R,n,d,\Delta d)$ describes the FPI transmission fringe pattern, whose fringes are symmetrical and equidistant [6] in frequency. This function is given by the Airy formula [7] which for normal incidence can be expressed by

$$I_{FP}(\nu,R,n,d,\Delta d)=\frac{1}{1+\dfrac{4R}{(1-R)^2}\sin^2\left(\dfrac{4\pi nd\nu}{2}\right)} \tag{3.4}$$

where R is the mirror reflectivity, nd is optical thickness of the FPI, and ν is the frequency in vacuum. Furthermore, another important parameter that needs to be

defined here is the separation between two consecutive FPI fringes, which is known as the Free Spectral Range (FSR), expressed in term of wavenumbers is given by [7]

$$\mathrm{FSR} = \frac{1}{2nd}. \tag{3.5}$$

Spectral shift of the FPI fringes is achievable by changing the optical thickness given by Δd. Hence, to shift one fringe over one FSR we need to vary the optical thickness by one half of the reference wavelength $(n(d - \Delta d) = nd - \lambda_0/2)$.

The transmission through the gas pathlength is given by $T(\nu)$ and it can be calculated using the Beer-Lambert Law given by

$$T(\nu) = \exp[-l\alpha(\nu)C] \tag{3.6}$$

where l is the gas pathlength (cm), C is the concentration of the target molecule (molecules/cm^3), and $\alpha(\nu)$ is the monochromatic absorption coefficient; generally expressed in units of 1/molecule-cm^{-2} [8]. For instance, the simulated monochromatic absorption spectrum profile for the CO_2 molecule in the region of the 4.3 μm is shown in figure 3.4. Finally, $Fil(\nu)$ describes the band pass filter performance, and the source profile is given by $S(\nu)$.

As was stated before, to induce modulation the FPI cavity length is scanned by $\lambda_0/2$ producing a shift of the FPI fringes along the wavenumber axis which changes the total transmission. However whilst the FPI fringes scan are shifted by the cavity length the filter response $Fil(\nu)$, the source profile $S(\nu)$ and the absorptions due to the molecule $T(\nu)$ are not affected. Consequently, the product of these three functions will remain constant regardless the cavity length scan; thus, it is possible to rewrite equation (3.2) as

$$I_D(R, n, d, \Delta d) = \int_0^\infty I_{FP}(\nu, R, n, d, \Delta d)\, G(\nu) \mathrm{d}\nu \tag{3.7}$$

where

$$G(\nu) = T(\nu)\, Fil(\nu)\, S(\nu). \tag{3.8}$$

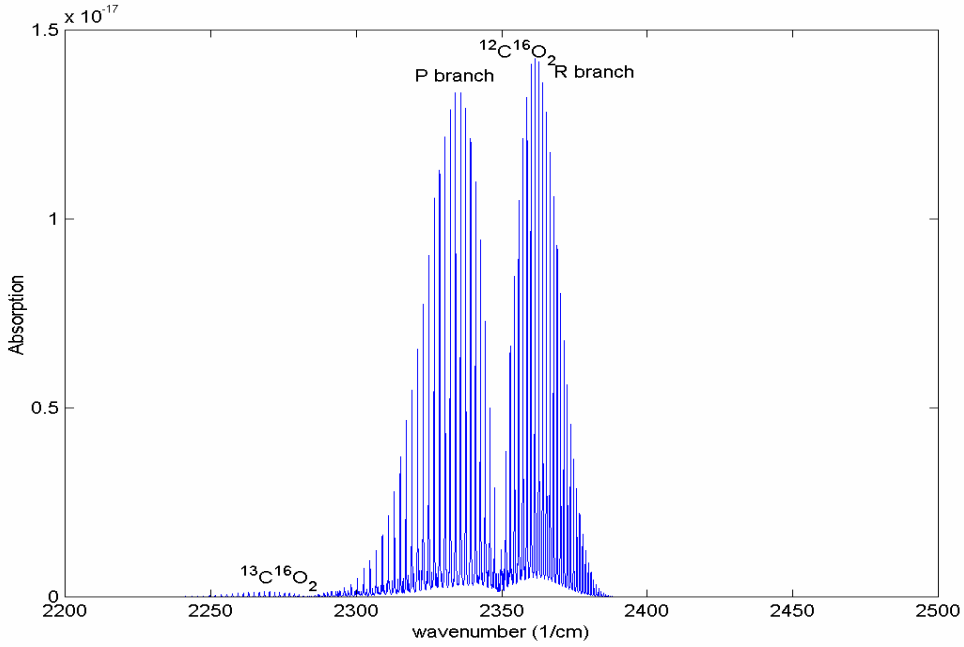

Figure 3.4- Simulated monochromatic absorption spectrum of CO_2. It model includes the spectra for the $^{12}C^{16}O_2$, $^{13}C^{16}O_2$ and $^{16}O^{12}C^{18}O$ isotopomers.

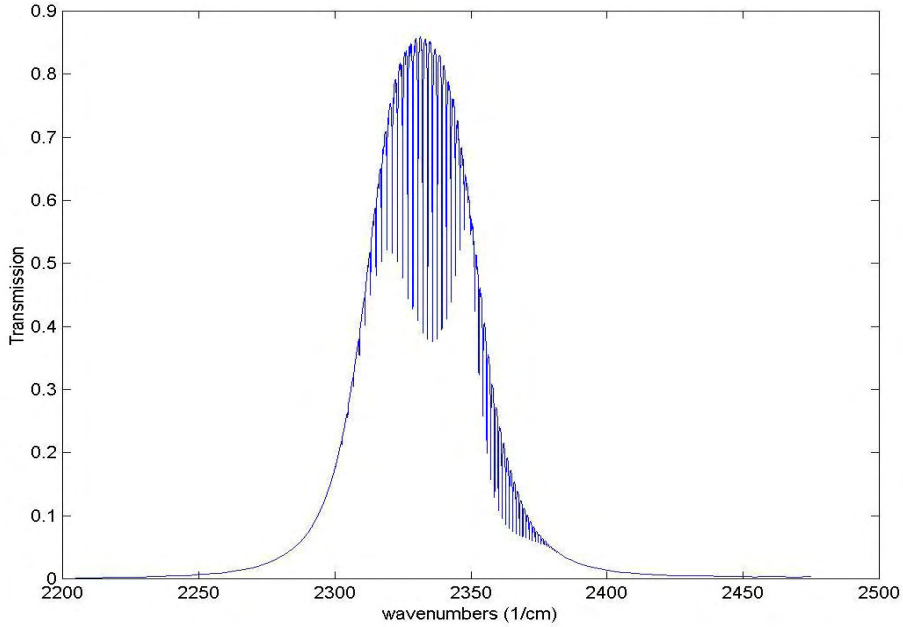

Figure 3.5- Transmission Profile $G(\nu)$.

An example of the transmission profile of $G(\nu)$ is shown in figure 3.5, this was generated using a CO_2 concentration of 500 ppm, a pathlength of 5 cm and $S(\nu) = 1$.

The overall shape of the function profile $G(\nu)$ is described by the filter band-pass shape whilst the absorption lines observed in the $G(\nu)$ profile are produced by the ro-vibrational absorption lines of CO_2. In this example, we use as $Fil(\nu)$ an experimental measurement taken with a Perkin Elmer 2000 spectrometer, the filter was kindly provided by Dr R Dennis of Edinburgh Sensors.

3.3. System Response described as a convolution.

A small shift in the FPI's fringes along the wavenumber axis $(\Delta\nu)$ is produced for each small change in the cavity length Δd (Fig. 1.1). It is important to recall that the cavity length scan Δd is given in centimetre units, while the fringes shift $(\Delta\nu)$ is expressed in wavenumbers units. Therefore, here it is useful to make a change of variable in (3.7):

$$I_D(R,n,d,\Delta\nu) = \int_0^\infty I_{FP}(\nu,R,n,d,\Delta\nu)\, G(\nu)\mathrm{d}\nu. \tag{3.9}$$

Now, considering that the width of the FPI's fringes and their symmetry do not vary when they are shifted over one FSR equation (3.9) can be rewritten as

$$I_D(R,n,d,\Delta\nu) = \int_0^\infty I_{FP}(\nu-\Delta\nu,R,n,d)\, G(\nu)\mathrm{d}\nu. \tag{3.10}$$

Hence, the system response described by equation (3.2) was reduced into equation (3.10) which has the form of

$$h(t) = \int_{-\infty}^{\infty} f(\tau - t)\, k(\tau)\mathrm{d}\tau, \tag{3.11}$$

which is the definition of the convolution and it can be easily solved by using the Fourier transform $(\mathbf{FT})$. It is important to recall that the Fourier transform of a convolution $(*)$ is given by

$$\mathbf{FT}\left\{f\left(t\right)*k\left(t\right)\right\}=H\left(\omega\right)=F\left(\omega\right)K\left(\omega\right);\tag{3.12}$$

Therefore to solve equation (3.10) it is necessary just to evaluate the Fourier transforms of two functions $I_{FP}\left(\nu,R,n,d,\Delta d=0\right)$ and $G\left(\nu\right)$ involved in (3.9), all this can be expressed as

$$\mathbf{FT}\left\{I_D\left(R,n,d,\Delta\nu\right)\right\}=I_D\left(R,n,d,\xi\right)=I_{FP}\left(\xi,R,n,d\right)G\left(\xi\right);\tag{3.13}$$

where

$$I_{FP}\left(R,n,d,\xi\right)=\mathbf{FT}\left\{I_{FP}\left(R,n,d,\nu\right)\right\},\tag{3.14}$$

and

$$G\left(\xi\right)=\mathbf{FT}\left\{G\left(\nu\right)\right\}.\tag{3.15}$$

Equation (3.13) describes the Fourier transform of the systems response. Now to obtain the system response in terms of the FPI's fringes shift $\Delta\nu$ it is necessary to apply the inverse Fourier transform $\left(\mathbf{IFT}\right)$ to the product given by equation (3.13).

Here it is important to mention that in our work the units in the Fourier domain are centimetres, so ξ is in terms of centimetres (cm). This can be very confusing since generally the signals are in the time domain (expressed in seconds) so when the Fourier transform is applied the Fourier domain it is in units of Hertz (1/s). However, ours is a special case since our signal is already in the frequency domain with wavenumbers units (cm^{-1}), so when we apply the Fourier transform the units that we get for a particular Fourier domain in centimetres (cm). Therefore in this chapter when we mention frequency represented by ξ it will be in units of centimetres.

After the inverse Fourier transform is applied to equation (3.13), $\mathbf{IFT}\left\{I_{FP}\left(R,n,d,\xi\right)G\left(\xi\right)\right\}$, the system response expressed it is expressed in terms of in terms of $\Delta\nu$ rather than in terms of the cavity length scan Δd (centimetres). However this can be easily done by extracting a segment from $\mathbf{IFT}\left\{I_{FP}\left(R,n,d,\xi\right)G\left(\xi\right)\right\}$. Here, a cavity length scan $\Delta d_{\max}=\lambda_0/2$ shifts the FPI fringes by one FSR along the wavenumber axis which it is given by

$$\Delta\nu_{\max} = \mathrm{FSR} = \frac{1}{2nd}; \tag{3.16}$$

Where the maximum cavity length scan it is defined by

$$\Delta d_{\max} = \frac{\lambda_0}{2}. \tag{3.17}$$

Therefore, from $I_D(R, n, d, \Delta\nu)$ we just need to extract the segment from 0 to 1 FSR is equivalent to have a cavity length scan from 0 to $\lambda_0/2$ cm.

3.3.1. The convolution method

Representation of the system response as a convolution is very useful, since this representation is more convenient than the initial form given by (3.2). Using this representation the system response can be easily calculated, since we only need to evaluate two Fourier and one inverse Fourier transform. The convolution method as used to evaluate the amplitude modulation consists in five steps

1. Evaluate the two Fourier transforms $\mathbf{FT}\{I_{FP}(R, n, d, \nu)\}$ and $\mathbf{FT}\{G(\nu)\}$.
2. Multiply these Fourier transforms functions to obtain $I_D(R, n, d, \xi) = I_{FP}(R, n, d, \xi)G(\xi)$.
3. To get the system response as a function of the wavenumber shift apply the inverse Fourier transform to the previous product, $I_D(R, n, d, \Delta\nu) = \mathbf{IFT}\{I_{FP}(R, n, d, \xi)G(\xi)\}$
4. From $I_D(R, n, d, \Delta\nu)$ extract the segment corresponding to $0 \le \Delta\nu \le \mathrm{FSR}$ which is equivalent to a cavity length scan $0 \le \Delta d \le \lambda_0/2$. The system response is now a function of the cavity length scan $I_D(R, n, d, \Delta d)$.
5. Finally to get *AM* evaluate the difference between the maximum and the minimum of the system response as $AM = I_D(R, n, d, \Delta d)_{\max} - I_D(R, n, d, \Delta d)_{\min}$.

The main advantages of the convolution method are that it is much faster than the numerical evaluation of (3.2), and gives better insight into the system design.

For instance, let us evaluate the amplitude modulation as a function of the concentration for a CO_2 gas sensor using the next parameters:

- Our target for sensing the CO_2 absorption bands in the 4.3 μm region.
- A fixed gas pathlength $l = 10$ cm;
- a flat source profile $S(\nu) = 1$;
- a band pass filter which is described by

$$Fil(\nu) = \begin{cases} 1 & 2350 \leq \nu \leq 2380 \\ 0 & \text{otherwise} \end{cases}, \tag{3.18}$$

  which it is shown in figure 3.6.
- The FPI has a fixed $R = 0.30$, and the optical thickness $nd = 0.28$ cm.
- The gas concentration is varied from 0 to 500 ppm.

Firstly, in order to apply the convolution method we evaluate the transmission profile $G(\nu) = T(\nu)\, Fil(\nu)$. After that we evaluate the Fourier transforms of $G(\nu)$ and of the FPI fringes $I_{FP}(R, n, d, \nu)$ and we continue applying all the steps of the convolution method listed previously. The amplitude modulation for this sensor obtained by both the convolution and the direct calculation methods are presented in figure 3.6. Both results are practically the same however the convolution method is much faster than the direct numerical calculation of equation (3.2).

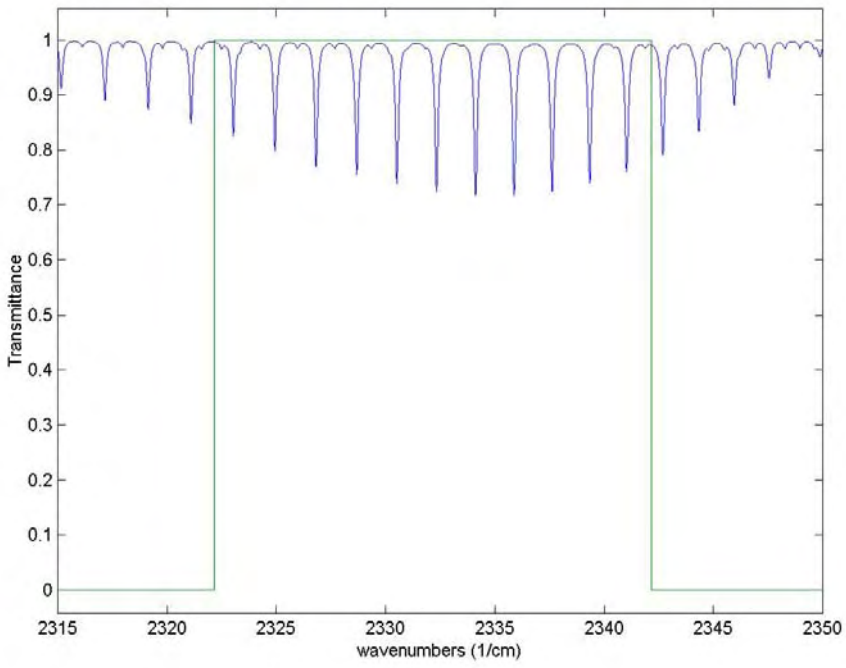

Figure 3.6- Filter response and some ro-vibrational absorption lines of CO_2

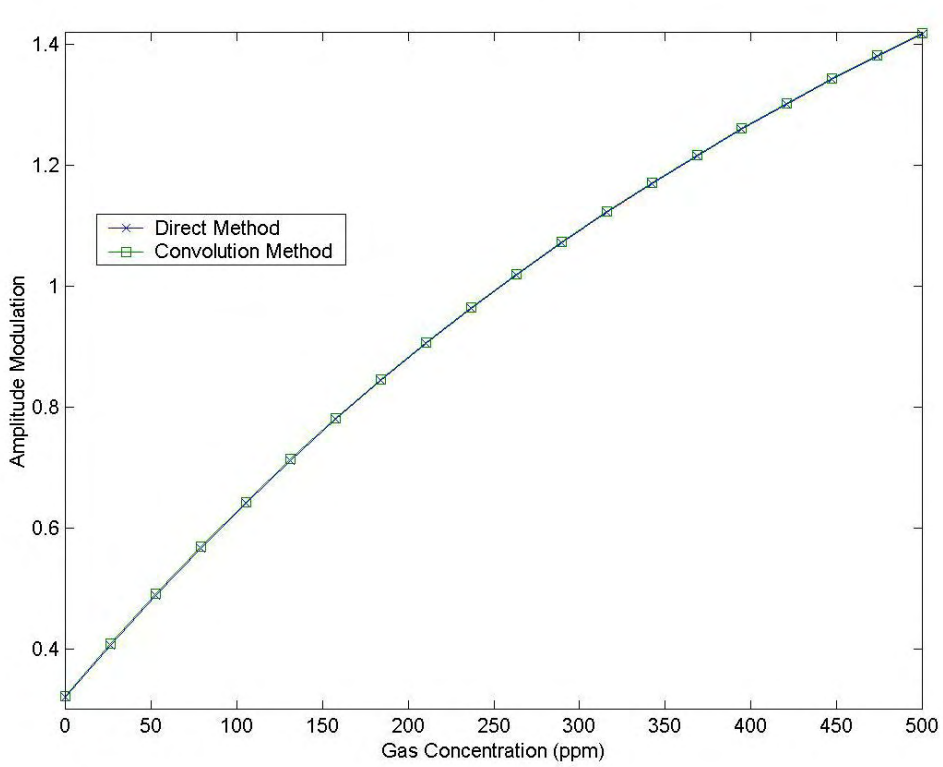

Figure 3.7- Amplitude Modulation as a function of the gas concentration (Amplitude Modulation in Arbitrary Units).

The convolution method is faster since it requires less basic computational operations. We evaluated an estimated number of operations required to calculate the sensor response by using both methods. For the direct numerical method, the first step consists in compute the product $I_{FP}(\nu)\,T(\nu)\,Fil(\nu)\,S(\nu)$; here if each function it is represented by 1d array with N elements it means that we require $4N$ multiplication operations. In the second step we need to evaluate the integration of the resulting array which contains the product of the four functions. Here if we calculate the integration using the trapezoidal rule with equidistant intervals we will require at least $2N$ sums and 1 product. Here the overall number of operations (sums and multiplications) to compute one point of the sensor response is $6N+1$. Furthermore this procedure must be computed for each cavity length scan Δd step; here we will use M to represent the number of steps of Δd. Therefore the total number of operations required to evaluate the sensor response as a function of the cavity length scan using the direct numerical method is $O_{\mathrm{DNM}} = M\,(6N+1)$.

Now for the convolution method we will require to compute the function $G(\nu) = T(\nu)\, Fil(\nu)\, S(\nu)$. Here if each one of the functions it is represented by 1d array with N elements we will require $3N$ multiplication operations. After we need to evaluate the Fourier transform of the functions $I_{FP}(\nu)$ and $G(\nu)$; by using the fft algorithm the number of basic operations (sums and multiplications) computed to evaluate the Fourier transform of a 1d array is $2N\log_2 N$ [9]. Here as there are two transform we require $4N\log_2 N$ operations. Now we require to compute the product $I_{FP}(\xi)G(\xi)$, this means that N multiplications must be evaluated. Finally we require to evaluate the inverse Fourier transform of the product $I_{FP}(\xi)G(\xi)$, which basically requires $2N\log_2 N$ basic operations. Therefore the overall number of computational operations (sums and multiplications) required to evaluate the sensor response using the convolution method is $O_{\mathrm{C}} = (4N + 6N\log_2 N)$. Hence to evaluate efficiency of the convolution method we evaluate the number of additional operations the must be evaluated when the Direct Numerical Method (DNM) $O_F = (O_{\mathrm{C}} - O_{\mathrm{DNM}}) \times 100\%/O_{\mathrm{DNM}}$. In Table 3.1 we present the estimated efficiency for some arrays of N points. To get a sufficiently accurate sensor response we usually used in or simulations arrays of $N = 2^{15}$ or 2^{16} points, while the cavity length scan was performed using $M = 20$ or 24. In this work we did not perform a detailed analysis of the computational efficiency of the convolution method and we just evaluate and estimation of the number of operations required for each method. This is because we are not really interested in this issue, for us the relevance of the convolution method is that it provides very important information regarding to the sensor design. The computational efficiency can be seen as an extra advantage.

Table 3.1- Efficiency of the Convolution method over the Direct Numerical Method. Here we are considering the overall number of basic operations (sums and multiplications)

N	$O_F(\%)$			
	M			
	18	**20**	**22**	**24**
2^{10}	22.72	36.36	50.00	63.63
2^{15}	14.89	27.66	40.42	53.19
2^{16}	8.00	20.00	32.00	44.00

3.4. Fourier transform characterisation of the system functions.

In this section it will be shown that using the characteristics of the Fourier transforms of the system functions it is possible to determine the optimal FPI cavity length. Moreover the convolution method permits us to determine the optimum reflectivity much more quickly. Hence, the sensor is going to be optimized for a band pass filter shape, source and for the ro-vibrational absorption lines of the target gas. Therefore in this section the Fourier transform characteristics of the $G(\nu)$ and $I_{FP}(R,n,d,\nu-\Delta\nu)$ functions are reviewed.

3.4.1. Fourier characterisation of the FPI fringes

For simplicity we will start by analyzing the Fourier transform of the Fabry-Perot transmission fringes given by the Airy Formula (3.13). This equation can be expanded as a cosine series [10] which is quite convenient since the Fourier transform of this series can be easily evaluated. The Airy formula, for normal incidence, expanded as a cosine series is given by [10]

$$I_{FP}(\nu,R,n,d,\theta)=\frac{(1-R)}{(1+R)}\left\{1+2\sum_{m}^{\infty}R^{m}\cos\left(m4\pi nd\nu\cos\left(\theta\right)\right)\right\}; \qquad (3.19)$$

where θ is the angle of incidence and therefore for a collimated beam at normal incidence $\cos\theta=1$. At this point is possible to observe that the Airy function is given by a sum of cosine functions of 'frequency' $\xi=m2nd$. These 'frequencies' are due to the period of the fringes which is defined by the free spectral range, $\mathrm{FSR}=1/(2nd)$, which is the separation between two consecutive fringes peaks or valleys. Thus, the first harmonic (fundamental) of the Airy function has a 'frequency' of $2nd$, the second harmonic has a 'frequency' of $4nd$, the third harmonic of $6nd$, and so on. The amplitudes of these cosine functions are given by

$$A_m=\frac{(1-R)}{(1+R)}2R^{m} \quad m=1,2,..\infty \qquad (3.20)$$

Now the Fourier transform of the Airy function, defined by equation (3.19), can be expressed as

$$\begin{aligned}\mathbf{FT}\left\{I_{FP}\left(R,n,d,\nu\right)\right\} &= \mathbf{FT}\left\{\frac{1-R}{1+R}\right\} + A_1\mathbf{FT}\left\{\cos\left(4\pi nd\nu\right)\right\} + A_2\mathbf{FT}\left\{\cos\left(8\pi nd\nu\right)\right\} \\ &+ A_3\mathbf{FT}\left\{\cos\left(12\pi nd\nu\right)\right\} + \cdots + A_m\mathbf{FT}\left\{\cos\left(4m\pi nd\nu\right)\right\} \\ &= \mathbf{FT}\left\{\frac{1-R}{1+R}\right\} + \sum_{j=1}^{m} A_j\mathbf{FT}\left\{\cos\left(4j\pi nd\nu\right)\right\}\end{aligned} \tag{3.21}$$

This expression simplifies the problem since now we only need to calculate the Fourier transform of the cosine functions, and after that sum their respective transforms. Here it is useful to recall that the Fourier transform of a cosine function is given by a pair of impulses which can be defined by

$$\left|\mathbf{FT}\left\{A\cos\left(2\pi\omega_0 t\right)\right\}\right| = \begin{cases}\frac{A}{2} & \left|\omega\right| = \omega_0 \\ 0 & \left|\omega\right| \neq \omega_0\end{cases}. \tag{3.22}$$

Therefore, substituting (3.22) into (3.21) we have that the Fourier transform of the FPI fringes it is given by

$$\begin{aligned}I_{FP}\left(R,n,d,\xi\right) &= \frac{1-R}{1+R}\delta\left(0\right) + \frac{A_1}{2}\delta\left(\xi-\xi_1\right) + \frac{A_1}{2}\delta\left(\xi+\xi_1\right) \\ &+ \frac{A_2}{2}\delta\left(\xi-2\xi_1\right) + \frac{A_2}{2}\delta\left(\xi+2\xi_1\right) + \frac{A_3}{2}\delta\left(\xi-3\xi_1\right) \\ &+ \frac{A_3}{2}\delta\left(\xi+3\xi_1\right) + \cdots + \frac{A_m}{2}\delta\left(\xi-m\xi_1\right) + \frac{A_m}{2}\delta\left(\xi+m\xi_1\right) \\ &= \frac{1-R}{1+R}\delta\left(0\right) + \sum_{j=1}^{m} A_j\left[\delta\left(\xi-j\xi_1\right) + \delta\left(\xi+j\xi_1\right)\right]\end{aligned} \tag{3.23}$$

where $\xi_1 = 2nd$ cm. Equation (3.23) shows that the Fourier transform of the FPI transmission fringes (Airy function) consists of a set of impulses at 'frequencies' $m2nd$ and magnitudes $A_m/2$.

For instance, in figure 3.8 the magnitude of the Fourier transform of a set of FPI transmission fringes is presented, here $R = 0.3$ and $nd = 0.28$ cm were selected. In this figure it is clear that the impulse related with the first harmonic 'frequency' is centred at $\xi = 2nd = 0.56$ cm, the impulse due to the second harmonic is found at

$\xi = 4nd = 1.12$ cm, the third at $\xi = 6nd = 1.68$ cm and so on. It is important to point out that the Fourier transform magnitude of the impulses just depends on the reflectivity value as defined by equation (3.19). For instance the magnitude of the first five impulses of $I_{FP}(R, n, d, \xi)$ as a function of the reflectivity are shown in figure 3.9. It is important to stress that the cavity length does not affect the magnitude of the impulse, it just determines the impulse position in the Fourier domain which it is given by $\xi_m = m2nd$.

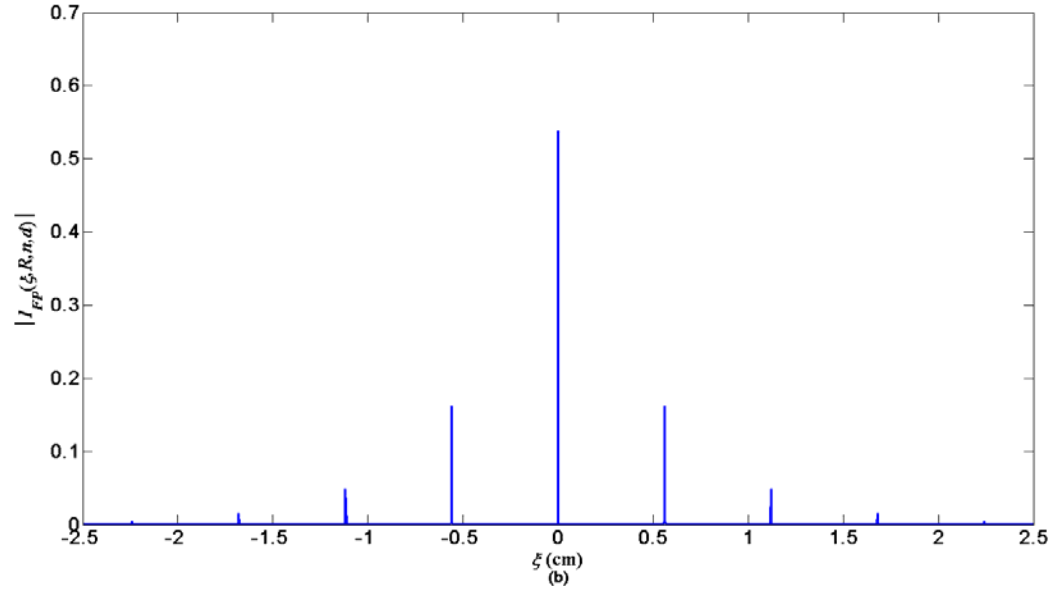

Figure 3.8- Fourier Transform of the Airy Function $I_{FP}\,(R, n, d, \xi)$.

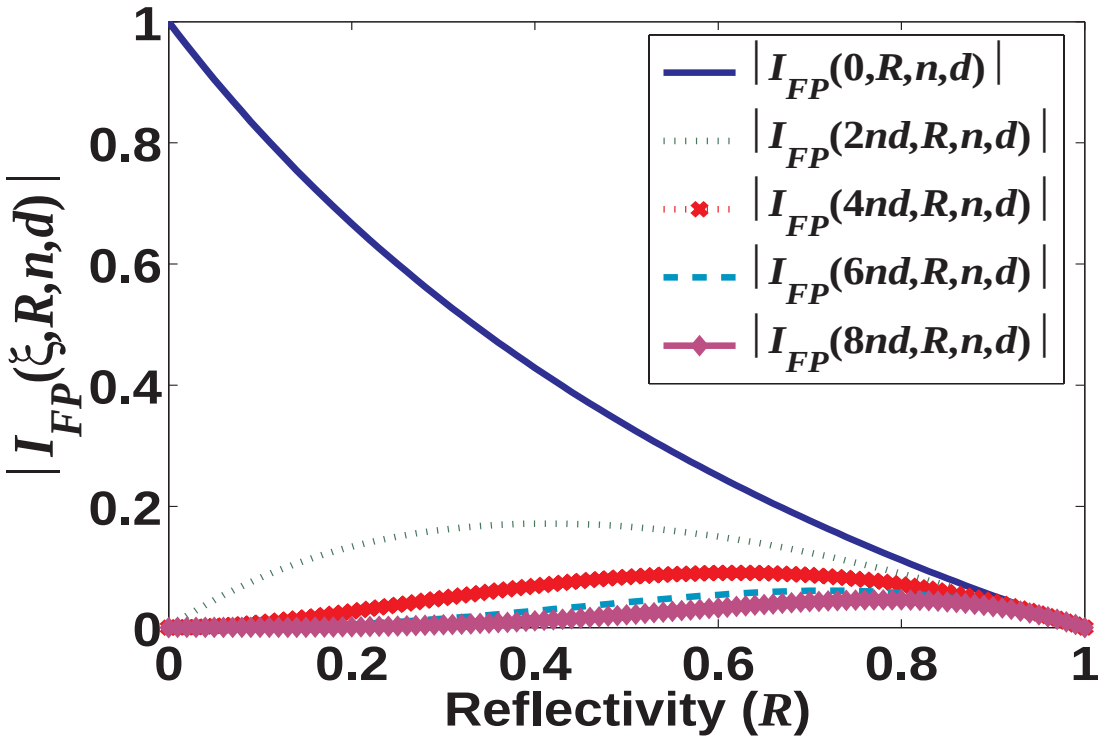

Figure 3.9- Magnitude for the impulses of $I_{FP}\,(R, n, d, \xi)$ as a function of the reflectivity.

3.4.2. Fourier characterisation of the system response.

The Fourier transform of the system response $I_D(R,n,d,\xi)$ can be expressed as

$$\begin{aligned} I_D(R,n,d,\xi) &= \frac{1-R}{1+R}G(0)\,\delta(0) + \frac{A_1 G(\xi_1)}{2}\delta(\xi-\xi_1) + \frac{A_1 G(\xi_1)}{2}\delta(\xi+\xi_1) \\ &+ \frac{A_2 G(2\xi_1)}{2}\delta(\xi-2\xi_1) + \frac{A_2 G(2\xi_1)}{2}\delta(\xi+2\xi_1) \\ &+ \frac{A_3 G(3\xi_1)}{2}\delta(\xi-3\xi_1) + \frac{A_3 G(3\xi_1)}{2}\delta(\xi+3\xi_1) \\ &+ \cdots + \frac{A_m G(m\xi_1)}{2}\delta(\xi-m\xi_1) + \frac{A_m G(m\xi_1)}{2}\delta(\xi+m\xi_1) \\ &= \frac{1-R}{1+R}G(0)\,\delta(0) + \sum_{j=1}^{m}\frac{A_j}{2}G(j\xi_1)\left[\delta(\xi-j\xi_1)+\delta(\xi+j\xi_1)\right] \end{aligned} \tag{3.24}$$

Equation (3.24) shows that the Fourier transform of the system response is given by a sum of impulses. The position of these impulses depends only on the cavity length of the FPI which are described by $\delta(\xi \pm m\xi_1)$. Moreover their amplitude are related to the FPI reflectivity and the magnitude of the of $G(m\xi_1)$. Finally, to obtain the system response in terms of the wavenumber shift it is just necessary to evaluate the inverse Fourier transform of equation (3.24). The inverse Fourier of equation (3.24) leads to a sum of sinusoidal functions of frequencies $m\xi_1 = m2nd$ whose amplitudes are given by $A_m G(m\xi_1)/2$.

3.4.3. Fourier characterisation of the $G(\nu)$ function.

The $G(\nu)$ function was defined in equation (3.8), and it is given as the product of the source $S(\nu)$, the filter transmission function $Fil(\nu)$ and the transmission through the gas pathlength $T(\nu)$. Therefore the Fourier transform of the $G(\nu)$ profile will contain information related to the separation of the absorption ro-vibrational lines of the target molecule and also it will contain sidelobes which are related to the filter function and source profile. For instance the $|G(\xi)|$ function corresponding to the CO_2 sensor system presented previously (see Figure 3.5) is shown in figure 3.10. In this figure we present different $|G(\xi)|$ functions corresponding to different CO_2 gas concentrations. The sidelobes very close to the DC component ($|\xi| < 0.05\text{cm}$) are more related to the filter's shape rather than to the target molecule, since their magnitudes do not change

appreciably as the concentration of the target molecule increases (Figure 3.10). In contrast, the sidelobes at frequencies $|\xi| \approx 0.56\text{cm}$ and $|\xi| \approx 1.12\text{cm}$ cm are strongly related to the target molecule, since clearly their magnitude increases with the molecule concentration. Therefore, these sidelobes give information about where the impulses due to the Fourier transform of the FPI fringes must be placed.

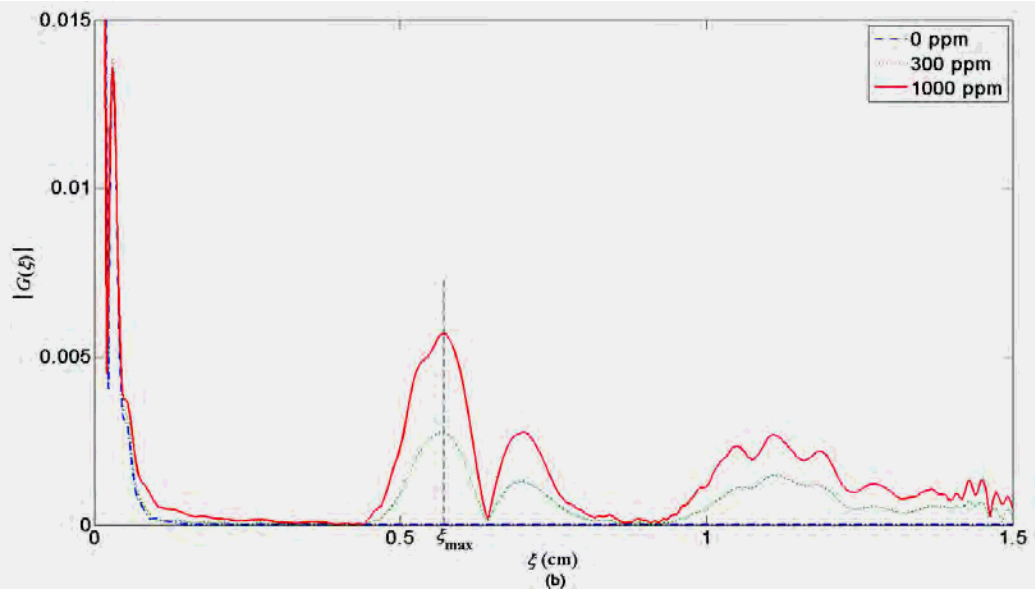

Figure 3.10- Typical $|G(\xi)$ for a CO_2 sensor.

The strong sidelobes in $|G(\xi)|$ that increase with the gas concentration are produced by the ro-vibrational absorption lines of the target molecule which are related to the monochromatic absorption coefficient $\alpha(\nu)$ (Figure 3.4). In this figure $\alpha(\nu)$ shows the ro-vibrational absorptions of CO_2 at 4.3 μm and here the two branches, P and R, due to the fundamental absorption band of CO_2 at 4.3 μm are clearly seen. Here it is important to recall that the average separation of the ro-vibrational lines belonging to the P branch is different to the separation of the R branch lines; this is because the rotational constants for the upper and lower ro-vibrational energy levels are different and also because the selection rules for the P and the R branch are different $J' = J" - 1$ and $J' = J" + 1$ respectively, for further details see section 2.1.1.2. The absorption spectrum presented in figure 3.4 also includes several hotbands for the $^{12}C^{16}O_2$, $^{13}C^{16}O_2$, and other less abundant isotopomers.

A very good exercise is to apply the Fourier transform to the monochromatic absorption spectrum of CO_2, that is $\mathbf{FT}\{\alpha(\nu)\} \Longrightarrow \alpha(\xi)$. The Fourier spectrum

$|\alpha(\xi)|$ is very interesting (Figure 3.11) since it presents two strong sidelobes at very similar 'frequencies', one $\xi \approx 0.56$cm and the other one at $\xi \approx 0.74$cm. One of these sidelobes is related to the P branch and the other to the R branch. This is explained since the separation of the R branch ro-vibrational lines is different from the lines of the P branch changing the sidelobe positions related to each branch. The sidelobes produced by the R branch are placed at higher 'frequency' than the produced by the P branch.

Now, imagine that we place a 'square' filter that passes only the ro-vibrational lines of the R branch 'side' ($2348.7 - 2400\,\text{cm}^{-1}$) after applying the Fourier transform we obtain the $|\alpha(\xi)|$ shown in the upper-right inset of figure 3.11. Here just one strong sidelobe at $\xi \approx 0.74$cm is present, whilst the other at $\xi \approx 0.56$cm is attenuated, practically eliminated. In contrast if we select a square filter that lets pass just the ro-vibrational lines of the P branch side ($2275 - 2348.7\,\text{cm}^{-1}$) and we apply the Fourier transform to these lines we obtain the $|\alpha(\xi)|$ shown in the upper-left inset of figure 3.11. Here, the strongest sidelobe occurs at $\xi \approx 0.56$ cm, while the sidelobe at $\xi \approx 0.74$ cm disappears. Therefore, it is possible to say that the position of the strongest sidelobe $|\alpha(\xi)|$ depends of the ro-vibrational lines passed by the filter. This is also true for the function $|G(\xi)|$ since this depends directly on $|\alpha(\xi)|$.

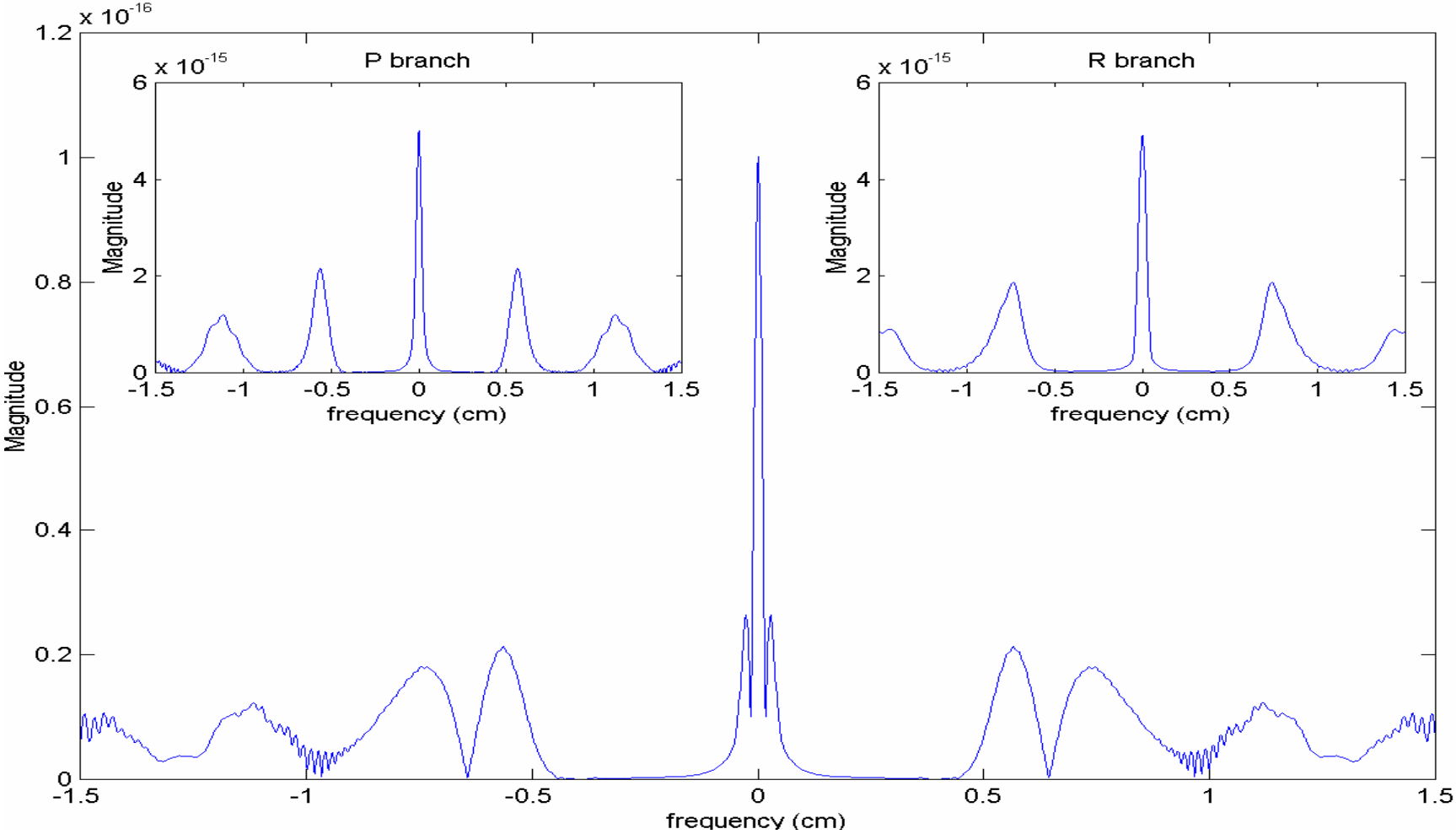

Figure 3.11- Fourier transform of the monochromatic absorption coefficient $(|\alpha(\xi)|)$ for the CO_2 at 4.3 μm. The inset figures show the Fourier Transform $(|\alpha(\xi)|)$ considering just the P and the R branches.

3.4.3.1. Optimal value of the cavity length

Previously we showed that the Fourier transform of the system response can be expressed as a sum of impulses, see equation (3.24). The position of these impulses is related directly to the FPI's cavity length ($\xi_1 = 2nd$) and the magnitude of these impulses depends on the reflectivity of the FPI's mirrors. From equation (3.24) can be inferred that in order to have the maximum amplitude for the first harmonic of the system response we need to place the first Fourier impulse due to the Fourier fringes $I_{FP}(R, n, d, \xi)$ where the peak of the strongest sidelobe of $G(\xi)$ occurs, which is labelled as $\xi_{\max} = \xi_1$ (Figure 3.10). Therefore, if we know $\xi_{\max}$ we can determine the optimal cavity length value of the FPI as $d = \xi_{\max}/2n$. The main advantage of this approach is that the optimal FPI cavity length can be calculated by direct observation of the Fourier transform magnitude of $G(\xi)$.

Here, let us analyse one example to corroborate the accuracy of our approach to calculate the optimal FPI cavity. For simplicity we will work with the CO_2 sensor used in previous sections, where the $G(\nu)$ profile is shown in figure 3.5, and the magnitude of its Fourier transform $|G(\xi)|$ is presented in figure 3.10. In this figure it can be observed that the peak of the strongest sidelobe occurs at $\xi_{\max} = 0.56$cm, therefore the optimal FPI cavity length for this sensor is $d = 0.28$ cm if *n* is equal to 1. Now, in order to validate this value we evaluate the amplitude modulation as a function of the cavity length by direct numerical calculation of equation (3.2), and the result is presented figure 3.12. The maximum amplitude modulation occurs at $d = 0.28$ cm which is the same value predicted by our approach.

Additionally the amplitude modulation as a function of the cavity length but evaluated by using the convolution method it is presented in figure 3.13. The results obtained by the convolution method are the same as those obtained by the direct numerical calculation of equation (3.2), supporting the convolution method approach.

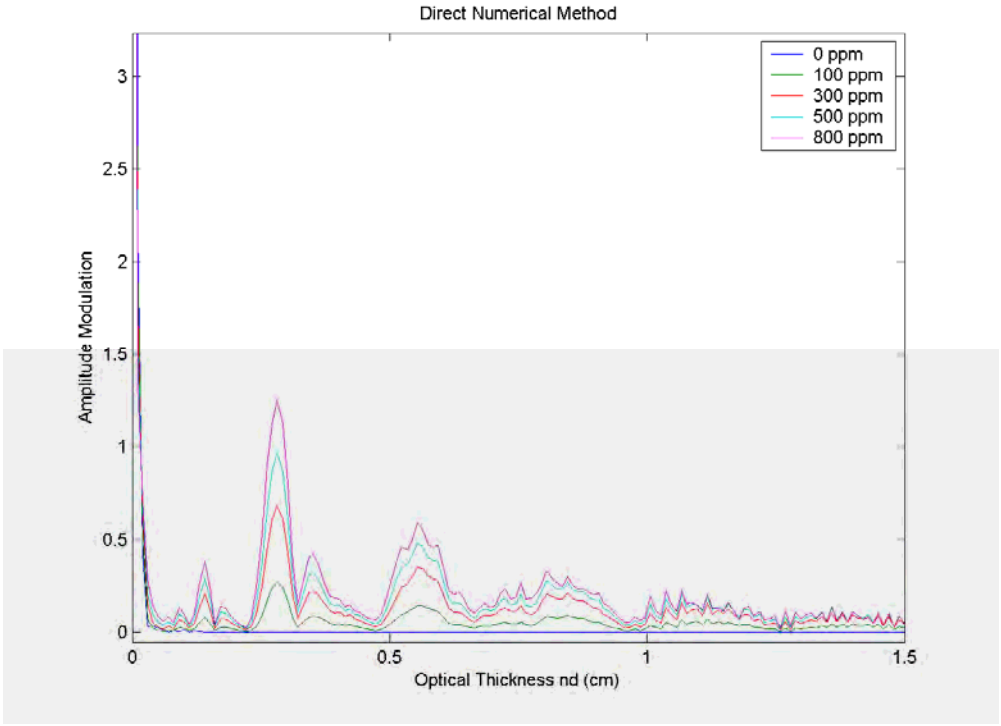

Figure 3.12- Amplitude Modulation as a function of the optical thickness (nd); evaluated by direct calculation of equation (3.2). The reflectivity was fixed as $R = 0.30$. (Amplitude Modulation in arbitrary units)

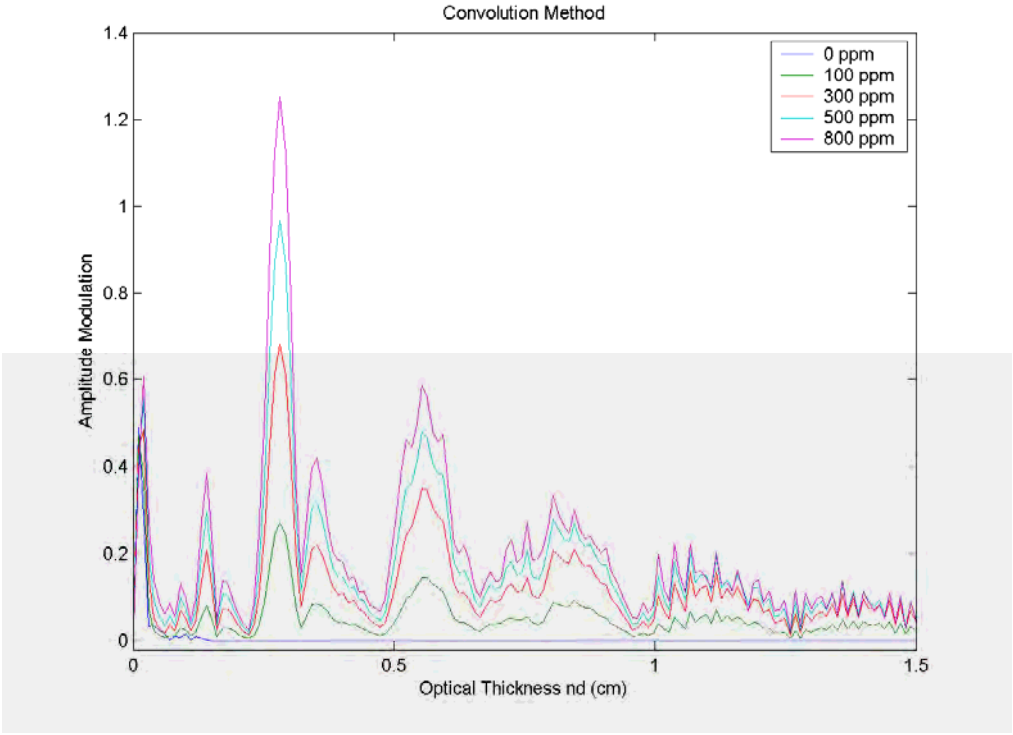

Figure 3.13- Amplitude Modulation as a function of the optical thickness (nd); evaluated using the convolution method. The reflectivity was fixed as $R = 0.30$. (Amplitude Modulation in arbitrary units)

From the last example it can be observed that both methods, the direct calculation and the convolution method, produce practically the same results except for very small values of the cavity length ($d \approx 0$). This can be explained as follows, if we have $d = 0$ therefore the transmission of the FPI is flat and equal to one, $I_{FP}(\nu, R, n, d, \Delta d = 0) = 1$, and when the cavity length is scanned to a quarter of the wavelength ($d + \Delta d = \lambda_0/4$ cm) the FPI transmission drops to a minimum given by $I_{FP}(\nu, R, n, d - \lambda/4) = [(1 - R)/(1 + R)]^2$, as shown in figure 3.14. Hence when $d \approx 0$ the FPI transmission profile is quite flat and does not have fringes over a wide range of wavenumbers. Consequently, one of the necessary convolution conditions is broken, since the function which is shifted along the wavenumbers axis changes its shape and symmetry. Therefore, the convolution method fails to predict the response of the system when the optical thickness of the FPI is very close to zero. Despite this failure, the convolution method is useful since we are interested in modulating the ro-vibrational absorption lines of the molecule with very well defined FPI fringes and therefore the cavity length values are considerably larger than zero. A FPI with $nd \approx 0$ can be used as spectral chopper since here we can have an on and off states, this type of modulator can be employed in other applications such as to sense molecules with no well defined ro-vibrational lines.

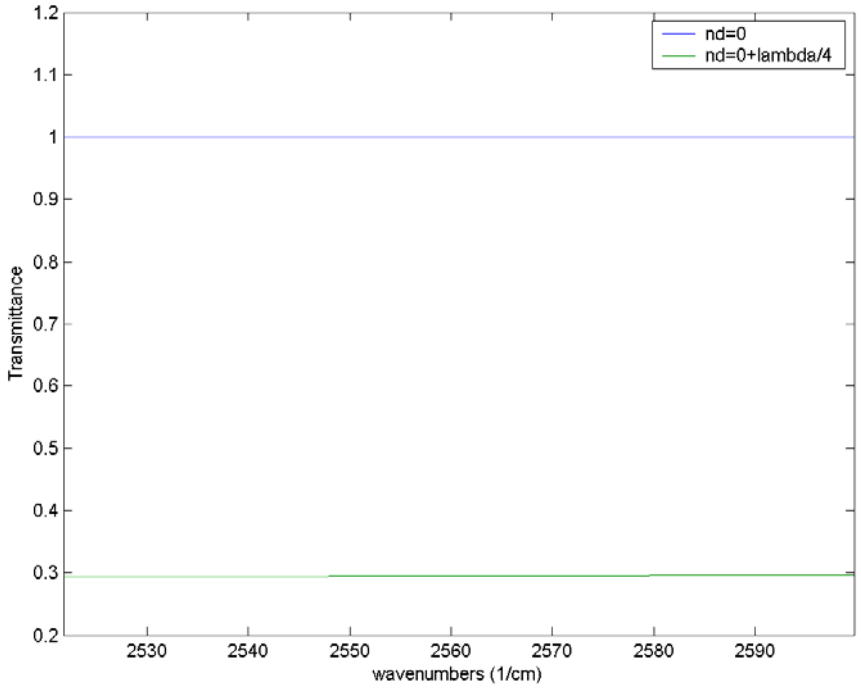

Figure 3.14- FPI Transmission for $d = 0$ and for $d = 0 + \lambda_0/4$.

3.4.4. Optimal Reflectivity value.

The optimal reflectivity value R can easily be evaluated by using the convolution method presented in section 3.3.1. In previous sections it was shown how the optimum cavity length can be determined using the Fourier transform characteristics of $|G(\xi)|$. Here the amplitude modulation it is evaluated as a function of the reflectivity in order to determined at which R the maximum amplitude occurs.

In the convolution method two Fourier transforms, $I_{FP}(R, n, d, \xi)$ and $G(\xi)$, must be evaluated and thence multiplied. Afterwards the inverse Fourier transform of their product is calculated. Hence to evaluate the amplitude modulation as a function of the reflectivity, with $G(\nu)$ fixed, $I_{FP}(R, n, d, \xi)$ should be evaluated for each value of R $(0 \leq R \leq 1)$. As it is necessary to evaluate $G(\xi)$ just once the processing time is reduced significantly. Therefore, using this procedure the amplitude modulation as a function of R is obtained very quickly and the optimal value of R can be easily found.

For instance let us retake the example of the CO_2 gas sensor described previously. For this sensor its $G(\nu)$ profile was shown in figure 3.5, and its magnitude $|G(\xi)|$ is presented in figure 3.10. The optimal FPI cavity length for this sensor was obtained in section 3.4.3.1 and it is equal to $d = 0.28$cm. Now if we keep fixed the $G(\nu)$ function and the FPI cavity length, while R is varied from 0 to 1 the amplitude modulation as a function of R is obtained as shown in figure 3.15. In this figure we also present the result produced by direct numerical calculation of equation (3.2). Here it is clear that both methods produce the same results and optimal $R = 0.45$, however the convolution method the result are computed much faster.

It is very common to use a phase sensitive detector (PSD or lock-in amplifier) to recover the signal produced by the optical gas sensors. Depending of the design it can be done that the PSD recovers and amplifies only the first harmonic of the signal, while the higher harmonics are attenuated by using a low pass filter [11]. This is probably the most typical PSD amplifier design. However a PSD that recovers another harmonic can be also designed. In our case we will consider that the PSD is recovering and amplifying the first harmonic of the sensor signal response. Therefore we would like to have the largest amplitude modulation in the first harmonic of the system response as

possible, and this depends on the FPI reflectivity. Therefore, it is possible to determine the optimal value of R for the case when the signal will be recovered with a PSD.

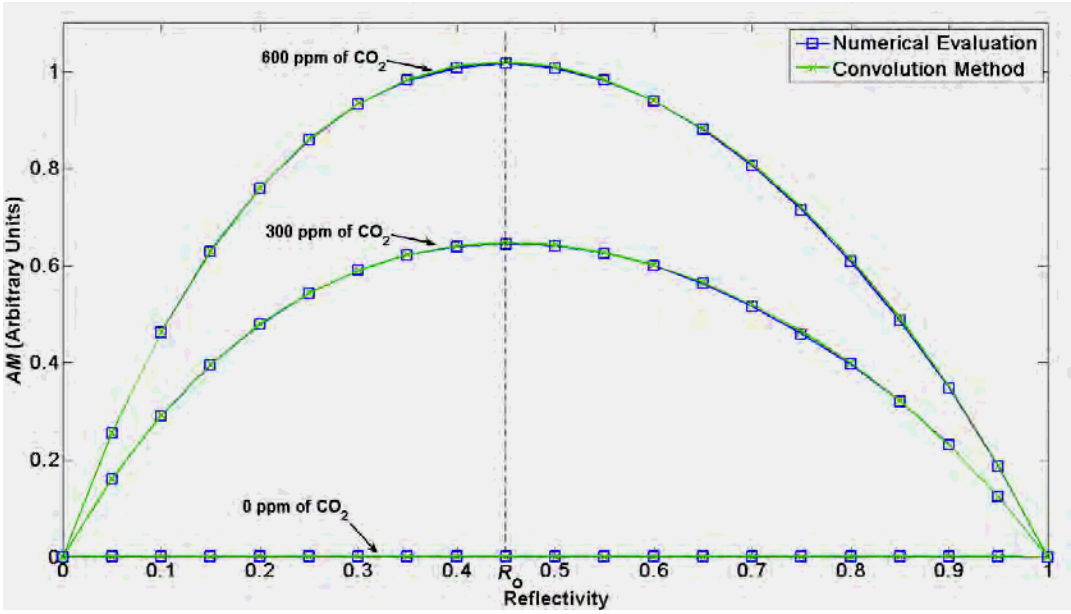

Figure 3.15-Amplitude Modulation as a function of the Reflectivity (*AM* in arbitrary units).

As was mentioned in section 3.4.2 the system response consists of a series of cosine functions. The amplitude of these cosine functions is described in the Fourier domain by the product $I_{FP}(R,n,d,\xi)\,G(\xi)$. As the magnitude of the sidelobes of $G(\xi)$ will remain fixed, unless there is a change in the concentration of the gas, the magnitude of this function is constant whilst the gas concentration is fixed. However, the magnitude of the impulses of $I_{FP}(R,n,d,\xi)$ can be manipulated by changing the reflectivity of the FPI mirrors (Figure 3.9) which consequently modifies the amplitudes of the system response harmonics. Therefore, in order to have the maximum amplitude in the first harmonic of the system response it is necessary to find the value of R for which the magnitude of the first impulse of $I_{FP}(R,n,d,\xi)$ is a maximum. The magnitude of the FPI impulses as a function of the reflectivity are given by

$$|A_m| = \frac{(1-R)}{(1+R)}R^m \qquad m = 1,2,..\infty \tag{3.25}$$

Hence, the magnitude of the first impulse due to the first harmonic $(m=1)$ is given by

$$|A_1| = \frac{1-R}{1+R}R. \tag{3.26}$$

From differentiation of equation (3.26) it is found that the maximum of $|A_1|$ occurs at $R = 0.41$ (figure 3.9). This is very useful result since show that if we will use a PSD to recover the sensor signal the optimal value of R is 0.41 regardless the cavity length.

3.4.5. Design of a CO gas sensor an example

In order to recapitulate the optimization method presented in this chapter let us analyse a new gas sensor design. Here, the goal is to find the optimal FPI parameters, cavity length and reflectivity, for a CO sensor. In this design we will work with the target absorption spectrum of CO occurring at 4.7 μm; the CO concentration was fixed at 35 ppm and the gas pathlength at 20 cm. The function $G(\nu)$ showing the filter response and the absorption through the gas is shown in figure 3.16. Thence we proceed to evaluate the amplitude modulation as a function of the cavity length and the reflectivity using the computationally slow optimization method, the direct numerical calculation of (3.2), and the results are presented in figure 3.17. Thus it is found that the maximum amplitude modulation occurs at $R = 0.46$ and $nd = 0.14$cm for the $G(\nu)$ shown in figure 3.16.

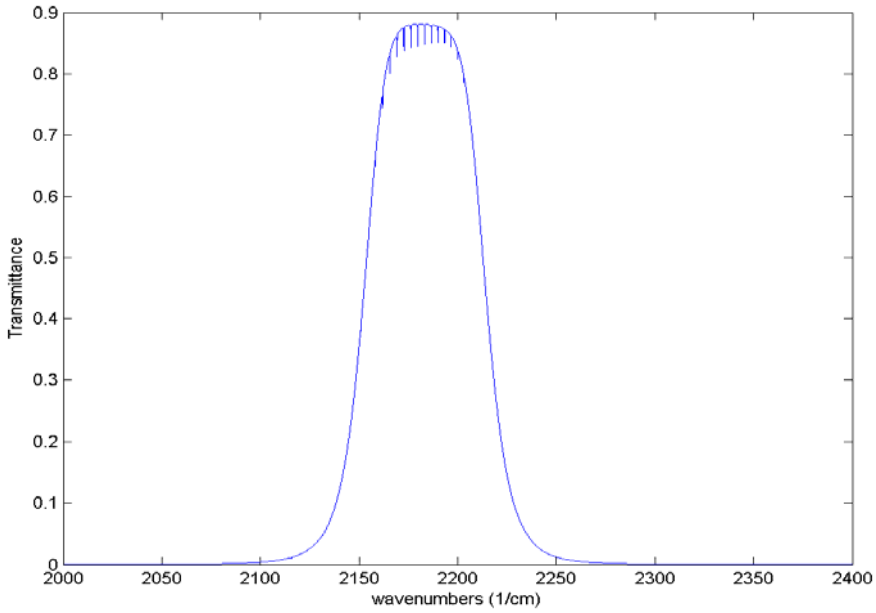

Figure 3.16- $G(\nu)$ profile for the CO sensor.

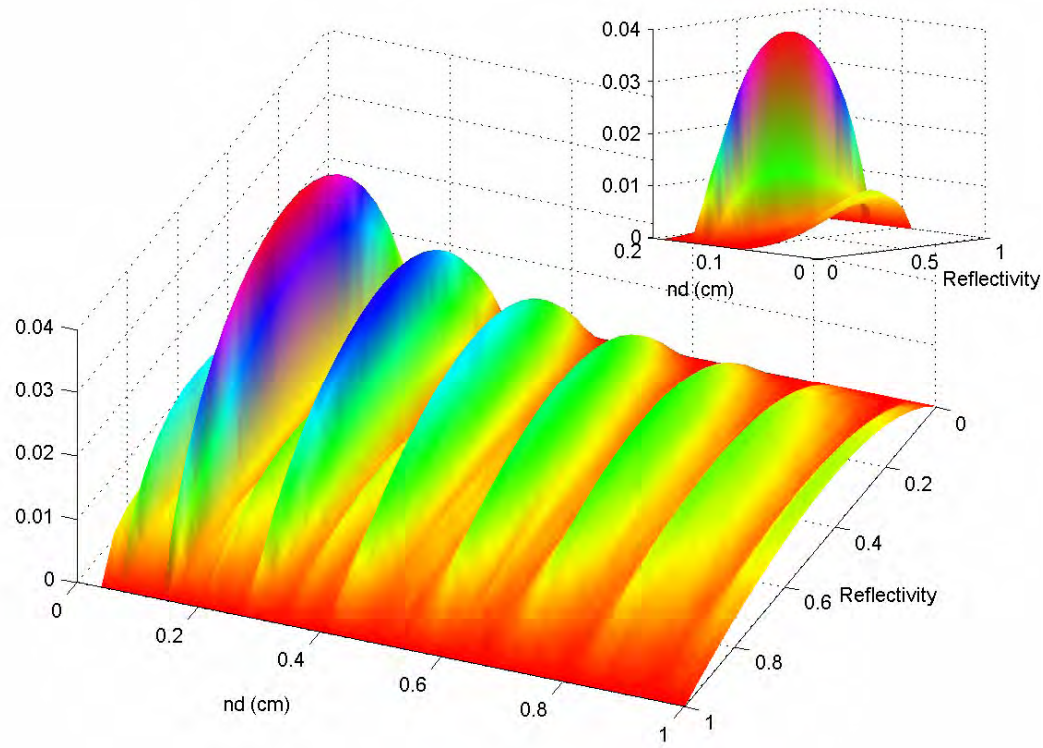

Figure 3.17- Amplitude Modulation as a function of R and nd evaluated by direct calculation. (*AM* in arbitrary units)

Now using our method, we firstly evaluate the Fourier transform of $G(\nu)$, the magnitude in the Fourier domain of this function is shown in figure 3.18. In this figure can be clearly appreciated that the CO ro-vibrational lines produce a set of very well defined sidelobes. If we compared the sidelobes produced by CO and the sidelobes produced by CO_2 we find that the CO sidelobes are closer and sharper than the obtained for CO_2. They are closer to $\xi = 0$ because the separation of the CO ro-vibrational lines is larger. Moreover $|G(\xi)|$ of the CO sensor has sharper sidelobes because the CO ro-vibrational lines have a more constant separation than those of CO_2. In figure 3.18 the first sidelobe has it maximum at $\xi_{\max} = 0.28\text{cm}$, which means that the optimal optical cavity length it is given $d = \xi/2 = 0.14\text{cm}$, assuming $n = 1$. This value is the same as the obtained with the direct numerical calculation $(nd = 0.14\text{cm})$. A detail of the first sidelobes of $|G(\xi)|$ of the CO sensor it is shown in the upper box of figure 3.18. Moreover, $|G(\xi)|$ has practically the same shape compared with the amplitude modulation as a function of *nd* evaluated with the direct calculation (figure 3.17).

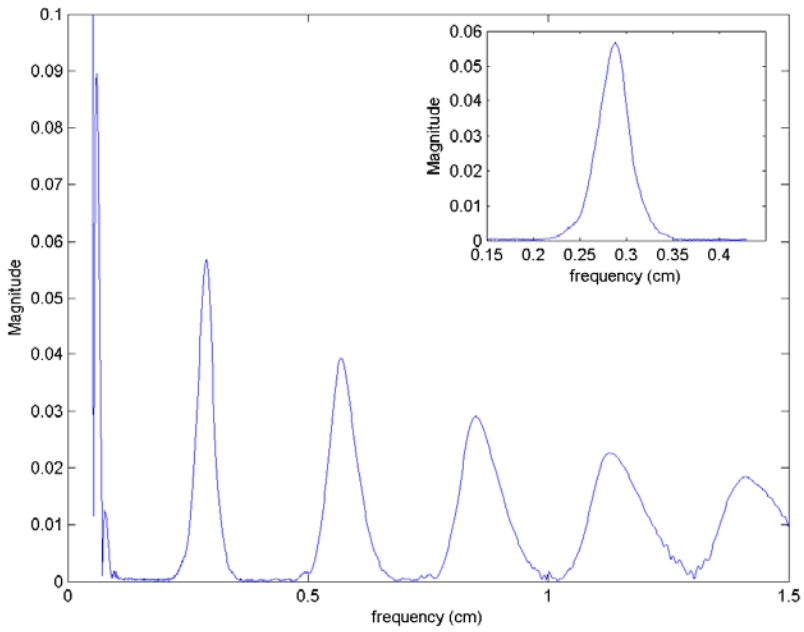

Figure 3.18- $|G(\xi)|$ for the CO sensor.

After the optimal nd is found the optimum R can be determined by applying the convolution method given in section 3.4.4. The amplitude modulation as a function of the reflectivity for the CO sensor it is shown in figure 3.19, where the optimal reflectivity is found to be $R = 0.46$. This value is practically the same as the obtained with the direct numerical method ($R = 0.48$) (Figure 3.17).

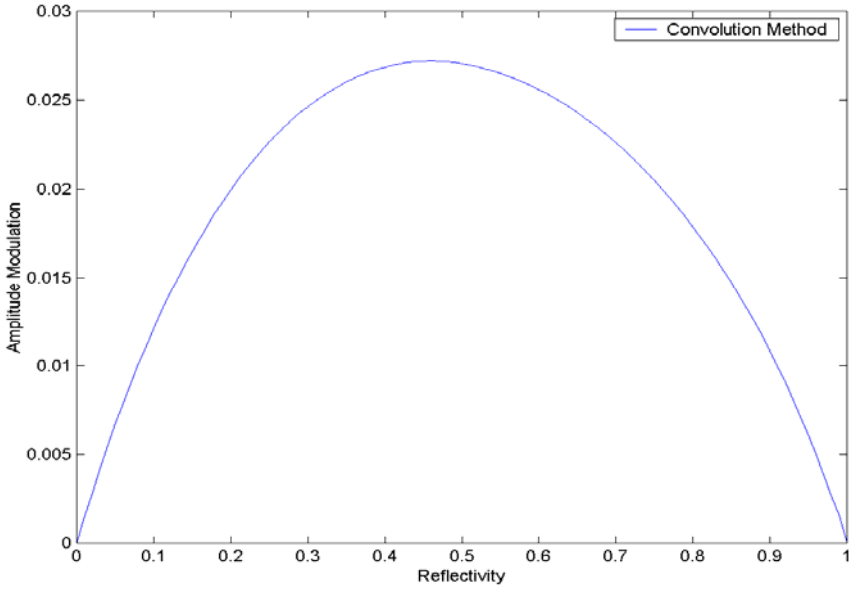

Figure 3.19- Amplitude Modulation as a function R for the CO sensor. (*AM* in arbitrary units)

3.5. Filter selection approach

Initially we mentioned that an optimization procedure should look for the parameters that guarantee the maximum amplitude modulation produced by the sensor when the target gas is present; this part is completed using the optimisation methods that we presented above. However, it is also necessary to guarantee that our gas sensor produces a background amplitude modulation, when there is a zero concentration of the target gas $T(\nu) = 1$, which is as close to zero as possible. Therefore we need to determine what factors help us to minimise the background amplitude modulation, otherwise our sensor can loose its sensitivity to very small gas concentrations. In this section we show that the band pass filter plays an important role in the background amplitude modulation. Moreover it is shown that the band pass filter shape can help to reduce the background amplitude modulation.

The background amplitude modulation is a particular case of the amplitude modulation and it occurs when there is a zero concentration of the target molecule in gas pathlength it is $T(\nu) = 1$. For the background it is possible to reduce the $G(\nu)$ function into $G_{Bk}(\nu)$, which can be expressed as

$$G(\nu) = Fil(\nu)\, S(\nu)\, T(\nu) \implies G_{Bk}(\nu) = Fil(\nu)\, S(\nu)\,. \tag{3.27}$$

In equation (3.27) the $G_{Bk}(\nu)$ function depends just on the filter performance $Fil(\nu)$ and the source profile $S(\nu)$, since the $T(\nu) = 1$. As was stated by equation (3.13) the Fourier transform of the sensor response $I_D(R, n, d, \xi)$ is related to $G(\xi)$ and $I_{FP}(R, n, d, \xi)$. Therefore the background Fourier transform $I_D(R, n, d, \xi)$ can be evaluated using equation (3.13), just replacing $G(\xi)$ with $G_{Bk}(\xi)$. In section 3.4.2 it was stated that the inverse Fourier transform of $I_D(R, n, d, \xi)$ leads to a sum of cosine functions whose amplitudes are related to the product of the magnitude of the impulses of $|I_{FP}(R, n, d, \xi)|$ and $|G_{Bk}(\xi)|$. Here, considering that the cavity length and the reflectivity are constant and that the gas concentration is changing therefore the impulses of $|I_{FP}(R, n, d, \xi)|$ will remain constant. However $|G_{Bk}(\xi)|$ will be varying with the concentration and therefore it will 'control' the background amplitude modulation.

Hence, the Fourier transform of the sensor response for the background amplitude modulation case can be expressed as

$$\begin{aligned} I_D(R,n,d,\xi)_{BK} &= \frac{1-R}{1+R}G(0)_{BK}\,\delta(0) + \frac{A_1 G(\xi_1)_{BK}}{2}\delta(\xi-\xi_1) + \frac{A_1 G(\xi_1)_{BK}}{2}\delta(\xi+\xi_1) \\ &+ \frac{A_2 G(2\xi_1)_{BK}}{2}\delta(\xi-2\xi_1) + \frac{A_2 G(2\xi_1)_{BK}}{2}\delta(\xi+2\xi_1) \\ &+ \frac{A_3 G(3\xi_1)_{BK}}{2}\delta(\xi-3\xi_1) + \frac{A_3 G(3\xi_1)_{BK}}{2}\delta(\xi+3\xi_1) \\ &+ \cdots + \frac{A_m G(m\xi_1)_{BK}}{2}\delta(\xi-m\xi_1) + \frac{A_m G(m\xi_1)_{BK}}{2}\delta(\xi+m\xi_1) \\ &= \frac{1-R}{1+R}G(0)_{BK}\,\delta(0) + \sum_{j=1}^{m}\frac{A_m G(m\xi_1)_{BK}}{2}\left[\delta(\xi-m\xi_1)+\delta(\xi+m\xi_1)\right] \end{aligned} \tag{3.28}$$

where A_m represents the magnitude due to the FPI fringes. Therefore, using the last equation we can say that if we require our sensor to produce a signal equal to zero for the background case it is required that $G_{Bk}(m\xi_1) = 0$.

Furthermore, if the optimal FPI parameters (reflectivity and cavity length) are known, the minimum background amplitude modulation will depends on the $G_{Bk}(\nu)$ function. The optimal FPI parameters can be evaluated using the approaches presented in previous sections. In this case the problem consists in determining which $G_{Bk}(\nu)$ function produces the minimum background modulation for a given cavity length and reflectivity.

Now if the gas sensor will operates in the mid infrared region (MIR) and that a thermal broad band infrared source is going to be it is reasonable to set $S(\nu) = 1$. Here the function $G_{Bk}(\nu)$ can be reduced to

$$G_{Bk}(\nu) = Fil(\nu), \tag{3.29}$$

this is very helpful since it shows that the background modulation produced by our sensor will depend directly on the band pass filter. Therefore the background amplitude modulation can be minimised by selecting a band pass filter whose Fourier transform satisfies the condition $G_{Bk}(m\xi_1) \approx 0$.

3.5.1.1. Minimising the Background modulation for the CO_2 sensor

In this section we present a simple example of how to use the Fourier transform properties of $G_{Bk}(\nu)$ to minimise the background amplitude modulation for the CO_2 sensor, already defined in previous sections. Here for simplicity we fixed the FPI reflectivity as 0.45 and the cavity length as 0.28cm. These were the optimal parameters obtained previously; obviously the optimal FPI cavity length depends on the ro-vibrational lines passed by the filter. Therefore, in this example we select some filters, all of them with the same central wavelength (CWL) and the same full-width at medium high (FWMH), in order to pass the same ro-vibrational lines. The filters utilised in this example are three ideal filters, a square pulse (F2), a trapezium (F3), a trapezium with 'soft corners' (F4) and finally a measured filter performance (F1) as shown in figure 3.20.

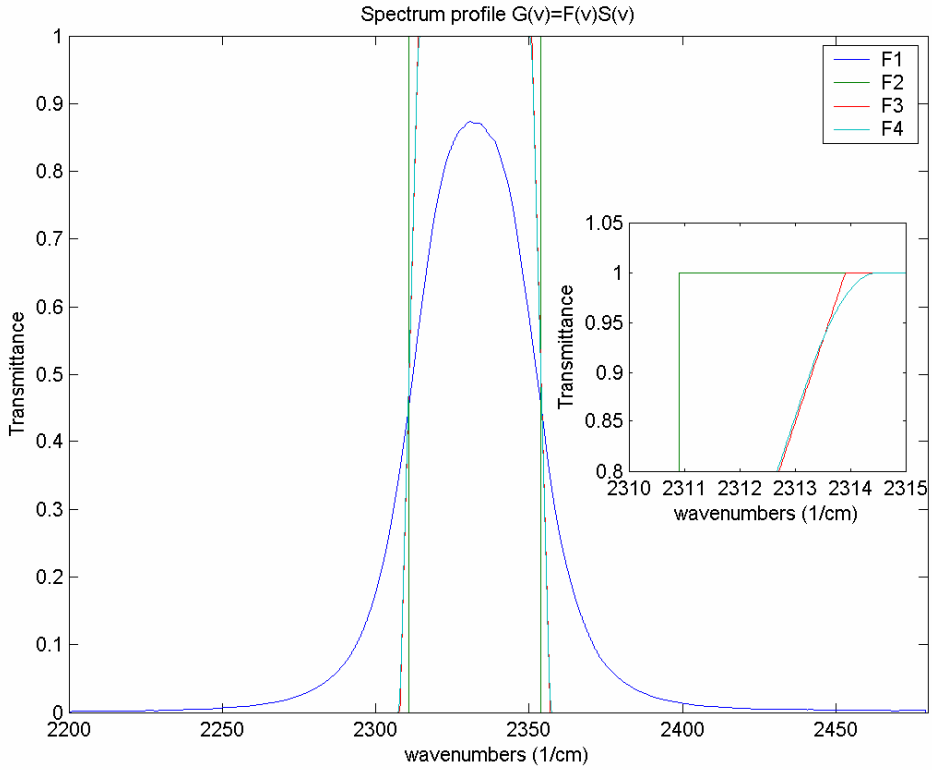

Figure 3.20. Trial filter performance for a CO_2 sensor.

The goal in this example is to decide which filter of this set will produce the lowest background amplitude modulation. Therefore as was mentioned before it is necessary to apply the Fourier transform to these filters. From figure 3.21 it can be quickly observed

that the magnitude of the Fourier transform of the square filter has the strongest sidelobes. In contrast the real filter has the smallest sidelobes in Fourier transform magnitude. The upper-left inset in figure 3.21 shows the magnitude of the Fourier transform of the four filters in the region where the first impulse due to the FPI fringes occurs. If we take the optimal value of the cavity length as 0.28 cm, then the first impulse is located at $\xi_1 = 2nd = 0.56$cm. Therefore in order to have the smallest amplitude of the first harmonic of the sensor signal we need to choose the filter whose $|G_{Bk}(\xi_1)|$ is the lowest. Hence in our example the filter having the lowest $|G_{Bk}(\xi_1)|$ is the commercial filter while in contrast the square filter has much larger sidelobes around ξ_1.

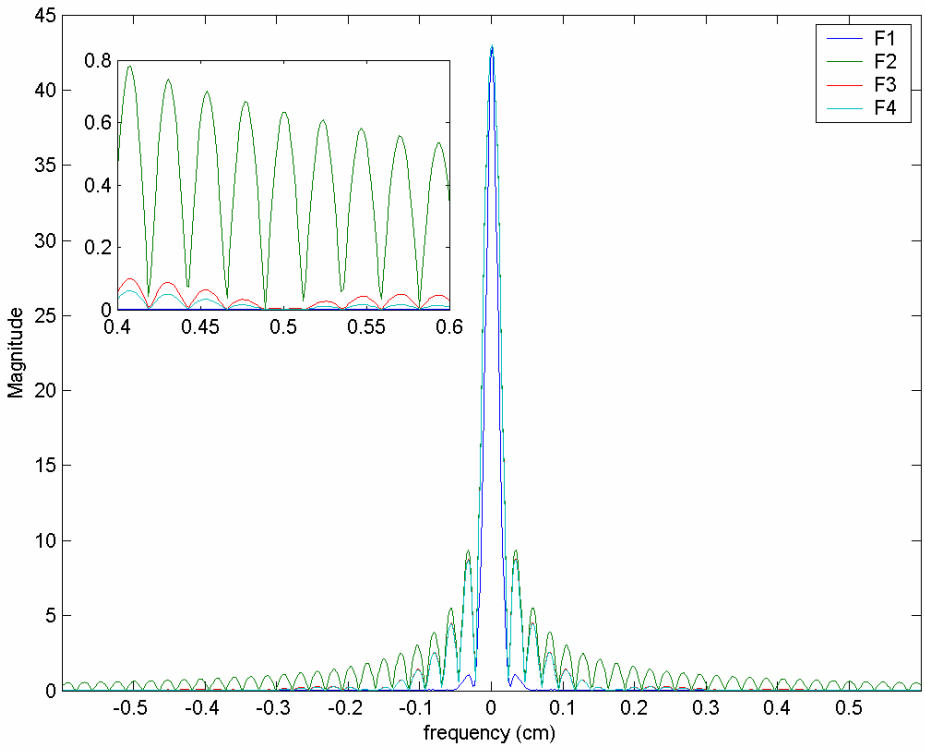

Figure 3.21- Magnitude of the Fourier Transform of the filters for the CO_2 sensor.

In order to validate our prediction we evaluated the background amplitude modulation as a function of the cavity length using the convolution method and this is presented in figure 3.22. It is clear that the square filter produces the largest background amplitude modulation, while the real filter produces the lowest background amplitude modulation, in accordance with the prediction. The inset in figure 3.22 presents the

background amplitude modulation around the optimal optical thickness $nd = 0.28$cm. Here, the background modulation for the square filter is larger, even by some orders of magnitude, than that obtained with the other filters. It is very important to mention that for this example the background modulation when $nd = 0.28$cm is not so large even with the square filter because the FWMH of this filter makes $|G_{Bk}(\xi_1 = 0.56)| \approx 0$. However it is possible in practice it is extremely difficult to fabricate a filter that produces a zero exactly at ξ_1, since a high accuracy in filter width ($\ll \mathrm{FSR}$) is required. This severely complicates the filter design and requires extremely precise process control increasing the cost; indeed it is probably impractical. As the peak sidelobe can occur at any point therefore for simplicity the best filter is the one with the lowest sidelobe magnitude in the region around $\xi_1 = 2nd$.

The background amplitude modulation is very important since this is related to the lower concentration limit of our sensors. Therefore it is convenient to analyse how the amplitude modulation changes as a function of the gas concentration considering the different filters. In figure 3.23 the amplitude modulation as a function of the concentration is shown, for a gas path length of 3.5 cm at one atmosphere. In this figure we can observe firstly, that when the filter with steepest sides is selected (F2) the amplitude modulation for low concentration levels (background inclusive) is severely affected. Secondly, the system response is less sensitive to the filter characteristics as the concentration increases. It can be seen that the modulation for higher gas concentrations is practically the same for all the filters, which means that choosing a filter which produces a low background amplitude modulation does not reduce the sensor response when the target gas is present. Additionally, we can deduce that when a filter with 'soft' sides is used (eg. F1), the amplitude modulation for low concentration levels is governed mainly by the gas concentration rather than by the filter characteristics. This produces a far more linear sensor response to the gas concentration since the background amplitude can be reduced over an order of magnitude depending of the filter, and so the gas sensor performance is greatly improved. For example, the amplitude modulation using F2 is quite flat from 0 to around 100 ppm (Figure 3.23), making it essentially impossible to determine the correct gas concentration. In contrast, the amplitude modulation is described by a straight line when F3 is employed.

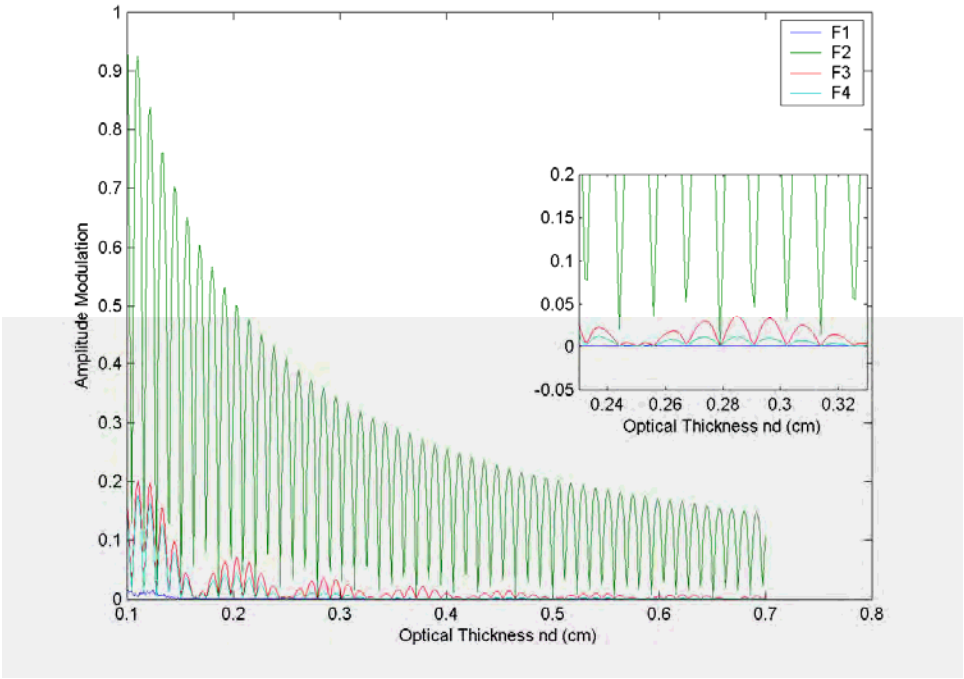

Figure 3.22- Background Amplitude Modulation as a function of the optical thickness. (*AM* in arbitrary units)

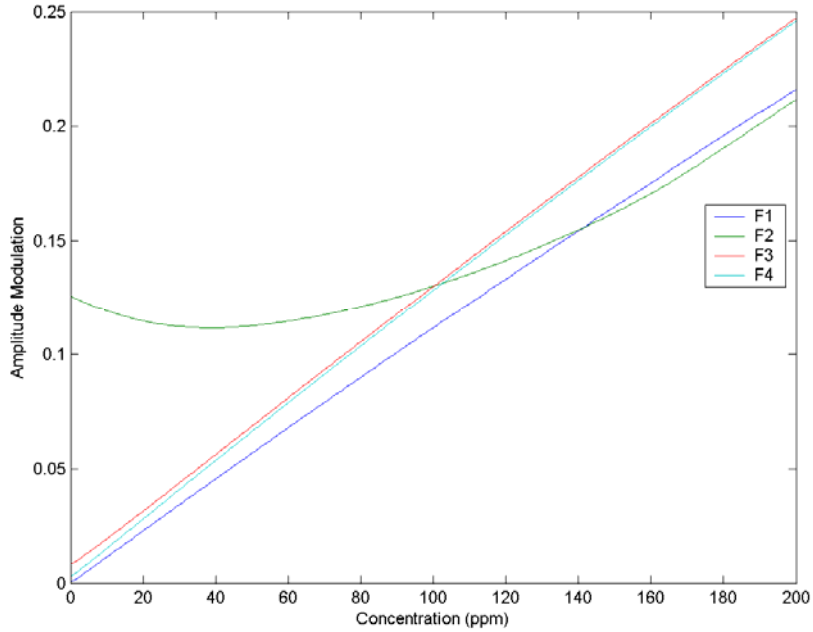

Figure 3.23- Amplitude Modulation as a function of the Concentration. (*AM* in arbitrary units)

3.5.1.2. Minimising the Background modulation in for CO sensor

As a second example of using the filter selection approach let us review the case of the CO sensor. Here four ideal commercial filters will be considered [12]; their transmission curves are shown in figure 3.24 these plots were generated using TFcalc software [13]. Hence, to predict the background amplitude modulation the filters' Fourier transform is calculated; their transforms are shown in figure 3.25. The inset in this figure shows a detail of the magnitude of the Fourier transforms around $\xi_1 = 0.28$cm where the optimal frequency for this sensor as stated before lies. From this figure, it is possible to predict that the filter F3 will produce the highest background amplitude modulation, and in contrast the filters F1 and F2 will produce lower background amplitude modulation. Finally, the background amplitude modulation as a function of the optical thickness, in the region from 0.1 to 0.2 cm, was evaluated and it is shown in figure 3.26. In this plot the amplitude modulation for the filter F3 is the largest and the filters F1 and F2 produce smaller background modulation; which is in agreement with the prediction.

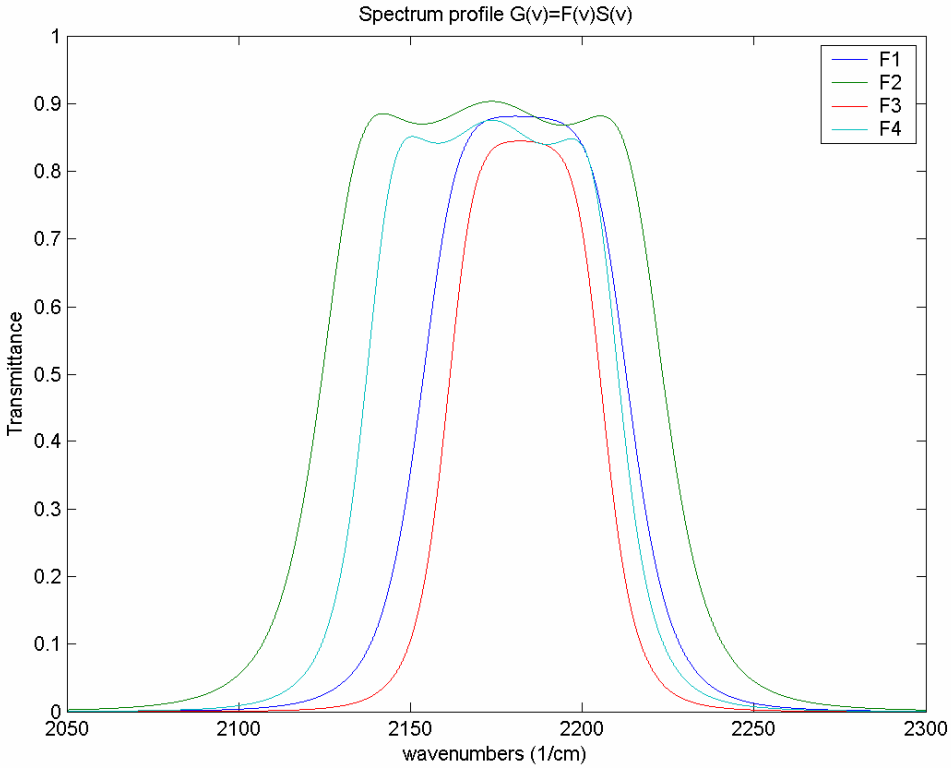

Figure 3.24- Filter performances for a CO sensor.

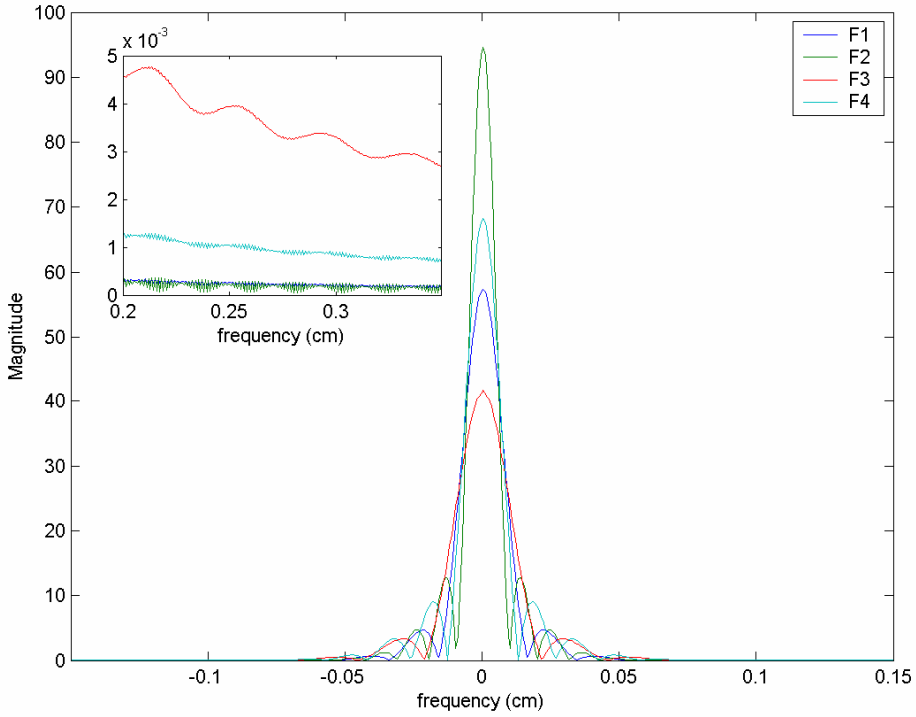

Figure 3.25- Fourier transforms of the filter performances for the CO sensor.

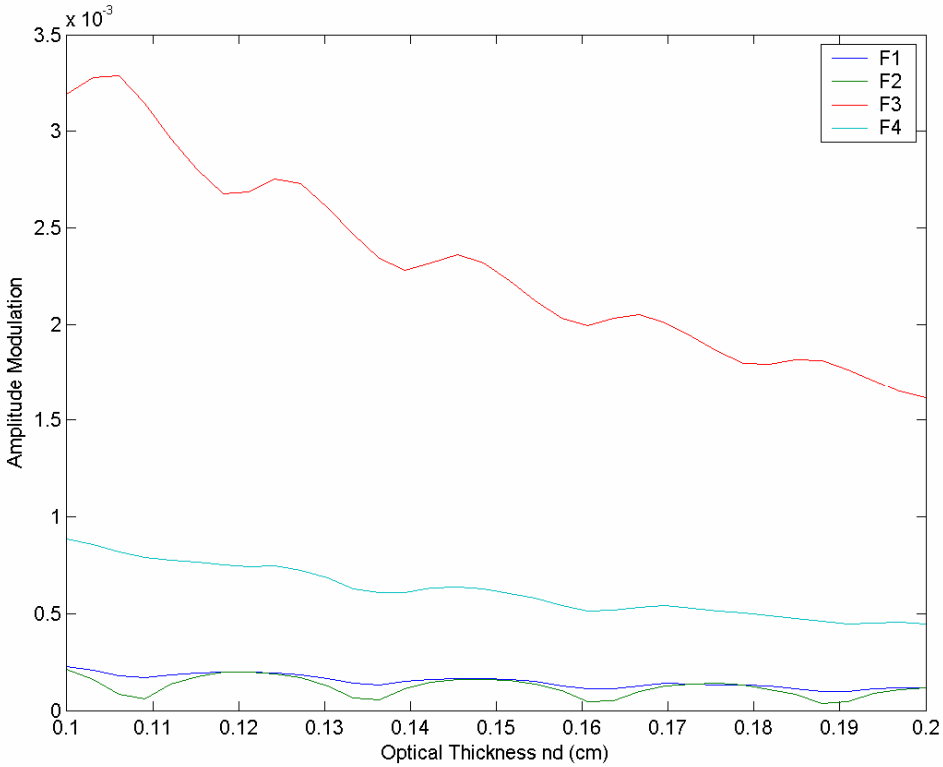

Figure 3.26- Background Amplitude Modulation for the CO sensor. (*AM* in arbitrary units)

In conclusion, the background amplitude modulation can be minimised using the filter selection approach. This simple approach just requires the evaluation of $|G(\xi)|$ and by observation of its sidelobes around ξ_1 the best filter for the application can be choosed. The optimal frequency ξ_1 can be found using the method described in section 3.4.3.1. The filter selection approach predicts that the filter with the strongest magnitude around ξ_1 will be the filter that produces the largest background amplitude modulation. In contrast, the filter with the weakest magnitude around ξ_1 is the filter that will produce the lowest background amplitude modulation.

3.5.2. Manufacturing errors.

A further benefit of the filter selection approach is that the effect of filter manufacturing tolerances can be easily investigated. As steep sided filters with complex design and high sensitivity to manufacturing errors are not required, therefore simple three or even two cavity filters [14] are a good choice for the application. In order to show how robust the system is to filter manufacturing errors, let us to consider an ideal filter that transmits in the 4.3 μm region [12], where the strong antisymmetric stretch, parallel absorption band of CO_2 lies. The thicknesses of the most sensitive layers of the filter were varied intentionally to compute the performance of filters with simulated manufacturing errors. TFCalc software [13] was utilised to compute the most sensitive layers of the filter. The response of the ideal filter and of two more filters with a thicknesses error in a highly sensitive layer are shown in figure 3.27. To determine if the background amplitude modulation will be seriously affected by errors in the filter, the FT approach is applied. Here, the optimal optical thickness $nd = 0.28$cm was determined in a example stated before. Hence, we need to determine the magnitude of the filters' Fourier transform in the region around $\xi_1 = 2nd$, where the fundamental frequency of the Airy function falls. A detail of these transforms around $2nd = 0.56$cm is presented in figure 3.28. We see that the magnitudes of the filters' Fourier transform are similar, thus similar background amplitude modulation will be obtained with the three filters. A full simulation, by direct calculation of equation (3.2) of the amplitude modulation for the three filters and as a function of the concentration is shown in figure 3.29. For a 0 ppm CO_2 concentration, which corresponds to the background case, the system response has a similar value for all the filters, which is in accordance with the prediction given by our approach. Also, from figure 3.29 it can be observed that if the

filter's transmission is seriously reduced by manufacturing errors in layer thicknesses, only the amplitude modulation response is reduced. This is reasonable since the average transmission through the system is reduced. Consideration of the Fourier transform of the filter bandpass shape, including errors, enables us to safely conclude that the only effect of the filter's manufacturing errors is reduction in transmission, and with no degradation of the background signal. These results relax the filter design requirements for this kind of sensor.

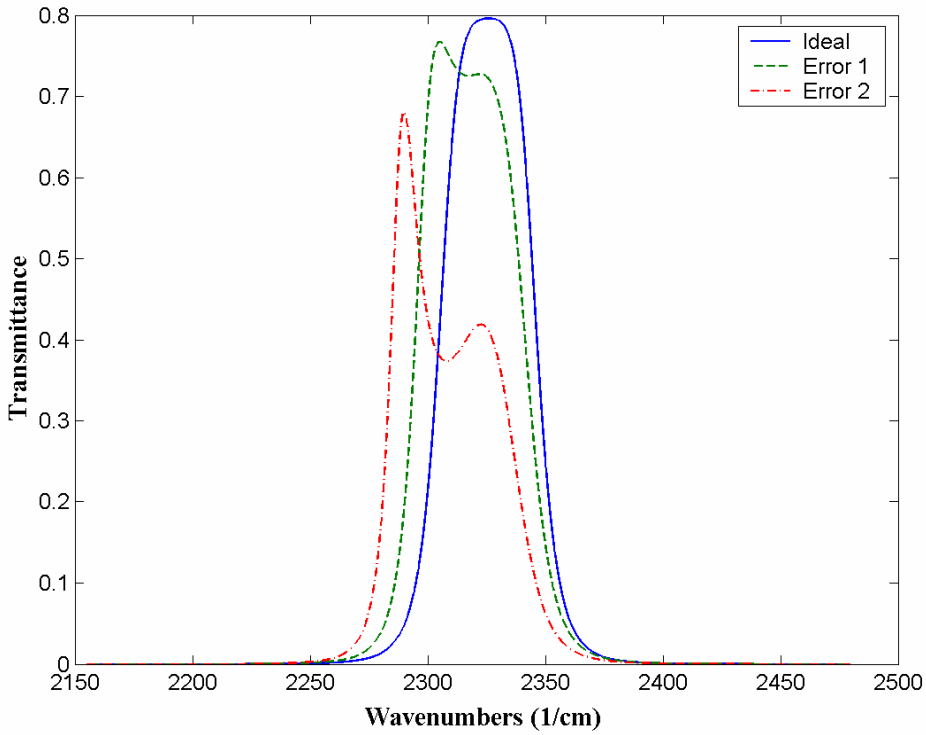

Figure 3.27- Filter performances with error tolerances.

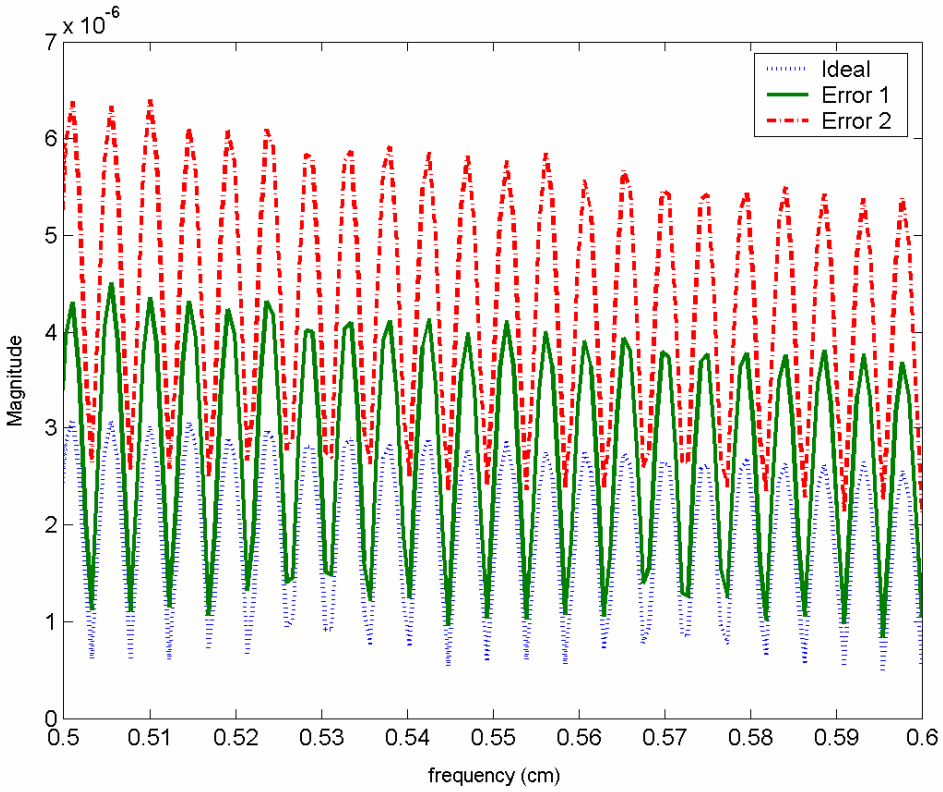

Figure 3.28- Fourier Transform of the filters shown in figure 3.27.

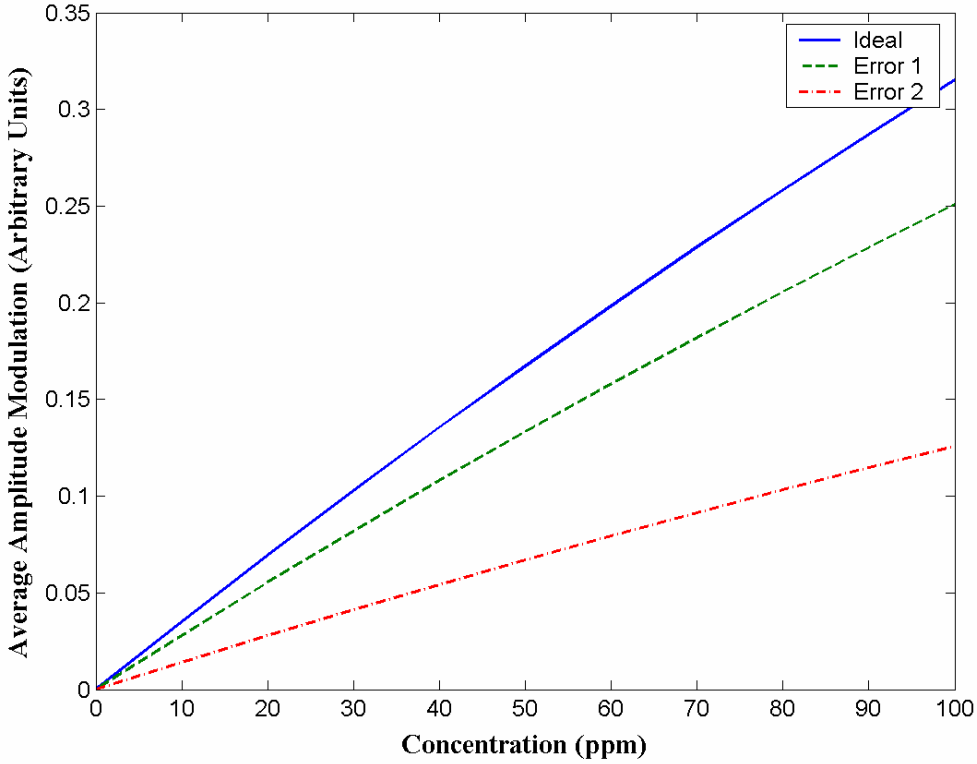

Figure 3.29- Amplitude Modulation for the CO sensor considering error in the filters.

3.6. Conclusions

The mathematical model of a sensor based on correlation spectroscopy using a FPI modulator can be represented as a convolution. Therefore, taking advantage of this representation the sensor system response can be easily and quickly evaluated using the convolution method presented in section 3.3.1. Furthermore, the optimal cavity length nd is obtained simply by looking for the frequency at which the first sidelobe of $|G(\xi)|$ has it maximum value as shown in section 3.4.3.1. The optimal value of the reflectivity R can be obtained using the convolution method presented in section 3.4.4. Here it was shown that if the sensor signal will be recovered by using a PSD the optimum reflectivity it is $R = 0.41$ regardless the other parameters. Finally, the effect of the filter characteristics on the background amplitude in gas sensors using an FPI as a modulator in a form of correlation based device has been analysed in section 3.5. From this analysis we present a mathematical procedure to show why some filters produce high background amplitudes, and we present a simple approach to select the best filter for this type of sensor. An important point derived from this work is that narrow band, with very steep sided 'square' shaped pass-bands filters will produce high background modulation, because the FT of these filters has high sidelobes, whilst filters with more gradual transitions to the stop-band have low sidelobes. This reduces the cost of the system, because in general filters with 'soft sides' are the best choice for the application and these filters are relatively cheap and easy to fabricate. The method also provides a quick and easy way to evaluate the effect of manufacturing tolerances on the IR filters, by observing their effect on the Fourier Transform of the bandpass function, without extensive full scale simulations.

3.7. References

1. J. P. Dakin, Review of Fibre Optic Gas Sensors, *The Plessey Company PLC*, 1988

2. W. Jin, G. Stewart, B. Culshaw, S. Murray, *et al.*, Absorption measurement of methane gas with a broadband ligth and interferometric signal processing, *Optics Letters* **18**, p. 1364-1366, 1993

3. A. Mohebati and T. A. King, Remote detection of gases by diode laser spectroscopy, *Journal of Modern Optics* **35**, p. 319-324, 1998

4. J. J. Barrett and S. A. Myers, New Interferometric Method for Studying Periodic Spectra Using a Fabry-Perot Interferometer, *J. Opt. Soc. Am.* **61**(9), p. 1246-1251, 1971

5. E. Hecht, *Optics*, Third edition, United States of America, Addison Wesley, 409-418, 1998

6. H. Kuhn, New Techniques in Optical Interferometry, *Reports on Progress in Physics* **14**, p. 64-94, 1951

7. M. Born and E. Wolf, *Principles of Optics*, 3rd Edn Great Britain, Pergamon Press, 1965

8. L. S. Rothman, C. P. Rinsland, A. Goldman, S. T. Massie, *et al.*, The HITRAN Molecular Spectroscopic Database and Hawks (HITRAN Atmospheric Workstation): 1996 Edition, *Journal of Quantitative and Radiative Transference* **60**, p. 665-710, 1998

9. J. W. Cooley and J. W. Tukey, An Algorithm for the Machine Calculation of Complex Fourier Series, *Mathematics of Computation* **19**(90), p. 297-301, 1965

10. J. M. Vaughan, *The Fabry-Perot Interferometer History, Theory, practice and applications*, USA, Adam Hilger, 1989

11. SRS, About Lock-In Amplifiers, 2007

12. G. J. Hawkins, Private Communication, 2003

13. TFCalc, Software Spectra Inc, http://www.sspectra.com/ (last accessed 26/10/2004).

14. H. A. Macleod, *Thin-Films Optical Filters* Bristol, Institute of Physics Publishing, 2001

Chapter 4

4. Analysis of a FPI illuminated with a converging beam.

Generally, in gas detectors that use a FPI as a modulator the illumination is considered to be collimated, so that that all the rays arriving at the FPI have the same incidence angle (see chapter 3). However in our particular case we will use a different setup (Figure 4.1) where the light source beam is collected a focused with a bi-convex lens. Here, the FPI and the optical detector are placed at the image point and therefore the FPI is illuminated with a converging light beam. Consequently the incident light, in form of a cone, has a set of rays with angles from 0 to θ (Figure 4.1). Thus, the spectral FPI fringe pattern is given by the integration of the transmission trough the FPI over the range of angles of incidence. This will produce some changes in the spectral FPI transmission fringe pattern, such as changes in the fringe's contrast and width. As this is relevant for our gas sensor design in this chapter we briefly review how to evaluate the FPI fringes considering a converging beam and additionally we analyse how to reduce

the adverse effects produced by the converging beam and by inherent effects of the mirrors substrates.

4.1. The Gas Sensor Optical Setup

For convenience in our system we are proposing to place the FPI at the source image point (Figure 4.1). This model is simpler because it just needs one lens for imaging the source, rather than two lenses; one for collimating the incident light and a second one for focusing it. Despite the reduction in optical components and reduction in size, this configuration will introduce some problems, especially some effects on the FPI fringe pattern. This arrises because a set of rays with different angles of incidence, from 0 to θ, is illuminating the FPI (Figure 4.1).

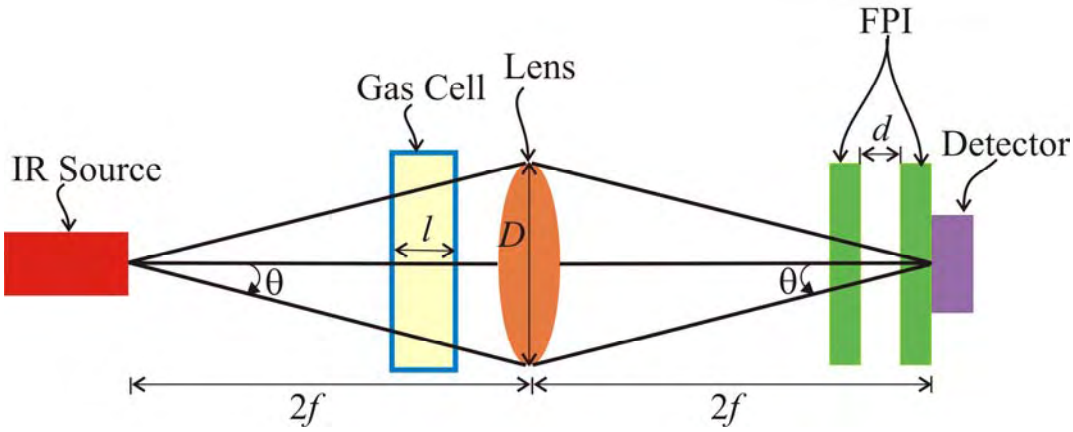

Figure 4.1-FPI placed at image point $(2f)$.

The FPI transmission fringe pattern is described by the Airy Formula [1] which can be expressed as

$$I_{FP} = \frac{1}{1 + F\sin^2(2\pi nd\nu\cos\theta)} \tag{4.1}$$

where the F factor is given by $F = 4R/(1-R)^2$. As the FPI is now being illuminated with a cone of rays, a FPI fringe pattern is produced for each incident ray at angle θ. Here it is useful to recall that the spectral FPI fringe pattern is shifted along the wavenumber axis for small changes in the incidence angle θ. For instance, some FPI fringe patterns produced for different angles of incidence are shown in figure 4.2.

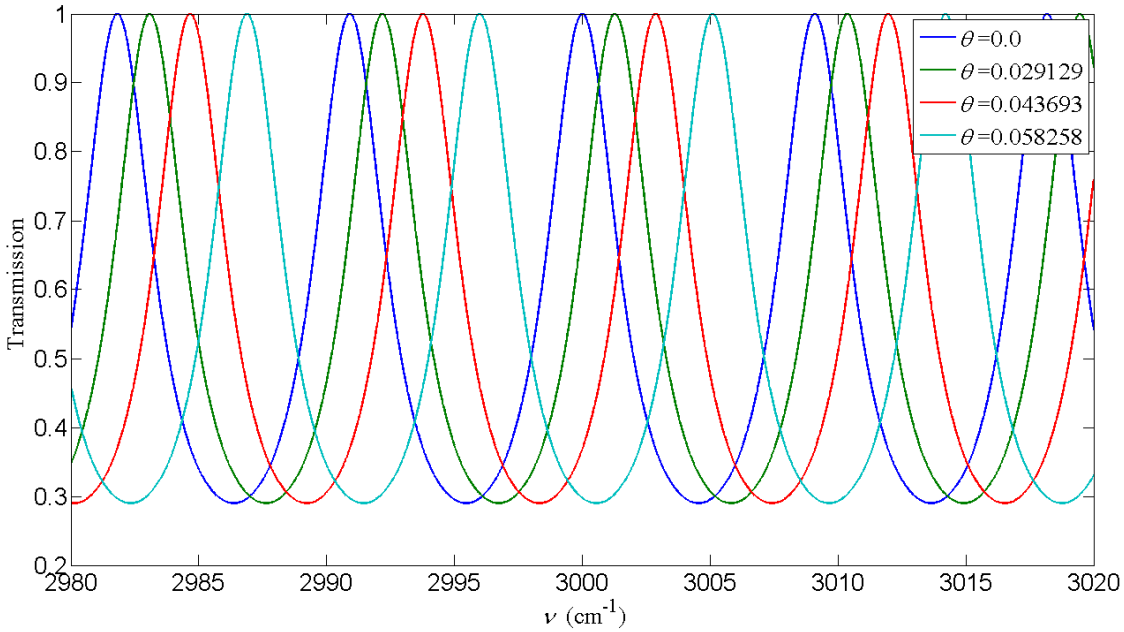

Figure 4.2- FPI fringes considering different angles of incidence. $R = 0.30$, $nd = 0.05$ cm.

Furthermore, for gas sensing applications it is common to use IR sources based on filaments held at high temperatures. This type of IR source can be assumed as a blackbody radiator which is in thermal equilibrium and produces unpolarized (non-coherent), continuous radiation [2]. An ideal blackbody is a perfect Lambertian radiator so radiates the same in all directions from the emitting surface. However, the amount of flux per solid angle (intensity) will depend on θ [3]. This implies that not all the incident rays have the same intensity since this depends on the solid angle.

The shifts along the wavenumber axis (Figure 4.2) and the changes in intensity due to the angle of incidence will produce changes in the overall FPI fringe pattern which is given by the integrated transmission trough the FPI over all angles of incidence. Therefore, the final FPI fringe transmission pattern is no longer simply given by equation (4.1). Hence, in order to evaluate this fringe pattern correctly we need to take into account the angle of incidence, the flux distribution as a function of the solid angle, and the optical thickness of the FPI.

4.2. Flux Distribution as a function of the solid angle

In a simple approach the amount of flux, in Watts, transferred from the source to the object is given by

$$\phi = LA\Omega, \tag{4.2}$$

where L is the amount of power radiated per unit of projected source area per unit of solid angle (Watt/cm^2-sr), it is called radiance [3]; A is the area of the illuminated object, and Ω is the solid angle. The solid angle is measured in steradians and in three-dimensional geometry it is possible to define steradians of solid angle as the ratio of illuminated surface area to the square of the distance from the source to the object [3]. For instance, the solid angle of the lens which is in front of the IR source shown in figure 4.1 is given by

$$\Omega = \frac{A_{lens}}{(2f)^2}\,(\mathrm{sr})\,. \tag{4.3}$$

Furthermore, the flux transferred from the source to the detector for the setup presented in figure 4.1 can be expressed as [3]

$$\phi = \frac{LA_{lens}A_{source}}{(2f)^2} = \frac{LA_{lens}A_{image}}{(2f)^2}, \tag{4.4}$$

Where the blackbody spectral radiance L in terms of power $[\mathrm{Watts}/\,(\mathrm{cm}^2 - \mathrm{sr})]$ it is given by [3]

$$L = \frac{2hc^2\nu^3}{\exp\left(\dfrac{hc\nu}{kT}\right) - 1}\mathrm{d}\nu \tag{4.5}$$

where h is the Planck's constant ($h = 6.626076 \times 10^{-34}$ m^{2}Kg/s), c is the light speed in vacuum ($c = 2.997921 \times 10^{10}$ cm/s), k is the Boltzmann's constant ($k = 1.3806586 \times 10^{-23}$ m^{2}Kg s^{-2}K^{-1}), ν is the frequency in wavenumbers, and T is

the absolute source temperature. It is important to recall that $1\ \mathrm{Watt} = 1\ \mathrm{m^2 Kg/s^3}$. The exitance, which is the amount of power per unit area that leaves a surface (in this case the source) $(\mathrm{Watts/cm^2})$ can be expressed as [3]

$$M = \pi L \tag{4.6}$$

Equation (4.4) is a simple approach to calculate the total flux arriving at the detector surface; however this equation does not give any information about the flux distribution as a function of the incident angle. In order to evaluate the final FPI fringe pattern we must consider the flux distribution as a function of the incident angle. Therefore equation (4.4) is not sufficient to evaluate correctly the final FPI fringe pattern.

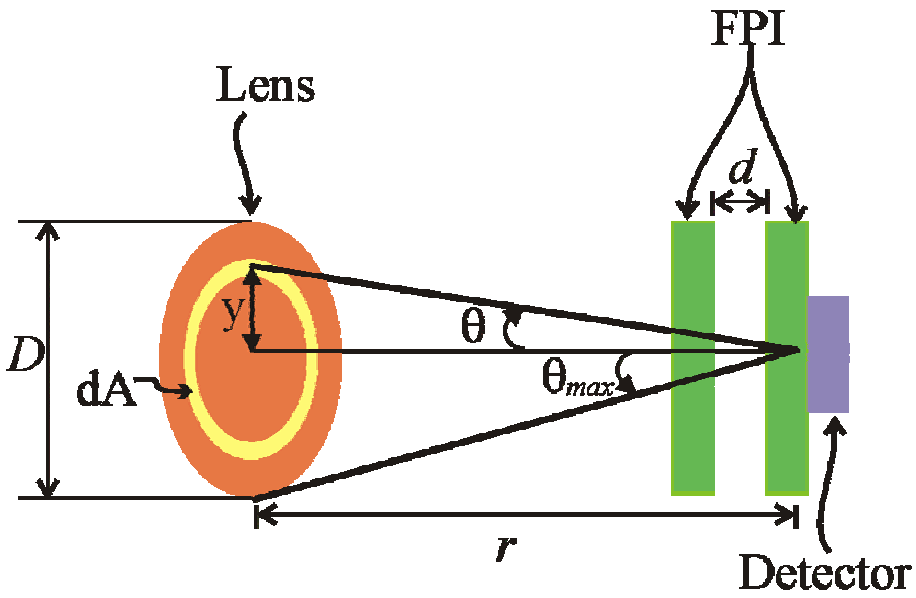

Figure 4.3- Differential of source area viewed by the detector/FPI for a given θ. (Adapted from Dereniak and Boreman 1996 [3]).

An ideal thermal source (blackbody) is a perfect Lambertian radiator. In this type of source the radiance is the same in all directions from the emitting surface. However, the amount of flux per solid angle (intensity) will depend on θ [3]. Hence, let us assume initially that the FPI is not in the system, and just an extended Lambertian source is in front of the detector; in our system we can consider the imaging lens (Figure 4.3) as an intermediate extended Lambertian source. In this case the flux filling the detector as a function of the solid angle is given by [3]

$$\phi = 2\pi L A_d \Omega = 2\pi L A_d \int_0^{\theta_{\max}} \cos\theta \sin\theta \mathrm{d}\theta = 2\pi L A_d \frac{1}{2} \sin^2\theta_{\max}, \tag{4.7}$$

where A_d is the detector's area and $\theta_{\max}$ can be defined from figure 4.3 as

$$\theta_{\max} = \tan^{-1}\left(\frac{D/2}{r}\right) \approx \frac{D/2}{r}, \tag{4.8}$$

where D is the diameter of the lens and r is the distance from the source to the image. Here, it is important to remark that the $\sin^2\theta_{\max}$ can be expressed in terms of the lens diameter and the distance from the lens to the detector as follows

$$\sin^2\theta_{\max} = \left(\frac{D/2}{\sqrt{r^2 + D/2}}\right)^2 = \frac{1}{4\left(r/D\right)^2 + 1} = \frac{1}{4\left(f/\#\right)^2 + 1}; \tag{4.9}$$

The relationship between the distance from the lens to the object and the diameter of the lens (r/D) is called the f number of the lens $(f/\#)$. For our system (figure 4.1) the f number is given by $f/\# = 2f/D$. The lens f number is very useful since this gives the amount of power gathered by a lens [1]. The larger the $f/\#$ lower the power transferred from the source to the object.

By substitution of (4.9) into (4.7) the total flux reaching the detector's area can be expressed as

$$\phi = \frac{\pi L A_d}{4\left(f/\#\right)^2 + 1}. \tag{4.10}$$

Equations (4.7) and (4.10) are more helpful than equation (4.4), for evaluation of the FPI overall response for a finite f number since these equations are a function of the solid angle. These equations can be used to normalize the proportion of flux per solid angle arriving at the FPI; the solid angle Ω depends on the angle θ as described in equation (4.7). From equation (4.7) it is possible to observe that the flux distribution arriving at the detector has the form $\cos\theta \sin\theta$ (Figure 4.4).

In figure 4.4 it can be observed that each differential element of angle $(\mathrm{d}\theta)$ produces a differential of source area $(\mathrm{d}A_s)$. Each differential element of source area will have different proportions (weightings) of the incident flux. For instance, the shaded area in figure 4.4 shows the proportion of incident flux for the differential of angle $(\mathrm{d}\theta)$. Hence, the normalized proportion of transmitted flux per solid angle can be expressed as

$$\frac{1}{1/2\sin^2\theta_{\max}}\int_0^{\theta_{\max}}\cos\theta\sin\theta\mathrm{d}\theta = 1. \tag{4.11}$$

Equation (4.11) can be utilised to normalize proportion of flux transmission per element of angle and obtain in this way the proportion of flux transmitted per differential element of angle $(\mathrm{d}\theta)$.

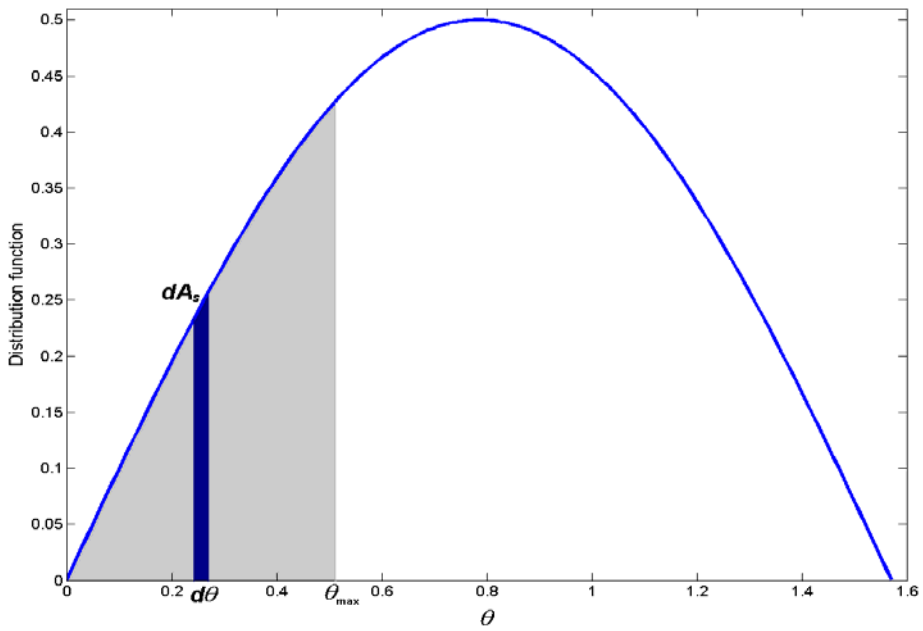

Figure 4.4- Flux distribution as a function of the solid angle. A differential element of source area $(\mathrm{d}A_s)$ is formed per each differential element of solid angle.

4.3. FPI fringes considering the $f/\#$

As was stated our FPI will be placed just in front of the image point, so the incident beam has a cone of angles from 0 to $\theta_{\max}$. For each ray at angle θ a FPI fringe pattern will be formed presenting a shift along the wavenumber axis (Figure 4.2) and each

pattern will have different average transmission (Figure 4.4). Therefore, in order to evaluate the final spectral transmission FPI fringe pattern all these factors should be combined. The final FPI fringe pattern is defined by the integration of the partial FPI fringe patterns produced for each angle of incidence θ multiplied by the proportion of flux transmission correspondent to each angle θ. This the final FPI fringe pattern can be expressed as

$$I_{FP}\left(R,n,d,\nu,\theta_{\max}\right)=\frac{1}{1/2\sin^2\theta_{\max}}\int_0^{\theta_{\max}}\frac{\cos\theta\sin\theta}{1+F\sin^2\left(2\pi nd\nu\cos\theta\right)}\mathrm{d}\theta. \quad (4.12)$$

For instance in figure 4.5 some average spectral FPI transmission profiles per differential element of angle are shown. In this example we took $nd=0.05$cm, $R=0.30$, and a $f/\#=8$ (the f number it is commonly expressed as $f/8$). In this figure the FPI fringes have different average transmission levels since the transmitted flux changes with the angle of incidence θ. The final FPI fringe transmission pattern taking into account all the cone of angles of incidence for $f/8$ it is shown in figure 4.6. In this figure it is seen that the $f/\#$ effect produces a reduction in the FPI fringes contrast and in the fringes width in comparison with the ideal FPI ($\theta_{\max}=0$). Up to here we considered as negligible the changes in R due to different angles of incidence.

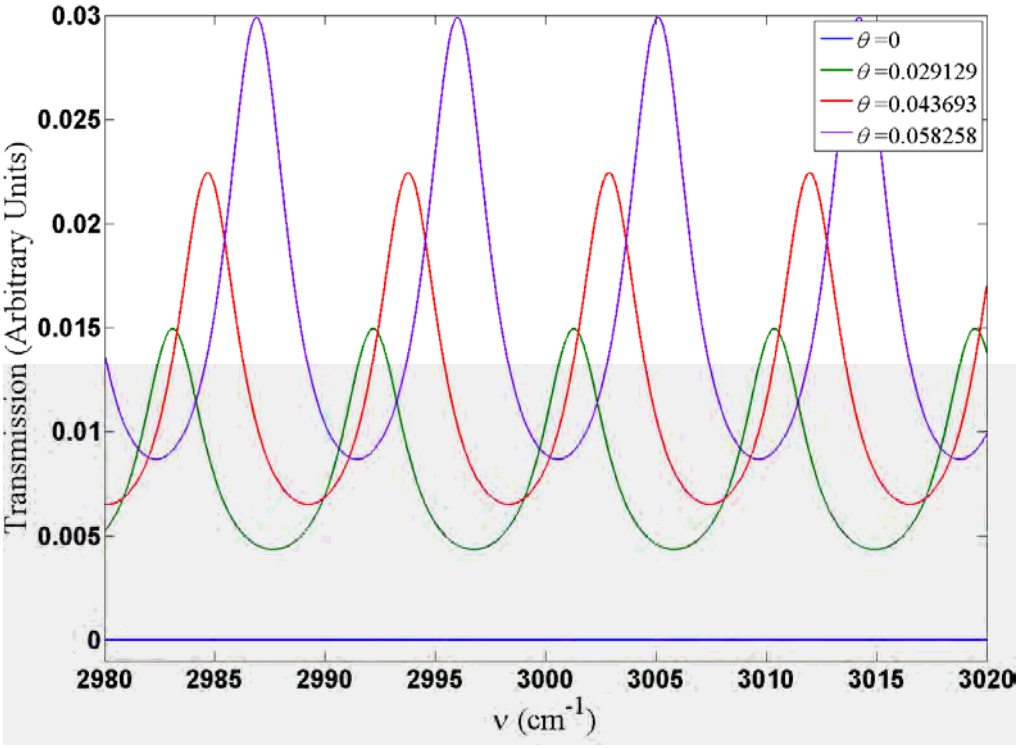

Figure 4.5- Average spectral FPI transmission profiles per differential element of solid angle. $R=0.30$, $nd=0.05$cm, $\theta_{\max}=0.0624$rad.

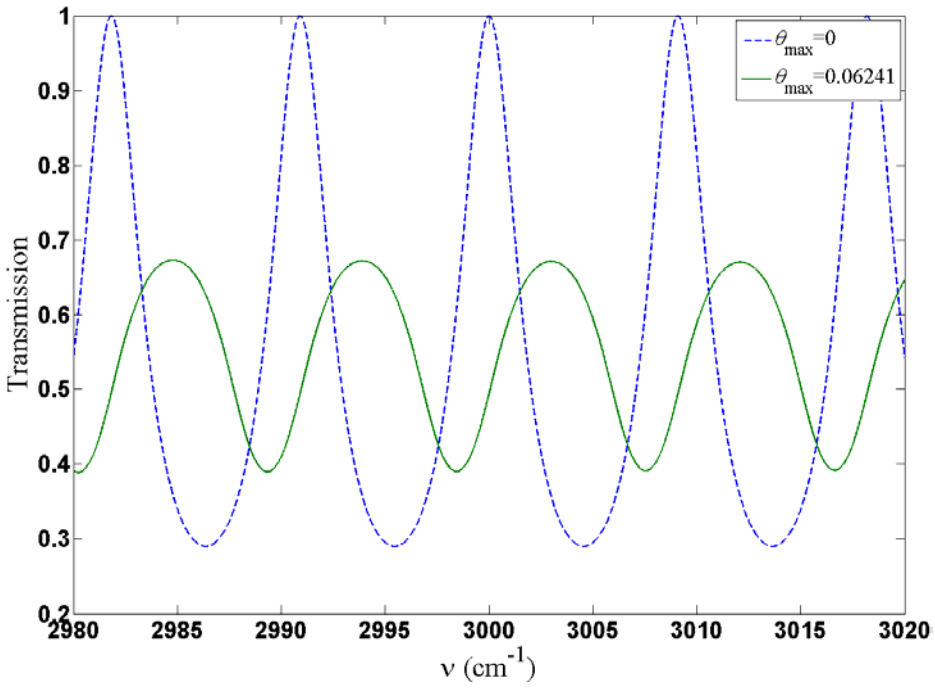

Figure 4.6- Final FPI transmission fringe pattern over all the angles of incidence. Here $R = 0.30$, $nd = 0.05$cm, $\theta_{\max} = 0.0624$rad.

4.3.1. $f/\#$ effect and FPI's optical thickness.

The degree of change in the FPI fringes depends directly on three values; the F number, FPI's cavity length and the wavelength. Therefore, in this section we present some examples in order to check in what cases the FPI fringes are seriously affected.

4.3.1.1. Narrow gap FPI

As a first example, let us analyse the $f/\#$ effect on the FPI fringes if the interferometer's cavity length (sometimes called the *gap*) is very narrow ($0 \leq d \leq 10$ μm), here we will classify these cavity length values as short gap. Ideally, these short cavity lengths produce spectral wider FPI transmission fringes, which are practically flat over some relatively large wavelength region (Figure 4.7). When the FPI cavity length is equal to zero $(d = 0)$ the FPI fringe pattern is equal to 1. Moreover, if the cavity length is around $d = \lambda/4$ the transmission will drop to a minimum whose value depends on the reflectivity (Figure 4.7). As FPIs with short cavity length are practically insensitive to the $f/\#$ effect it is possible to use a $f/\#$ as low as $f/1$ or $f/2$. This is a good since the amount of power arriving at the detector drops rapidly with increasing f

number by approximately $1/\left[4\left(f/\#\right)^2\right]$. Hence as low $f/\#$ values are allowed therefore lower source temperatures are required, saving power and increasing reliability.

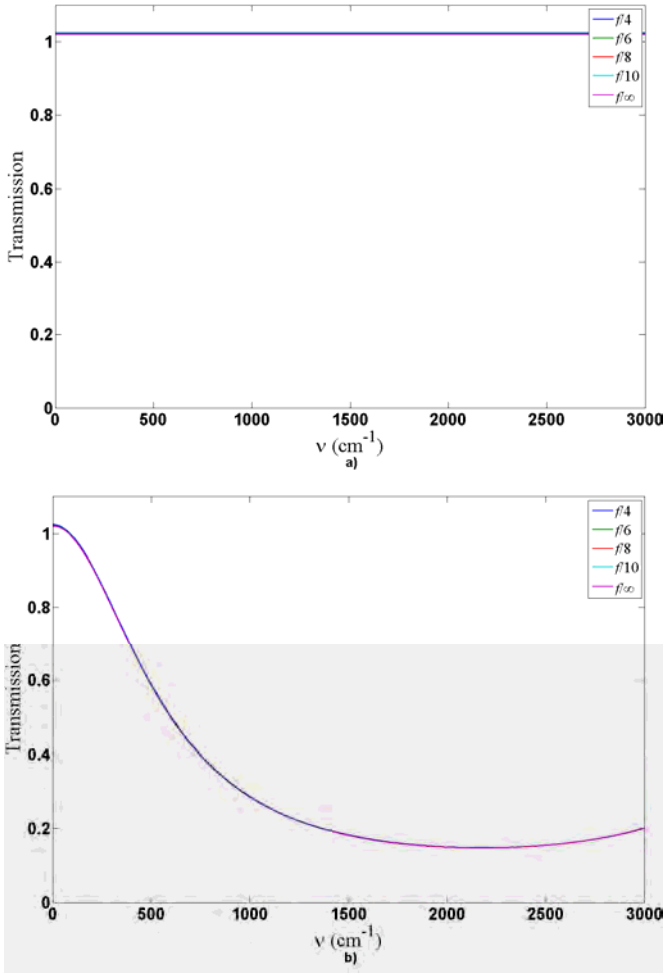

Figure 4.7- Typical FPI transmission fringe pattern for short cavity lengths and different $f/\#$ values. a) cavity length $d = 0$ µm; b) cavity length $d = 1.15$µm. In both cases $R = 0.45$.

FPIs with narrow cavity lengths can be employed as a spectral chopper which can be exploited to design another type of gas sensor. For instance in figure 4.7 the transmission is 1 at 2300 cm^{-1} when $d = 0$ µm and this drops to near 0.15 when $d = 1.15$ µm. This change in transmission can be utilised to induce modulation and in combination with a band pass filter a reliable gas sensor can be designed. Thus modulation can be induced by scanning the cavity length should by $\Delta d = \lambda_0/4$ µm. This cavity length scan move the FPI minimum transmission point to the wavelength λ_0, ideally where the absorption band centre of the target molecule occurs.

4.3.1.2. Medium gap FPI

As a second example, let us review a FPI with larger cavity length value, in the region of $10 \leq d \leq 50$ μm. For this cavity length range the FPI fringes will have a very large free-spectral range (FSR). These fringes combined with an infrared narrow band pass filter can also be employed to design a gas sensor; which we called the 'the medium gap sensor'. Here, one wide FPI fringe covers practically all the absorption band of band the target molecule, to induce modulation the cavity length is scanned producing a FPI fringe shift. For instance, in figure 4.8 the FPI fringes for two cavity lengths, $d = 10$ μm and 50 μm, and different $f/\#$ are presented. Here it is seen that for the medium gap the $f/\#$ effect is not severe when using low f numbers (ie $f/4$) just causing a small loss in the transmission peaks. The $f/\#$ effect on the FPI fringes can be practically eliminated by selecting a slightly larger $f/\#$ (i.e. $f/8$) with a penalty of a power reduction.

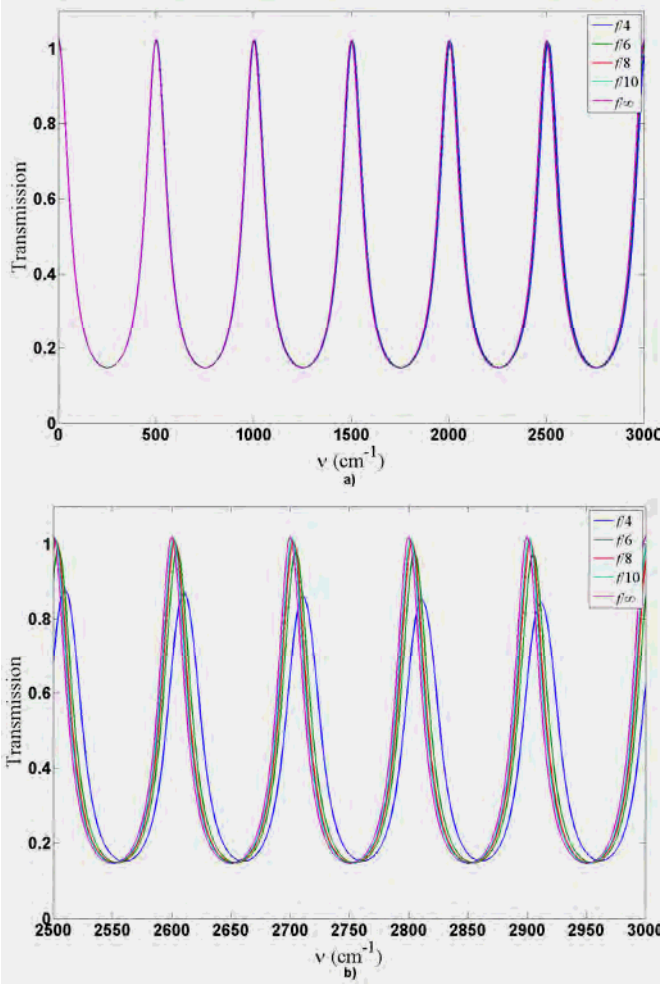

Figure 4.8- FPI transmission fringes with cavity lengths of 10-50 μm and different $f/\#$ values. a) cavity length $d = 10$μm; b) cavity length $d = 50$μm.

4.3.1.3. Wide gap FPI

Another case of interest is the FPI with cavity length within the range $0.055 \leq d \leq 0.3$ cm. This cavity length range is called here the wide gap and indeed the gas sensors presented in this work utilise FPIs with these characteristics. Therefore here we will review the $f/\#$ effect for two FPIs one with $d = 0.05$ cm and other with $d = 0.28$ cm.

In the first case when $d = 0.05$ cm the FPI fringes have a $\mathrm{FSR} = 10\mathrm{cm}^{-1}$ which can match some ro-vibrational absorption lines of CH_4 in the 3100 cm^{-1} region. In figure 4.9 some FPI transmission fringes patterns for different $f/\#$ values are shown; we used $R = 0.45$ and $nd = 5 \times 10^{-2}$cm. In this figure the FPI fringe patterns with lower $f/\#$ are severely affected, in contrast the FPI fringe pattern less affected are those for which the $f/\#$ is larger. Consequently, it is essential to look for an optimum $f/\#$ value that guarantees the best compromise between the FPI fringes deformation and the amount of power transferred to the detector.

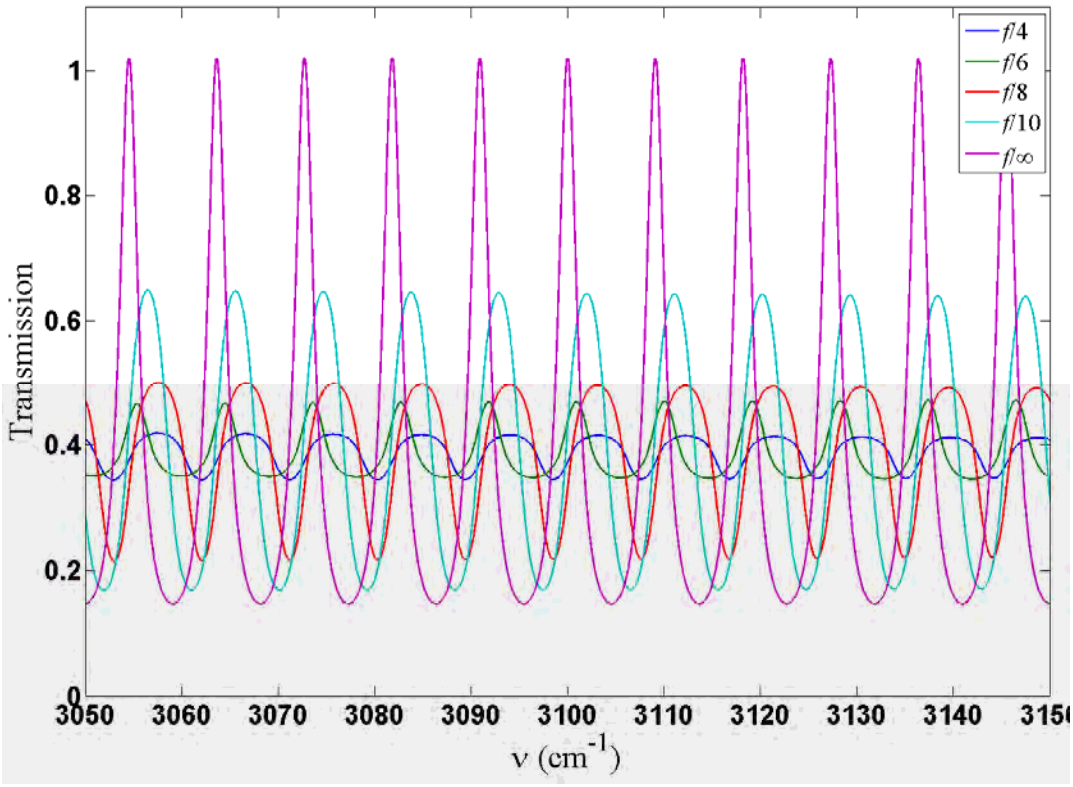

Figure 4.9- FPI transmission fringes considering a cavity length $d = 5 \times 10^{-2}$cm and different $f/\#$ values.

Finally, let us analyse a FPI with cavity length $d = 0.28$cm, a typical value for a CO_2 sensor since this cavity length value produces FPI fringes that match some of the CO_2 absorption ro-vibrational lines of the fundamental band at 4.3 μm. As this cavity length is quite large strong effects on the FPI fringes are expected. For instance, some spectral FPI fringes for different $f/\#$ values and $R = 0.45$ are shown in figure 4.10. Here for low $f/\#$ values $(< f/8)$ the FPI fringes are practically destroyed in the 2300 cm^{-1} region, as in the case of $f/2$ where the FPI fringes are quickly affected and practically a flat transmission of 40% is obtained, which is disastrous for the wide gap sensor! In contrast at higher $f/\#$ values $(f/18)$ the FPI fringes are better defined in the region of 2300 cm^{-1}. This implies that in order to get well defined FPI fringes when $d = 0.28$ it is essential to use large $f/\#$ values $(\geq f/18)$ (Figure 4.11). This represents a problem since the power reaching the detector will be compromised by the high $f/\#$. Consequently it is vital to use an optimization procedure to find the optimum $f/\#$ value that guarantees the best compromise between FPI fringe contrast and transferred power. In figures 4.10 and 4.11 the captions $F/\# = \text{ideal}$ are for a FPI illuminated with a collimated beam (f/∞).

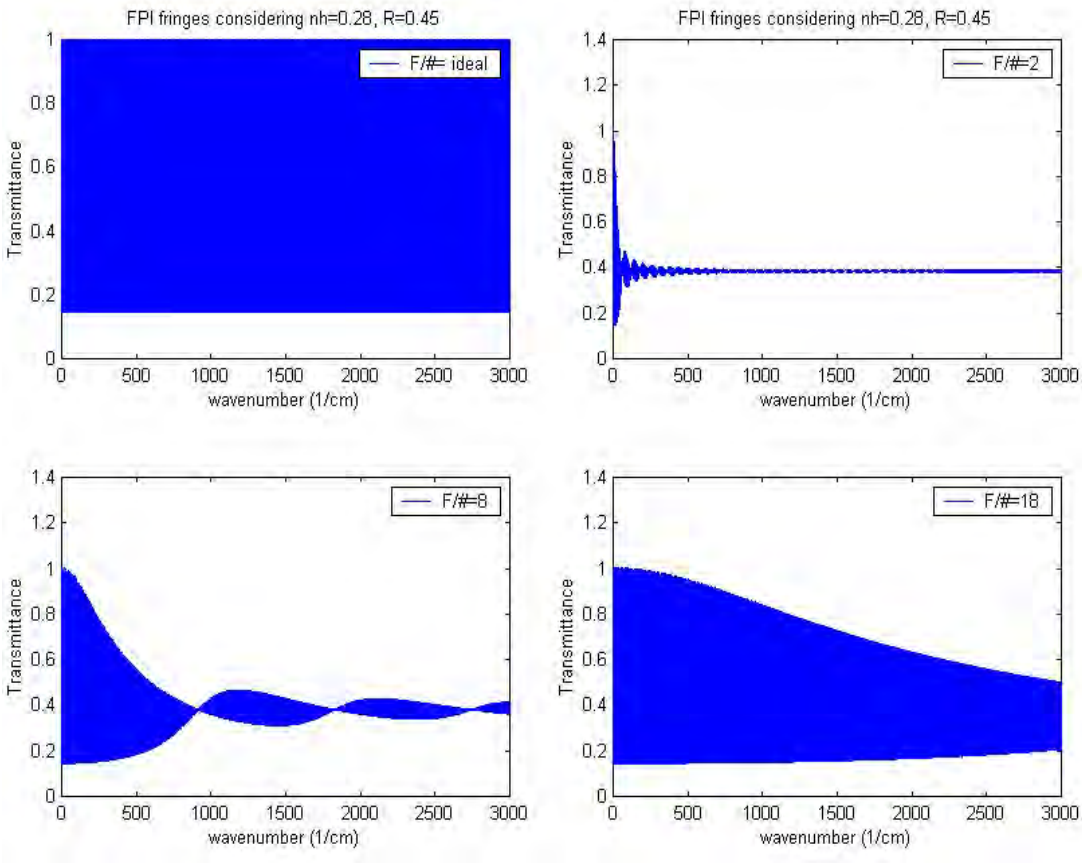

Figure 4.10- FPI transmission fringes considering a cavity length $d = 0.28$ cm and different $f/\#$ values

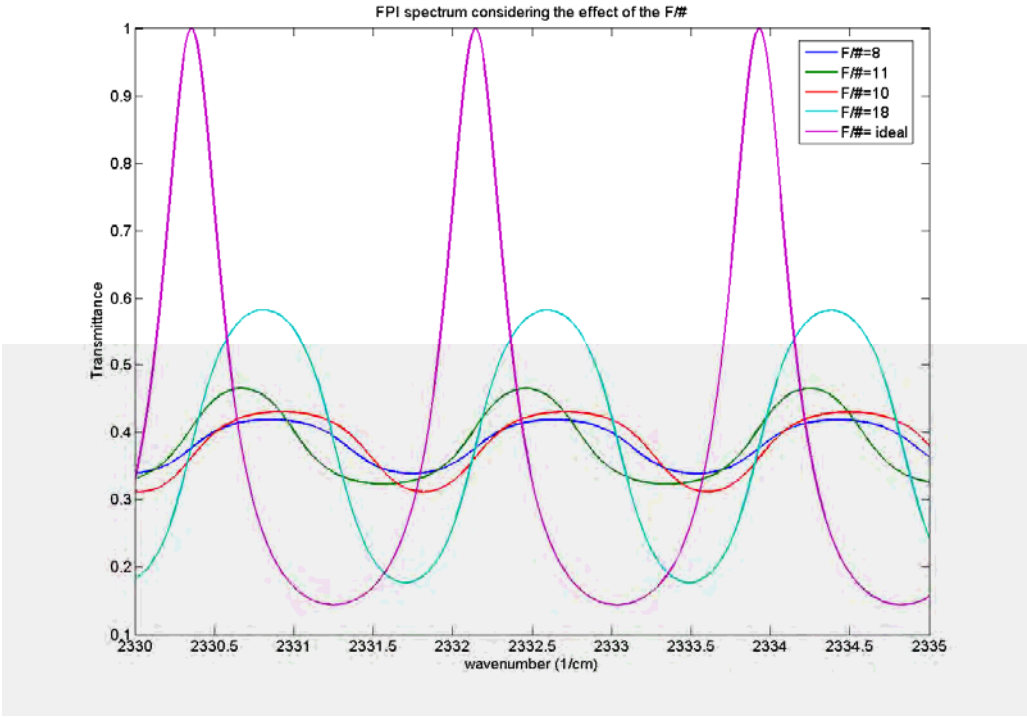

Figure 4.11- FPI transmission fringes considering a cavity length $d = 0.28$cm and large $f/\#$ values.

4.4. Parasitic reflection effects

Additionally to the $f/\#$ effect over the spectral FPI transmission fringe pattern reviewed in previous section other effects can affect the transmission fringe pattern. In the real FPI additional spectral FPI fringe patterns can be present which are due to internal reflections occurring in the FPI mirrors (Figure 4.12), we call these 'spectral parasitic reflection fringes' (SPRF). These SPRF can produce effects on the main FPI fringe pattern since these can produce a sort of interference. In practise our FPI is formed by two plane parallel mirrors (Figure 4.1) so we have two 'sources' of SPRF. As stated before SPRF are basically Fabry-Perot fringes [1], and therefore these are described by the Airy formula given in equation (4.1) and for clarity let us rewrite this for the SPRF as

$$I_{mul}\left(R_m, n_m, d_m\right) = \frac{1}{1 + \left(\frac{4R_m}{1-R_m}\right)^2 \sin^2\left(2\pi n_m d_m \nu \cos\theta\right)}, \tag{4.13}$$

where R_m is the reflectivity of the plates surfaces, n_m is the refractive index of the plate and d_m is the plate thickness.

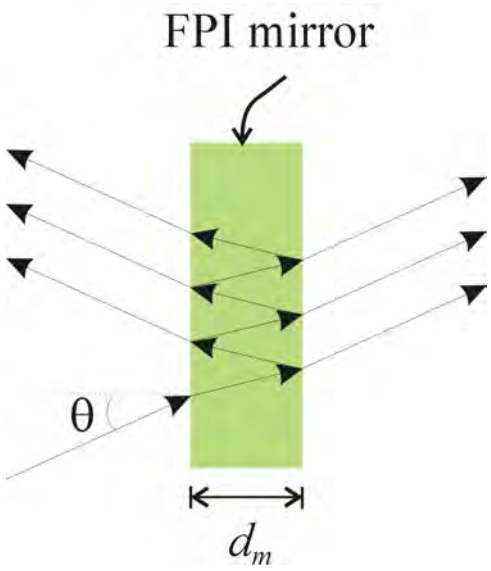

Figure 4.12- Multiple beam fringes on the FPI mirrors.

For instance, we recorded an FTIR transmission scan of a 0.2 mm thickness pyrex substrate which was coated with a 444 nm thickness ZnS layer (Figure 4.13); the FTIR resolution scan was 1 cm^{-1}. SPRF due to the pyrex substrate are clearly seen in the inset of figure 4.13 which shows a detail of the FTIR scan. The free spectral range (FSR) of these SPRF is related to the thickness d_m and the substrate refractive index n_m which led to have $\mathrm{FSR} = 1/(2n_m d_m) = 17.24 \mathrm{cm}^{-1}$ with $n_m = 1.47$ (pyrex refractive index). It is seen that the measured FSR match very well with the calculated value.

SPRF can introduce several undesirable effects on the final FPI fringe pattern, especially losses in fringe contrast. SPRF can be reduced and sometimes practically eliminated by using an antireflection coating on the incident surface of the plate or by wedging the plate. The wedge can be conceived as a type of defect in the parallelism of the plate however it is useful in some cases and therefore the plates can be deliberately fabricated with a wedge angle. Hence, let us review carefully some practical cases to check where SPRF are troublesome and additionally we propose possible solutions to reduce these fringes.

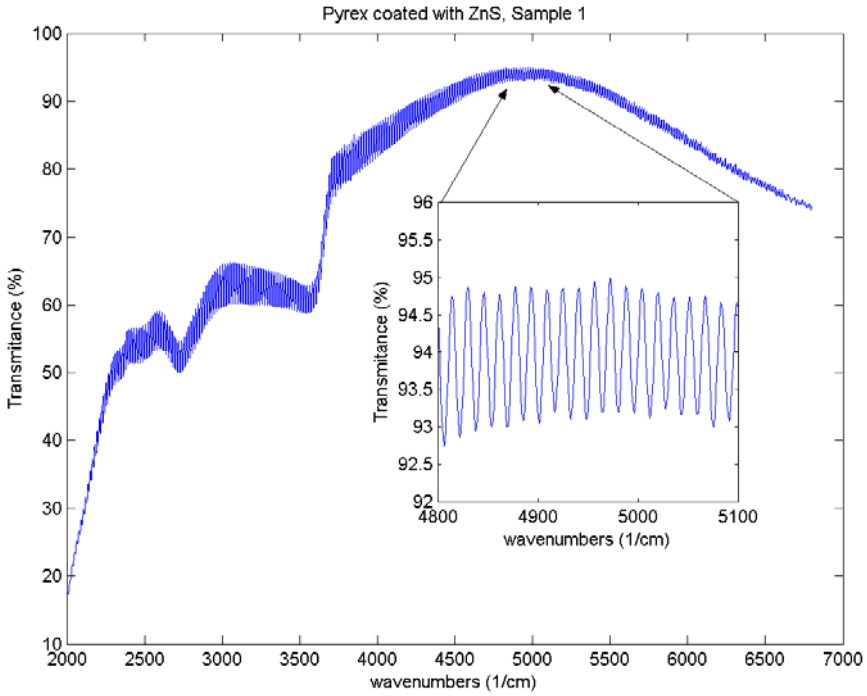

Figure 4.13- FTIR scan of a Pyrex substrate 0.2 mm thickness coated with a ZnS layer 444 nm. In the small box a detail of the scan shows the SPRF produced on the pyrex substrate.

A practical FPI that needs to be analysed is the one formed by two plane and parallel mirrors (Figure 4.14). Here, the FPI mirrors are coated to produce the required reflectivity, whilst the incident surfaces are uncoated. The coating is a thin layer of thickness d_{z1} and d_{z2} and refractive index n_z.

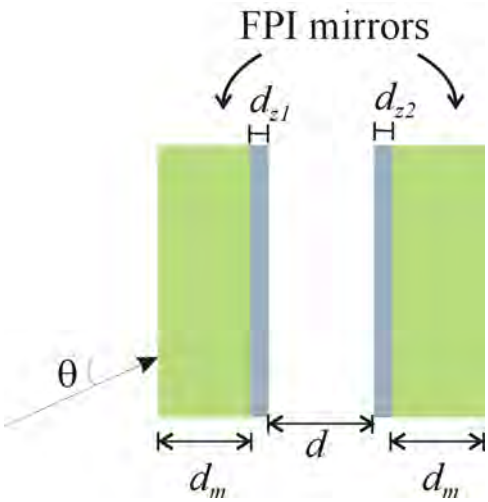

Figure 4.14- FPI with two plane and parallel mirrors coated with a thin film layer.

Here, if the full FPI is seen as a pile of thin films the final FPI transmission fringe pattern can be calculated using the characteristic matrix. The characteristic matrix of the whole medium can be expressed as [1]

$$\mathbf{M} = \prod_{j=1}^{N} \mathbf{M}_j = \begin{bmatrix} a & ib \\ ic & d \end{bmatrix}, \tag{4.14}$$

where $\mathbf{M}_j$ is the characteristic matrix of the jth film, which for an unpolarised beam it is given by [4]

$$\mathbf{M}_j = \begin{bmatrix} \cos\left(2\pi n_j d_j \nu \cos\theta_j\right) & -\frac{i}{n_j}\sin\left(2\pi n_j d_j \nu \cos\theta_j\right) \\ -i n_j \sin\left(2\pi n_j d_j \nu \cos\theta_j\right) & \cos\left(2\pi n_j d_j \nu \cos\theta_j\right) \end{bmatrix}. \tag{4.15}$$

The reflectance of the thin films assembly can be obtained by using the following definition [4]

$$\begin{bmatrix} B \\ C \end{bmatrix} = \begin{bmatrix} a & ib \\ ic & d \end{bmatrix} \begin{bmatrix} 1 \\ n_e \end{bmatrix}, \tag{4.16}$$

where n_e is the refractive index of the exit medium. Thus, the reflection coefficient is given by

$$r = \frac{n_0 B - C}{n_0 B + C}, \tag{4.17}$$

where n_0 is the refractive index of the incident medium, finally the reflectivity of the full assembly is given by

$$R_{FP}\left(\nu, R, n, d, \theta\right) = \left(\frac{n_0 B - C}{n_0 B + C}\right)\left(\frac{n_0 B - C}{n_0 B + C}\right)^{*}. \tag{4.18}$$

Therefore, the FPI fringe transmission pattern assuming no absorption in the layers is given by

$$I_{FP}(\nu, R, n, d, \theta) = 1 - R_{FP}(\nu, R, n, d, \theta). \quad (4.19)$$

Finally, as in our project we intend to place the FPI at the image point it is necessary to take into account the $f/\#$ effect. Hence by substitution of equation (4.19) into equation (4.12) the spectral FPI transmission fringe pattern pondering all the factors, the $f/\#$, the optical thickness and SPRF, can be obtained by

$$I_{FP}(R, n, d, \nu, \theta_{\max}) = \frac{1}{1/2\sin^2\theta_{\max}} \int_0^{\theta_{\max}} \cos\theta \sin\theta \left[1 - R_{FP}(\nu, R, n, d, \theta)\right] \mathrm{d}\theta. \quad (4.20)$$

To get an idea of how the etalon fringes affect the final FPI fringe pattern let us review some examples. In these examples the FPI is formed by two CaF_2 substrates of 1 mm thickness, and refractive index $n_m = 1.43$ which are coated with a ZnS layer of 380 nm thickness, and refractive index $n_{z1} = n_{z2} = 2.25$ $n_{z1} = n_{z2} = 2.25$. In our simulations we neglect changes in the refractive index as a function of the frequency (cm^{-1}). These mirrors have reflectivity $R \approx 0.30$ at 4.3 μm.

4.4.1.1. Narrow gap FPI and SPRF.

In order to observe both effects, due to SPRF and to the $f/\#$, we evaluated the spectral FPI transmission fringe pattern for different cavity length (d) values. In the first example we considered a narrow gap FPI with $d = 0$ and $d = 1.15$ μm, whose FPI fringe patterns for different $f/\#$ were calculated using equation (4.20) and the results are shown in (Figure 4.15). Here, when $d = 0$ cm there are two sets of SPRFs one is due to the CaF_2 substrate and the other one is due to the ZnS layer. The SPRF due to the CaF_2 have a $\mathrm{FSR} \approx 3.49 \mathrm{cm}^{-1}$ and are the 'oscillations' observed over the main FPI transmission curve (Figure 4.15a). The second set of SPRF which is due to the ZnS has a $\mathrm{FSR} \approx 2923.97 \mathrm{cm}^{-1}$. This long FSR is due to $d = 0$ cm and therefore the separation between the ZnS layers is 0 cm, so ideally the two layers are joined together making a layer of $2d_{z1}$ thickness, consequently the $\mathrm{FSR} = 1/(2n_{z1}2d_{z1}) = 2923.97 \mathrm{cm}^{-1}$ (Figure 4.15a). Moreover in this figure the FPI fringe patterns for the ideal collimated beam (f/∞) do not present SPRF; this is because we want to remark the changes in the patterns due to the f number and the SPRF effects.

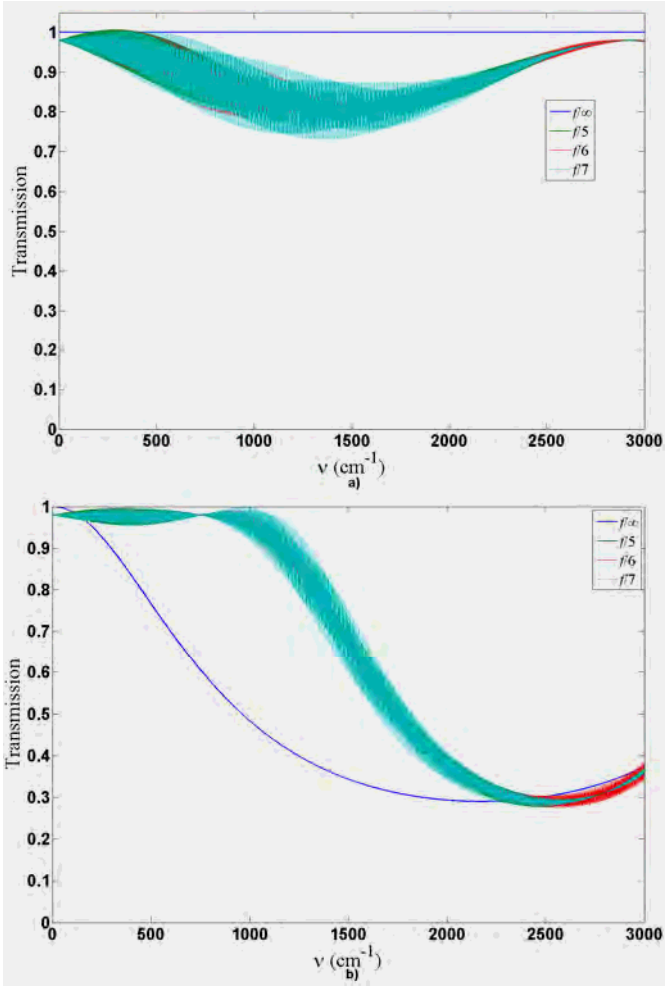

Figure 4.15- FPI fringes for a narrow gap FPI considering the $f/\#$ and SPRF. a) $d = 0\,\mu m$, b) $d = 1.15\mu m$.

4.4.1.2. Medium gap FPI and SPRF.

As a second example let us analyse a FPI with cavity length of $d = 10.7\mu m$ whose FPI transmission fringe pattern, counting the $f/\#$ effect and SPRF, is shown in figure 4.16. Here, SRPF looks like noisy oscillations over the principal FPI transmission fringe. The contrast of the FPI fringes is less affected at 2000-3000 cm^{-1} since the reflectivity of the CaF_2/ZnS mirrors is maximum at this region. As in previous section the FPI fringe pattern for the collimated beam (f/∞) do not present SPRF (Figure 4.16). This to remark the changes in the fringe patterns due to the f number and the SPRF effects. In figure 4.17 a measured FTIR background spectrum it is shown; the scan was taken using a $0.5cm^{-1}$ resolution. The background spectrum shows the energy measured by the FTIR; the FTIR's f number it is around $f/7$. From these figures we can say that the $f/\#$ effect and the SPRF do not affect dramatically the FPI fringe pattern

when narrow gaps are used. In figure 4.17 the simulated transmission pattern was normalized to one. The measured spectrum represents the FTIR background spectrum which means that it is normalized, and here we need to consider that the light source and the FPI reflectivity are changing with frequency. Here to compare with the simulated spectrum we can measure the FPI fringe contrast, which is basically the ratio between the peak of the fringe and the valley of the fringe. By carrying out this operation we can get that the measured FPI fringes contrast is very close to the simulated fringes contrast.

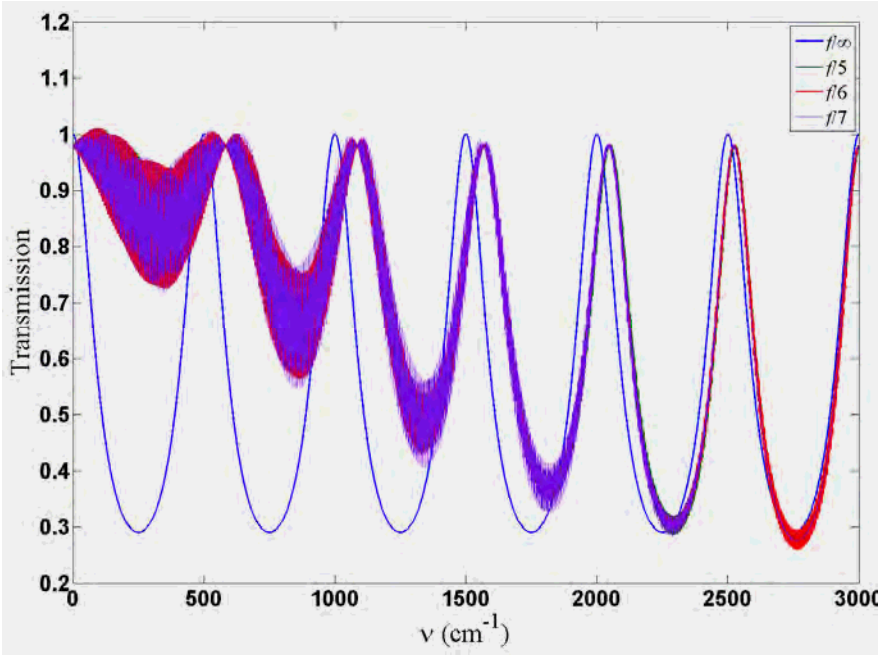

Figure 4.16- FPI fringes for a cavity length $d = 10\mu m$ counting the $f/\#$ and SPRF.

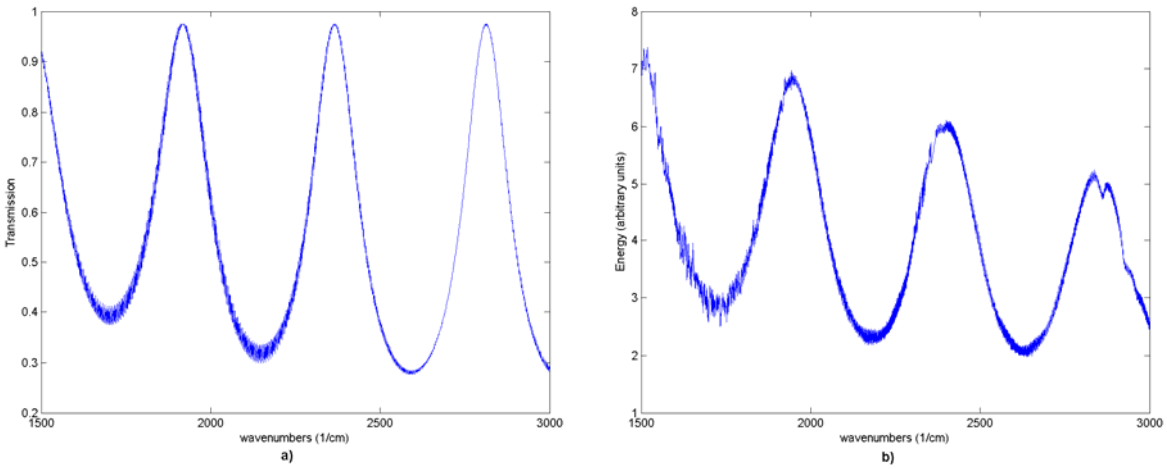

Figure 4.17- Simulated and measured FPI fringe patterns pondering the $f/\#$, SPRF and $d = 10\mu m$. a) simulation results, b) Measured FTIR background spectrum with a resolution of 0.5 cm^{-1}. (Arbitrary units).

4.4.1.3. Wide gap FPI and SPRF

As third example, let us review the case of a FPI with a cavity length $d \approx 0.05$cm, which is of relevance for the CH_4 sensor. The simulated FPI fringes taking into account the $f/\#$ effect, SPRF and its cavity length are shown in figure 4.18. Here it is seen that for some combinations of substrate thickness, substrate refractive index, cavity length and the $f/\#$ the SPRF effect on the FPI fringe pattern can be very strong, seriously reducing the fringe contrast. For instance in figure 4.19 a couple of FTIR background measurements for a FPI with cavity length $d = 0.045$ cm are is shown, the SPRF effect it is seen better on the FTIR scan with higher resolution.

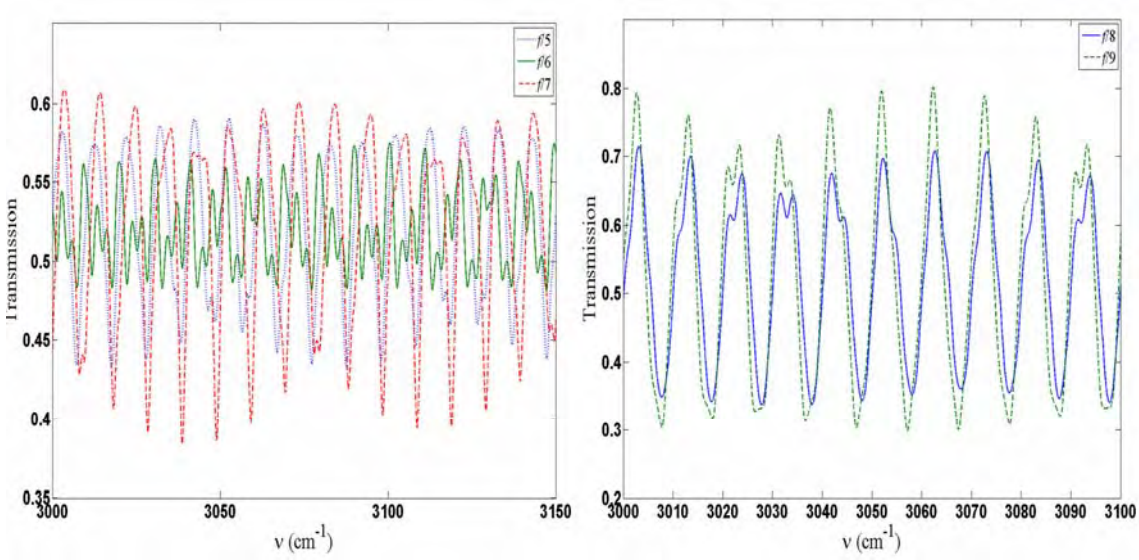

Figure 4.18- Simulated FPI fringe pattern considering $d = 0.05$ cm SPRF and the $f/\#$.

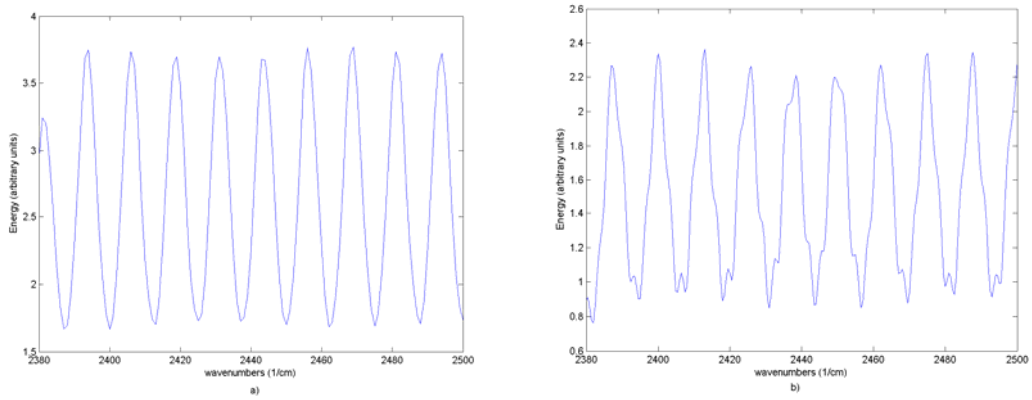

Figure 4.19- FTIR measurements for a FPI with $d = 0.045$cm. a) Background FTIR scan with resolution 4 cm^{-1}; b) Background FTIR scan with resolution 2 cm^{-1}.

Therefore, as a fourth example let us analyse the case of a FPI with cavity length $d \approx 0.28$ cm, as would be utilised in a CO_2 sensor. The simulated FPI fringe pattern

including the $f/\#$ effect (for $f/7$) and SPRF are shown in figure 4.20. In this plot we observe big losses in transmission on the FPI fringes but furthermore that these fringes are not equally separated, which represents a problem for gas sensors based on correlation spectroscopy. A measured background FTIR scan with a resolution of 1 cm^{-1} of a FPI with $d \approx 0.28$ cm is presented in figure 4.21. Here, the strong effect of the etalon fringes on the FPI fringes is clearly observed, also the measurement is close to the simulation, the small differences in the FPI fringes separation is due to small variation in the cavity length.

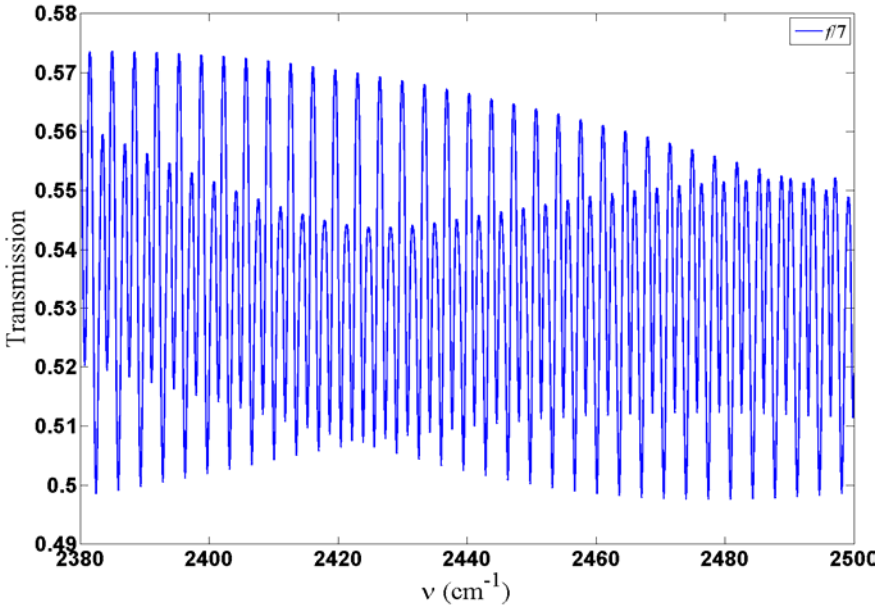

Figure 4.20- Simulated FPI fringe pattern pondering a $d = 0.29$cm, $f/7$ and the SPRF.

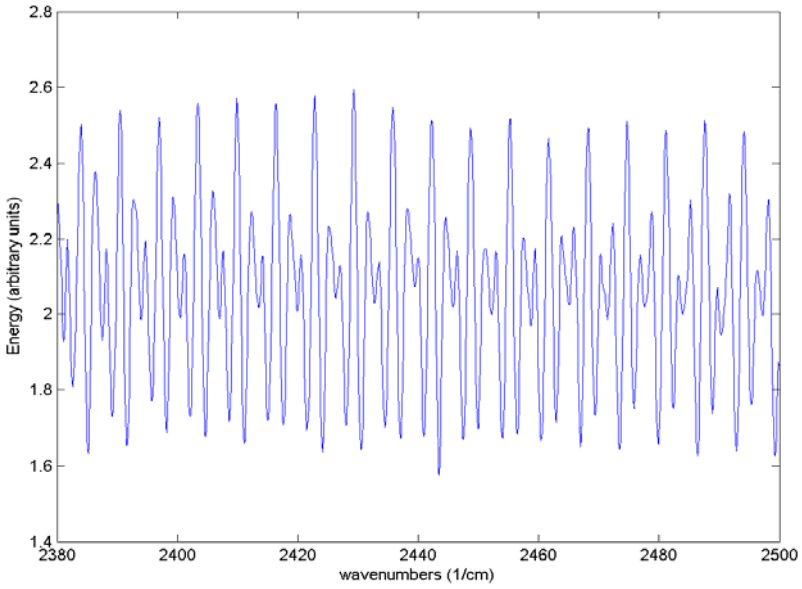

Figure 4.21- FTIR background spectrum for a FPI with cavity length $d = 0.29$cm.

4.4.2. Minimizing the SPRF effects

The SPRF can be reduced by several methods, one is by applying an antireflection coating on the incident and exit side of the FPI mirrors. Another way is by selecting the thickness of the substrates which can help to reduce the SPRF depending of the required FSR of the FPI transmission fringes. A third solution to reduce the SPRF is by use wedged mirrors.

The thickness of the mirrors can help to reduce the SPRF effect, for instance in the examples presented in previous section we consider CaF_2 substrates of 1 mm thickness, which leads to a FSR of the SPRF equal to $\mathrm{FSR} \approx 1/(2 \times 1.43 \times 0.1) \approx 3.49\mathrm{cm}^{-1}$ which is almost 2 times the FSR of the main FPI fringe pattern. In figure 4.21 we observe an alternation of FPI fringes 1 strongly affected and the next one less affected; which can be explained by the fact that for every 2 FPI fringes there is 1 SPRF which produce a sort of destructive interference. Hence it is possible to change the mirror's thickness to try to reduce the effect of the SPRF.

For instance assuming two FPIs formed by two CaF_2/ZnS mirrors but in one FPI the CaF_2 substrates are 0.2 mm thickness while in the other substrates are 5mm thickness, and for both FPIs the mirrors ZnS coating layers are 380 nm thickness. For this cases the simulated FPI fringe pattern for the FPI with 0.2mm substrates it shown in figure 4.22, while the FPI fringe pattern for the 5mm substrates is shown in figure 4.23. In both cases the strong SPRF effects are reduced in comparison with the FPI fringe pattern obtained when substrates of 1mm are used (Figure 4.20). Moreover, in the case of the 0.2 mm thickness CaF_2 mirror wide SPRF are observed which have a $\mathrm{FSR} = 17.48\mathrm{cm}^{-1}$. In this case SPRF fringes are not strongly affected by the $f/\#$ since the thickness of the substrate is very thin so it behaves as a narrow gap FPI. Now in the case of the 5 mm thickness CaF_2 substrate the SPRF are reduced even more, here the SPRF are affected by the $f/\#$ since the CaF_2 substrate behaves as a FPI with very wide gap, therefore in this case the $f/\#$ effect helps to destroy the CAF_2 SPRF. It makes necessary a careful selection of the thickness to reduce the SPRF effects.

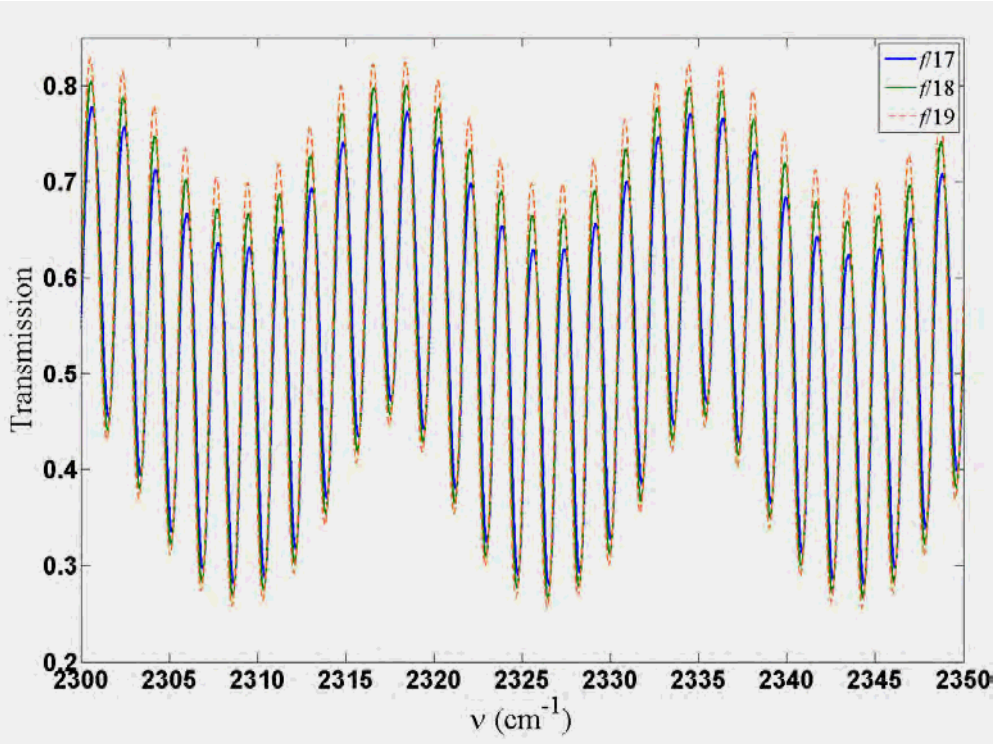

Figure 4.22- Simulated FPI fringes; $d = 0.28$cm, CaF_2 substrates 0.2 mm thickness.

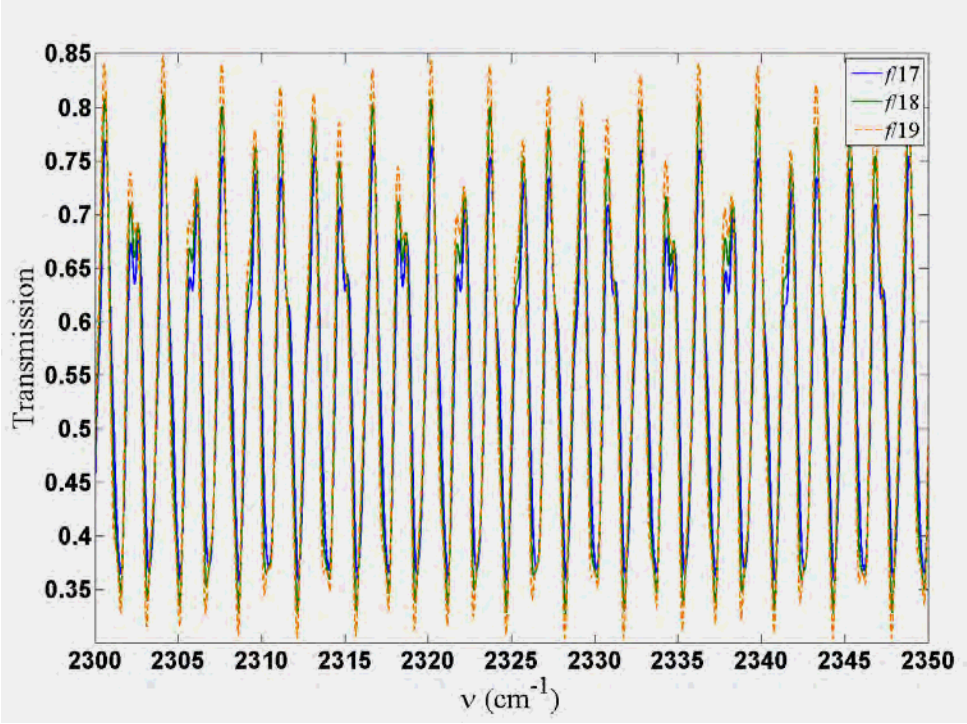

Figure 4.23- Simulated FPI fringes; $d = 0.28$cm, CaF_2 substrates 5 mm thickness.

As in some practical cases thick mirrors are not a good solution other methods to reduce the SPRF must be analysed. Another relatively simple method is by coating one

side of the FPI mirrors with an antireflection coatings (AR) as shown in figure 4.24 where $z3$ and $z4$ are the AR layers. Here the final FPI fringe pattern can be calculated using equation (4.20) as in the previous examples just that here we need to add two more thin layers (AR).

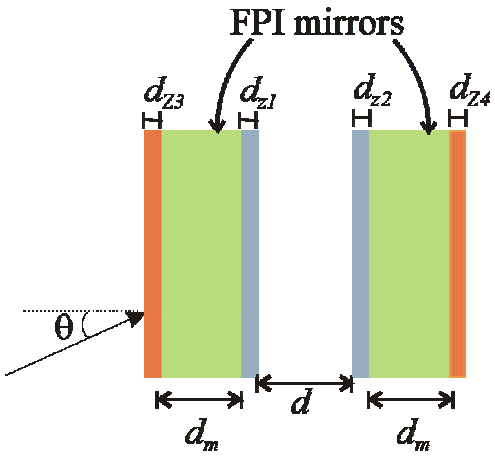

Figure 4.24- FPI with flat and parallel mirrors with AR coatings.

Therefore in order to check how the AR coatings can help to reduce the SPRF we calculated the final FPI fringe pattern considering CaF_2/ZnS mirrors with AR coatings. The mirrors of the FPI are the same as in previous example, so we have 1 mm thickness CaF_2 substrates coated in one side with ZnS and in the other side with AR. Hence, for instance, we select Cryolite (Na_3AlF_6) as the AR layer as it has a low refractive index, $n_{z3} = n_{z4} = 1.35$ and the thickness of these layers is given by $\lambda_0/(4n_{z3})$, for the CO_2 sensor $\lambda_0 = 4.3$µm. Here, the final FPI fringe pattern including the $f/\#$, SPRF and the AR coatings it is shown in figure 4.25. It is seen that the cryolite AR coatings help to reduce the SPRF and here a more uniform spectral FPI fringe pattern is produced. Moreover, to reduce even more the SPRF we can use thick mirrors coated with AR coatings as shown in figure 4.26 where the FPI fringe pattern is improved, here 5 mm CaF_2 substrates were considered. The correct choice of the AR coating and even the thickness of the FPI mirrors will depend directly on the FPI mirrors' substrate material.

Finally, the SPRF can be reduced as well by deliberately fabricating wedged FPI mirrors. Mansfield and Rutt 2002 [5] give a simple formula to select the wedge angle to reduce the number of etalon fringes on the substrate; this formula depends on the

refractive index of the substrate material and the clear aperture, in the next chapter we will discuss this with more detail.

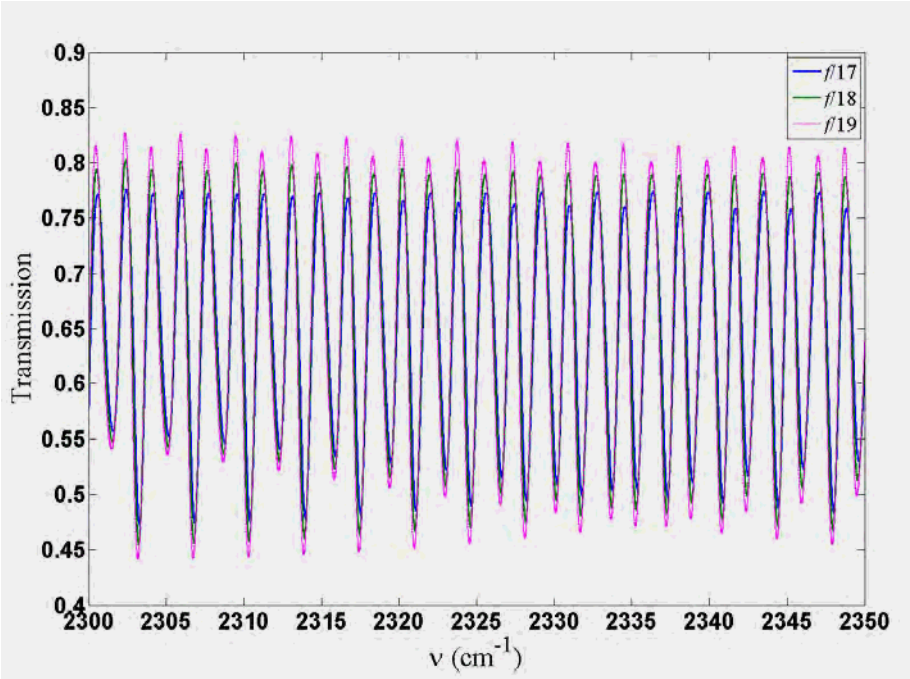

Figure 4.25- Simulated FPI fringe pattern for $d = 0.28$cm, CaF_2 substrates 1mm thickness with AR Cryolite layers.

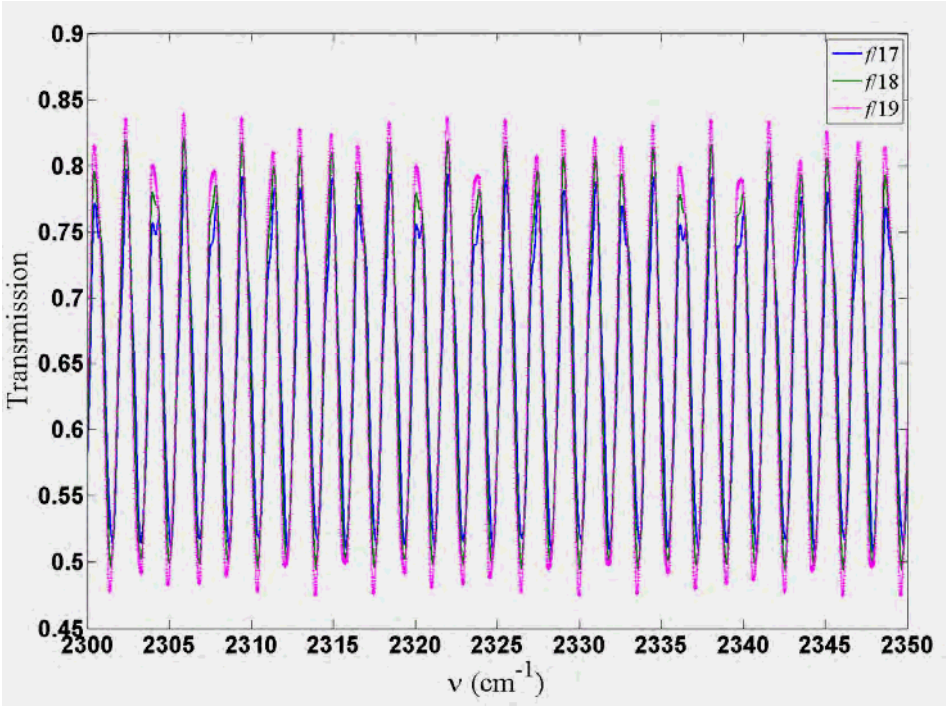

Figure 4.26- Simulated FPI fringe pattern for $d = 0.28$cm, CaF_2 substrates 2mm thickness, with AR Cryolite layers.

4.5. Conclusions

In this section the effect on the FPI transmission pattern when it is illuminated with a converging beam was reviewed. It is found that for narrow cavity lengths the f number effect is not important. For FPI with medium gap this effect can represent a problem for some combinations of cavity length, f number (especially low $f/\#$) and reference wavelength. However it is shown that for a FPI with wide gap this effect is really important and must be carefully pondered to correctly calculate the FPI transmission fringe pattern. We also reviewed the effect of the 'spurious parasitic reflection fringes' (SPRF) which occurs within the FPI mirrors substrates. Moreover it was shown that this can be an issue especially for FPIs with wide gaps. Finally we present some options to reduce the SPRF, the best option will depend on the application. For instance a thicker substrate can be a solution in some cases however in some applications this is unreliable as in MEMS integration where the best solution may be antireflection coatings. Based on all this information we can conclude that the SPRF, the $f/\#$ effect, the reference wavelength and the cavity length should be carefully taken into account to correctly calculate the performance of a gas sensor based on spectroscopy correlation using a FPI with long cavity length.

4.6. References

1. M. Born and E. Wolf, *Principles of Optics*, 3rd Edn Great Britain, Pergamon Press, 1965

2. P. L. King, M. S. Ramsey, and G. A. Swayze, *Infrared Spectroscopy in Geochemistry, Exploration Geochemistry, and Remote Sensing*, Canada, 2004

3. E. L. Dereniak and G. D. Boreman, *Infrared Detectors and Systems*, USA, John Wiley and Sons Inc., 1996

4. H. A. Macleod, *Thin-Films Optical Filters* Bristol, Institute of Physics Publishing, 2001

5. C. D. Mansfield and H. N. Rutt, Evaluation of Multiple beam interference effects in infrared gas spectroscopy, *Meas. Sci. Technol.* **10**, p. 206-210, 1999